Synthesis of Organic Materials for Optoelectronic Applications

Frances Mary Tracey

Thesis submitted in fulfilment of the requirements for the degree of Doctorate of Philosophy

School of Chemistry

College of Science and Engineering

University of Glasgow

February 2024

Abstract

Organic electronics have seen a rapid development of research in this area in both academia and industry due to being lighter, more flexible and less expensive than conventional inorganic materials. This thesis describes the synthesis and characterisation of novel organic materials with the aim of optoelectronic applications.

The first chapter provides an introduction to organic semiconductors, focussing on their working principle from both a chemical and physical perspective. This is followed by a discussion on a few recent technologies developed in this field including some exemplar materials.

The second chapter describes the design and synthesis of spiro-OMeTAD based polymers for application in perovskite solar cells. Spiro-OMeTAD is the benchmark hole transporting material for these devices due to its high performance on doping. Preliminary conductivity measurements determine the potential for these polymers to act as additives in perovskite solar cells. One of the polymer materials was incorporated into a device and the key parameters discussed.

In chapter three, the development of green chemistry inspired materials for perovskite solar cells were outlined. Initially, the design and synthesis of several imine-based small molecules were discussed. The optical, electronic and thermal properties are extensively studied. The triphenylamine derivatives were further studied in the later section of this chapter to determine their potential as hole transporting materials in perovskite solar cells.

Two flavin-fused truxenes are presented in chapter four. First, details of the successful synthesis and characterisation of these molecules are discussed before a variety of applications were attempted for these materials including organic light emitting diodes, organic field-effect transistors and sensors.

Finally, the last chapter describes a variety of fluorescent bio-mimetic materials based on either the flavin moiety or green fluorescent protein chromophore. The chapter is separated into two parts to discuss these individually. Flavins are natural redox-active molecules which have good stability and structural versatility. Green fluorescent proteins have been studied due to their good photoluminescence, photostability and sustainable production. Therefore, both have the potential for applications in optoelectronics.

Table of Contents

Acknowledgements

Firstly, I would like to thank my supervisor Professor Graeme Cooke for giving me the opportunity to undertake research in his group and for the continued guidance and support he has provided throughout my PhD. Thanks also to the EPSRC for funding my research.

I would like to thank the mass spectroscopy service, NMR service and the rest of the technicians and staff at the school of chemistry for their help.

I would also like to thank all the people who contributed to the worked described in this thesis in some way, with emphasis on our collaborators: Prof. Ifor Samuel and Prof. Graham Turnball at the University of St. Andrews, Prof. Peter Skabara, Dr. Pablo Docampo and Prof. Dave Adams at the University of Glasgow. Particular thanks to Dr. Ramakant Sharma, Dr. Joseph Cameron, Dr. Namrata Pant and Benjamin Vella for taking time to work on my materials.

A huge thanks to my colleagues and friends, both past and present Cooke group members, for their support and guidance throughout my PhD. Special hanks to postdoctoral researchers Dr. Michele Cariello, Dr. Alex Harkiss, Dr. Liam McCarron and Dr. Dylan Wilkinson for their expertise and time. To the PhD students that helped me at the start but left for new, exciting ventures Cosma Gottardi and Sondos Almahmoud. I'd like to give a huge thanks to the rest of the group who made my lab experience so enjoyable, namely Lewis Mackenzie, Ben Vella, Abdul-Wasir Shaka, Abarna Sekar, Wai Kin You, Gregor Macleod and my friends from around the Joseph Black Building particularly Marcin Giza, Nicki Fairbairn, Valentina Gauci, Connor MacDonald and Carolina Ojeda Porras.

To those I have failed to mention by name, I'm sorry but thanks to you too.

I would also like to thank my family members who have been a constant provider of motivation including my Aunt Beatrice, Grampa Robert and late Aunt Madge. I also appreciate the time spent out of the lab with good friends including Jess Goddard, Tess Stewart and Jenny Bone.

Finally, I would like to thank my parents, even though they had no idea what my research meant their constant support and encouragement helped me in so many ways throughout my PhD and I am forever grateful.

Author's Declaration

This thesis represents the original work carried out by Frances Mary Tracey, unless otherwise stated in the text.

The research described herein was carried out at the University of Glasgow, in the Department of Chemistry, under the supervision of Prof. Graeme Cooke, during the period of October 2019 – February 2024.

COVID Impact

My lab was closed from March 2020 – June 2020. On return to the lab, due to the number of Cooke group members and the size of the lab, a week-on week-off rota was put in place from July 2020 – December 2020. I was also unable to enter the lab in January 2021 due to postdoctoral grant funding ending and therefore taking priority for lab time. This prevented my research moving forward at the normal rate I expected. During the bi-weekly lab access I performed a number of reactions which needed to be halted at an earlier step than I would like to prevent decomposition before my return. Due to this lack of access a larger quantity of computational calculations were performed during this period. It also meant that final materials were produced later in my PhD than predicted, preventing delivery to collaborators with sufficient time to receive all the data.

Abbreviations

2-MA	2-methylanisole
a.u.	Absorbance units (dimensionless)
ACQ	Aggregation-caused quenching
AFM	Atomic force microscopy
AIBN	Azobisisobutyronitrile
AIE	Aggregation induced emission
AM 1.5G	Air mass 1.5 global
BFP	Blue fluorescent protein
BHJ	Bulk heterojunction
CFP	Cyan fluorescent protein
CIE	Commission Internationale de l'éclairage
CV	Cyclic voltammetry
DF	Delayed fluorescence
DFT	Density functional theory
DMF	N, N-dimethylformamide
DNT	2,4-Dinitrotoluene
DSSC	Dye-sensitised solar cell
EA	Electron affinity
E_F	Fermi level
E_g	Band gap
EIL	Electron injection layer
EL	Electroluminescence
EML	Emission layer
EQE	External quantum efficiency
ETL	Electron transporting layer
eV	Electron volt
FAD	Flavin adenine dinucleotide
Fc	Ferrocene
Fc^+	Ferrocenium
FF	Fill factor
FK209	Tris(2-(1H-pyrazol-1-yl)-4-$tert$-butylpyridine)cobalt(III) tri[bis(trifluoromethane)sulfonimide

FMN	Flavin mononucleotide
FP	Fluorescent protein
FRET	Fluorescence resonance energy transfer
FTO	Fluorine-doped tin oxide
GFP	Green fluorescent protein
GPC	Gel permeation chromatography
HIL	Hole injection layer
HMDS	Hexamethyldisilazane
HOMO	Highest occupied molecular orbital
HTL	Hole transporting layer
HTM	Hole transporting material
HWLED	Hybrid white light emitting diodes
IC	Internal conversion
I_{DS}	Source-drain current
IP	Ionisation potential
IQE	Internal quantum efficiency
IR	Infrared
IRENA	International Renewable Energy Agency
ISC	Intersystem crossing
ITO	Indium tin oxide
J_{SC}	Short circuit voltage
J-V	Current- voltage
K	Kelvin
LED	Light emitting diode
LiTFSI	bis(trifluoromethane)sulfonimide lithium salt
LUMO	Lowest unoccupied molecular orbital
MG	Microgel
MMA	Methyl methacrylate
MOF	Metal-organic framework
MOS	Metal-oxide semiconductor
MOSFET	Metal-oxide semiconductor field effect transistor
MP	Max power
MS	Mass spectrometry
NAC	Nitroaromatics

NMR	Nuclear magnetic resonance spectroscopy
OFET	Organic field effect transistor
OLED	Organic light emitting diode
OPV	Organic photovoltaic
OSC	Organic solar cell
OTFT	Organic thin film transistors
P3HT	Poly(3-hexylthiophene)
PAH	Polycyclic aromatic hydrocarbon
PCE	Power conversion efficiency
PDI	Perylenediimide
PL	Photoluminescence
PLQY	Photoluminescence quantum yield
PMMA	Poly(methyl methacrylate)
ppm	Parts per million
PSC	Perovskite solar cell
PTAA	Poly[bis(4-phenyl)(2,4,6-trimethylphenyl)amine]
PV	Photovoltaic
R_f	Retention factor
RFP	Red kaede fluorescent protein
RISC	Reverse intersystem crossing
rt	Room temperature
S_0	Ground state
S_1	Singlet excited state
SCLC	Space charge limited current
SHE	Standard hydrogen electrode
Spiro-OMeTAD	2,2'7,7'-tetrakis(N,N-di-p-methoxyphenyl-amine)9,9'-spirobifluorene
SPR	Surface plasmon resonance
SWV	Square wave voltammetry
T	Temperature
T_1	Triplet excited state
TADF	Thermally activated delayed fluorescence
TBAF	Tetra-*N*-butylammonium fluoride
t-BP	4-T*ert*-butyl pyridine
TC	Triple cation

TCO	Transparent conductive oxide
TD-DFT	Time delayed density functional theory
T_g	Glass transition temperature
THF	Tetrahydrofuran
TiO_2	Titanium dioxide
TLC	Thin layer chromatography
TNT	Trinitrotoluene
TOF	Time-of-flight
TPD	N, N'-bis(3-methylphenyl)-N, N'-diphenylbenzidine
TTF	Tetrathiafulvalene
UV	Ultraviolet
V_{DS}	Source-drain voltage
V_{GS}	Source-gate voltage
Vis	Visible
V_{OC}	Open circuit voltage
V_T	Threshold voltage
ΔE_{ST}	Energy gap between triplet and singlet state
ϵ	Molar extinction coefficient
π	pi bonding orbital
π^*	pi antibonding orbital
σ	sigma bonding orbital

1 Introduction

1.1 Preface

Climate change is a major concern affecting our planet, with some of these changes occurring at a more rapid rate than scientists previously predicted.[1–4] It has been determined that the worlds' current warming trend is predominantly a result of human activities, in particular the use of fossil fuels as our main energy source which produce greenhouse gases, most notably carbon dioxide, which trap heat in our atmosphere and reduce air quality.[5,6] When discussing alternative energy sources, renewable energy (including solar energy, wind energy, ocean energy, bioenergy, hydropower and geothermal energy) is generally the focus due to their cleanliness and availability.[7]

In the introduction an overview of the underlying principles of semiconductors, followed by a discussion on recent technologies relevant to this thesis will be discussed. A brief history and the fundamental aspects of each application will be introduced as well as a few example organic molecules used in the various architectures. A more in-depth discussion of organic materials for such application will be highlighted in the relevant chapters.

1.2 Organic Electronics

For decades it has been established that semiconductors are the backbone of electronic devices. Traditionally, inorganic semiconducting materials such as silicon, germanium and gallium arsenide are used in these devices which include transistors, light emitting diodes, solar cells and lasers.[8] However, in more recent years organic materials have been considered as a feasible alternative due to their lower cost, lower energy consumption and almost endless size range, increasing the design possibilities and electronic properties compared to those of inorganic materials.[9]

1.2.1 Semiconductors

As stated previously, semiconductors are an essential component in electronic devices which is a result of their unique properties enabling current conduction under specific conditions. The band theory of solids, describing the quantum states of electrons, is necessary for understanding the semiconductors properties.[10] When two or more atoms are bonded together, the atomic orbitals are converted into bonding, antibonding and non-bonding molecular orbitals of different energies. This is explained by the Pauli exclusion principle which dictates that no two electrons can have the same

quantum number. As more atoms are added, tending towards infinity, so too does the number of atomic orbitals which leads to the spacing between the bonding, antibonding and non-bonding orbitals becoming indistinguishable and therefore the orbitals can be considered as one continuous band (Figure 1.1).
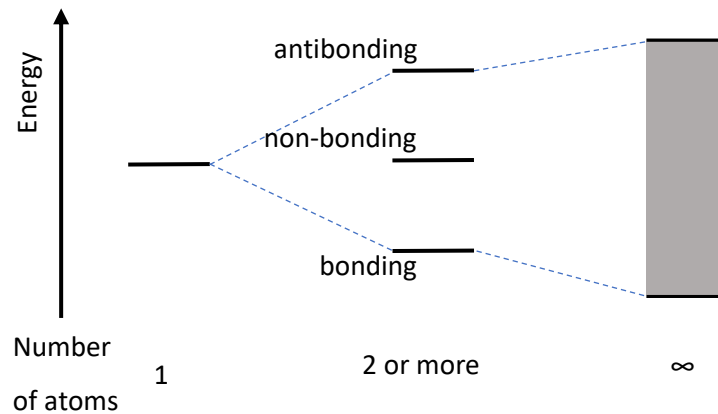

Figure 1.1: Band Theory Schematic

At absolute zero temperature, 0 K, the highest energy level that an electron can occupy is called the Fermi level, E_F. The Fermi level is situated between the valence band and the conduction band. At temperatures above 0 K electrons can be excited by the thermal motion of atoms which may have sufficient energy to occupy the empty orbitals in the conduction band. In a conductor, such as a metal, there is no distinction between the valence band and the conduction band thus allowing easy excitation and mass population of electrons in the conduction band. Conversely, in an insulator there is a gap between the valence band and the conduction band, referred to as the band gap, E_g, which is too significant and prevents electrons from being promoted to the conduction band. A semiconductor has an electrical conductivity situated between that of metals and insulators, the key feature of semiconductor conductivities being their ability to vary over several orders of magnitude. There are two types of semiconductor, namely intrinsic and extrinsic. The intrinsic type being the chemically pure form (most common example being silicon), while the extrinsic type contains a small amount of impurity, also known as a dopant, which allows for the electronic, optical and structural properties to be tuned which allows the conductivity of the material to increase. Extrinsic semiconductors are divided into two categories, n-type and p-type. N-type contain dopant atoms which provide additional conduction to the host material (e.g. phosphorous to silicon), resulting in an overabundance in negative electron charge carriers which occupy otherwise empty bands. Alternatively, in p-type the impurity contained fewer electrons than the host material (e.g. silicon doped with boron). This dopant attracts electrons, removing them from the filled band resulting in

holes being formed thus acting like a positive charge and allowing the remaining electrons to move (Figure 1.2).[11]
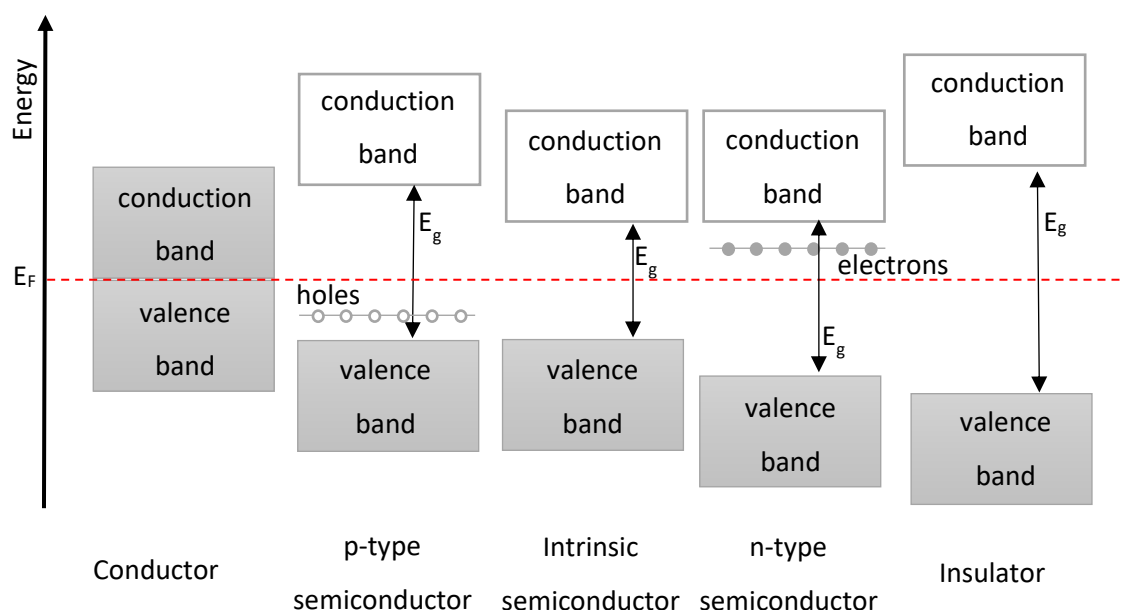
Figure 1.2: Band Structure of conductors, semiconductors (intrinsic and extrinsic) and insulators

1.2.2   Organic Semiconductors

Organic semiconductors are a class of organic molecules based on sp^2-hydridised carbon atoms (heteroatoms can also be present) which are comprised of a σ bonded backbone and hybridization between the lone p_z orbitals form weak π (bonding) and π* (antibonding) orbitals which promote the delocalization of electrons along the molecule.

In a simple two carbon system, like ethene, the two unpaired $2p_z$ electrons prefer to occupy the two spin-allowed π-states leaving the π* states unoccupied due to the energy gap being too large. Consequently, the molecule is not conductive. Increasing the number of carbon atoms in the chain and thus the conjugation length, causes the gap between the π orbital (highest occupied molecular orbital (HOMO)/valence band) and π* orbital (lowest unoccupied molecular orbital (LUMO)/conduction band) to decrease, which eventually results in the $2p_z$ orbitals forming continuous bands which have semiconducting properties. For example, the E_g of ethene is 6.7 eV but by controlling the degree of polymerisation to make polyacetylene (the first organic material identified to contain intrinsic semiconducting properties)[12] the E_g can reduce to around 1.5 eV (Figure 1.3).
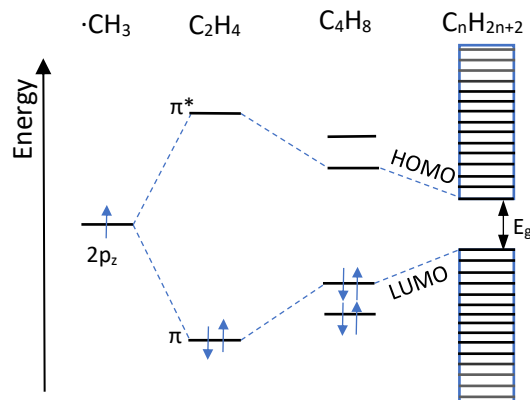
Figure 1.3: Simplified molecular orbital diagrams showing only 2pz and π/π* orbitals from methyl radical → polyacetylene

A similar principle can also be applied to discrete organic molecules. There are a number of ways in which the band gap can be manipulated, including molecular design and intermolecular interactions. Molecular design doesn't just imply conjugation, it also incorporates electronic effects caused by varying the substituents on the molecule. The introduction of electron rich substituents to a conjugated molecule typically culminates in a rise in the HOMO level while the addition of electron withdrawing groups will lower both the HOMO and LUMO. Intermolecular interactions occur when the π orbitals of neighbouring molecules overlap, this allows delocalisation to occur overall several layers of molecules. The π-π stacking is critical for charge transport as well as lowering the optical band gap. By utilising this information, organic molecules can be synthesised with band gaps suitable for any pre-determined application.

1.2.3   Absorption and Emission in Organic Materials

A molecule in space has several forms of energy (including electronic, vibrational and rotational) and can switch from one energetic state to another through transitions which require a discrete amount of energy. The Franck-Condon principle states that during an electronic transition, a change from one vibrational energy level to another will have a greater probability if the two vibrational functions overlap to a large extent. This can be ascribed to the fact that nuclei are significantly heavier than electrons and thus the electronic transitions can occur much faster (femtoseconds) than the nuclei can react. This can be visualised as a vertical line between potential energy curves of two distinct states (Figure 1.4).

Figure 1.4: Vertical Absorption and Emission between two states
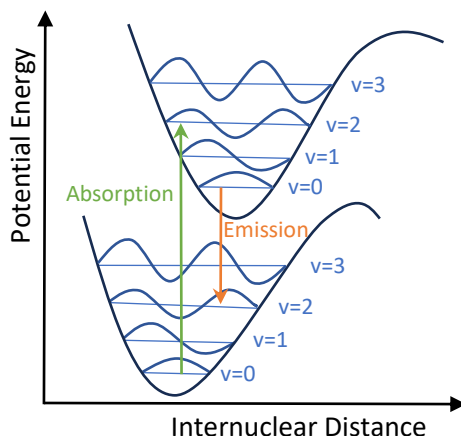
Organic semiconductor materials generally possess larger bandgaps than inorganic semiconductor materials which implies that thermal excitation alone is insufficient for generating free carriers in the excited state and consequently absorption of a photon of appropriate energy is required for an electron to transition from the ground state to the excited state. This energy usually corresponds to absorption in the ultraviolet (UV), visible (Vis) or infrared (IR) region of the electromagnetic spectrum.[13]

The Jablonski diagram (Figure 1.5) is an effective tool for visualising the possible transitions that can occur when a molecule is photoexcited, be that a radiative or non-radiative energy transition. An electron in a molecule is promoted from its ground state to a higher excited state by absorption of a photon with energy equal to the gap between states. Generally, organic molecules have a singlet ground electronic state (S_0). When an electron enters an excited state it can have different spin multiplicity depending on whether the total spin angular momentum is conserved (producing a singlet excited state (S_1)) or not (producing a triplet excited state (T_1)). The selection rules state that absorption transitions must occur only between same spin electronic states (for example $S_0 \rightarrow S_1$). Each state has several vibronic sublevels with similar energy and the electron can transition from higher to lower sublevels by releasing energy before transitions to other excited states are possible (such as $S_2 \rightarrow S_1$). This non-radiative process is called internal conversion (IC).

Relaxation of the electron to the ground state is electronically preferrable. There are several relaxation processes including fluorescence, phosphorescence, thermally activated delayed fluorescence (TADF) and non-radiative processes. Fluorescence is the emission of a photon solely from the singlet state. In accordance with Kasha's rule this usually occurs from the lowest energy of a given multiplicity.[14] Phosphorescence utilises both the singlet and triplet states, a result of

intersystem crossing (ISC) which involves the spin forbidden transition from a singlet to triplet state ($S_1 \rightarrow T_1$). This transition allows the molecule to return to the ground state from the triplet state. However, due to the unlikely spin forbidden transition this relaxation process occurs at a much slower rate (10^{-2} s) than fluorescence (between 10^{-9} and 10^{-7} s).[14] TADF is dependent upon the energy gap between the singlet and triplet states (ΔE_{ST}) being small, typically several hundred meV and possibly as low as 0.01 eV.[15] This reduced energy gap allows the thermal energy (25 eV) to promote reverse intersystem crossing (RISC) from the triplet to the singlet state resulting in delayed fluorescence (DF), named due to this being an energetically uphill process.[16,17]

Manipulation of molecular design can produce organic materials that undergo specific relaxation processes which are essential for efficient organic electronic applications.
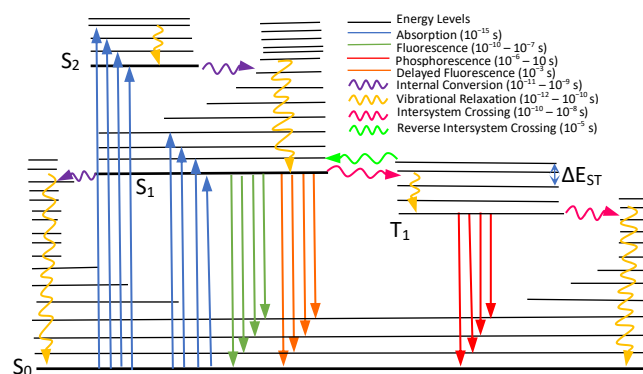
Figure 1.5: Jablonski diagram displaying some electronic transitions

1.2.4   P-N junction

A p-n junction occurs when p-type and n-type semiconductors are placed in contact with each other, the resulting behaviour is drastically different than either could attain individually. P-n junctions are utilised in several modern electronics including light-emitting diodes (LED), transistors and solar cells. In a 'reverse bias' p-n junction, the p-type semiconductor is connected to the negative electrode and the n-type semiconductor connected to the positive electrode. When a voltage is applied the majority carriers are attracted away from the junction towards the electrodes (electrons in the n-type move to the positive electrode and holes in the p-type move to the negative electrode). The thickness of the non-conducting depletion region increases and consequently charge does not flow. In a 'forward bias' p-n junction, the p-type semiconductor is connected to the positive electrode and the n-type to the negative electrode. Charge can flow across the junction, with the electrons in the n-type moving towards the positive electrode and holes moving in the opposite direction to the negative electrode. As electrons and holes move across a p-n junction under forward

bias, recombination can occur and release energy (Figure 1.6). In order to achieve high efficiency in electronic devices this recombination must be kept to a minimum to ensure charge transport through the p-n junction to the respective electrodes.[18] The regulation of this is crucial to ensure a reasonable output and efficiency. Particularly in organic semiconductor-based technologies such as organic solar cells (OSC), organic light-emitting diodes (OLED) and organic field-effect transistors (OFET) which are more amorphous than their inorganic counterparts.
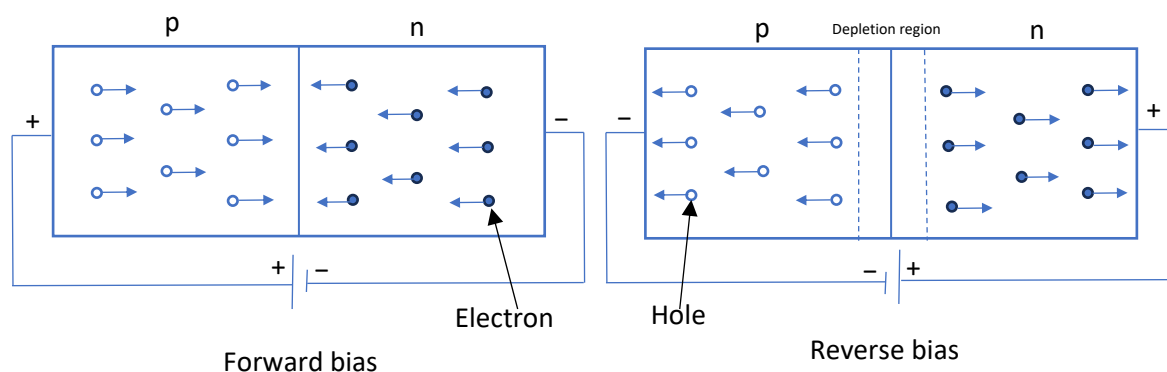
Figure 1.6: p-n junction under forward and reverse bias

1.3 Technological Applications

1.3.1 OLEDs

OLEDs have received considerable attention since the pioneering work by Tang and Van Slyke in 1987,[19] as a result of their remarkable applications in full colour display panels and eco-friendly light sources. An OLED is an electroluminescent device with the potential to produce light within the organic emissive layer under external voltage. Extensive investigation into OLED technology by both academia and industry has been undergone due to their apparent advantages including facile preparation, low cost, light weight, flexibility, low driving voltage and fast response.[20]

OLED devices typically have a multi-layered device structure which is conducive to restricting the recombination sites of electrons and holes to an emissive layer of the device.[21] The device is generally constructed as follows: a glass substrate (transparent and conductive substrate with high work function), transparent anode, hole injection layer (HIL), hole transporting layer (HTL), emission layer (EML), electron transport layer (ETL), electron injection layer (EIL) and cathode (Figure 1.7a).[22] The organic layers are stacked to improve device performance, the transport layers reduce power consumption and therefore increase efficiency while the injection layers aid in extending the device lifetime.[21] When a voltage is applied across the OLED, electrical current flows through the device

generating mobile electrons and holes. The cathode supplies electrons to the emissive layer while holes are injected from the anode, resulting in exciton pairs in the EML (Figure 1.7b).
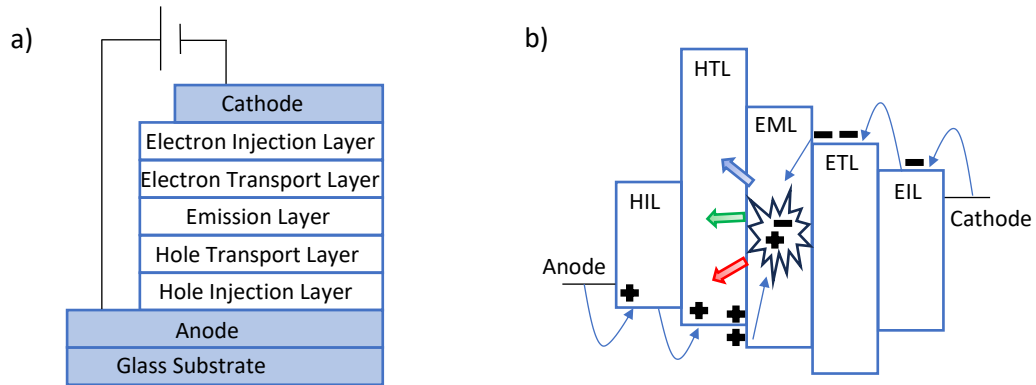
Figure 1.7: Diagrams of a) A typical OLED device structure and b) the working mechanism of an OLED device

Organic materials in the EML are excited by recombination of the holes and electrons, resulting in emission when the excited state returns to the ground state.[23] The organic EML plays a vital role in determining the performance of OLED devices, such as colour and efficiency.[20]

The standard method for assessing the colour of light is by the Commission Internationale de l'éclairage (CIE) coordinates and is based on humans' perception of light (Figure 1.8). Red, green and blue emitters are the most desirable as their combination can create any colour of light. Consequently, OLED display pixels are based on this principle.[24]
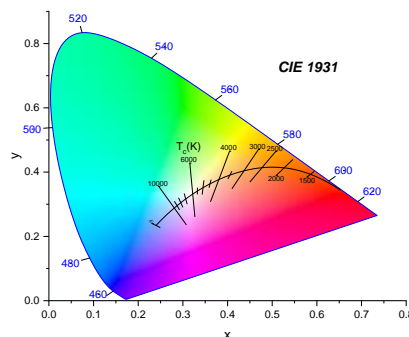
Figure 1.8: CIE 1931 colour space captured from Origin

The light emission efficiency of an OLED is characterised by its quantum efficiency. The external quantum efficiency (EQE) is the best indicator for performance when comparing different emitting OLEDs as it presents the ratio of extracted photons over injected charges.[16] The EQE can be expressed as the result of four parameters, given by the following equation:

$$EQE = \gamma \times \eta_{ST} \times \Phi_{PL} \times \eta_{out} = IQE \times \eta_{out}$$

where γ is the charge carrier balance in the EML which can be influenced by charge carrier dynamics. η_{ST} is the fraction of radiative excitons of the generated excitons that are spin-statistically allowed to radiatively decay. Φ_{PL} is the photoluminescence quantum yield (PLQY) of the emissive molecules, revealing the efficiency at which the spin allowed excitons decay radiatively.[25] These parameters can be summarised as the internal quantum efficiency (IQE), defined as the ratio of number of generated photons to the number of injected charges.[26] The final factor η_{out} is the out coupling efficiency, which is the ratio of photons leaving the device.[22]

During recombination, singlet and triplet excitons can be formed with a 1:3 ratio, decided by spin statistics. Only singlet excitons can decay radiatively to the ground state by emitting a photon due to triplet-singlet transitions being spin forbidden. Therefore, the maximum quantum efficiency (photons emitted per electrons injected) theoretically available is only 25%. TADF is a process which aims to overcome this issue. Excitons generated in the triplet state are collected to increase the efficiency of a fluorescent material. This process can only occur if ΔE_{ST} is small and therefore permits RISC, so electrons from the triplet state can be promoted to the singlet state before electrons relax to the ground state.

1.3.1.1 Emissive Layer

The most distinguishable layer of the OLED device is the EML as the emission colour, contrast ratio and external efficiency are all controlled by this layer's materials. The key properties required for the EML are good light emission properties and transparency in the visible spectrum range, lower band gap and good band alignment with the appropriate electrode (for hole injection the HOMO and anode must have a low energy barrier and for electron injection the LUMO and cathode must have a low energy barrier).[27]

Fluorescence materials were the first to be utilised in OLED devices (Figure 1.9). In 1963, Pope *et al*. observed bright blue electroluminescence (EL) in single crystal anthracene by applying a high voltage across the crystal which encouraged further research in this area.[28] Lu *et al*. synthesised blue emissive 1,2-diphenyl-phenanthro[9,10-*d*]imidazole (**PPI**) which exhibited excellent thermal stability,

highly efficient fluorescence and balanced carrier injection.[29] Bi *et al*. developed *N,N'*-di(*n*-butyl)-2,9-difluoroquinacridone (**C₄-DFQA**) doped in Alq₃, showing low driving voltage (2.5 V) and high power efficiency.[30] The pronounced EL was accredited to improved electron injection induced by introduction of the fluorine atoms.

Anthracene   **PPI**   **C₄-DFQA**
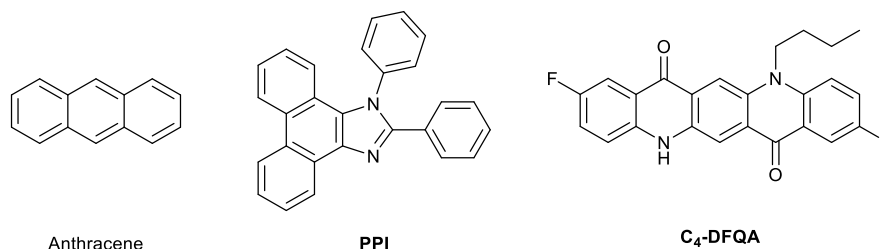
Figure 1.9: Molecular structure of fluorescent materials used in EML

TADF is the most advanced and renowned technique for the EML as it can achieve high energy efficiency and display a full range of colour in CIE (Figure 1.10).[31] The most recognised diphenylsulfone-type blue emitter is *bis*[4-(9,9-dimethyl-9,10-dihydroacridine)phenyl]sulfone (**DMAC-DPS**). OLED devices based on this material were made, achieving blue emission with a maximum EQE of up to 23.0%[32] for doped and 19.5%[33] for non-doped materials. 1,2,3,5-Tetrakis(carbazol-9-yl)-4,6-dicyanobenzene, 2,4,5,6-Tetrakis(9*H*-carbazol-9-yl) isophthalonitrile (**4CzIPN**) is the most famous TADF material. Adachi and coworkers designed **4CzIPN** in 2012 and produced doped OLED devices with EQE as high as 19.4% which is a vast improvement to traditional fluorescent emitters which can only achieve a maximum of 5% EQE.[34]

DMAC-DPS   **4CzIPN**
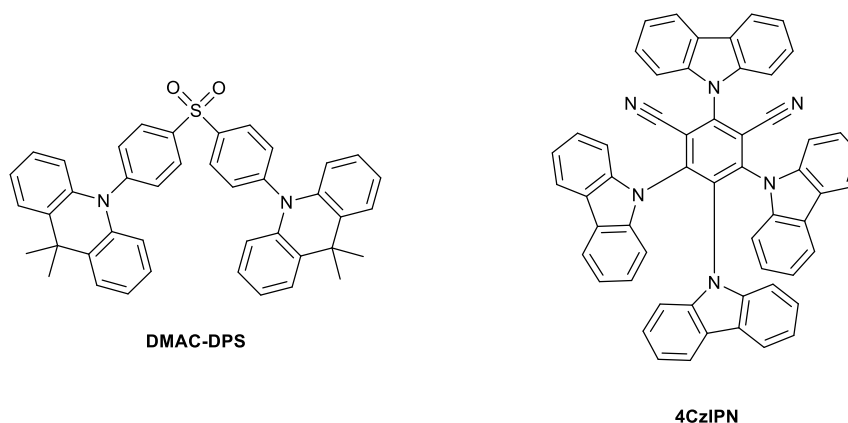
Figure 1.10: Molecular structure of TADF materials used in EML

1.3.2 OFETs

The emergence of OFETs occurred in the late 1980s, almost concurrently with OLEDs.[35,36] OFETs have a huge technological appeal because they can provide the basic unit for on/off switches in a broad range of electronic and optoelectronic applications. The interest in OFETs has drastically increased in recent years due to the emergence of flexible electronics such as displays, smart tags and sensors. OFETs provide multiple advantages including mechanical flexibility, low-cost fabrication, readout integration, large area coverage and power efficiency which provide synergy.[37]

OFETs are generally composed of four components: a source-drain electrode, a semiconducting layer, a dielectric (insulator) layer and a gate electrode. The arrangement of these components depends on the order in which the layers are deposited, four architectures can be fabricated which can then be separated into coplanar and staggered categories (Figure 1.11).[38] Coplanar refers to the source, drain and conducting channel being located on the same plane (Figure 1.11 a and d) while staggered means the conducting channel is offset from the plane of the source and drain contacts (Figure 1.11b and c).[39] In all architectures it is crucial that the semiconducting layer is in direct contact with the source/drain electrodes and the dielectric layer must be in contact with the gate contacts, known as the gate electrode. The thin film conducting layer can be deposited with solution or vacuum processes. Source/drain electrodes are always metal contacts while the gate electrode can be a metal or a conductive polymer. Each structure has its own unique advantages and disadvantages therefore the type of structure applied depends on its application.
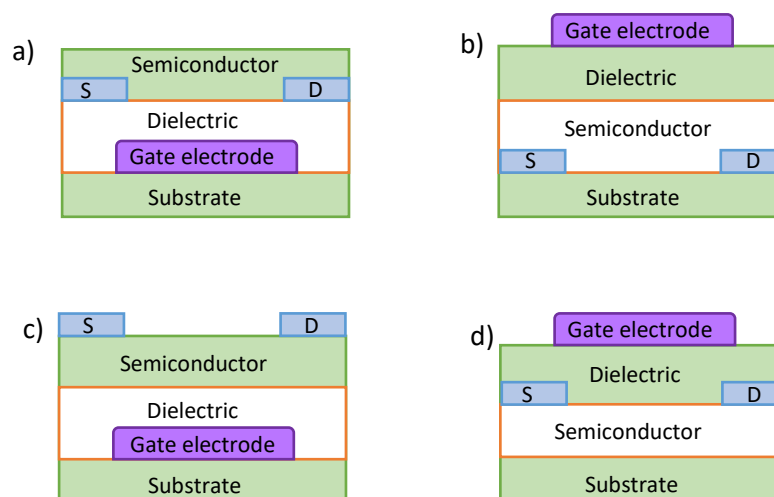

Figure 1.11: Cross section of OFET architectures: a) bottom-gate, bottom contact, b) top-gate, bottom contact, c) bottom-gate, top contact and d) top-gate, top contact

The performance of OFETs is generally evaluated by output and transfer characteristics. Output is determined by a plot of source-drain current (I_{DS}) versus source-drain voltage (V_{DS}) at different but constant source-gate voltage (V_{GS}), while transfer is established by a plot of I_{DS} versus V_{GS} at constant V_{DS}. On application of V_{GS}, a charge accumulation layer can be formed at the semiconductor/ insulator interface.[40] When V_{DS} is zero no current can flow through the channel since the charges are distributed uniformly. A gradient distribution occurs when $V_{DS} < (V_{GS} - V_T)$ is applied between the source and drain (V_T is the threshold voltage).[41] This causes a linear regime for the OFET, where its performance follows:

$$I_{DS} = \frac{W}{L} \times \mu C_i (V_{GS} - V_T) \times V_{DS}$$

Where L is the channel length, W is the channel width, μ is the field-effect mobility and C_i is the capacitance per unit area of dielectric layer. During operation, current is injected from the source electrode into the conducting layer and collected by the drain electrode. When a high V_{DS} is imposed ($V_{DS} > V_{GS} - V_T$) the device works in a saturation region and I_{DS} is given by:

$$I_{DS} = \frac{W}{2L} \times \mu C_i (V_{GS} - V_T)^2$$

Consequently, conductance of the semiconducting layer can be readily modulated by gate bias with off and on stages via capacitance coupling with a dielectric layer. I_{on}/I_{off} refers to the ratio between the highest and lowest I_{DS} in the range of gate voltage sweep at certain V_{DS}. It is therefore a crucial factor for switching behaviours of OFETs and a large I_{on}/I_{off} is desired for their application.[40]

1.3.2.1   Organic semiconductors in OFETs

A wide range of conjugated small molecules and organic polymers are utilised as the active semiconductor in OFETs due to their flexibility, high molecular density, low cost, low temperature processability and outstanding compatibility with flexible substrate.[37,42] The most important criteria for selecting these materials depends on the HOMO and LUMO energy levels of the molecule and their closeness to the work function of metals.[43] A bandgap in the range of 1 eV to 3 eV is suitable for flexible device applications. Mobility of OFETs depends on both the chemical structures of the conjugated frameworks and the intermolecular π-orbital overlapping.

These materials can be categorised as p-type or n-type based on their differences in charge transport carriers. Pentacene is a classic organic semiconductor material with a 7C bonded conjugate system and a high hole mobility due to the orbital overlap between molecules in the crystal lattice (Figure 1.12). Apart from its high mobility, pentacene retains chemical stability under harsh

environmental conditions and has a good interface contact with metal electrodes such as gold or aluminium.[44] Sekitani *et al.* reported flexible OFETs using pentacene as the active layer at a voltage of 2 V and mobility of 0.5 cm^2 V^{-1} s^{-1}, displaying extreme bending.[45] A flexible OFET based on 6,13-bis(triisopropylsilylethynyl) pentacene (TIPS-pentacene) was fabricated by Tiwari and coworkers which exhibited excellent p-channel characteristics, with a field effect mobility up to 0.12 cm^2 V^{-1} s^{-1} and an I_{on}/I_{off} ratio > 10^4 at low V_T of −0.2 V (Figure 1.12).[46]

Improving the performance by n-type semiconducting materials is more challenging compared to p-type semiconducting materials. N-type materials are sensitive to air and water in the environment therefore requiring nitrogen protection and a vacuum on device preparation. Naphthalene tetracarboxylic acid diimide has a mobility of below 0.57 cm^2 V^{-1} s^{-1} in air and 6.2 cm^2 V^{-1} s^{-1} in inert atmosphere, showing the potential to use these types of derivatives as electron transporting materials to prepare n-channel flexible OFETs with comparable electron mobility (Figure 1.12).[47]
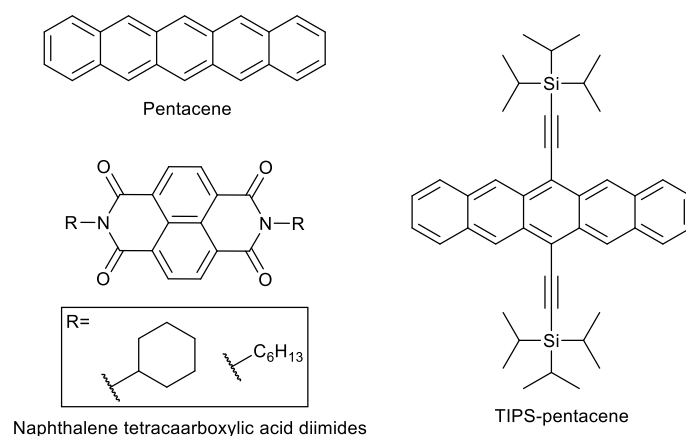
Figure 1.12: p- and n- type organic semiconductors used in flexible OFETs

1.3.3 Sensors

Sensors have become an indispensable technology in the modern world which are used for detection, monitoring, measuring, diagnosis and other measurement work. Multiple sectors utilise sensors including manufacturing, energy, environment pollution, medical diagnostics and life-science studies. Sensors are devices which can detect and respond to some type of input from the physical environment be that light, heat, motion, moisture etc.[48] A microprocessor then processes the electrical impulses to provide outputs which correspond to a set of measures (Figure 1.13). The system then transmits the output to a designated place in the designed device for analysis or further processing.[49] Sensors make it possible to collect and process data about a specific environment to

monitor, manage and control that factor in a simple and efficient way. Sensors can capture the required data by continuous monitoring which aids in simplifying the operation.

Figure 1.13: Block diagram describing the working of sensors

Sensors are generally categorised by the type of environmental factor being monitored, a few examples include accelerometer, optical, humidity, level, motion, pressure, proximity, temperature, touch and chemical.

Optical sensors identify the physical amount of light rays present and converts it into an electrical signal that can be interpreted by a human or electronic device. Various industries imple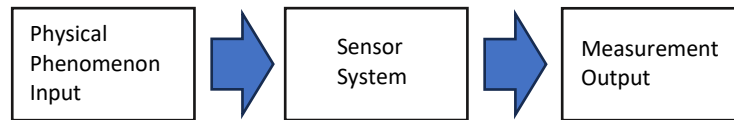ment these detectors in applications such as ambient light detectors, digital optical switches and optical fibre communications.[50]

Chemical sensors are used to detect liquid or chemical changes in the air. They are utilised in a wide range of applications including environmental monitoring and process control, detecting harmful chemicals released intentionally or inadvertently, explosive and radioactive detection, pharmaceutical industries and laboratories.[51–53] Gas sensors are similar to chemical sensors except they measure the concentration and/or identify sensed gas by analysing the reactions between the sensing material and the gas or vapours. They are used in the oil and gas industries, chemical laboratory research, pharmaceuticals and related products.[54–56]

Semiconductors have been used in sensors since the 1950s. Silicon is most commonly used as the semiconductor in sensors but other group III to V elements are also used due to their availability, ease of use, physical properties and cost effectiveness.[57] The basis for most semiconductor sensors are p-n diode, metal-oxide semiconductor (MOS) capacitors or MOS field-effect transistors (MOSFETs) (Figure 1.14).

Figure 1.14: Schematic diagram of a) basic MOS capacitor and b) MOSFET

Organic semiconductors have received increasing interest for applications in sensors due to their unique characteristics such as tunability of electronic properties via chemical synthesis, compatibility with mechanically flexible substrates, low-cost manufacturing and facile integration with chemical and biological functionalities.[58,59] Devices based on organic semiconductors cannot surpass single-crystalline inorganic semiconductors due to their relatively low mobility resulting in three times lower charge carrier mobilities. Therefore, devices based on organic semiconductors are not appropriate for applications requiring high switching speeds. However, devices like organic field effect transistors (OFETs) and organic thin film transistors (OTFTs) can be easily constructed by low temperature deposition and solution processing methods.[60,61] Consequently, organic semiconductor materials have been applied in a wide range of sensor applications.

1.3.3.1 Organic Semiconductors in Gas Sensors

In sensor applications, organic materials have been used as the sensing layer because they are sensitive to a wide range of stimuli such as pH value, presence of gas molecules or biomolecules. One type of gas sensor is electrochemical, most electronic gas sensors used commercially are based on metal-oxide materials, usually requiring high operation temperatures which hinders their application in low-power combustible and explosive gas detection. Utilisation of OFETs as gas sensors has attracted increased attention due to the high selectivity, repeatable response and low-cost production.[62] In OFETs the active layer consists of organic semiconductors that interact with gas analytes, causing a reversible change of source-drain current, threshold voltage shift, mobility etc. Therefore, OFETs can offer a multi-parameter control over device characteristics and have a great potential as portable, yet reliable, sensors.[63]

Kumar *et al*. developed OFET devices based on poly [*N*-9'-heptadecanyl-2, 7-carbazole-alt-5, 5-(4', 7'-di-2-thienyl-2', 1', 3'-benzothiadiazole] (**PCDTBT**) for the detection of NO_2 gas at the parts per million (ppm) level (Figure 1.15).[64] The electron removal from the NO_2 molecule by the p-type semiconducting polymer PCDTBT resulted in an increased conductivity. For a dose of 2 ppm of NO_2 at −10 V gate bias, the sensor exhibited a typical response (16.2 s) and recovery time (171 s) values.
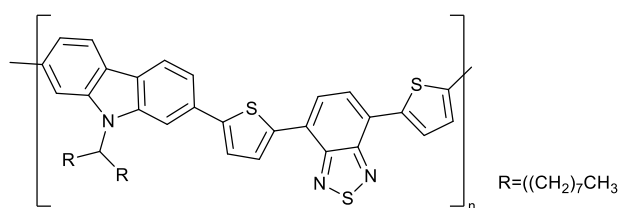
Figure 1.15: Molecular structure of PCDTBT

Zhou *et al*. designed and developed ambipolar OFETs, fabricated with a 2,5-bis(4-biphenylyl)bithiophene (**BP2T**) and copper hexadecafluorophthalocyanine (**F₁₆CuPc**) bilayer, therefore providing two types of charge carriers.[65] They were able to respond to the four redox gases studied: NO_2, NH_3, H_2S and SO_2 under different gate bias values, producing significantly improved charge transport ability and response values compared to the unipolar. This shows the ambipolar transistors provide promising advantages for attaining highly selective and sensitive gas detection.
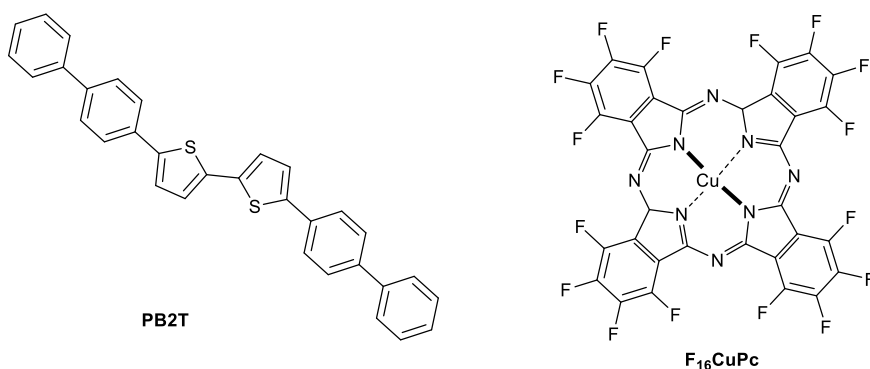
Figure 1.16: Molecular structure of PB2T and F₁₆CuPc

1.3.3.2   Organic Semiconductors in Optical Sensors

Optical sensors are usually based on the following techniques: fluorescence sensors, surface plasmon resonance (SPR), IR and Raman spectroscopy, colorimetric sensors etc.[53] Fluorescent sensors involve specific fluorescent probes, the concentration of analyte can be determined by monitoring the change in fluorescence intensity after interactions with given analytes. Normal single fluorophore-based sensors and the fluorescence resonance energy transfer (FRET) technique can be used to sensitively detect chemicals.

Tang *et al*. developed three generations of fluorescent carbazole dendrimers with spiro-bifluorene cores to detect nitroaromatic explosives by fluorescent quenching (Figure 1.17).[66] Stern-Volmer measurements were taken in solution with a series of nitrated analytes including 2,4-dinitrotoluene (DNT) and 2,3-dimethyl-2,3-dinitrobutane (DMNB). An increase in electron affinity and therefore quenching efficiency was observed between the first- (**G1**) and second- (**G2**) generation dendrimers. For many organic fluorescent sensors, the quenching of fluorescence is irreversible due to strong bonding interactions between the thin film of the sensor and the analyte.[67,68] In this case, by applying heat the analytes are desorbed and the fluorescence sensor is recovered.
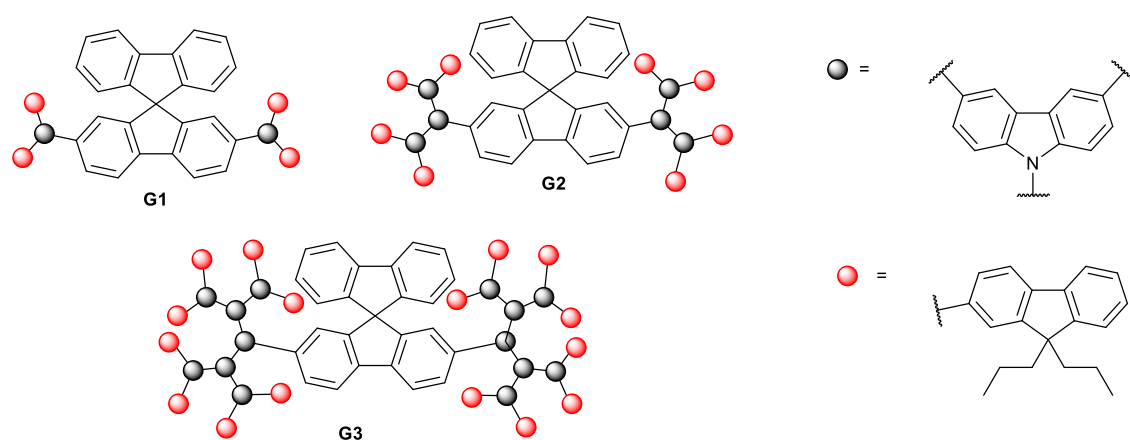
Figure 1.17: Molecular structures of three generations of fluorescent carbazole dendrimers

Turnball and coworkers developed ultra-sensitive fluorescent sensors for detecting trace vapours of explosives, observed by fluorescence quenching.[69] The commercially available fluorescent polymer Super Yellow (SY) was utilised in thin-film fluorescent sensors using simple solution processing. A 90 nm SY film was exposed to DNT vapour at room temperature, resulting in a photoluminescence (PL) decrease without effecting the spectrum. On raising the temperature, a rapid increase in PL occurs as the DNT vapour is released from the SY film. Addressing the challenge of selectivity and reusability of fluorescent sensors for trace detection of explosives.
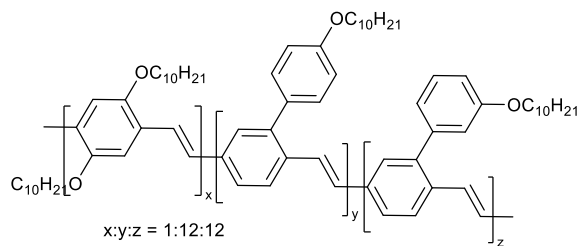
Figure 1.18: Molecular structure of Super Yellow polymer

1.3.4 Perovskite Solar Cells

Sunlight is the most naturally abundant source of energy available throughout the world. Photovoltaic (PV) cells harvest this energy to yield photogenerated power using semiconductors that exhibit the photovoltaic effect (when photons of light excite electrons into a higher energy state, providing them with the potential to act as charge carriers for an electric current).[70] In the past PVs were the most expensive form of renewable energy. However, due to the extensive research and development in this area the latest International Renewable Energy Agency (IRENA) report outlines that between 2010 and 2019 the unit costs of solar energy decreased by 85%.[71]

Traditional PVs are based on inorganic semiconductors such as silicon, particularly for commercial purposes due to its high-power conversion efficiency (PCE) and durability. However, due to their high manufacturing and installation costs, weather dependency and space requirements alternative technology was investigated. The emerging organic semiconductor technology aims to alleviate some of these issues with ease of manufacture using low temperature processing (such as solution processing by printing and coating techniques), mechanical flexibility and light-weight properties.[72]

Perovskite solar cells (PSC) are a third-generation solar cell which can be constructed using easy fabrication techniques and require inexpensive materials.[73] The highest PCE, to date, for these devices is 26.1% which makes it one of the leading types of third generation solar cell.[74] However, these devices are susceptible to environmental degradation as a result of the perovskite being sensitive to heat and humidity which impedes their large-scale production.[75] Miyasaka and coworkers were the first to implement perovskite materials in solar cells in 2009 by utilising it as a sensitiser in dye-sensitised solar cells (DSSC) to achieve a PCE of around 3.8%.[76] The substitution of a solid-state hole transporting material (HTM) for the liquid electrolyte in 2012 was crucial for improving the efficiencies of PSCs.[77,78] Variables of methylammonium lead halide, $CH_3NH_3PbX_3$ (X = Cl, Br, I) are the most successful perovskite materials used in solar cells thus far. Organometal halide perovskites were employed due to their strong light absorption, bipolar transport abilities, suitable

band gap, high charge carrier mobility, small exciton binding energy and ambipolar nature (operates as a light absorber, electron conductor and hole conductor).[79,80]

Various structures of PSCs have been developed and can be divided into the conventional n-i-p and inverted p-i-n architectures depending on whether the ETL or the hole transporting layer (HTL) is in contact with the transparent conductive substrate. N- and p- respectively refer to n-type and p-type charge carrier transporting materials and i refers to the perovskite optical absorption layer.[79] In the conventional planar PSC devices a flat ETL is deposited on the transparent conductive oxide (TCO) substrate such as fluorine-doped tin oxide (FTO) or indium tin oxide (ITO) which act as the cathode, the perovskite material is then deposited by spin coating or vacuum evaporation onto the ETL before the flat HTL and metal cathode (Au or Ag) are deposited on top. The only difference in structure for the inverted PSC is the position of the ETL and HTL which are swapped. Comparison of the planar and mesoporous n-i-p PSCs identified the only variation being the mesoporous metal oxide scaffold. In the mesoporous PSC, the perovskite absorber is self-assembled within the gaps of the mesoporous metal oxide by sintering nanoparticles, the absence of this in the planar architecture means the high temperature processing is no longer required (Figure 1.19).
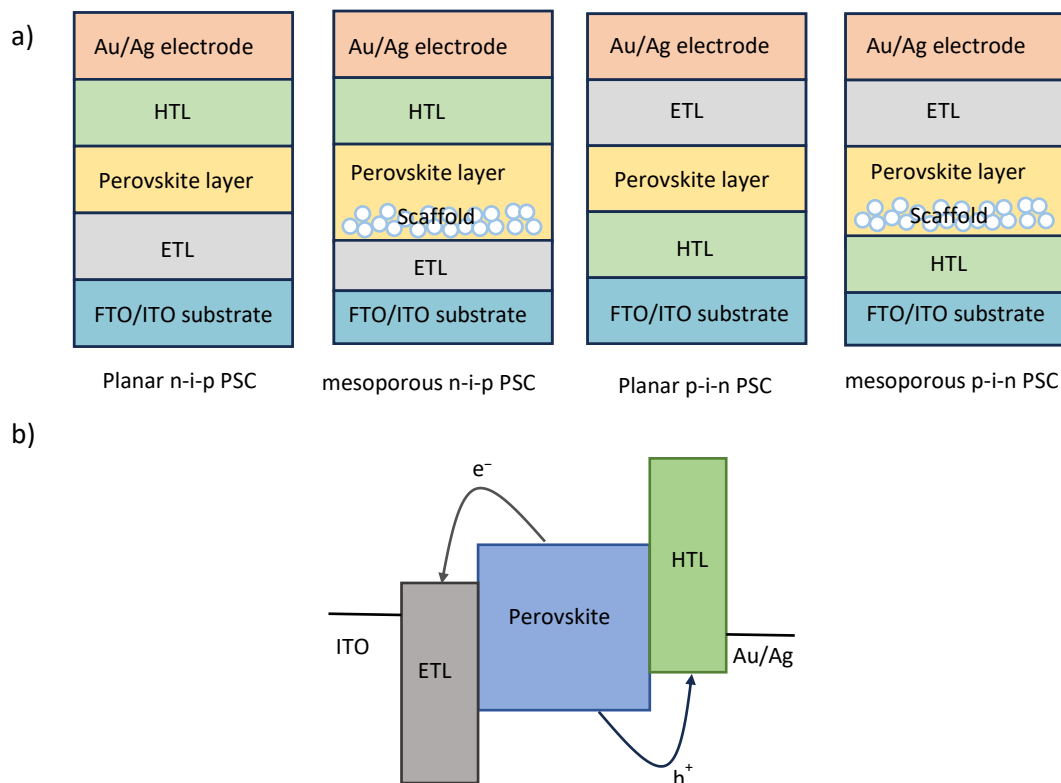

Figure 1.19: a) Schematic diagram showing the layered structure of four typical PSCs and b) Band diagram and operation principles of PSCs

In order to transform solar energy (an incident photon) into electricity a number of charge transfer processes are necessary. A highly efficient PSC generally possesses two interfaces: the ETL/perovskite and HTL/perovskite which enable charge separation and collection. Figure 1.20 depicts the various charge carrier kinetics of these two interfaces which encompasses charge transfer, charge carrier collection and charge carrier recombination. The desirable processes include: photo-excitation in the perovskite (1) which forms electron-hole pairs; electron transfer to the ETL (2); and hole transfer to the HTM (3). These charges are then collected at the anode and cathode of the solar cell to generate the photocurrent. The undesirable processes include: bulk recombination of photo generated species (4); back charge transfer at the interfaces of the ETL (5) and charge transfer at the HTL with the perovskite (6); and charge transfer between the ETL and HTL (which can occur when the perovskite is absent in some areas, for example nanoparticles or voids are present).[81,82] Processes (4) – (7) must be executed at a slower rate than the charge generation and extraction processes (1) – (3) in order to generate high PCE devices.

Figure 1.20: Charge transfer processes occurring in PSCs
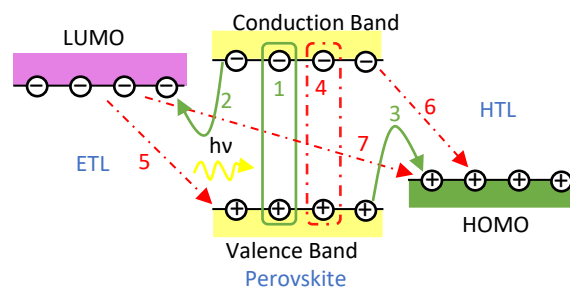
1.3.4.1 Efficiency

As noted above, efficiency of a solar cell is a crucial parameter for commercialisation and is defined by its capacity to convert light into electricity. In order to ensure that different solar cells are compared consistently, a standard formula is used to define PCE:

$$PCE = \frac{P_{OUT}}{P_{IN}} = \frac{J_{SC} \cdot V_{OC} \cdot FF}{I_{light}}$$

Where J_{SC} is the short circuit current density (measured in A/m²), V_{OC} is the open circuit voltage (measured in V), FF is the fill factor and I_{light} is the incident solar radiation (measured in W/m²). P_{IN} (incident power irradiance) is dependent on the solar simulator light source which should provide power irradiance of 1 sun, 1000 W/m² at the device surface. These parameters can be ascertained by measuring the current vs density (J/V). In these measurements the output current of the device is quantified at incremental voltages producing a J-V curve (Figure 1.21).
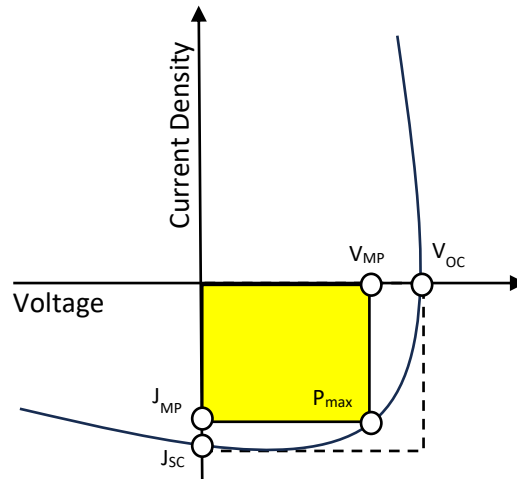
Figure 1.21: Typical J-V curve for solar cells

J_{SC} is the current through the cell when the voltage across the solar cell is zero and is greatly influenced by the light intensity (I) and carrier mobility. A broad absorption spectrum for the photoactive materials and an optimised morphology is desired to aid in improving these properties.

V_{OC} is the maximum voltage produced by a solar cell when there is zero current. In general, it is defined by the energy difference between the quasi-fermi levels of the ETL ($E_{F,e}$) and HTL ($E_{F,h}$):

$$-qV_{OC} = E_{F,e} - E_{F,h}$$

where q is the charge of an electron. In PSCs, the V_{OC} is defined as:

$$-qV_{OC} = E_g - \varphi_n - \varphi_p - \Delta E_{loss}$$

where φ_n (φ_p) is the electron (hole) injection barrier height and ΔE_{loss} is the energy losses in transporting charge carriers to the electrodes.[83] It has been observed that free charge carrier generation occurs at the perovskite/HTL interface via hole transfer. Consequently, V_{OC} is predominantly affected by the energy difference between the perovskite conduction band and the HOMO of the HTM.

Lastly, the FF is determined by dividing the max power (MP) output of a cell by its actual output. FF is heavily influenced by the charge carrier mobility as well as the degree of charge recombination.[84]

1.3.4.2 Hole Transporting Materials

HTMs are crucial for managing the charge dynamics in PSCs, such as the processes of interfacial charge separation and electron recombination. An ideal HTM contender must possess several basic requirements including high hole mobility, well-aligned energy levels with perovskite material, good solubility in organic solvents, easy accessibility with low cost and high photochemical and thermal stability.[85] HTMs can be divided into three categories: inorganic, conjugated polymers and small molecules.

Inorganic HTMs have good stability, high hole mobility, low cost etc. Copper iodide (CuI) was the first inorganic HTM implemented in PSCs by Kamat and coworkers, achieving a 6% PCE.[86] Copper thiocyanate (CuSCN) has also been implemented in mesoporous n-i-p PSCs and planar p-i-n PSCs, achieving 12.4%[87] and 15.6%[88] PCE, respectively by optimising the layer thickness. Despite these inorganic materials high hole mobility and low cost there are concerns that the deposition solvent can partially dissolve the perovskite compromising device stability.

Compared to small organic molecules used in PSCs, polymeric HTMs have several advantages including high thermal and optical stability, superior film forming property, excellent carrier mobility and the potential for enabling industrial production through roll-to-roll printing techniques.[89] Poly[bis(4-phenyl)(2,4,6-trimethylphenyl)amine] (**PTAA**) was the first polymer tested in PSCs[90] and continues to retain one of the highest PCEs (20.2%) reported for polymeric HTMs (Figure 1.22).[91] Poly(3-hexylthiophene) (**P3HT**) has obtained considerable study for the pursuit of stable, low-cost and highly efficient PSCs. Xu *et al*. designed PSC devices using **P3HT** and 2-((7-(4-(bis(4-methoxyphenyl)amino)phenyl)−10-(2-(2-ethoxyethoxy)ethyl)−10H-phenoxazin-3-yl)methylene)malononitrile (**MDN**) which acts as a molecular bridge, anchoring to the perovskite and forming π-π stacking with **P3HT** to form a charge transport channel (Figure 1.22).[92] A PCE of 22.87% was achieved, effectively surpassing the efficiency of pristine **P3HT** devices. Li *et al*. developed a series of thiazolothiazole-thiophene based polymer HTMs and applied them in PSCs (Figure 1.22).[93] They produced good performance and stability in the absence of dopants which was attributed to the crystallinity of the polymer which can be controlled by adjusting the thiophene units on the backbone. The highest PCE reached was 14.02% for **P2**.
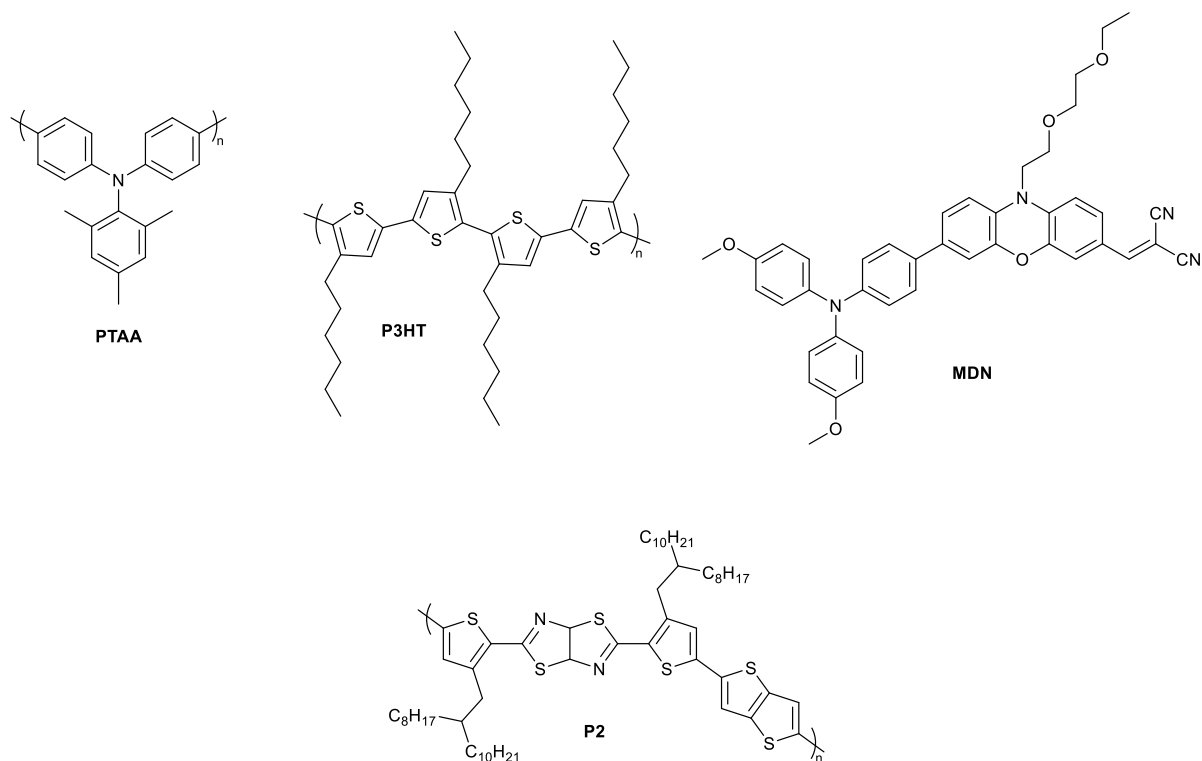
Figure 1.22: Molecular structures of polymer HTMs: PTAA, P3HT and P2 and molecular bridge MDN

Small organic molecules have produced the highest number of novel HTMs. Spiro-OMeTAD remains the benchmark HTM for PSCs as it has achieved the highest efficiencies in devices to date.[94] Although spiro-OMeTAD has many positive attributes, which will be discussed in more detail later in this thesis, the high production cost, dependency on additives, long term stability and degradation issues, poor coating technology compatibility and the hysteresis effect has caused many research groups to design alternative, low-cost and high conductivity substitutes.[95] Zhu and coworkers have recently synthesised a spirofluorene-dithiolane based HTM, **SFDT-TDM** (Figure 1.23).[96] The C-H π interactions in adjacent **SFDT-TDM** aid in improving the hole mobility and the 1,3-dithiane groups serve as Lewis bases which passivate the defects on the surface of perovskite films, leading to suppressed non-radiative recombination and enhanced charge extraction at the perovskite/HTM interface. As a result, PSCs with **SFDT-TDM** as the HTM realize the highest PCEs of 21.7% and 20.3% for small-area (0.04 cm^2) and large-area (1.0 cm^2) devices, respectively. Liu *et al*. reported a star shaped HTM, **LD29** which consists of a carbazole core and triphenylamine side arms (Figure 1.23).[97] This material was applied in doped and dopant-free PSCs, achieving PCEs of >18% and 14.29%, respectively. This material required less production cost and obtained higher stability compared to spiro-OMeTAD. Phenoxazine has been utilised as a HTM core by Cheng and coworkers which exhibited suitable energy levels and displays strong absorption in the visible region, high hole

mobility and conductivity (Figure 1.23). Dopant-free devices incorporating a benzothiazole linker achieved a higher PCE of 12.8% compared to the thiophene linker HTM with PCE of 11.5%.[98]
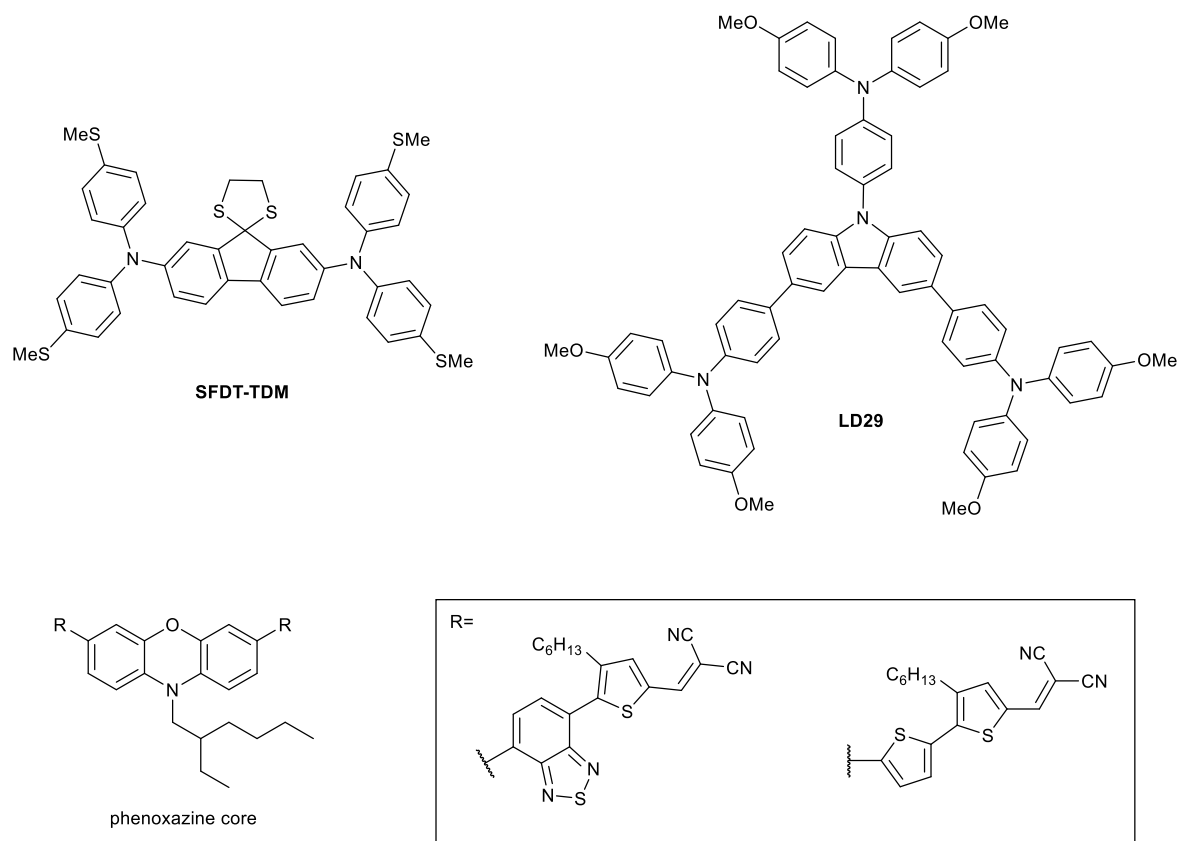

Figure 1.23: Molecular structure of small molecule HTMs

2 Spiro-OMeTAD containing polymers as additives in PSCs

2.1 Introduction

2.1.1 Pristine Spiro-OMeTAD

Spiro-linked molecules feature extended π-systems with identical or different functions connected by sp³-hybridised atoms.[99] Currently, the twisted spirobifluorene based molecule 2,2'7,7'-tetrakis(N,N-di-p-methoxyphenyl-amine)9,9'-spirobifluorene (spiro-OMeTAD) is the most studied small organic molecule used as a HTM (Figure 2.1). Spiro-OMeTAD possesses a moderate glass transition temperature (T_g), amorphous glassy properties, morphological stability and compatibility with solution methods while maintaining good electronic properties and preventing crystallisation.[95] Crystallisation hinders the formation of good contact between the mesoporous TiO_2 surface and hole conductor while also changing the film morphology after device fabrication which is highly undesirable. The energy band alignment of spiro-OMeTAD matches well with commonly used hybrid perovskite materials. The LUMO of spiro-OMeTAD is above the conduction band minimum of a variety of photoactive perovskites, typically >2 eV, which provides a good electron blocking ability.[100] Meanwhile, the HOMO is positioned higher than the valence band maximum with an offset on the hundreds of meV order, beneficial for hole extraction at the interface (the electron donating properties of the methoxy group help adjust the HOMO level to this position). Spiro-OMeTAD was first utilised for PSC applications by Grätzel and coworkers in 2012[101] and remains the highest performing HTM in terms of efficiency and therefore became the benchmark for future HTMs.
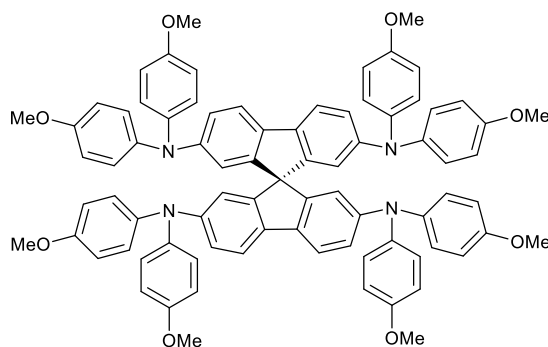

Figure 2.1: Molecular structure of spiro-OMeTAD

Pristine spiro-OMeTAD has low hole mobility (10^{-4} cm^2 V^{-1} cm^{-1}) and an intrinsic hole density as low as 10^{14} cm^{-1} which induces a hole conductivity smaller than that of perovskites by multiple orders of magnitude.[102] Spiro-OMeTAD exhibits a poor electric property which restricts the charge transport within the HTL and instigates severe charge accumulation at the interface[103] which lowers the photovoltaic performance, in particular the V_{OC} and FF.[104] Many endeavours have been undergone to develop an ultra-thin spiro-OMeTAD layer to shorten the distance of hole transport in the HTL. Unfortunately, reduction of the spiro-OMeTAD film thickness results in poor coverage on the relatively rough perovskite film and sometimes results in direct contact between the perovskite film and the electrode, reducing the reproducibility of high-performance PSCs as the charge recombination increases and V_{OC} decreases.[105,106] The hole mobility of the spiro-OMeTAD single crystal with triclinic space group at room temperature is amplified by three orders of magnitude compared to the thin-film which demonstrates the requirement for mesoscale ordering and crystallinity for advancing the performance of spiro-OMeTAD.[107,108] One way of improving the PCE of devices is by device optimisation and HTL optimisation by incorporating additives and p-type dopants to the precursor solution.

2.1.2 Doping Spiro-OMeTAD

An ideal dopant should have the following characteristics: able to steadily increase the conductivity and hole mobility of spiro-OMeTAD; capable of producing minimal by-products or the by-products should not negatively affect the device performance or stability; and the synthesis is simple and low-cost.[109] The doping process in organic materials usually involves chemical oxidation and reduction while charge transport requires redox reactions.[110] P-type doped spiro-OMeTAD contains a positively charged, oxidised molecule that functions as the dopant.[109] The HOMO of the oxidised spiro-OMeTAD is slightly deeper than the HOMO of the pristine molecule, providing a thermodynamic driving force for charge hopping from the pristine to oxidised forms.[111] The dopant can become chemically identical to the bulk matrix provided that it is reduced after accepting an electron. Simultaneously, another dopant is produced after losing an electron (or analogously receiving a hole). This cycle is repeated across the HTL as holes are extracted from the adjacent perovskite and transported towards the metal electrode.[112] The mobility and conductivity of the doped spiro-OMeTAD can be increased by at least one order of magnitude compared to the pristine spiro-OMeTAD.[103]

The most extensively used additives for doping spiro-OMeTAD include bis(trifluoromethane)sulfonimide lithium salt (LiTFSI),[113] 4-*tert*-butyl pyridine (*t*-BP)[114] and tris(2-(1H-

pyrazol-1-yl)-4-*tert*-butylpyridine)cobalt(III) tri[bis(trifluoromethane)sulfonimide (FK209) (Figure 2.2).[115] For the solution processed spiro-OMeTAD HTL, the pristine spiro-OMeTAD powder and additives are dissolved in an organic solvent, usually chlorobenzene, and the homogeneous mixture spin-coated on top of the perovskite layer.[95] The, as-prepared, HTL needs to be further exposed to an O_2 atmosphere or ambient air conditions with controlled relative humidity.[116] It is widely acknowledged that the pristine spiro-OMeTAD molecules react with O_2 in the presence of light and an electron is transferred, leading to the formation of a radical cation (spiro-OMeTAD$^+$) and an oxygen anion.[117] Post doping, exposure to O_2 and light are necessary to increase the doping efficiency. The p-type doping is realised once a certain concentration of radical cations is generated and stabilised. The radical cation species is considered to be responsible for the p-type doping and improving the conductivity of the spiro-OMeTAD HTL.[118]
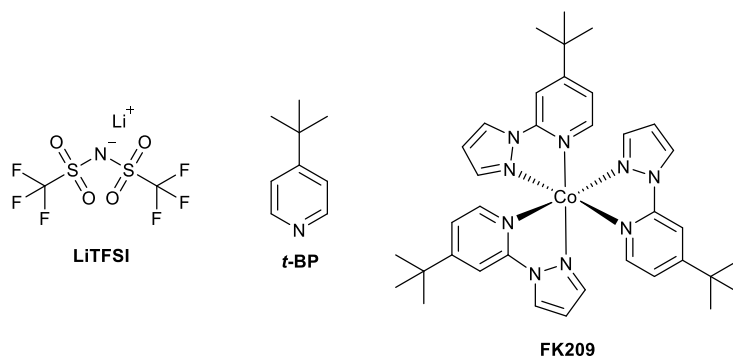

Figure 2.2: Molecular structure of dopants LiTFSI, t-*BP and FK209*

LiTFSI supplies Li$^+$ ions to the system, allowing the electrochemical properties of the TiO_2 to be controlled by the adsorption and intercalation processes of the Li$^+$ cations.[119] The TFSI$^-$ anion further stabilises the radical cation. It has been confirmed by the space charge limited current (SCLC) mode and time-of-flight (TOF) transient hole-current measurements that the presence of LiTFSI enhances charge carrier mobility.[120] Although a low concentration of radical cation may be generated in the HTL by exposure to light, O_2 or LiTFSI separately, it is hypothesised that all three factors are required to create the desired concentration for successful doping.

t-BP is another indispensable additive for preparing high quality HTL, forming an interfacial layer between the spiro-OMeTAD and TiO_2 layer, thus preventing their direct contact and resulting in low charge-recombination and enhanced device performance.[121] Devices with a blend of spiro-OMeTAD, LiTFSI and *t*-BP have significant improvements in their photovoltaic parameters, with the *t*-BP

improving the homogeneity of the HTM film and solubility of LiTFSI.[118] The oxidation process of LiTFSI and *t*-BP co-doped spiro-OMeTAD relies on the conditions such as O_2 penetration speed, temperature and humidity, generally requiring a few hours to a day to fully oxidise.[122]

FK209 is one of the most efficient oxidants and well-known cobalt-based salts for p-doping organic semiconductors, developed to replace oxygen and providing fast, efficient doping during the pre-oxidation process. By reducing Co(III) to Co(II), spiro-OMeTAD can easily generate the radical cation and the film conductivity is increased.[115] In order to further increase the conductivity, the hygroscopic co-dopant LiTFSI is usually required. The oxidation process is accelerated without requiring post-exposure to the O_2 environment.[123] The strong tendency to crystallise and enhancing the π-π stacking aids the HTMs to extract carriers efficiently and dopants are prone to aggregate around the grain boundary which causes precipitation of Li salts or formation of pinholes in the film.[117,124] Therefore, alternative HTMs are continually being designed, some not requiring dopants, to produce more cost effective and efficient PSCs.

2.1.3   Derivatives of Spiro-OMeTAD

To overcome the limitations of spiro-OMeTAD in PSCs, different molecular designs based on the spirobifluorene core have been investigated to improve the device stability while maintaining the desirable properties.[125] In 2014 Jeon *et al*. analysed the influence of the methoxy group position on the devices electronic properties and found that shifting from *para*- to *ortho*-, **2.1**, enhanced the PSCs efficiency (Figure 2.3).[126] Tomkute-Luksiene *et al*. also moved the methoxy group position, but only on one side of the diphenylamine, to the *meta*- position, **2.2**, which was found to improve its stability due to an enhanced amorphous phase and the loss of symmetry reducing the likelihood of crystallisation (Figure 2.3).[127]
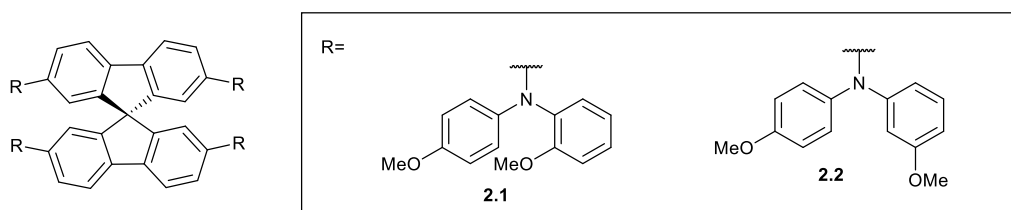

Figure 2.3: Molecular structure of HTMs based on methoxy manipulated spiro-OMeTAD

More recently, Chen *et al*. reported two spirobifluorene based HTMs with partial substitution of the methoxyphenyl terminal groups with either *N*-ethyl-carbazole or dibenzothiophene (Figure 2.4).[128] Both derivatives have lower HOMO levels than spiro-OMeTAD, improving the hole injection from the perovskite layer. On film deposition, **2.4** showed high crystallinity and poor solubility which caused pinholes to form while **2.3** had a low crystallinity and high solubility producing homogeneous films with good dopant distribution.

Solar cells employing dopant-free HTMs have also attracted a lot of interest due to the ease of production and cost reduction. Murakami and coworkers recently reported tetrasubstituted spirobifluorene derivatives bearing *N,N*-dimethylamino groups to replace the methoxy groups (Figure 2.4).[129] Two cyano groups were introduced at the *meta*-, **2.5**, or *ortho*-, **2.6**, positions of the nitrogen attached to the core. The presence of strong electron withdrawing groups lowers the HOMO and induces dipoles, facilitating charge transfer and intermolecular interactions while also causing the passivation effect due to cyano coordination to the lead ions. Both compounds obtain good thermal stability but a low hole mobility (10 times lower than spiro-OMeTAD). The best PCE obtained for dopant-free devices is 16.3% for **2.6**.
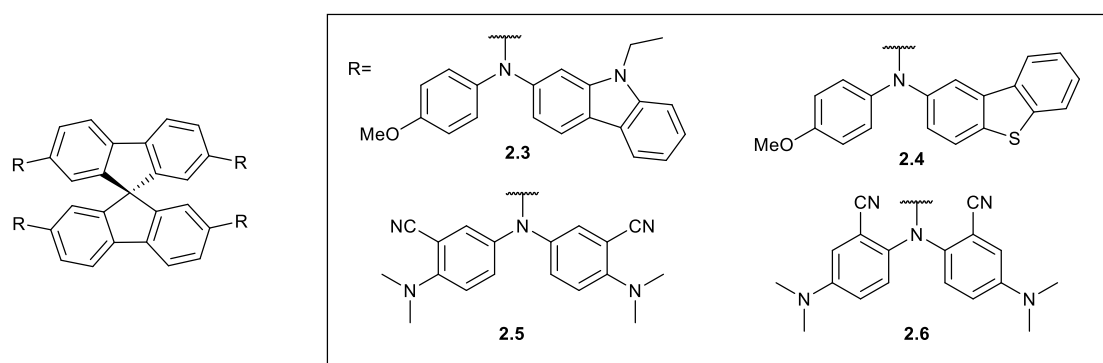
Figure 2.4: Molecular structures of HTMs based on the spirobifluorene core

Cooke and coworkers synthesised an unsymmetrically functionalised spiro-OMeTAD derivative, by exploiting the hydroxyl group reactivity, they produced a dimer and trimer (Figure 2.5).[130] The redox and optical properties of spiro-OMeTAD were retained and higher conductivities produced, attributed to higher porosity. The dimer showed a PCE of up to 16.4% compared to the benchmark spiro-OMeTAD of 16.1%. This monomer material has the potential to be used to create a wide range of new spiro-OMeTAD based materials.

Figure 2.5: Molecular structure of spiro-OMeTAD based dimer and trimer materials

2.1.4 Polymers as additives in HTL

As mentioned previously, the use of additives is a very common strategy for improving the charge mobility and J_{SC} in PSCs.[118] However, the use of doping agents has several disadvantages 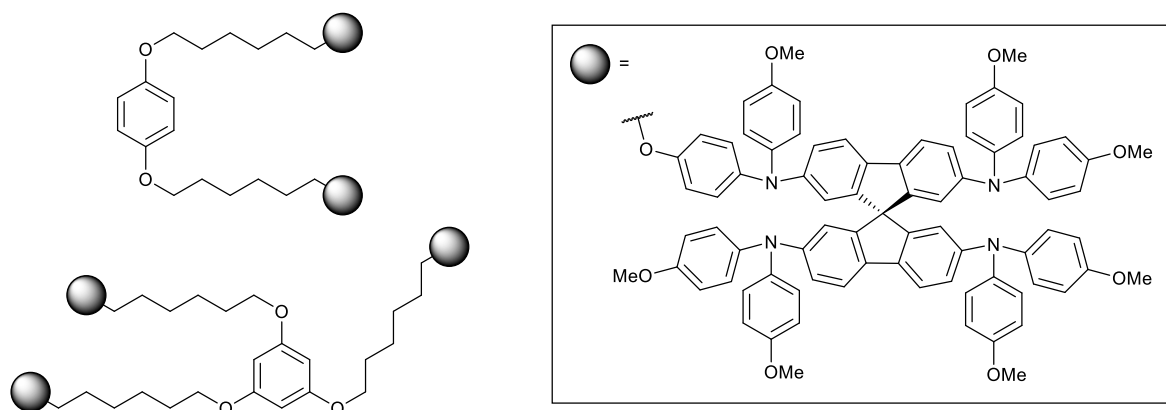that affect photovoltaic performances including the hygroscopic nature of some dopants causing migration into the perovskite layer during operation which reduces device performance.[131,132] Furthermore, their solution processability requires solvents which can dissolve perovskites and therefore partially degrade the light-harvesting layer. Consequently, a variety of other dopants have been tested as possible alternatives.[117,133,134] Organic polymers have been studied as a feasible way to improve performance and stability due to their high chemical and structural versatility. Polymers can be incorporated as additives in multiple layers of the PSC including the perovskite layer, ETL and HTL. Very few polymers have been reported as doping agents in the HTL to date, therefore this application has not been fully explored. Dopants used in the HTL are either incorporated into the PSC as passivation layers or blended with the HTM.

Wang *et al.* utilised poly(methyl methacrylate) (**PMMA**) as a passivation layer between the HTM, **2.7**, and Sn-Pb perovskite which led to an improved wettability to ensure good adhesion to the perovskite layer (Figure 2.6).[135] After optimisation by doping and surface engineering a PCE of 22.6% was obtained. The perovskite films possess improved crystallinity, reduced trap-state density and larger carrier mobility which greatly improved the PSC device stability. **PTAA** has been used by Liu and coworkers as an additive for their HTM, **2.8** (Figure 2.6).[136] The optimal concentration of the additive improved the performance of the pure HTM as well as the bare **PTAA**. **PTAA** hinders the aggregation of the small-molecule HTM due to its polymeric nature thus providing a better film crystallinity. Doping resulted in a better band alignment which improved the charge transferability and therefore increasing the J_{SC} and FF. In addition, the doped device produced a higher shelf-life

after 150 hours at ambient conditions, maintaining up to 90% of the initial performances compared to 70% achieved by the reference. The doped PSCs presented better stability against degradation in ambient air after 20 days without encapsulation compared to the control devices. Saunders and coworkers investigated whether insulating polystyrene microgel particles (MGs) (submicrometer-crosslinked polymer particles that can swell in certain solvents) could stabilise PSCs while replacing most of the HTM.[137] MGs were prepared using scalable emulsion polymerisation. Mixed HTM/MG dispersions were then spin-coated onto PSCs to form composite HTM-MG layers where the HTMs were **PTAA**, **P3HT** or spiro-OMeTAD (Figure 2.6). The resulting **PTAA**- and **P3HT**-MG composites were mechanically robust however the spiro-OMeTAD-MG contained microcracks due to the relatively small spiro-OMeTAD molecules being unable to interdigitate. Furthermore, the PCEs of the **PTAA**- and **P3HT**-MG PSCs only decreased by approximately 20% compared to the control devices despite **PTAA** and **P3HT** being the minority phase. Surprisingly, the MGs dispersed well within the **PTAA** matrix, aiding in the strong quenching of the $MAPbI_{3-x}Cl_x$ fluorescence. Moreover, the V_{OC} for the **P3HT**-MG PSCs increased by roughly 170 mV compared to the control devices. Since MGs can reduce conjugated polymer use and increase stability, they have potential to act as dual-role PSC additives.
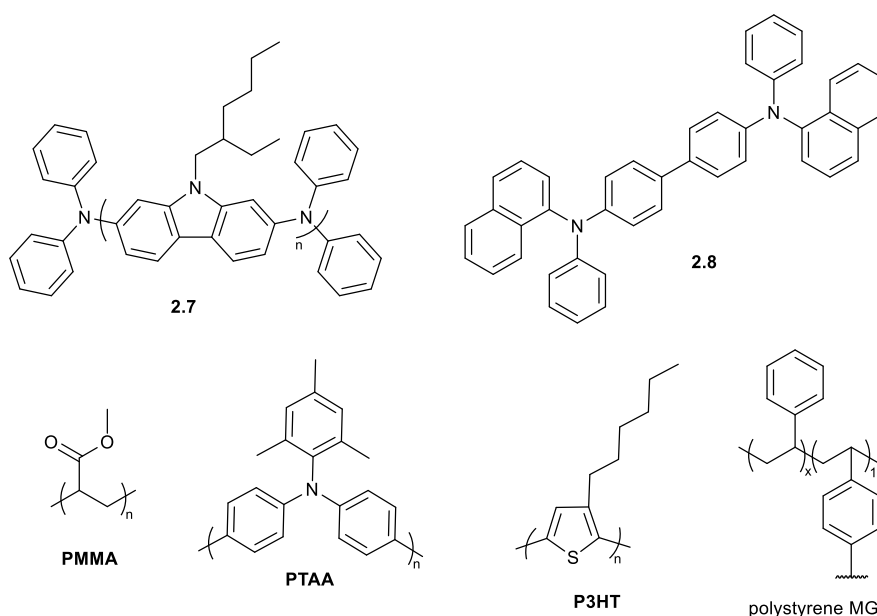

*Figure 2.6: Molecular structures of polymer additives and HTMs*

2.2 Aims

The initial aim of this project was to develop a route to synthesise polymers based on the unsymmetrically functionalised spiro-OMeTAD derivative previously developed in the Cooke group. The motivation for this synthesis originates from the results produced from the published dimer and trimer which retained the optical and redox properties of spiro-OMeTAD while producing higher conductivities due to the higher porosity.[130] The dimer, in particular, behaved better than spiro-OMeTAD due to its greater disorder which, in principle, indicates that a polymer featuring this spiro unit could achieve a better performance. PMMA has been extensively investigated as an additive, interlayer or encapsulating layer in PSCs. It has been noted to enhance hysteresis behaviour, performance and stability of the device by protecting the perovskite layer against oxygen and moisture.[138] Additionally, the carbonyl group of PMMA can form coordinative bonding with Pb^{2+} vacancies at the grain boundaries thereby passivating their defects.[139] It was hypothesised that incorporating the methacrylate group into the polymer and using the monomer, methyl methacrylate, as a linker or spacer could aid in stabilising the spiro-OMeTAD based device and reduce pinholes commonly found in the solution-processed perovskite film.[140]

2.3 Results and Discussion

2.3.1 Target Compounds Design

The optimised synthesis of the unsymmetrical functionalised spiro-OMeTAD has been achieved in the Cooke group. The reactivity of the hydroxyl group provides an effective handle for further synthesis. A glycol chain ending in a methacrylate group was used to improve solubility and provide a simple, effective group for radical polymerisation. Here, polymer derivatives were to be synthesised with varying percentages of methacrylate spacer groups to compare properties and the effect of the insulating group. Once synthesised, the multiple polymers were to be fully analysed with respect to their optical and electronic properties before being delivered to the Docampo group at the University of Glasgow to perform conductivity measurements in order to determine their potential for use in PSCs.
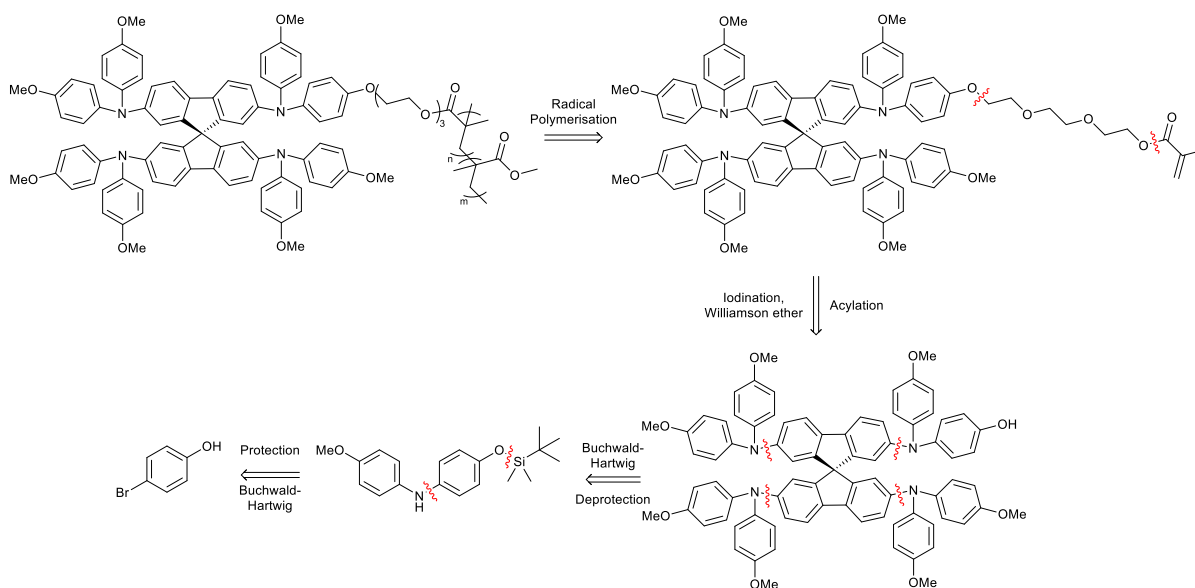
Scheme 2.1: Retrosynthesis of novel spiro-OMeTAD polymers

2.3.2   Synthesis

The initial synthetic steps for the formation of the spiro-polymers followed the more scalable bottom-up conditions published in previous Cooke group work.[130] First, the commercially available 9,9'-spirobifluorene was brominated using sodium bromide to achieve compound **2.9** to an excellent yield of 90%. These conditions were utilised as a higher yield and reproducibility was possible compared to other conditions previously attempted in the Cooke group. The strong acid helps push the conversion of NaBr to bromine with H_2O_2 acting as the oxidant (Scheme 2.2).
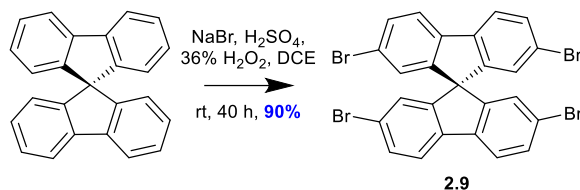
Scheme 2.2: Synthesis of compound 2.9

In order to make the unsymmetrical spiro building block **2.13**, an unsymmetrical diphenylamine must be synthesised. The first stage involves the protection of the alcohol of 4-bromophenol using *tert*-butyldimethylsilyl chloride, attaining a quantitative yield of compound **2.10** (Scheme 2.3). Compound **2.10** was subsequently subjected to Buchwald-Hartwig conditions, to achieve compound **2.11** at a very good yield of 87%.
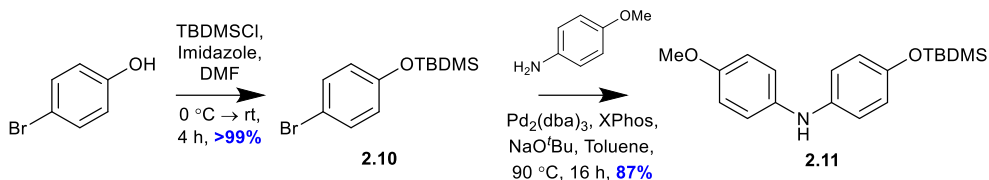
*Scheme 2.3: Synthesis of compound **2.11***

Compounds **2.9** and **2.11** were added at the same time to a microwave vial using the general method used in the literature for spiro-OMeTAD but may vary in catalyst and ligand applied, in this case tris(dibenzylideneacetone)dipalladium(0) and XPhos are employed.[127] Spiro-OMeTAD was also formed during this reaction but can be efficiently separated from the desired product, compound **2.12**, by column chromatography to obtain a 30% yield of the desired material (Scheme 2.4).
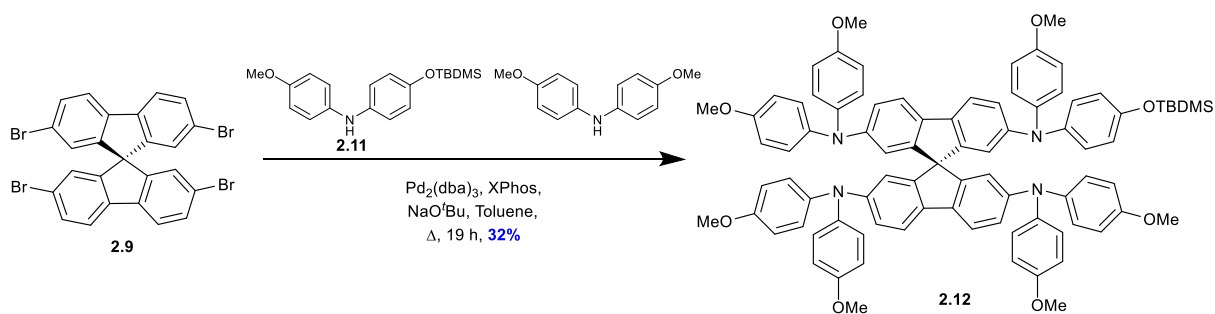
*Scheme 2.4: Synthesis of compound **2.12***

In order to do further synthetic manipulation to compound **2.12**, the protecting group must be cleaved from the molecule. To achieve this, the addition of a fluoride ion source is necessary which would lead to the Si–O cleavage, as the Si–F bond is stronger, while not affecting the rest of the molecule. In this case, tetra-*N*-butylammonium fluoride (TBAF) in *N*, *N*-dimethylformamide was utilised, thus making the hydroxyl group available to act as a nucleophile in future reactions (Scheme 2.5). The near quantitative yield was achieved by performing the reaction in a microwave vial to provide more concentrated, harsh conditions.
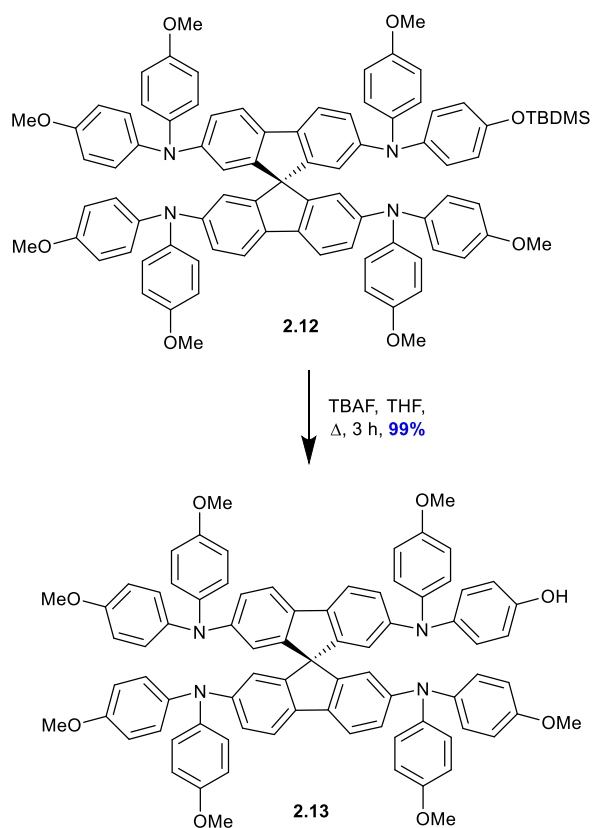
*Scheme 2.5: Synthesis of compound **2.13***

PMMA is one of the most widely used polymers, produced using a free radical indicator and the methyl methacrylate monomer via a low-cost and convenient radical polymerisation. Methyl methacrylate (MMA) is popular in polymer chemistry owing to its contribution towards durability, thermal stability, optical clarity, impact strength and scratch/abrasion resistance in the polymers.[141] Consequently, spiro-polymers functionalised with the methacrylate group were proposed and a route devised that utilised the commercially available 2-[2-(2-chloroethoxy)ethoxy]ethanol. This material was used to improve solubility while also attempting to reduce the steric hinderance at the polymer backbone. 2-[2-(2-Chloroethoxy)ethoxy]ethanol underwent iodination with sodium iodide, in order to make this material more reactive, to produce compound **2.14** to a very good yield of 87% (Scheme 2.6). Since the synthesis of compound **2.13** requires a challenging multistep synthesis, the methacrylation of compound **2.14** was attempted first to prevent any waste in material. Methacrylic anhydride was reacted with compound **2.14** to achieve a moderate yield of 44% for compound **2.15**.
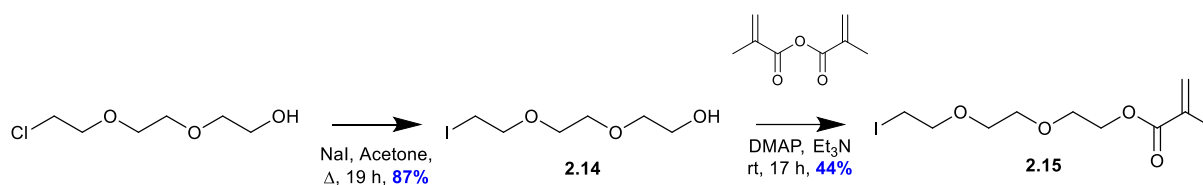
Scheme 2.6: Synthesis of compound **2.15**

Compounds **2.13** and **2.15** were then subjected to the Williamson ether synthesis reaction, on NMR analysis the methacrylate end group was observed to have cleaved from the molecule and instead a hydroxyl group was present (Scheme 2.7). It was hypothesised that any excess of the strong base, sodium hydride, after completion of the Williamson ether synthesis then reacted with the methacrylate end group and removed it from the molecule. This step was repeated with varying reaction times and achieved the same result. A further methacrylation could then be performed however this would require an extra synthetic step and reduce the overall yield. Therefore, an alternative route was formulated.
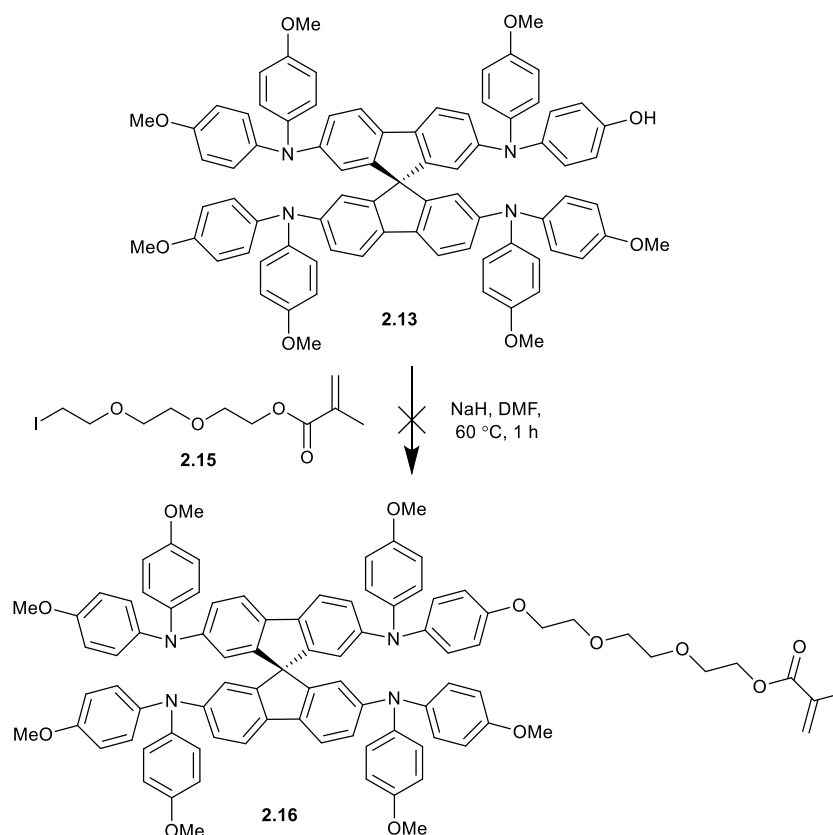
Scheme 2.7: Attempted synthesis of compound **2.16**

The newly proposed synthetic route switched the order of the methacrylation and Williamson ether reaction, adding compound **2.14** before the reaction with methacrylic anhydride to prevent the cleaving of the methacrylate group. Although previously mentioned that this may waste some of the material, it would require one less synthetic step than the previously attempted route thereby potentially improving the overall yield. Compound **2.13** underwent the Williamson ether reaction with compound **2.14** to achieve compound **2.17** to a moderate yield of 55% (Scheme 2.8).
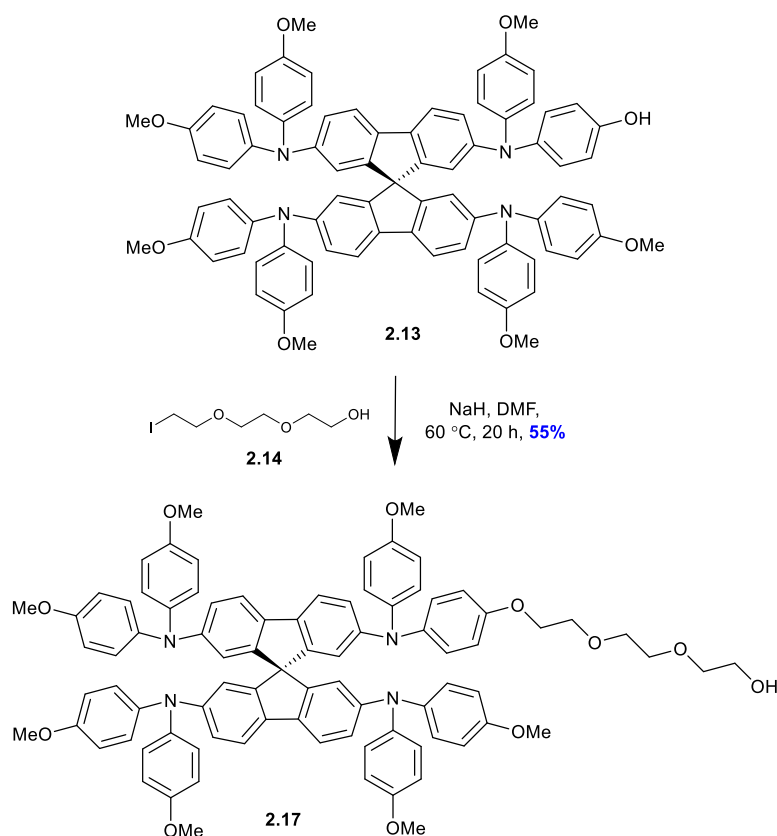
*Scheme 2.8: Synthesis of compound **2.17***

The final step of the monomer synthesis required methacrylic anhydride and was performed in a microwave vial due to a minimal volume of liquid being present. Methanol was added on reaction completion to quench any residual methacrylic anhydride and compound **2.18** was isolated in a moderate yield of 55% (Scheme 2.9).
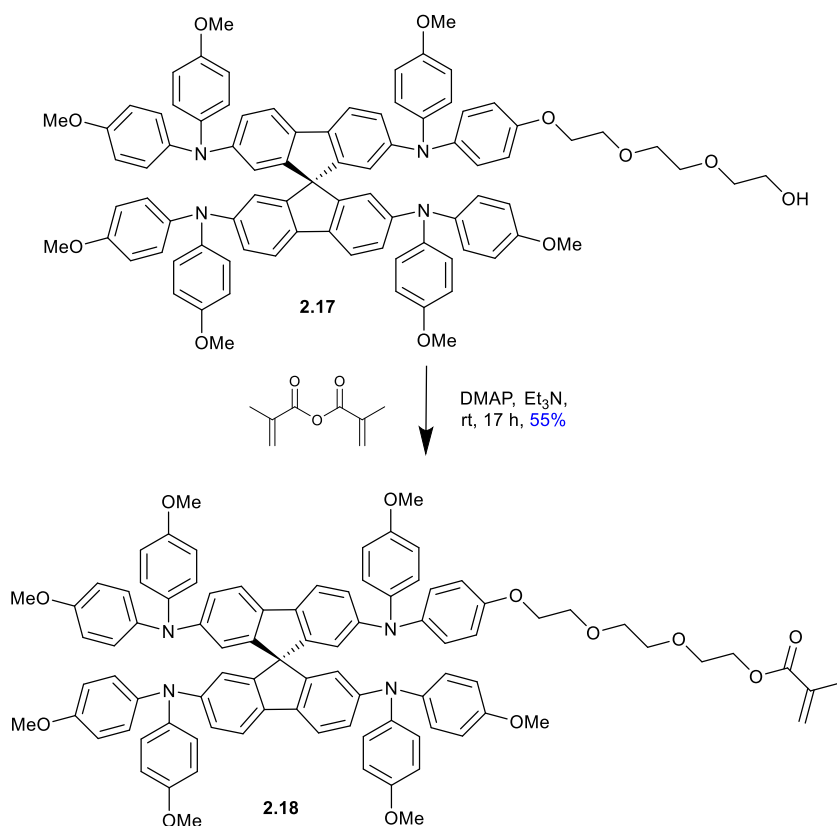
*Scheme 2.9: Synthesis of compound **2.18***

Free radical polymerisation is a widely used method for creating polymers from vinyl monomers. The relatively non-specific nature of free radical chemical interactions makes them one of the most versatile forms of polymerisation and allows facile reactions of polymeric free-radical chains and other chemicals or substrates. In this case, azobisisobutyronitrile (AIBN) is used as the initiator, as a nitrile stabilised radical is formed as it degrades on heating. As this is a random polymerisation it is unlikely that the same chain length or sequence will be achieved batch to batch. Therefore, enough material must be synthesised for full characterisation and subsequent device fabrication. To achieve the synthesis of a 100 mol% polymer **2.19**, a 2 mL microwave vial purged with nitrogen was used, containing monomer **2.18** and AIBN which were dissolved in a minimal amount of *N*, *N*-dimethylformamide (Scheme 2.10). Minimal solvent was used as it effects chain transfer, as radicals of the solvent are formed they can stop the polymerisation leading to low weight polymer synthesis.[142] Confirmation of polymerisation was qualitatively obtained by inspection of its ¹H NMR spectrum as the resonances became broader and the alkene resonances of the alkene moieties of the methacrylate unit disappeared and new signals for the polymer backbone emerged at a more upfield position.
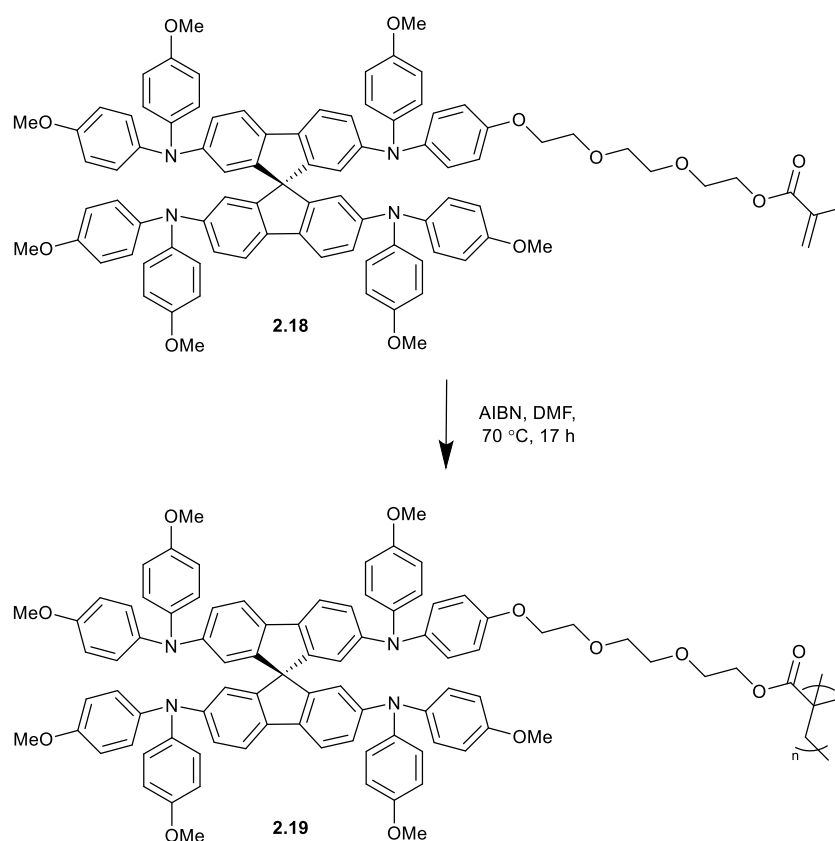
Scheme 2.10: Synthesis of 100 % polymer, **2.19**

Commercially available MMA contains a small amount of inhibitor to allow for safe storage. Therefore, filtration through a small plug of alumina was required to remove this before the radical polymerisation was attempted. In order to obtain a better understanding of the impact of the methacrylate spacer on the polymers properties a few co-polymers were synthesised with varying mol% of compound **2.18** to methyl methacrylate: 1%, 20% and 25%. For 25 mol% polymer **2.20**, this means there is a 1:3 ratio of monomer **2.18** to methyl methacrylate in the polymer solution (Scheme 2.11). In order to confirm the accuracy of the feed in percentage ratio, the NMR of the polymers were extensively studied. Figure 2.7 shows the NMR for the 25 mol% polymer **2.20** and outlines how the ratio of peaks were utilised to determine the percentage ratio. The peak at 6.81 ppm has previously been confirmed to represent two aromatic hydrogens and the peak at 4.09 ppm represents a CH_2 from the glycol chain of monomer **2.18**. The broad peak at 2.07 ppm represents the CH_2 linker between the methacrylate of both starting materials (**2.18** and methyl methacrylate). By applying the equation: A/(A+B) × 100 the percentage ratio was determined and found to agree with the monomer loading ratio for each polymer. The yields obtained for 1 mol% (**2.22**), 20 mol% (**2.21**) and 25 mol% (**2.20**) were 20%, 84% and 65%, respectively. Gel permeation chromatography (GPC) measurements were taken for each polymer to determine the molecular weight and weight

distributions. Each chromatogram showed a broad range of molecular weights with a M_n/M_w ratio of 1.88 (**2.22**), 1.95 (**2.21**) and 2.33 (**2.20**).
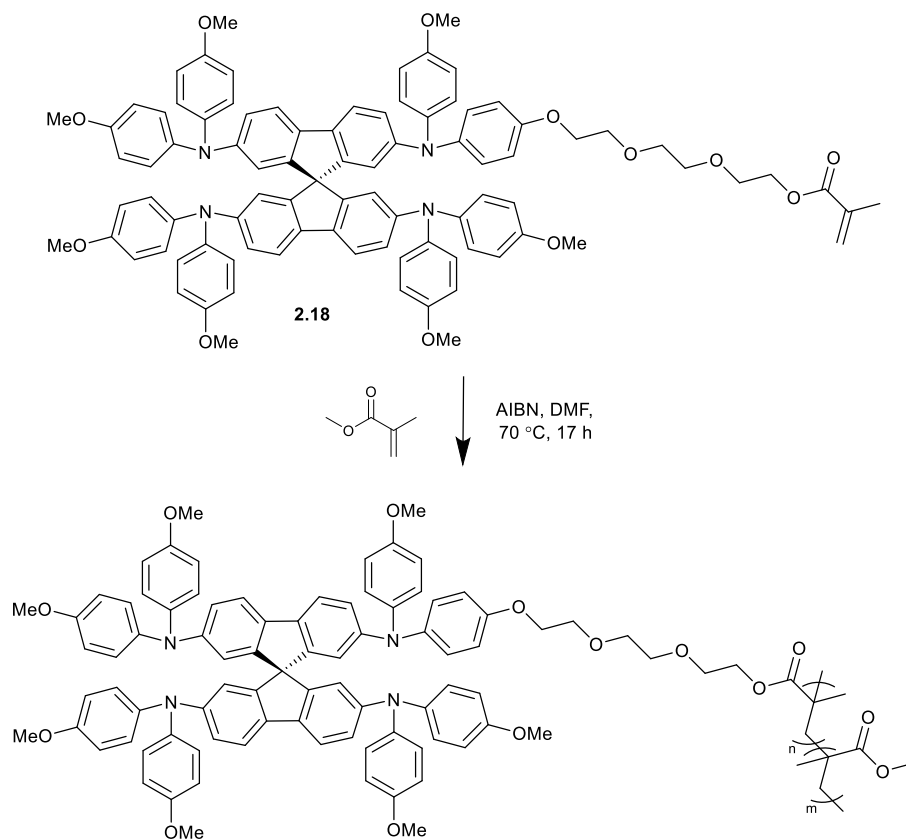
*Scheme 2.11: Synthesis of 1 mol% (**2.22**), 20 mol% (**2.21**) and 25 mol% (**2.20**) polymers*
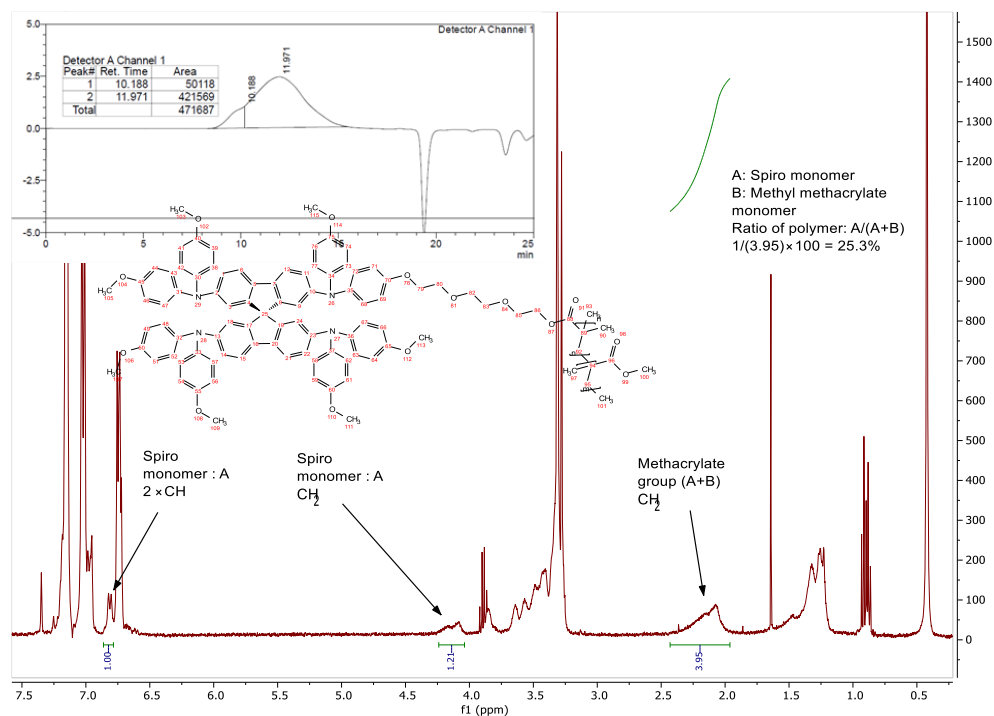

*Figure 2.7: NMR and GPC data for 25 mol% polymer **2.20***

2.3.3 Optoelectronic Properties

The UV-Vis and fluorescence spectra of the spiro-polymers **2.19**, **2.20**, **2.21** and **2.22** were evaluated and recorded in dichloromethane (CH_2Cl_2) solutions. The absorption and emission spectra are shown in Figure 2.8 and the corresponding photophysical data summarised in Table 2.1. The absorption spectra for compounds **2.19**, **2.20**, **2.21** and **2.22** appear at approximately the same position in the UV region, with the only change being the molar extinction coefficient (ϵ) which progressively decreases as the percentage of spiro-OMeTAD in the polymer decreases. This indicates that the only impact of the MMA linkers was to hinder the absorption of the material. The weak absorption in the visible region observed for all polymers can be attributed to the spiro-annulated fragments preventing conjugation through the molecules and should be able to produce good photovoltaic performance in devices as this will not affect the absorption of the perovskite. The estimated onset wavelength (λ_{onset}) for each material is shown in Table 2.1 which aid in determining the optical band gap ($E_{g, opt}$) for each material by applying the Einstein-Planck equation:

$$E_{g,opt} = \frac{hc}{\lambda_{onset}}$$

where h is Planck's constant (4.316×10^{-15} eV) and c is the speed of light (3×10^{17} nm s^{-1}).

The emission spectra for all spiro-polymers occurred at a similar wavelength of around 426 nm. The Stokes shift experienced by the spiro-polymers are relatively small, ranging from 37 – 46 nm (2401 – 2772 cm^{-1}). The Stokes shift is caused by vibrational relaxation and solvent reorganisation. Therefore, Stokes shift is a direct measure of the vibrational energies of the molecule and exhibit minimal electronic effect on emission.
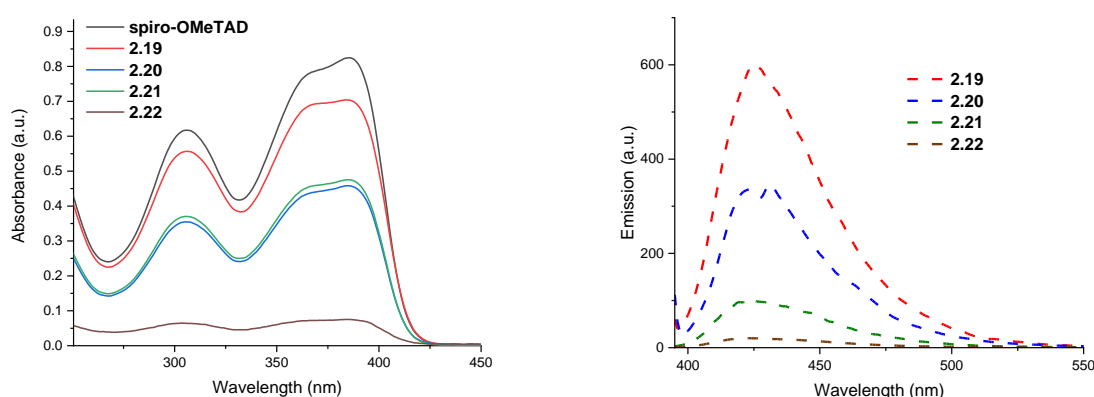

*Figure 2.8: Absorption (c = 1 × 10^{-5} M) and emission (c = 1 × 10^{-8} M) spectra for **2.19** (red), **2.20** (blue), **2.21** (green) and **2.22** (brown) in CH$_2$Cl$_2$ solutions*

Compound	λ_{max} (nm)	λ_{onset} (nm)	$E_{g, opt}$ (eV)	Emission (nm)	Stokes shift (nm/cm^{-1})	Molar extinction coefficient $\varepsilon \times 10^3$ (L mol^{-1} cm^{-1})
Spiro-OMeTAD	385	415	2.99	-	-	82.5
2.19	384	416	2.98	426	42/2567	70.4
2.20	385	414	3.00	431	46/2772	45.8
2.21	385	414	3.00	422	37/2277	47.5
2.22	384	415	2.99	423	39/2401	7.5

*Table 2.1: Summary of the optoelectronic properties of polymers **2.19, 2.20, 2.21** and **2.22**. $E_{g, opt}$ estimated from λ_{onset} of absorption.*

2.3.4 Electrochemical Properties

The electrochemical behaviour of the spiro-polymers was obtained by cyclic voltammetry (CV) and square wave voltammetry (SWV). The CV and SWV were performed in CH_2Cl_2 (1×10^{-4} M), the spectra are shown in Figure 2.9 and the corresponding data detailed in Table 2.2. Polymer compounds **2.19**, **2.20** and **2.21** show pseudo reversible oxidation peaks within the electrochemical window (+1.5/−1.5) while compound **2.22** does not show any visible redox properties, presumably due to the high methacrylate content preventing oxidation of the spiro-OMeTAD moiety at the electrode surface. Identification of the ionisation potential (IP) position is crucial for HTMs as this gives an estimation of the HOMO position which indicates how capable the material is at hole transfer with the perovskite valence band. The IPs were calculated with respect to the ferrocene external reference energy level.[143,144] E_{OX} were taken from the peak maximum of the SWV. The oxidation peaks of compounds **2.19**, **2.20** and **2.21** are wide, suggesting multiple oxidations. The literature states that the HOMO level of spiro-OMeTAD is −5.22 eV.[145] The data collected showed slightly higher values and the peaks shifted towards zero as more methacrylate was present indicating an increased difficulty to oxidise the spiro-OMeTAD part of the polymer. All IP levels calculated were higher than the perovskite (MAPbI$_3$), −5.43 eV, thus enabling hole transfer. V_{OC} increases with deeper HOMO levels therefore, from these results, the V_{OC} is predicted to decrease with increasing methacrylate linker from 100 mol% (**2.19**) to 1 mol% (**2.22**). The electron affinity (EA) was estimated using $E_{g, opt}$ calculated from the absorption spectra and provided values which would assure efficient electron blocking and reduce the probability of hole/electron recombination.[146]
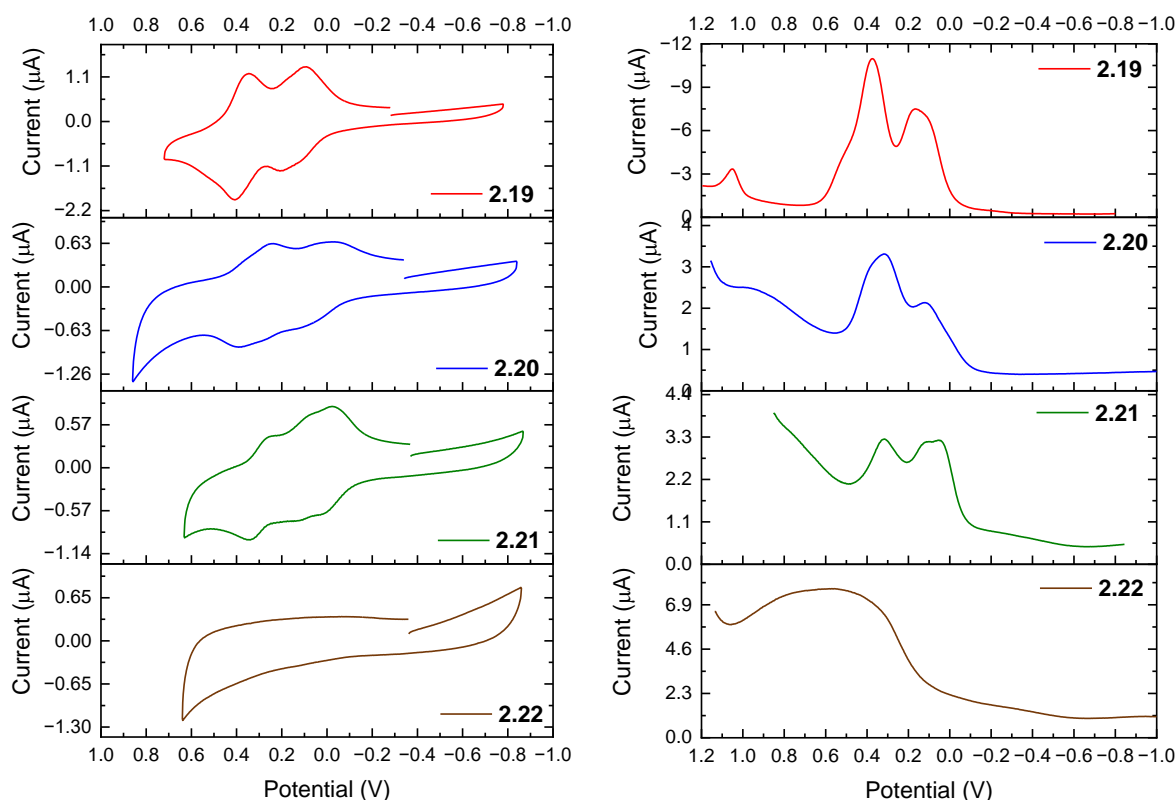
*Figure 2.9: CV and SWV plots of polymers **2.19** (red), **2.20** (blue), **2.21** (green) and **2.22** (brown) in solution (c = 1 × 10⁻⁴ M, in CH₂Cl₂) with a scan rate of 0.1 Vs⁻¹, performed using a Pt disk working electrode, a Pt wire counter electrode and a Ag wire reference electrode. TBAPF₆ (0.1 M) was used as supporting electrolyte and the redox potential of the Fc/Fc⁺ couple as internal standard.*

Compound	E_{ox} (V)	EA (eV)	IP (eV)
2.19	0.168	−4.97	−1.99
2.20	0.12	−4.92	−1.92
2.21	0.052	−4.85	−1.85
2.22	-	-	-

*Table 2.2: Summary of the electrochemical properties of polymers **2.19**, **2.20**, **2.21** and **2.22**. EA and IP calculated using following equations: $EA = -[E^{0.5}_{red} - (-4.80)]$ eV; $IP = EA - E_{g,opt}$ (calculated for grey EA)*

2.3.5   Conductivity Measurements

The conductivity measurements were performed by our collaborators in the Dr. Pablo Docampo research group in the University of Glasgow by Benjamin Vella. Conductivity measurements were obtained using compound **2.19** and spiro-OMeTAD following doping with LiFTSI in chlorobenzene before spin-coating onto an ITO substrate. An order of magnitude less conductivity is observed for compound **2.19** compared to spiro-OMeTAD (Figure 2.10). This may be caused by the methacrylate

backbone acting as an insulator, hindering the charge mobility and thus reducing their application in solar cells.
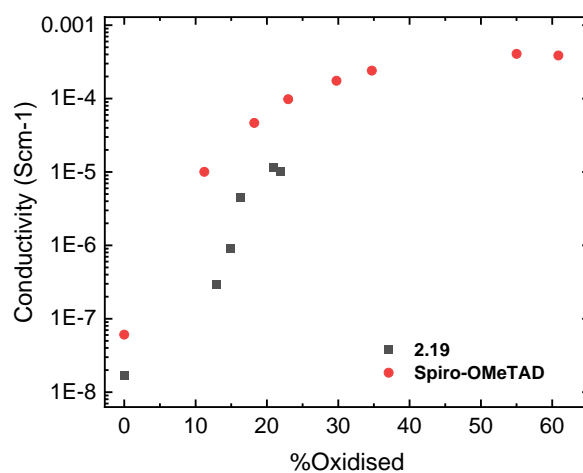

*Figure 2.10: Conductivity measurements of spiro-OMeTAD and compound **2.19** doped with LiTFSI*

Due to these findings, we decided that applying the polymers as an additive layer in a spiro-OMeTAD doped device would be a better application. The 100 mol% (**2.19**) and 20 mol% (**2.21**) polymers were analysed along with PMMA, as a control. Preliminary conductivity measurements obtained using the optimised general method used in the Docampo group[147,148] set up with FK209, LiTFSI, *t*-BP, spiro-OMeTAD and polymer spin-coated onto an ITO substrate from a chlorobenzene solution. The cobalt-based dopant, FK209, was used as the main oxidant as this dopant does not require oxygen, therefore eliminating any potential barrier properties that a large amount of polymer additive could present in the spin-coating process.

At 0 wt% polymer content there are no polymers present, making this the optimal spiro-OMeTAD doping concentration (Figure 2.11). As a larger amount of insulating PMMA is added to the solution a decrease in conductivity is observed, as expected due to the insulating nature of the polymer backbone. A similar trend is also noted for compounds **2.21** and **2.19** however to a lesser degree due to the presence of the conductive spiro-OMeTAD in these polymers. This implies that the conductivity is retained when more conductive groups are present in the polymer. Therefore, it would be interesting to observe the effects of the polymer devices, noting not just their efficiency but also device stability and overall performance.
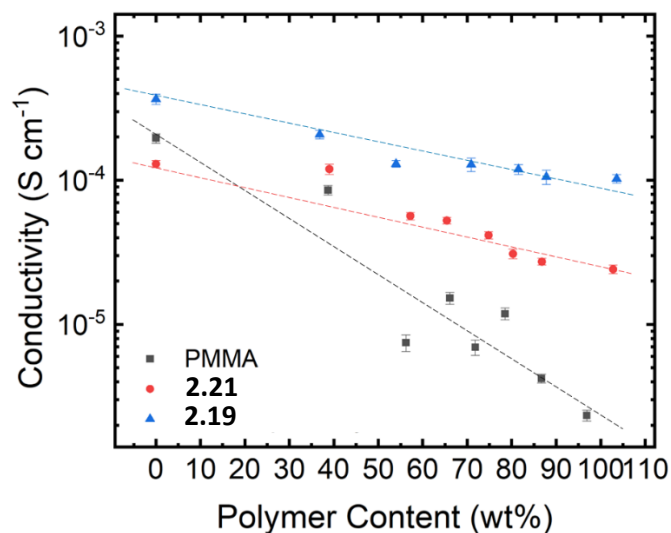
Figure 2.11: Conductivity measurements performed with varying concentrations of polymer

2.3.6 Spiro-Polymers in PSCs

The device fabrication was performed by Dr. Namrata Pant of the Dr. Pablo Docampo research group. Preliminary cells were fabricated using the planar n-i-p device architecture, employing Glass/FTO/SnO$_2$/Perovskite/spiro-OMeTAD: polymer/Au stacking. Each device was fabricated with a different HTM: polymer blend, namely spiro-OMeTAD (reference), spiro-OMeTAD + compound **2.20** and spiro-OMeTAD + compound **2.19** (The HTM is optimally doped using the method mentioned for the conductivity section). The J-V characteristics were measured under AM 1.5 G illumination on the day of device construction and after 2 days (Figure 2.12). Initial measurements taken for these devices showed comparable results with the devices containing the polymer additives having a slightly higher PCE of 16.76% (**2.20**) and 15.7% (**2.19**) to spiro-OMeTAD of 14.62%. However, on repeat analysis after 2 days compound **2.19** devices had a drastic drop in J$_{SC}$ from 21.01 mA cm^{-2} to 15.91 mA cm^{-2} showing a sharp degradation. Possibly this is caused by the porous nature of this polymer allowing water and oxygen to penetrate the device and therefore the PCE reduced to 15.91%. The devices based on spiro-OMeTAD and compound **2.20** retained its initial properties while increasing PCE by 5% and 2.6% respectively. Therefore, further studies comparing this polymer to spiro-OMeTAD devices were devised.
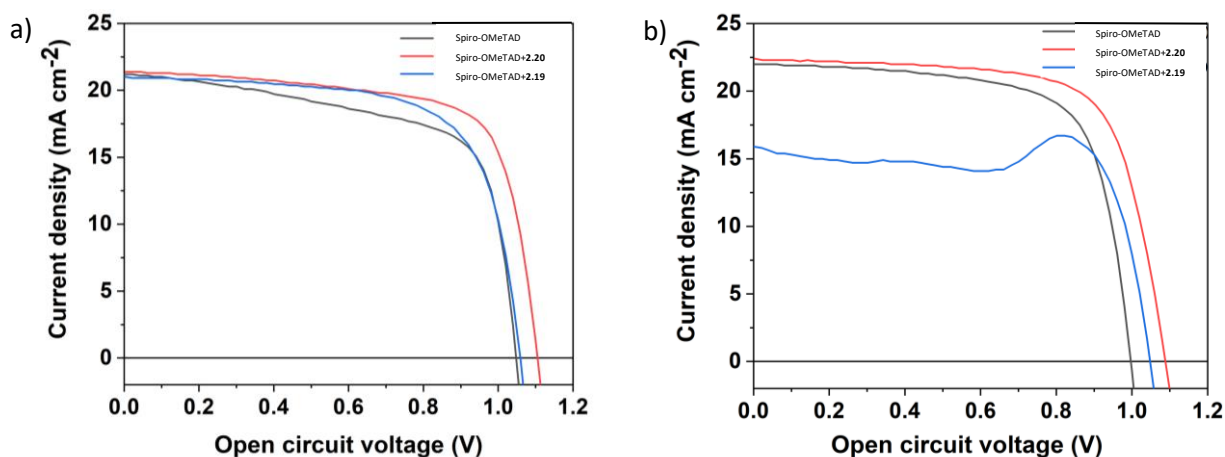
Device conditions	J_{SC} (mA cm^{-2})	PCE (%)	V_{OC} (V)	FF
Spiro-OMeTAD	21.24	14.62	1.05	0.66
Spiro-OMeTAD+**2.20**	21.39	16.76	1.11	0.71
Spiro-OMeTAD+**2.19**	21.01	15.17	1.06	0.68

Device conditions	J_{SC} (mA cm^{-2})	PCE (%)	V_{OC} (V)	FF
Spiro-OMeTAD	22.04	15.38	1	0.7
Spiro-OMeTAD+**2.20**	22.35	17.21	1.09	0.71
Spiro-OMeTAD+**2.19**	15.91	13.98	1.05	0.84

Figure 2.12: J-V curves of spiro-OMeTAD and spiro-OMeTAD with polymer additives a) on day of fabrication and b) after 2 days with corresponding solar cell parameters shown in the tables

Combining the results from Benjamin Vella's conductivity measurements and the preliminary device data, new devices were fabricated using the same architecture as previously mentioned (using a triple cation (TC) perovskite $Cs_{0.1}FA_{0.7}MA_{0.1}Pb(I_{5/6}Cl_{1/6})_3$) but different HTM: polymer blends. In this study spiro-OMeTAD, compound **2.20**, spiro-OMeTAD + compound **2.20**, spiro-OMeTAD + 6 mg/ mL PMMA and spiro-OMeTAD + 10 mg/ mL PMMA were used to identify the effect of polymer additives and also the effect of polymers containing a conductive part on the performance and stability of the device. The J-V characteristics were measured under AM 1.5G illumination (Figure 2.13) and the key solar cell parameters (V_{OC}, J_{SC}, FF and PCE) are reported in Table 2.3.

In regards to V_{OC}, the reference spiro-OMeTAD device has the lowest value of 0.99 V while compound **2.20** has the highest at 1.13 V due to a higher LUMO level for this material. The HTM: polymer blends all have similar V_{OC} of around 1.1 V, showing that addition of the insulating polymer lowers the LUMO level slightly.

FF and J_{SC} show similar trends, all HTM: polymer blends and spiro-OMeTAD devices have similar values while compound **2.20** has a lower value. This is presumably due to the high viscosity of this material increasing the series resistance which was indicated by a higher film thickness of this device

and resulting straight-line J-V curve. The HTM: polymer blends improve the morphology of the device, possibly due to closer intermolecular contact between molecules allowing a more facile charge generation.

The PCE of the HTM: polymer devices were similar to the spiro-OMeTAD device, achieving 21.54% (spiro-OMeTAD + compound **2.20**), 22.26% (spiro-OMeTAD + 6 mg/ mL PMMA) and 21.75% (spiro-OMeTAD + 10 mg/ mL PMMA) to 21.7% for spiro-OMeTAD. The compound **2.20** device only achieved a PCE of 2.82% showing pristine devices featuring this material were ineffective solar cells.
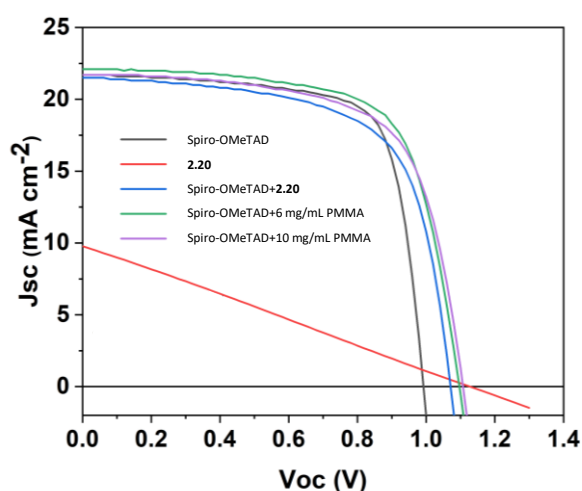

*Figure 2.13: J-V curves of spiro-OMeTAD, **2.20** and spiro-OMeTAD with polymer additives*

Device conditions	J_{SC} (mA cm^{-2})	PCE (%)	V_{OC} (V)	FF
Spiro-OMeTAD	21.7	15.9	0.99	0.73
2.20	9.77	2.82	1.13	0.26
Spiro-OMeTAD + **2.20**	21.54	16.63	1.1	0.7
Spiro-OMeTAD + 6 mg/mL PMMA	22.26	16.78	1.08	0.7
Spiro-OMeTAD + 10 mg/mL PMMA	21.75	15.93	1.11	0.66

*Table 2.3: Device characteristics of spiro-OMeTAD, **2.20** and spiro-OMeTAD devices with polymer additives*

The cells were left in a dry oxygen environment (desiccator) for 24 hours before the measurements were repeated to observe the impact of oxygen on the device properties, the J-V curve is shown in Figure 2.14 and the key parameters reported in Table 2.4. The spiro-OMeTAD device values all increased slightly while the compound **2.20** and spiro-OMeTAD + 10 mg/ mL PMMA device values had an increase in J_{SC} and PCE while V_{OC} and FF were unaffected. This may be due to the oxygen increasing the charge generation in the device but having no effect on the LUMO level. The spiro-OMeTAD + 6 mg/ mL PMMA device showed a reduced J_{SC} and PCE which may indicate the PMMA loading was too low in the device thus allowing oxygen to penetrate and increasing degradation of the materials. The optimal device performance was achieved by spiro-OMeTAD + compound **2.20**, which had an increase in all parameters and obtained the highest PCE of 18%. This indicated the potential for this blend of materials to produce high performance devices while also protecting it from oxygen to increase device stability. It is hoped that by further configuration of these materials

and optimising their ratio that highly efficient devices can be produced with greater stability than the benchmark spiro-OMeTAD devices.
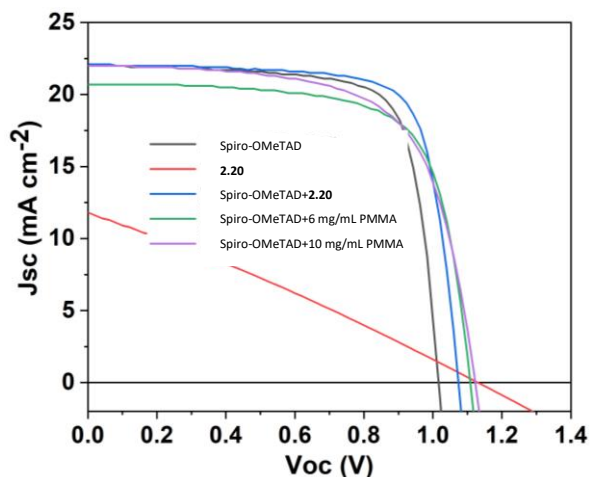

Figure 2.14: J-V curves of spiro-OMeTAD, **2.20** and spiro-OMeTAD with polymer additives after 1 day

Device conditions	J_{SC} (mA cm^{-2})	PCE (%)	V_{OC} (V)	FF
Spiro-OMeTAD	21.97	16.94	1.02	0.76
2.20	11.81	3.73	1.13	0.28
Spiro-OMeTAD + **2.20**	22.06	18	1.08	0.76
Spiro-OMeTAD + 6 mg/mL PMMA	20.74	16.27	1.11	0.71
Spiro-OMeTAD + 10 mg/mL PMMA	22.02	16.28	1.12	0.66

Table 2.4: Device characteristics of spiro-OMeTAD, **2.20** and spiro-OMeTAD devices with polymer additives

2.4 Conclusions and Future Work

A synthetic route was developed for the synthesis of spiro-OMeTAD based polymers. Following the previously established method in the Cooke group for the initial steps before a new methodology was established for the methacrylate monomer. The optoelectronic properties were measured for these compounds, showing a gradual decrease in both absorption and emission with increasing methyl methacrylate. The IP levels obtained by CV and SWV were higher than the published value of spiro-OMeTAD and as the ratio of methyl methacrylate in the polymers was increased, the more difficult it was for the spiro-OMeTAD part of the polymer to oxidise. This may be problematic in devices as it may cause a greater mismatch between energy levels which could hinder the performance of the devices. Preliminary conductivity measurements using these polymers as additives showed a similar downward trend in conductivity to that observed for the PMMA control, however, the spiro-OMeTAD containing polymers were more conductive than PMMA at the same mol% ratios. PSC devices fabricated using compound **2.20** as an additive in spiro-OMeTAD based devices produced an initial PCE of 16.63%. After 24 hours this had increased to 18%, outperforming the spiro-OMeTAD device and showing greater stability.

Potential future work would include performing atomic force microscopy (AFM) measurements which would enable the imaging of the device surface in order to identify whether the presence of polymer reduces the number of pinholes usually observed in a spiro-OMeTAD device. Research into these polymers is ongoing in the Cooke group with a colleague, Lewis Mackenzie, synthesising a 2 mol%, 5 mol% and 10 mol% polymers to provide a larger range of examples to compare their properties.

3 Greener Imine-based Hole Transporting Materials

3.1 Introduction

3.1.1 Green Chemistry inspired Hole Transporting Materials

Despite the PCE of PSCs having drastically increased from 3.8% in 2009 to 26.1%, there remains a number of device issues which still need to be resolved, particularly the improvement of long-term stability. The HTM is one of the key components necessary for producing an efficient and stable PSC device. However, HTMs are generally acknowledged to be complex structures which have caused issues such as increased cost and the presence of hazardous substances in the synthetic scheme which is particularly noticeable on transitioning from laboratory to manufacturing scale.[149] The most well-known organic HTMs are spiro-OMeTAD and PTAA, which unfortunately are included in this category, requiring multistep synthetic procedures involving metal catalysed cross coupling reactions, harsh reaction conditions and sizeable product purification which results in high material cost (impacting the overall cost of the device and large scale production).[150–152] This is due to these reactions being inclined to produce side-products and leave (metal) catalyst residues that can affect the performance of the resulting devices.[153] The employment of synthetic protocols which either reduce or eliminate the use of hazardous substances is highly desirable. In addition, simple reaction work up and purification may evidently reduce the final synthetic cost and environmental issues. Consequently, several research groups have focused their studies on developing new organic semiconductors, fine tuning the structure to reduce the number of synthetic steps that can be prepared via simple, cost-effective methods and using greener chemistry without forfeiting the efficiency of the device, while also being easily scalable at reasonable cost.

Daskeviciute-Geguziene *et al*. developed novel HTMs based on a cyclobutane core attached to two differently substituted photodimerized carbazole arms in a branched fashion (Figure 3.1). The bulkiness and sterically hindered rigid *trans*-configuration results in competition between the planarization and repulsive steric hinderance, which leads to a pseudo spiro-type arrangement with diverse torsion angles.[149] As a consequence of the cyclobutane fragment increasing T_g, the HTMs were more amorphous and morphologically stable compared to spiro-OMeTAD. The most efficient perovskite device contained **3.1** which achieved a PCE of 21% and excellent long-term stability.
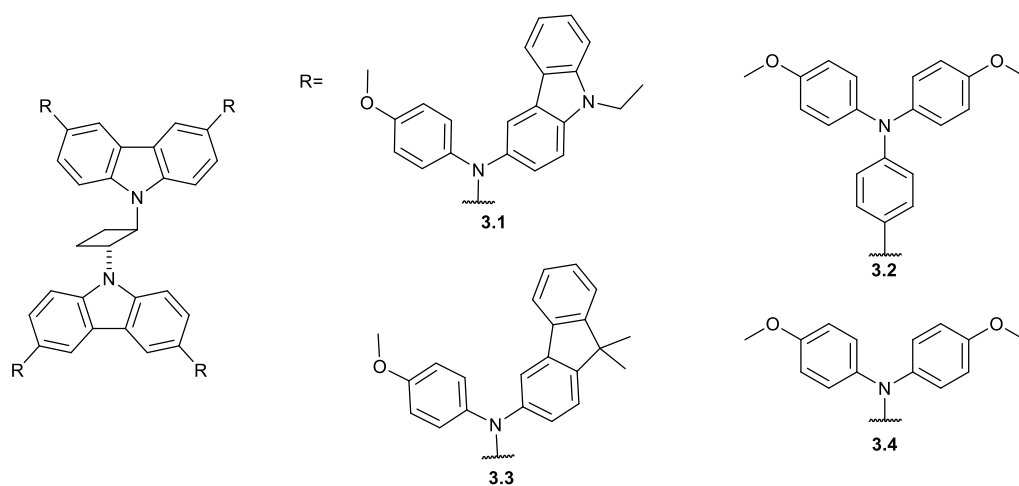
Figure 3.1: Novel HTMs based on substituted cyclobutane

Grätzel and coworkers developed three low cost HTMs based on phenothiazine (a versatile electron rich heteroaromatic unit which has been used to access a wide range of HTMs via relatively cheap synthetic procedures) which is connected to the peripheral groups by double bonds (Figure 3.2).[154] These HTMs were found to show high T$_g$, hole mobility and suitable HOMO energy level alignment. Compound **3.7** achieved PCEs of up to 19.7%, while also obtaining higher stability than the other analogues.
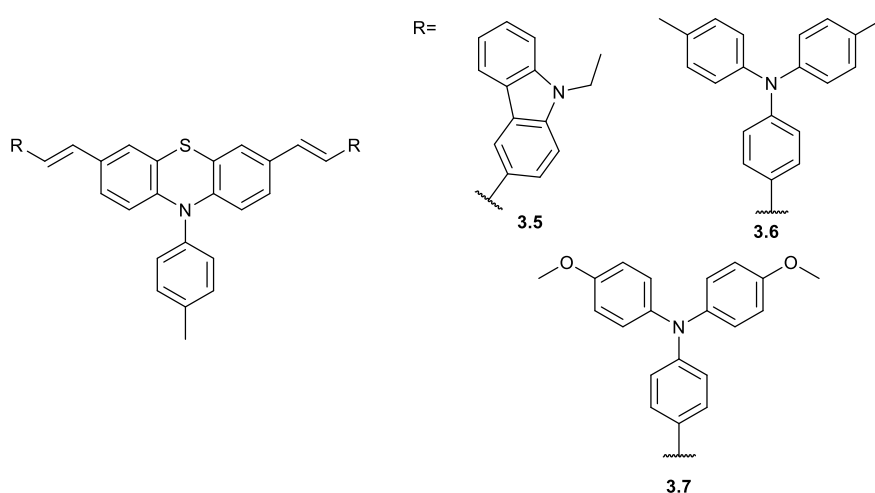

Figure 3.2: Chemical structures of HTMs based on phenothiazine

Grätzel and coworkers also designed and synthesised two thiophene based HTMs using simple, low-cost processes (Figure 3.3).[155] The double bond connected derivative **3.9** was synthesised using

cheap starting materials via the Horner-Wadsworth-Emmons reaction to achieve PCEs up to 20.1%, comparable to spiro-OMeTAD. They also observed that devices based on these materials obtained better stability than devices based on the benchmark spiro-OMeTAD. Both papers show that introduction of double bonds to the design of HTMs produces highly efficient and stable PSCs with low cost, which is crucial for commercial applications.
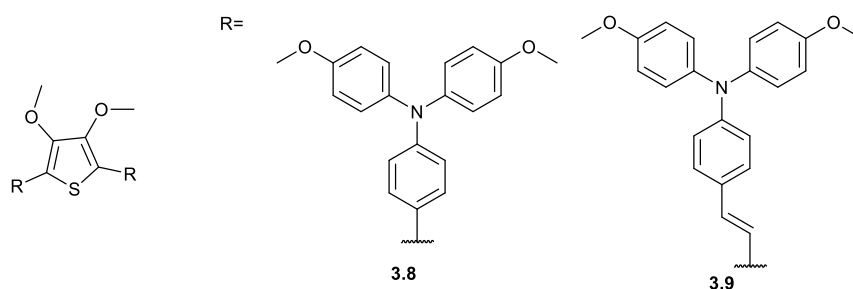
Figure 3.3: Chemical structures of HTMs based on thiophene

Synthesis of spiro-based derivatives with reduced hazardous chemicals and improved purification efficiencies is an area under increased scrutiny. Abdellah *et al.* developed a spiro fluorene-based HTM using inexpensive starting materials and a simple synthetic route (Figure 3.4).[156] Compound **3.10** shows promising charge transport ability and greater photocurrent density when compared to spiro-OMeTAD. PSCs fabricated with dopant free **3.10** attained a maximum PCE of 15.66%, comparable to Li-doped and exceeding dopant free spiro-OMeTAD. The PSCs based on dopant free **3.10** achieved impressive long-term stability and suitable conductivity, encouraging its application in future PSC devices.

Figure 3.4: Chemical structure of spiro fluorene based HTM

Zhai *et al*. reported two novel HTMs based on a double-spiro core unit (Figure 3.5).[157] The introduction of alkoxy side chains in **3.12** increased the polarity of t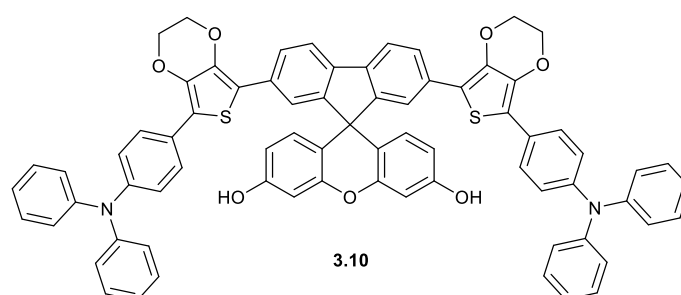he molecule, simplifying the purification and allowing it to be processed using the "green" solvent 2-methylanisole (2-MA). PCEs made using 2-MA-processed **3.12** achieved efficiencies up to 24.8% while also obtaining outstanding ambient operating stability. More crucially, **3.12** is able to chelate with lead and lithium ions, hindering ion migration and lead leakage. The key feature determined from this paper was the potential for this HTM to be scalable for commercial applications.
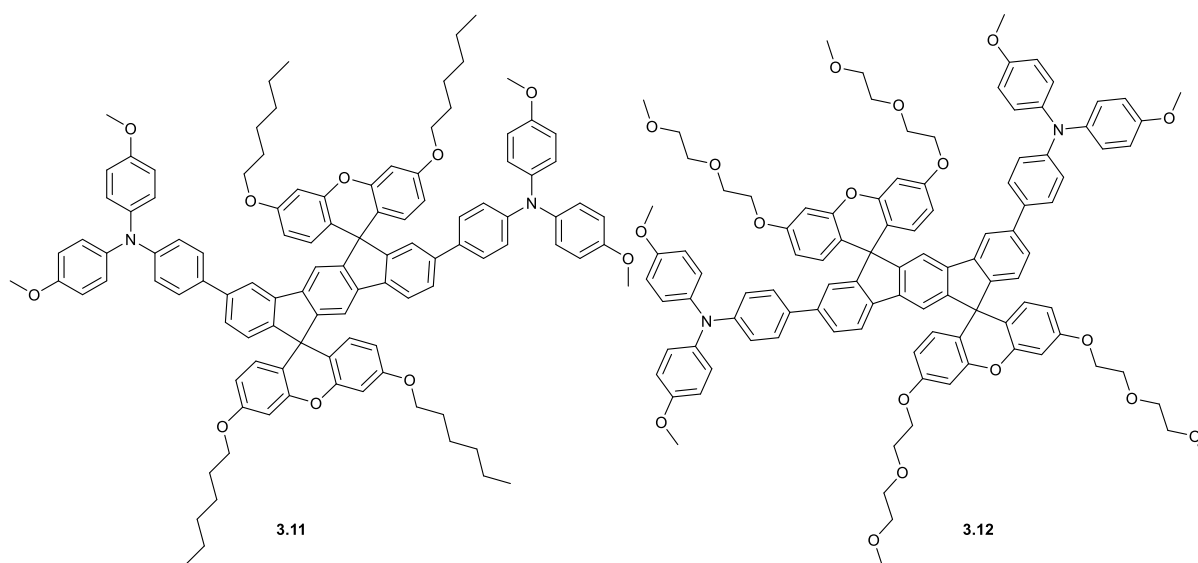
Figure 3.5: Chemical structure of HTMs based on a double-spiro core unit

Docampo and coworkers devised a new method for producing simple HTMs functionalised with an amide-based backbone, allowing for synthesis via a simple condensation reaction and observed exceptional charge carrier properties.[148] PSCs fabricated with **3.13** demonstrate PCEs of up to 20.3% and achieved a reproducibility which outperforms the benchmark spiro-OMeTAD. Moreover, the devices exhibit an improved lifetime due to superior stability, which is attributed to the coordination of the amide bond to the Li-additive and provides a novel strategy for hindering the migration of additives. This research illustrates that despite the lack of a conjugated backbone, HTMs based on an amide backbone can still outperform many current HTMs at a reduced cost.

Figure 3.6: Chemical structure of HTM functionalised with an amide based backbone

3.1.2 Imines and their properties

A variety of HTMs using condensation chemistry which can be conducted under ambient conditions without the need for expensive catalysts and only producing water as a side product, thus simplifying the work up, have recentl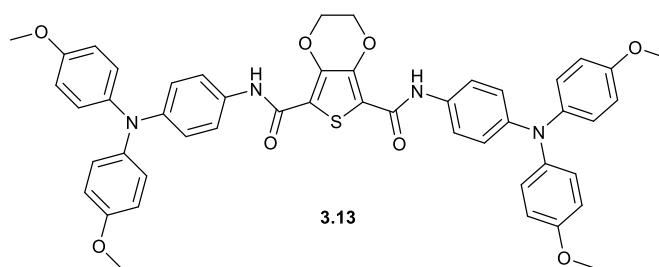y been developed. A number of groups have concentrated their research on the imine bond (-CH=N-, also known as azomethine or Schiff-base). Although the imine bond in aliphatic and a semi-aromatic compound it is liable to hydrolysis.

Koole *et al*. performed a study to compare conjugated imine derivatives with the vinyl-based analogues, functionalised with thiol groups to anchor to the gold electrode.[158] They observed comparable charge transport properties and that the structure change did not compromise the conductance in this class of molecules. This showed the potential for this chemistry to be utilised to produce high-quality organic semiconductors.
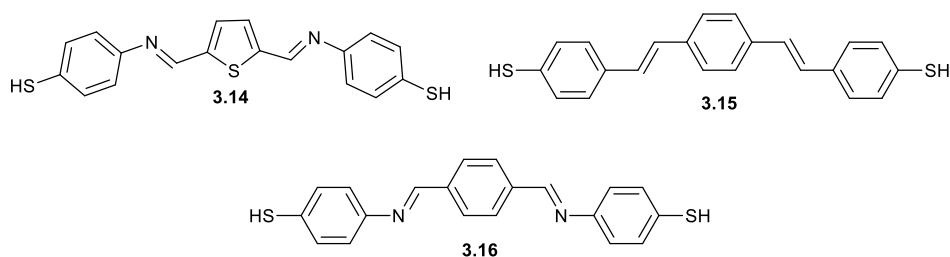
Figure 3.7: Chemical structure of symmetric imine derivatives

Docampo and coworkers have performed an extensive study on imine based HTMs, stressing the importance of the simple synthesis providing the potential to construct a series of materials.[159] The core and direction of the imine bond were altered to scrutinise their influence on the optoelectronic properties and photovoltaic performance of the PSCs. The core had a huge impact on the photovoltaic performance, with the best values obtained for the HTMs containing a strong dipole

within the core. Compound **3.23** showed a higher V_{OC}, outperforming spiro-OMeTAD while also achieving the same PCE as **3.17** of 14.4%. They also observe that these HTMs can act as an effective moisture barrier, resulting in a significant increase in the perovskite film stability.
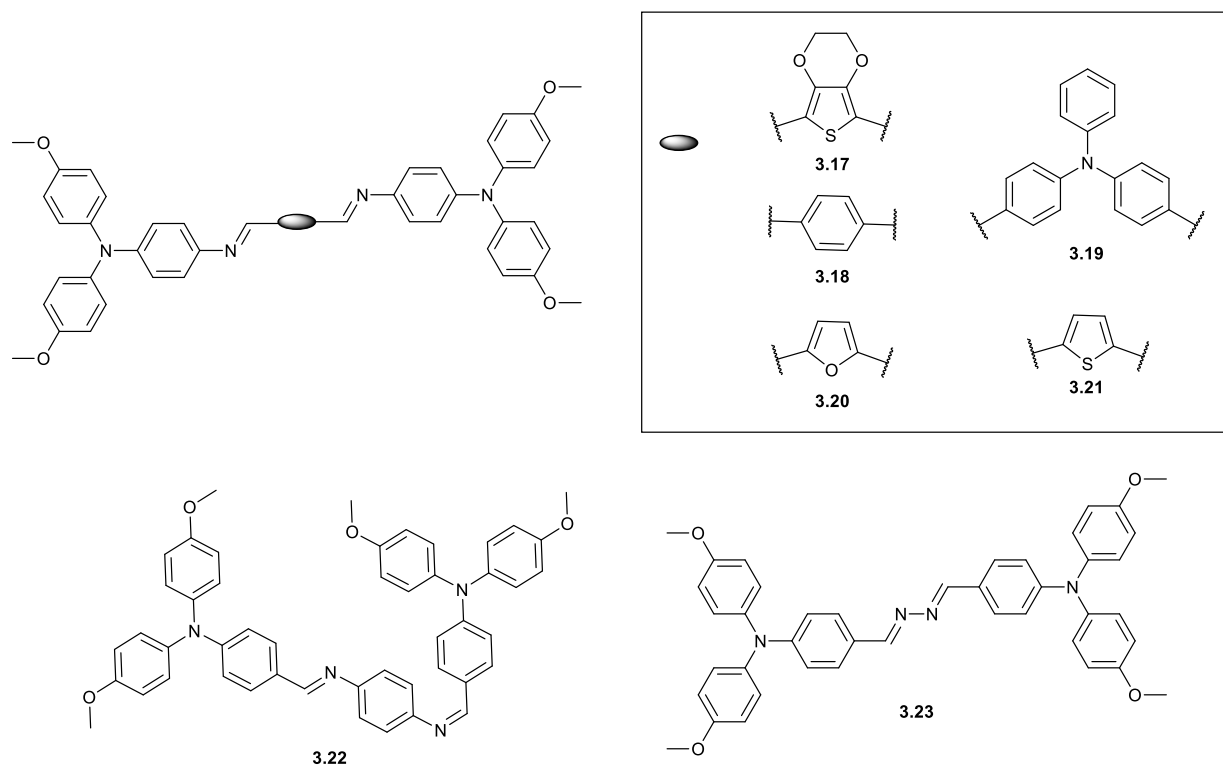
Figure 3.8: Chemical structure of different imine-based HTMs with different imine bond orientations

3.2 Aims

The aim of this project was to synthesise a variety of imine derivatives using simple and green chemistry inspired protocols in order to reduce the cost of production and diminish any adverse environmental impact. The final step in the synthesis of imines involves a simple condensation reaction which only requires an acid to catalyse the reaction and therefore has reduced hazards to the environment. With inspiration from the literature, several molecules were designed with various aromatic cores and donor substituents.

Upon material synthesis, the aim was to investigate the optoelectronic, electrochemical and theoretical properties of the target materials. The final aim of this project was to work in collaboration with the Docampo group at the University of Glasgow to perform preliminary conductivity measurements to determine their effectiveness as HTMs in PSC devices.

3.3 Results and Discussion

3.3.1   Target Compounds Design

This area of research was initiated in the Cooke group by Benjamin Vella, with some target molecules being synthesised by Dr. Dylan Wilkinson. A variety of core materials were planned to be used including spiro-bifluorene, fluorene and truxene (Figure 3.9). As mentioned previously, spiro-OMeTAD is the benchmark HTM for PSCs and has many advantages therefore, spiro based materials have obtained substantial scrutiny in order to develop similar properties while attempting to produce a simpler yet effective HTM.[126,127,160] The fluorene chromophore has also been identified as one of the most popular structural building blocks for organic HTMs due to its simpler synthesis, structure and low cost. This building block could provide an effective material to test out the most effective reaction conditions before attempting the more complex spiro-derivatives.[161] Truxene based HTMs have shown promise due to its interesting structure and photoelectric properties which also supply a decent hole mobility.[162]
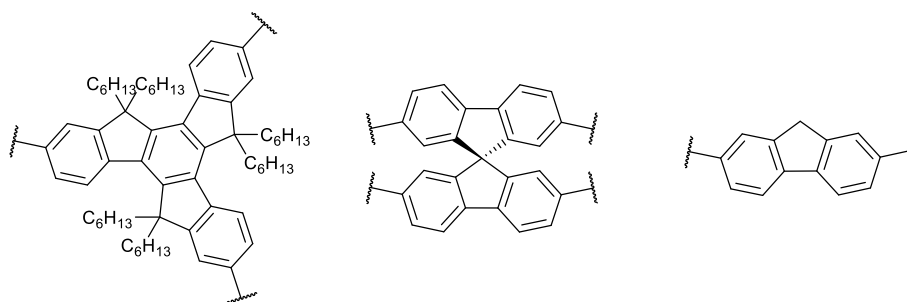
Figure 3.9: Structures of core materials for imine derivatives

To date, many imine derivatives have been synthesised with electron donating substituents. It was hypothesised that synthesising imine derivatives using one of the core materials from Figure 3.9 and substituting with one of the following electron donating substituents (carbazole, triphenylamine, ferrocene or tetrathiafulvalene (TTF)) would produce HTMs with interesting optoelectronic and charge transfer properties.

4,4'-Dimethoxytriphenylamine can be synthesised from bis(4-methoxyphenyl)amine via Buchwald-Hartwig cross-coupling before reaction with phosphoryl chloride to form the desired product, compound **3.28** (Scheme 3.1).
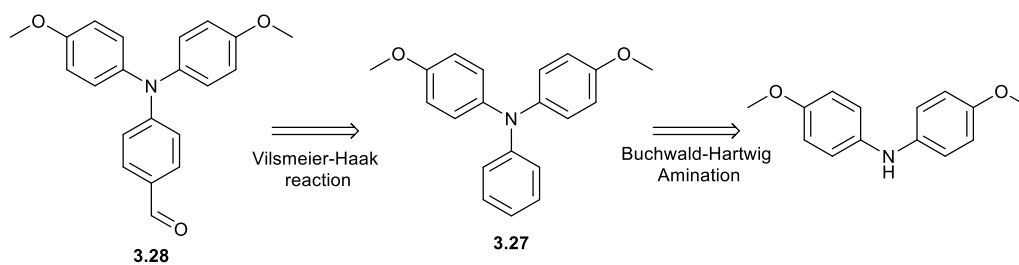
Scheme 3.1: Proposed retrosynthesis analysis for triphenylamine arm

For the carbazole arm synthesis, it was hoped that cross-coupling of 3-methoxyphenylboronic acid with 3-bromoanisole using Suzuki conditions, the subsequent di-bromination, Buchwald-Hartwig amination and final Vilsmeier-Haack reaction would form the desired carbazole compound **3.32** (Scheme 3.2).
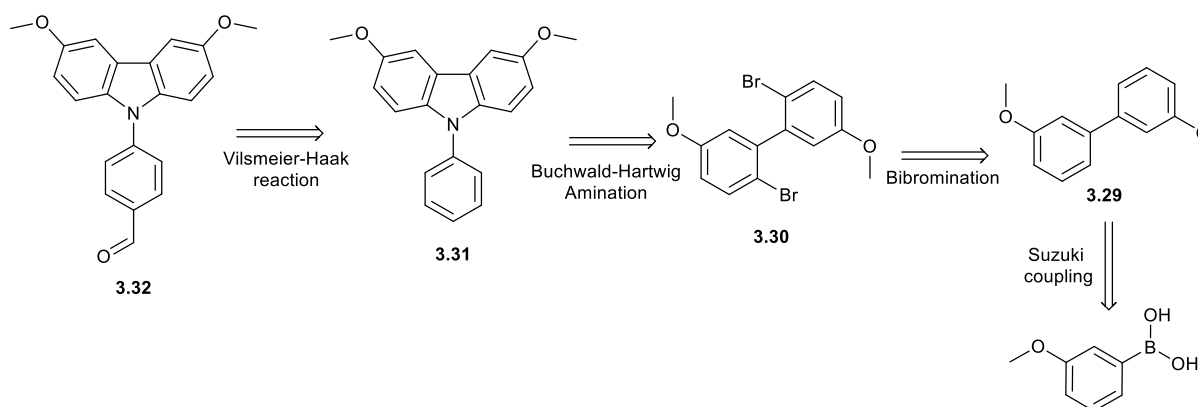
Scheme 3.2: Proposed retrosynthesis analysis for carbazole arm

Initially the core materials would be nitrated before being reduced to the appropriate amine. Finally, the arm and core would be reacted together via a condensation reaction to form the desired target compounds (Scheme 3.3).
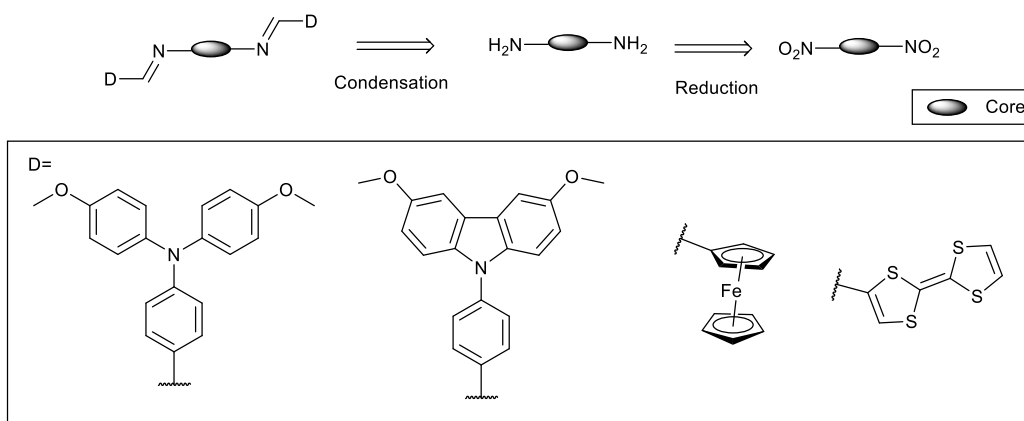
Scheme 3.3: Proposed retrosynthesis analysis for imine target compounds. D= donor moiety

3.3.2 Synthesis

Primary amines can react with ketones and aldehydes to form imines. Therefore, the presence of this nucleophilic functional group on the core material is necessary for its synthesis. In order to achieve this, commercially available 9,9'-spirobifluorene was first nitrated using fuming nitric acid to achieve compound **3.24** to a good yield of 85%. This material was then reduced using palladium on carbon to produce the amine compound **3.25** with an excellent yield of 91% (Scheme 3.4).
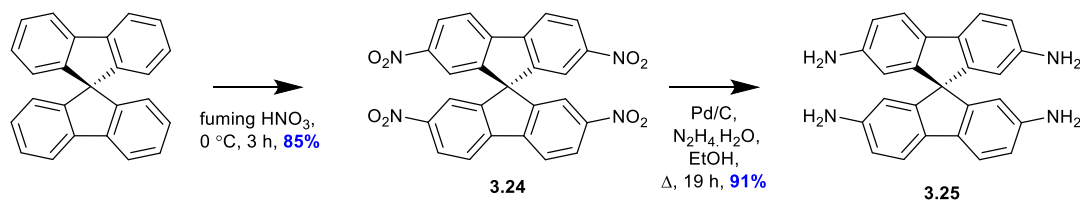
Scheme 3.4: Synthesis of compound **3.25**

2,7-Dinitrofluorene is a cheap, commercially available material and only requires reduction with palladium on carbon to produce the amine compound **3.26** to a good yield of 84% (Scheme 3.5).
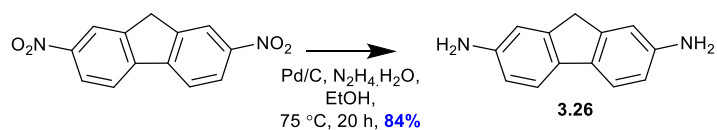
Scheme 3.5: Synthesis of compound **3.26**

The 4-(bis(4-methoxyphenyl)amino)benzaldehyde arm was synthesised following a procedure designed by Dr. Dylan Wilkinson (Scheme 3.6). First, the commercially available bis(4-methoxyphenyl)amine was subjected to Buchwald-Hartwig reaction conditions along with bromobenzene to produce compound **3.27** to a good yield of 80%. This material was then reacted with phosphorus oxychloride and *N*,*N*-dimethylformamide via the Vilsmeier-Haack reaction to produce the desired product, compound **3.28** to a good yield of 78%.
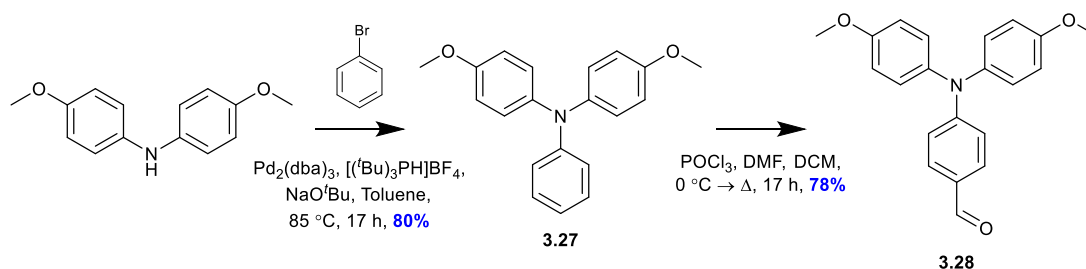
*Scheme 3.6: Synthesis of compound **3.28***

The carbazole based aldehyde arm, compound **3.32**, was next to be synthesised (Scheme 3.7). In an endeavour to accomplish this, the commercially available 3-methoxyphenylboronic acid was subjected to Suzuki cross-coupling conditions with 3-bromoanisole to produce compound **3.29** to a good yield of 88%. This was then di-brominated to form compound **3.30** to a moderate yield of 60%. Unfortunately, the double *N*-arylation with aniline was unsuccessful which may be a result of this being too sterically crowded.[163] Consequently, an alternative route was devised.
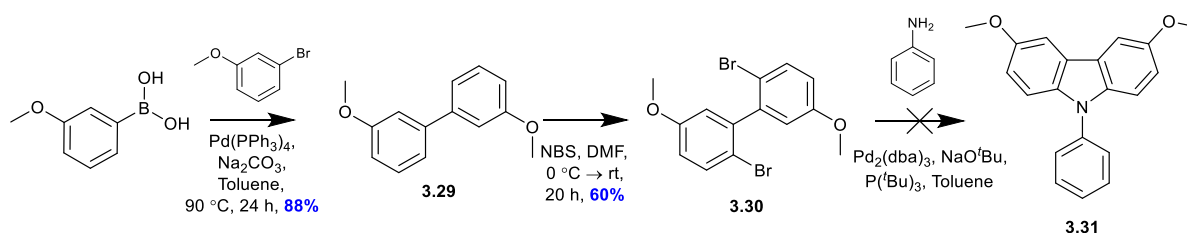
*Scheme 3.7: Attempted synthesis of compound **3.31***

This new route started with the commercially available carbazole which was di-brominated using *N*-bromosuccinimide to produce compound **3.33** to a good yield of 82% (Scheme 3.8). In order to form compound **3.34**, first sodium was dissolved in methanol to form sodium methoxide. This material

was then reacted with compound **3.33** in *N,N*-dimethylformamide by being catalysed with copper

iodide to produce compound **3.34** to a good yield of 74%. Originally the same procedure as that used

for the triphenylamine arm **3.31** was used, reacting compound **3.34** with bromobenzene via Ullmann

reaction conditions before undergoing the Vilsmeier-Haack reaction. Unfortunately, multiple

impurities were also formed and were difficult to separate by column chromatography therefore 4-

bromo benzaldehyde was used instead, reacting with compound **3.34** via Ullmann coupling to

produce the desired product, compound **3.32** to a moderate yield of 57%.
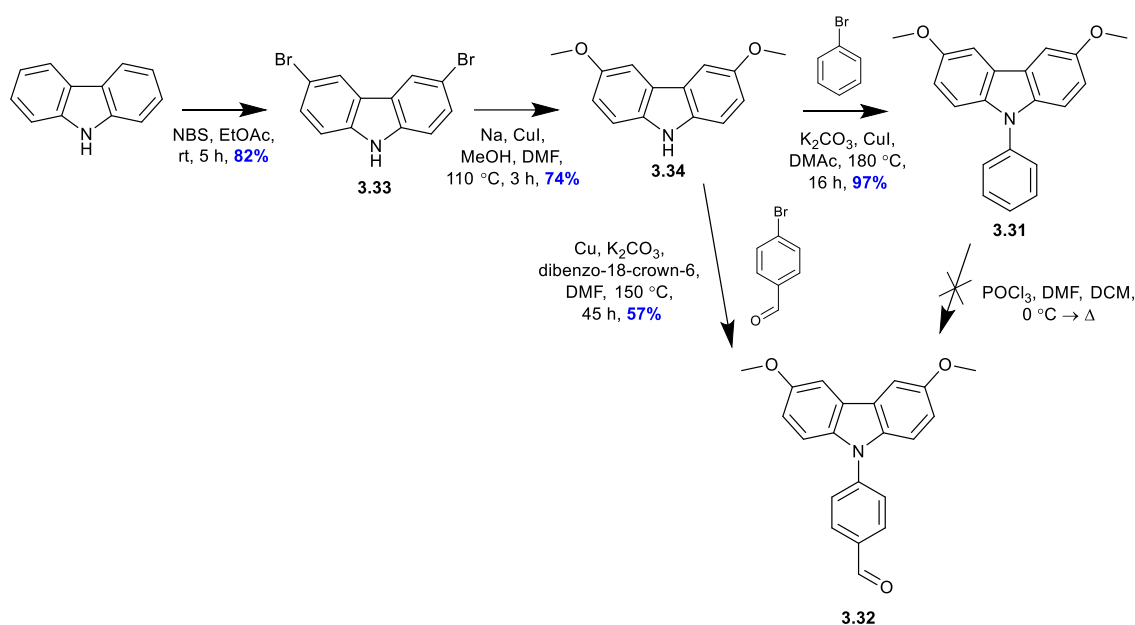
*Scheme 3.8: Synthesis of compound **3.32***

The first imine to be synthesised was achieved by the condensation of compounds **3.26** and **3.28**

with *p*-toluenesulfonic acid being utilised as the catalyst, performed using conditions identified by

Dr. Dylan Wilkinson who had previously synthesised this derivative using magnesium sulphate as a

drying agent. After purification by column chromatography, a similar yield of compound **3.35** was

achieved of 32% (Scheme 3.9). This material was synthesised for comparison to the carbazole

derivative, compound **3.36** discussed later in this section.
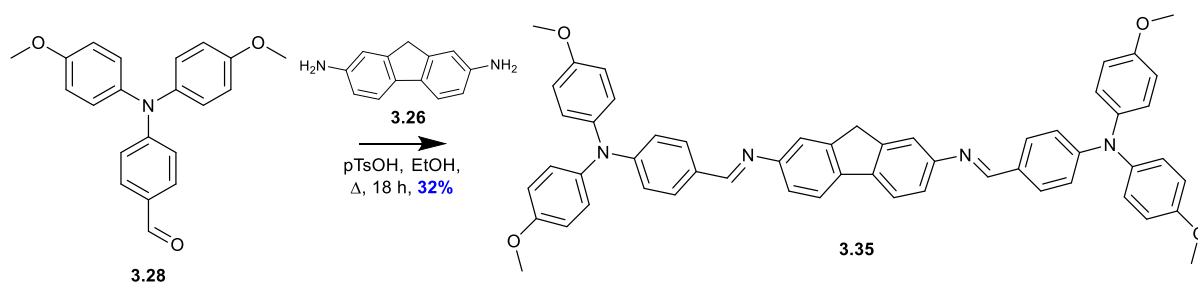
*Scheme 3.9: Synthesis of compound **3.35***

Since the synthesis of compound **3.35** was successful, the same reaction conditions were utilised for the carbazole derivative, including the use of molecular sieves as a drying agent (Scheme 3.10). This resulted in the fabrication of compound **3.36** which achieved a moderate yield of 30% after purification by column chromatography.
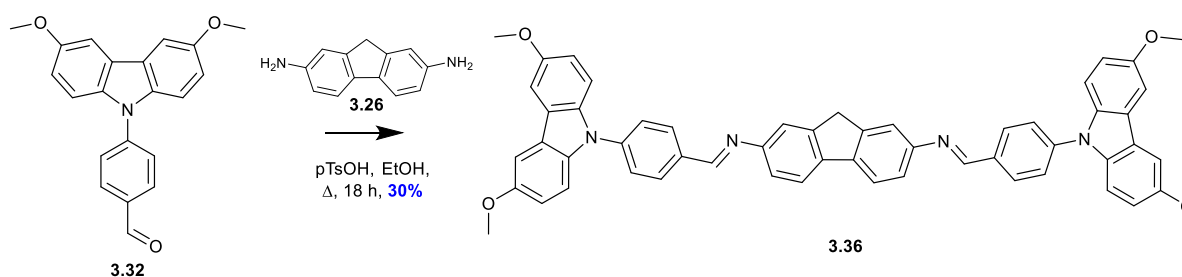
*Scheme 3.10: Synthesis of compound **3.36***

Ferrocene is an organometallic compound which has previously been employed as an electron donating unit due to the ease of functionalisation and aids in small molecule conjugation. Jia *et al*. synthesised triphenylamine derivatives containing ferrocenyl groups which obtained HOMO levels comparable to the valence band energy of $CH_3NH_3PbI_3$.[164] Consequently, an imine derivative utilising this material as substituents was devised.

The first venture was the imine based on the fluorene core, very mild conditions were utilised for this synthesis, only demanding dry methanol and magnesium sulphate at reflux temperature to achieve compound **3.37** to an 82% yield (Scheme 3.11). Unlike compounds **3.35** and **3.36** this only required a simple purification, precipitation and cold methanol wash, making this more appealing for industrial scale production.
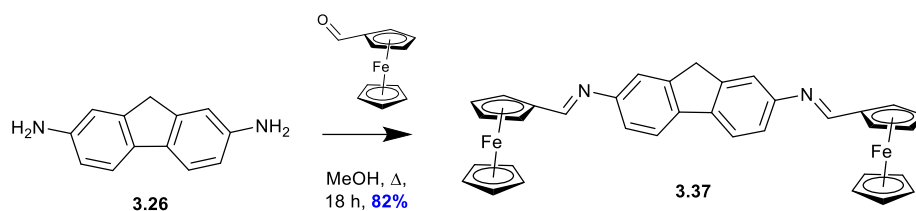
*Scheme 3.11: Synthesis of compound **3.37***

After the success of the fluorene derivatives synthesis, compound **3.25** was utilised as a core material for developing novel imine derivatives. This condensation reaction involving compounds **3.25** and **3.28** was attempted first (Scheme 3.12). Since four positions on the spiro-core were required to form the imine bond this synthetic step was extremely challenging and numerous conditions were attempted (Table 3.1). Purification by column chromatography was necessary as impurities were also observed by TLC and NMR, including the mono-, di- and tri-derivatives. After purification, NMR analysis confirmed that compound **3.38** was produced however on repeat analysis the compound had degraded. Dr. Dylan Wilkinson also found this issue on his attempts to synthesise this material. The equilibrium of the imine condensation reaction favours the starting materials which means a dehydrating agent is necessary to favour the product imine (magnesium sulphate or molecular sieves were used for each condition). It was hypothesised that over time water had permeated the material resulting in hydrolysis and therefore decomposition. Consequently, it was decided that research into alternative derivatives should be prioritised.
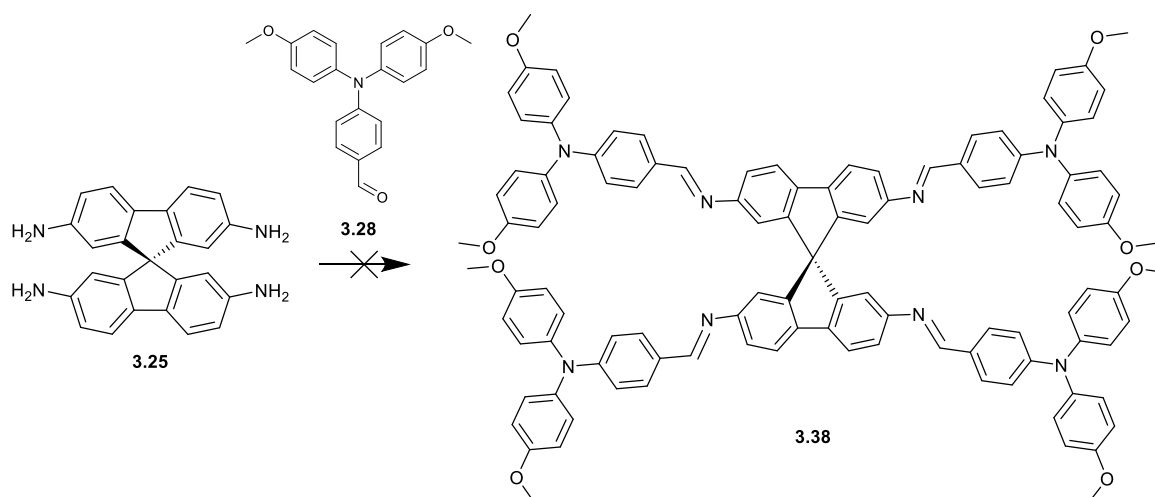
*Scheme 3.12: Attempted synthesis of compound **3.38***

Attempt	Conditions
1	Trifluoroacetic acid, Ethanol, *p*-toluenesulfonic acid, room temperature
2	Trifluoroacetic acid, Ethanol, *p*-toluenesulfonic acid, reflux

Table 3.1: Attempted reaction conditions for the synthesis of compound **3.38**

Although the spiro derivative was unsuccessful for the triphenylamine derivative **3.38**, it was nevertheless decided to attempt the synthesis for the carbazole derivative. Analogous results were observed for this material, but a wider variety of conditions were implemented (Table 3.2). Dean-Stark apparatus was utilised instead of the drying agents for a few attempts in an endeavour to prevent the water by-product from hydrolysing the desired imine product, compound **3.39** since the equilibrium already favours the starting materials. All conditions had a similarly undesirable result which may, in part, be due to the harsher conditions and multiple condensations being required in a small area increasing steric hinderance.
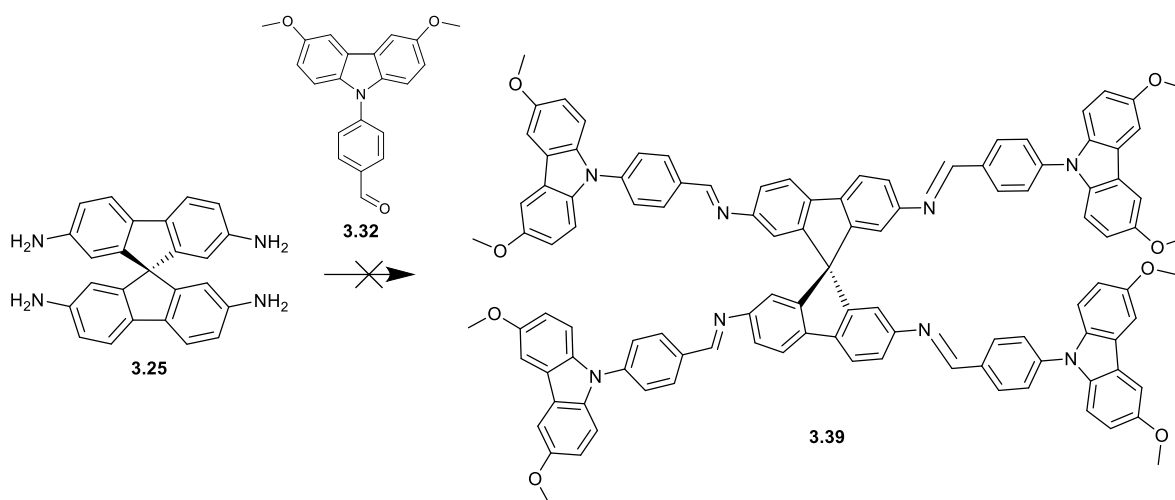
Scheme 3.13: Attempted synthesis of compound **3.39**

Attempt	Conditions
1	Trifluoroacetic acid, toluene, room temperature
2	Ethanol, *p*-toluenesulfonic acid, room temperature
3	Ethanol, *p*-toluenesulfonic acid, reflux
4	*p*-toluenesulfonic acid, toluene, reflux, Dean-Stark apparatus
5	*p*-toluenesulfonic acid, xylenes, reflux, Dean-Stark apparatus

Table 3.2: Attempted reaction conditions for synthesis of compound **3.39**

Since the fluorene derivative was so successful for the ferrocene derivative, the spiro derivative **3.40** was tackled using milder conditions than those used for compounds **3.38** and **3.39**. However, these conditions were found to be ineffective (Scheme 3.14). Dr. Dylan Wilkinson also endeavoured to synthesise this material using the same conditions discussed for compound **3.35** but reached the same result, either returning only starting material or producing a number of impurities of similar retardation factor. It was noted that on purification by column chromatography a number of new spots were observed on the TLC plate which may indicate the instability of this material and the imine bond on silica.
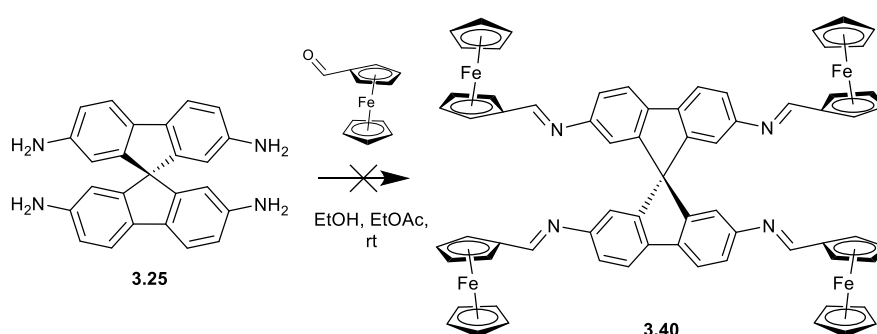
*Scheme 3.14: Attempted synthesis of compound **3.40***

TTF is well known for its excellent electron donating ability and reversible oxidation processes. It was hoped that TTF could produce a HTM with good charge transporting properties through effective π-stacking of the TTF units. Chen *et al*. developed a tetrathiafulvalene based HTM and introduced it into a PSC, obtaining a PCE of 16.7% due to the well aligned energy levels.[165] The synthesis of a spiro-imine with TTF substituents, compound **3.41**, was undergone utilising the same mild conditions as those used for the ferrocene compound **3.40**, this produced the same outcome (Scheme 3.15). Due to time constraints and the success of some of the triphenylamine, carbazole and ferrocene derivatives it was decided to focus on these materials for characterisation.
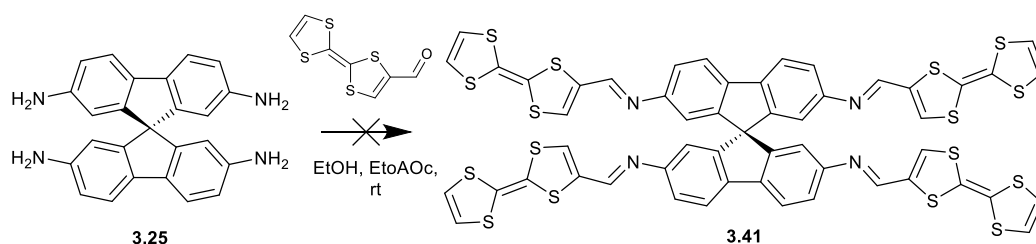
*Scheme 3.15: Attempted synthesis of compound **3.41***

Since the truxene amine compound **4.30** had previously been synthesised in Chapter 4 and has been shown to be an effective HTM core material, an imine based on this core was attempted. The condensation was accomplished by utilising compounds **4.30** and **3.28**, trifluoroacetic acid as the catalyst and molecular sieves as a drying agent (Scheme 3.16). Although a higher yield was expected to be achieved due to the simple condensation being performed a number of impurities were also formed, including the mono- and di-substituted product. Therefore, purification by column chromatography was necessary which reduced the yield to a modest 29%.
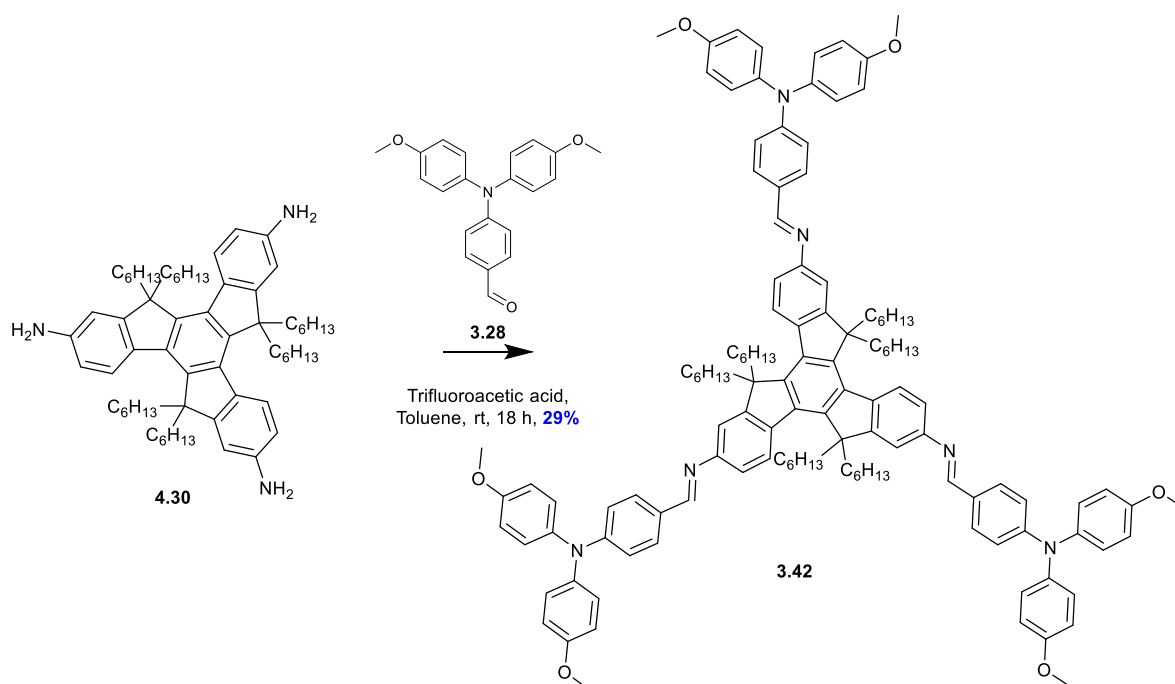
*Scheme 3.16: Synthesis of compound **3.42***

The carbazole derivative based on the truxene core **4.30** was then attempted. Initially, the same conditions as those used for compound **3.42** were utilised with molecular sieves as the drying agent

however to little consequence (Scheme 3.17). Alternative methods were also employed but a similar outcome was observed in that the significant compounds observed on work up were starting materials while a minimal new product was formed (Table 3.3). After purification by column chromatography, this material was no longer observable by TLC which may indicate its instability on silica and the need to find a simpler purification method, similar to compound **3.37**.
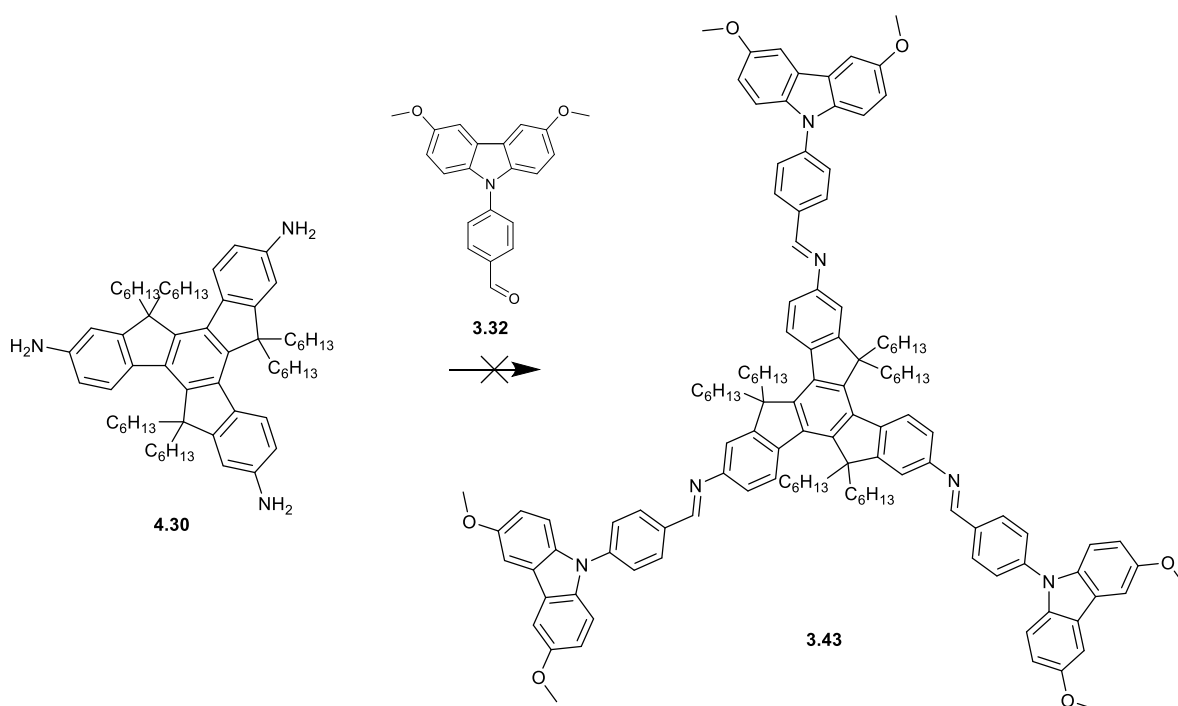
*Scheme 3.17: Attempted synthesis of compound **3.43***

Attempt	Conditions
1	Trifluoroacetic acid, toluene, room temperature
2	*p*-toluenesulfonic acid, toluene, reflux
3	*p*-toluenesulfonic acid, Ethanol, reflux

*Table 3.3: Attempted reaction conditions for synthesis of compound **3.43***

3.3.3 Optoelectronic Properties

The UV-Vis and fluorescence properties of the imine compounds **3.35**, **3.36**, **3.37** and **3.42** were evaluated and recorded in acetonitrile (MeCN), the normalised spectra are shown in Figure 3.10 and the data summarised in Table 3.4. Low absorption in the HTM layer is important for reducing optical losses, compound **3.37** required a 1×10^{-3} M solution (while the other materials are 1×10^{-5} M) therefore more molecules in solution were necessary to interact with light before any absorption

event was observed in the visible region indicating minimal absorption. Compounds **3.42** and **3.35** have very similar ε values and are higher than compounds **3.36** and **3.37** but only marginally for the carbazole compound **3.36**. All transitions are a result of π-π* transitions and as the conjugation increases a bathochromic shift in peak position is observed, the triphenylamine derivatives having the greatest conjugation and therefore furthest red shift.

The emission spectra have more distinguishable peak positions and separation from the absorption peak depending on the substituents on the material. Compounds **3.42** and **3.35** have corresponding peak positions and a Stokes shift of 130 nm (6000 cm^{-1}) and 120 nm (5428 cm^{-1}), respectively. In comparison, compound **3.36** is more blue shifted with a peak at 505 nm and with slightly smaller Stokes shift of 107 nm (5324 cm^{-1}). Compound **3.37** has the smallest Stokes shift of 50 nm (3218 cm^{-1}). The larger Stokes shift reduces the escape cone losses significantly (reduced emission lost through the front or back surface rather than being trapped by total internal reflection)[166] which gives the material a greater potential for achieving high efficiencies.

A larger band gap for a HTM aids in further reducing the optical losses, the optical band gap calculated from λ$_{onset}$ for compound **3.37** was determined to be marginally larger than the other derivatives. The various properties observed for these materials indicated their potential for application as HTMs in PSCs.
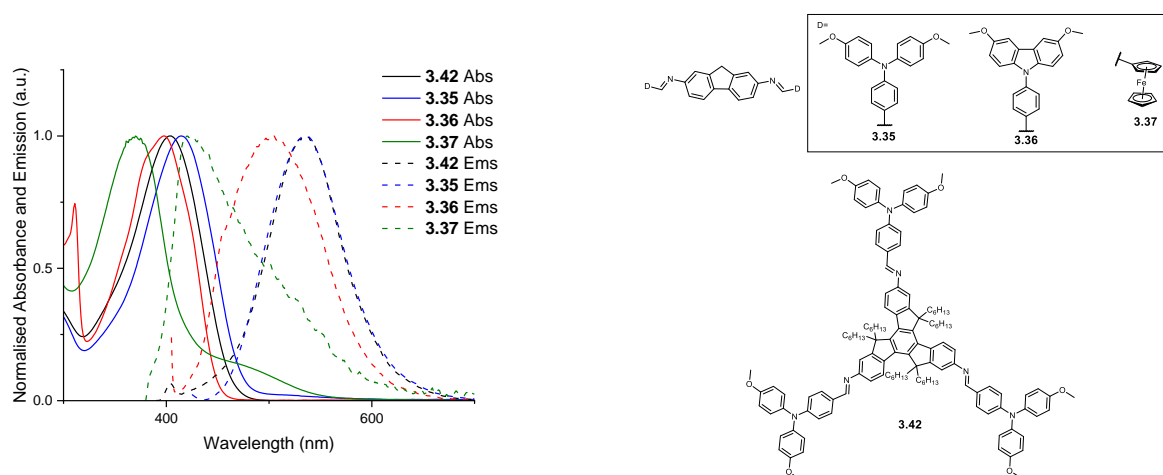
Figure 3.10: Normalised Absorption and emission spectra for **3.42** (black), **3.35** (blue), **3.36** (red) and **3.37** (green) in MeCN solutions

Compound	λ$_{max}$ (nm)	λ$_{onset}$ (nm)	E$_{g, opt}$ (eV)	Emission (nm)	Stokes shift (nm/cm^{-1})	Molar extinction coefficient ε × 10^5 (L mol^{-1} cm^{-1})
3.42	405	463	2.68	535	130/6000	1.75
3.35	414	473	2.62	534	120/5428	1.56

3.36	398	447	2.77	505	107/5324	1.03
3.37	370	422	2.94	420	50/3218	0.03

*Table 3.4: Summary of the optoelectronic properties of imine compounds **3.42**, **3.35**, **3.36** and **3.37**. $E_{g, opt}$ estimated from λ_{onset} of absorption.*

3.3.4 Electrochemical Properties

The electrochemical behaviour of the four imine derivatives were studied by CV and SWV in acetonitrile (1×10^{-4} M), the spectra are shown in Figure 3.11 and the data summarised in Table 3.5. Suitable alignment of the HOMO energy level of the HTM with the valence band of the perovskite valence band is crucial for minimising energy losses and achieving high open-circuit voltages in photovoltaic devices. CV and SWV determine the IP and EA of a material, although not an exact representation of the HOMO and LUMO it gives a close estimation and an indicator as to how appropriate or otherwise the material would be as a HTM.[146]

On recording the cathodic sweep for the solutions, all compounds exhibited a quasi-reversible oxidation. The variations in values are related to the triphenylamine, carbazole and ferrocene substituents as compounds **3.42** and **3.35** have similar peak values of 0.31 V and 0.34 V, respectively. In comparison, compounds **3.36** and **3.37** have peak values of 0.59 V and 0.15 V respectively. This results in EA values of −5.11 eV (**3.42**), −5.14 eV (**3.35**), −5.39 (**3.36**) and −4.95 eV (**3.37**). The valence band energy of perovskite $CH_3NH_3PbI_3$ is −5.43 eV therefore, compound **3.36** would be expected to have the least energy losses due to the best band alignment.

Compounds **3.35** and **3.36** have a quasi-reversible reduction peak at −0.11 V and −1.33 V respectively and therefore the IP can be calculated from this. Compounds **3.42** and **3.37** required the optical energy gap value, determined from the UV-Vis spectra, to estimate their IP positions. The IP calculated for compounds **3.35** and **3.36** are lower than the conduction band of $CH_3NH_3PbI_3$ while compounds **3.42** and **3.37** are higher, this would indicate that only the latter materials would be good electron blocking materials and therefore be effective HTMs.
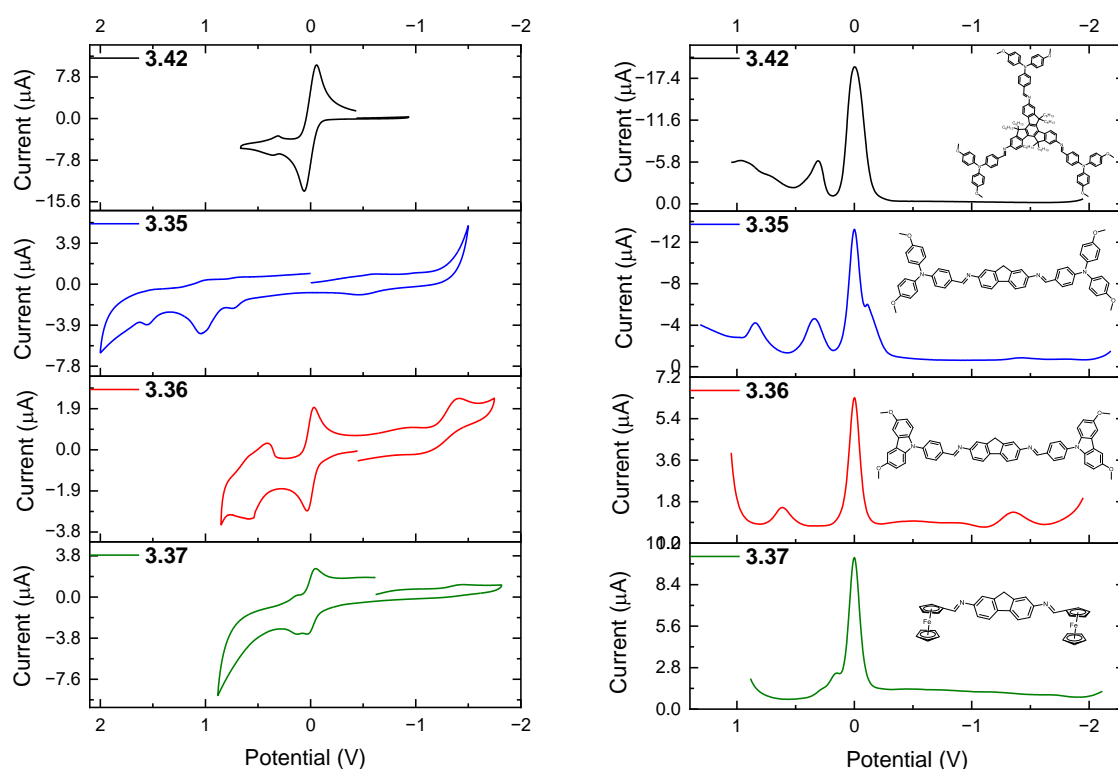
*Figure 3.11: Stacked CV (left internally referenced to Fc/Fc⁺(**3.35** externally referenced) and SWV (right) internally referenced to. Fc/Fc⁺ for imine derivatives **3.42** (black), **3.35** (blue), **3.36** (red) and **3.37** (green) in solution (c = 1 × 10⁻⁴ M, in MeCN) with a scan rate of 0.1 Vs⁻¹, performed using a Pt disk working electrode, a Pt wire counter electrode and a Ag wire reference electrode. TBAPF₆ (0.1 M) was used as supporting electrolyte and the redox potential of the Fc/Fc⁺ couple as internal standard.*

Compound	E_{red} (V)	E_{ox} (V)	EA (eV)	IP (eV)
3.42	-	0.31	−5.11	−2.43
3.35	−0.11	0.34	−5.14	−4.69
3.36	−1.33	0.59	−5.39	−3.47
3.37	-	0.15	−4.95	−2.01

*Table 3.5: Summary of the electrochemical properties of imine derivatives **3.42, 3.35, 3.36** and **3.37**. EA and IP calculated using following equations: $EA = -[E^{0.5}_{red} -(-4.80)]$ eV; $IP = EA - E_{g,opt}$ (calculated for grey EA)*

3.3.5   Theoretical Studies

To obtain a more detailed understanding into the geometric and electronic structure of the various imine derivatives, density functional theory (DFT) geometry optimisations B3LYP/6-311G(d,p) level were executed in the gas phase using the Gaussian09 program package. The alkyl chains on the truxene core of compound **3.42** were truncated to methyl chains to simplify the calculations. The HOMO for compounds **3.37** and **3.35** is distributed over the entire molecule with a greater intensity

over the core fluorene whilst for compounds **3.42** and **3.36** the HOMO distribution is more localized over one of the terminal substituents (either the triphenylamine or carbazole) (Figure 3.12). The HOMO energy level of compounds **3.36** and **3.37** (−5.15 eV and −5.34 eV, respectively) is lower than that of compounds **3.42** and **3.35** (−4.89 eV and −4.96 eV, respectively) which results in a better aligned with the valence band of the perovskite $CH_3NH_3PbI_3$.

The LUMO for compounds **3.42** and **3.35** is distributed over part of the core and the benzene ring closest to the core of the triphenylamine and compound **3.36** has a similar distribution but over both sides of the molecule. Compound **3.37** has a very different distribution to the other derivatives as it is over the entire molecule meaning complete overlap of the HOMO/LUMO. The LUMO energy level of the imine derivatives follow a similar trend to the HOMO energy level with compounds **3.42** and **3.35** having similar values of −1.55 eV and −1.51 eV, respectively and compounds **3.36** and **3.37** having similar values of −1.89 eV and −1.79 eV, respectively. Although positioning of the HOMO and LUMO varies between the imine derivatives, the fundamental band gaps are very similar, ranging from 3.26 eV for compound **3.36** to 3.55 eV for compound **3.37**.
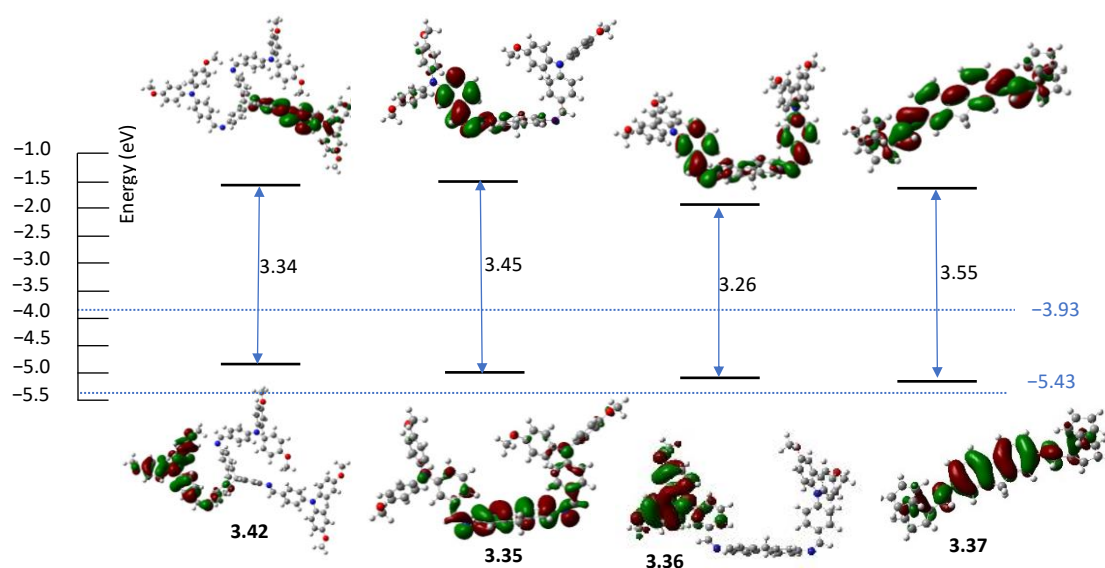
Figure 3.12: Frontier molecular orbital diagrams with HOMO and LUMO levels for ***3.42***, ***3.35***, ***3.36*** *and* ***3.37***. *The blue line indicates the valence and conduction bands of $CH_3NH_3PbI_3$*

The theoretical results slightly contradict the experimental values and general patterns observed in the electrochemical experiments. The experimental EAs are lower than the theoretical HOMOs except for compound **3.37**. In regards to the LUMO, the theoretical was noticeably higher than the IP particularly when the IP was determined from the reduction peaks. Consequently, the theoretical band gaps were greater than those determined experimentally. It is possible that acetonitrile had an effect on the position of the experimental IP and EA. Therefore, repeating the DFT calculations and

implementing acetonitrile into the calculation may improve the comparison. Alternatively, the CV and SWV could be repeated in a different solvent.

3.3.6 Conductivity Measurements

The film conductivity measurements were performed by Benjamin Vella of the Dr. Pablo Docampo research group at the University of Glasgow. In this collaboration we decided to first test compound **3.42** with the dopant FK209 to eliminate the effect of oxygen on the doping process.[167] The conductivities were obtained using standard current-voltage measurements. The pristine materials showed conductivities of 2×10^{-7} S cm^{-1}, upon doping with FK209 very little improvement is observed (Figure 3.13). Generally, increasing the dopant concentration results in greater recombination and reduced performance, as seen in this case. However, the overall poor conductivity on doping was hypothesised to be a result of the formation of charge transfer complexes between compound **3.42** and FK209 which is stabilised by electrostatic attraction and prevents charge carrier mobility. Therefore, it was concluded that these materials have insufficient hole conductivities for use in solar cells, where values of at least 10^{-5} S cm^{-1} are required for efficient device operation.
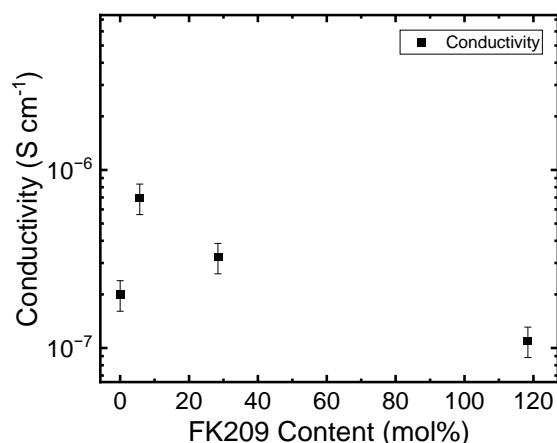
*Figure 3.13: Conductivity measurements performed on compound **3.42** with varying FK209 content*

Conductivity measurements were also performed on compound **3.35**. The pristine material showed lower conductivity than compound **3.42** of 4×10^{-9} S cm^{-1} and upon doping with FK209 only a slight improvement was observed into the 10^{-8} S cm^{-1} (Figure 3.14a). Although a slight improvement this is still insufficient for application in solar cells. Consequently, an alternative dopant was tested, namely

LiTFSI which requires oxygen to successfully oxidise a HTM. Upon doping compound **3.35** the conductivity increased to the 10^{-5} S cm^{-1} range, achieving sufficient hole conductivities for use in solar cells (Figure 3.14b). The conductivity remains consistent with increasing LiTFSI content. Doping in an organic system generally corresponds to chemical oxidation, thus a hole is introduced to the imine which can be transferred to nearby pristine material under an applied bias. In this case only the LiTFSI dopant is able to provide holes to the imine, thus increasing its conductivity. This proves that for these imine derivatives the choice in dopant is imperative for achieving sufficient conductivities for device application. A study into why this phenomenon occurred is currently being undergone in the Docampo group.

a)

b)
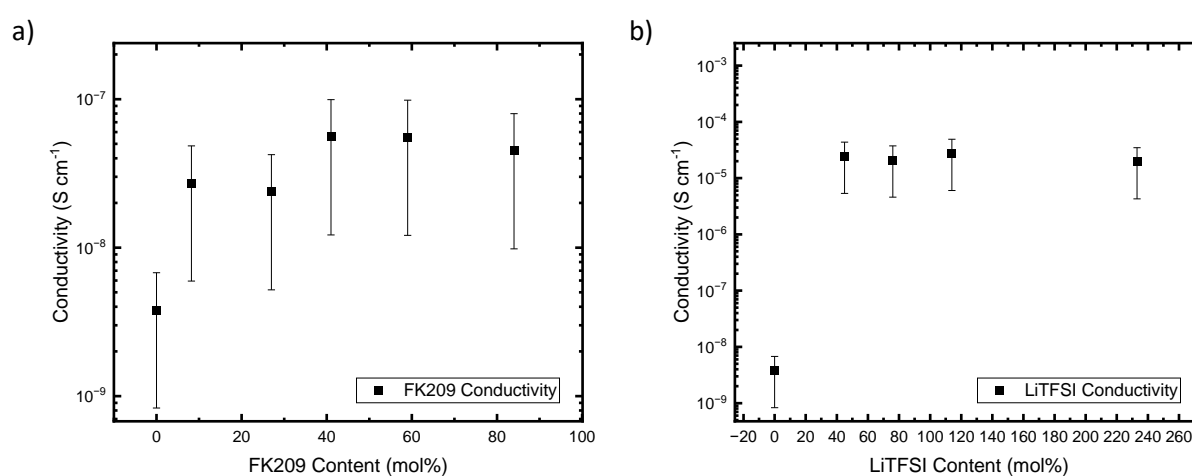
*Figure 3.14: Conductivity measurements performed on compound **3.35** a) with varying FK209 content and b) with varying LiFTSI content*

3.4 Conclusions and Future Work

Four novel imine derivatives were successfully synthesised using a final condensation reaction to reduce the amount of metal catalysts used in the synthesis of organic HTMs. The photophysical, electrochemical and theoretical properties were studied for each material. The absorption has a bathochromic shift with increasing push-character from the donor materials. The emission spectra have a more defined peak separation depending on substituents with compounds **3.42** and **3.35** having the largest Stokes shift and therefore a greater potential for achieving high efficiencies. The oxidation and reduction mechanisms of the imine derivatives are observed by CV and SWV which showed a better alignment with the perovskite valence band for compounds **3.36** and **3.35** thus reducing energy losses. Conductivity measurements of compounds **3.42** and **3.35** were performed by Benjamin Vella of Dr. Pablo Docampo research group which showed little improvement on doping

with FK209, possibly due to charge transfer complexes being formed. However, on doping compound **3.35** with LiTFSI a significant increase in conductivity was attained.

Future work will include, performing the conductivity measurements for compound **3.42** with LiTFSI to determine if the increase in values observed for compound **3.35** will be repeated in this derivative. Once completed, further analysis to explain this phenomenon will be endeavoured.

Docampo and coworkers, Sek *et al*. and Hindson *et al*. observed that the inversion of the imine bond significantly impacted the bandgap of the material.[159,168,169] Docampo and coworkers also discerned that the orientation of the imine bond influenced the optoelectronic and charge transport properties of the materials. Therefore, the synthesis of the inverted imine derivatives could improve the performance of the derivatives discussed in this chapter by tuning the bandgap and improving their properties. An example of the reaction scheme for the fluorene-imine-triethylamine derivative is shown below following similar conditions to Docampo and coworkers and Del Poeta *et al*. (Scheme 3.13).[170]

Spiro-imine derivatives were also attempted using a variety of conditions but to little success. Inverting the imine bond may impact the outcome of this synthesis. 9,9'-Spirobi[fluorene]-2,2',7,7'-tetracarbaldehyde has previously been synthesised by Che *et al*. via lithium-halogen exchange.[171] This material could potentially undergo the condensation reaction with compound **3.48** to produce the desired spiro-imine.
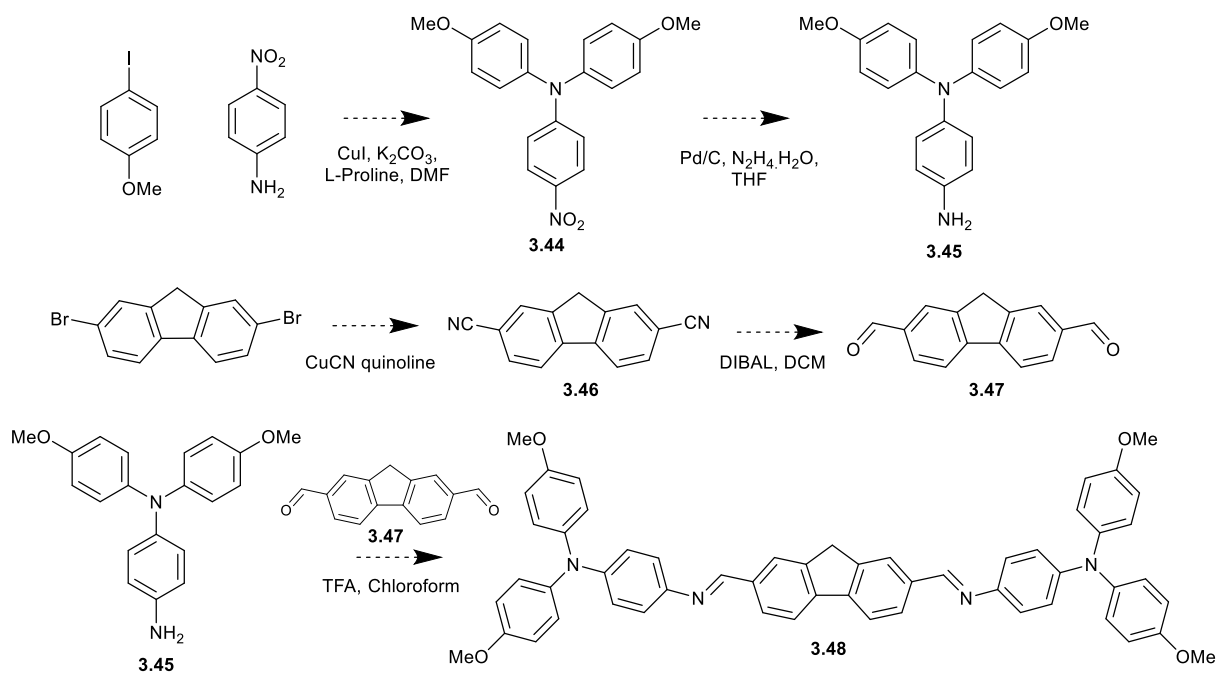
Scheme 3.18: Proposed future synthetic route for inverted imine derivative

4 An investigation of the optoelectronic properties of flavin-fused truxenes

4.1 Introduction

4.1.1 Truxene

The design, synthesis and physical properties of polycyclic aromatic hydrocarbons (PAHs) that contain two or more closed aromatic ring structures (such as truxene, fullerene (C_{60}), coronene and sumanene) have received increasing interest in recent years as a result of their unique optoelectronic and thermal properties (Figure 4.1).[172] A wide range of applications in numerous fields have been identified including bio-organic, medicinal chemistry, materials and environmental science.[173–177]

a: X=CH$_2$ **b**: X=NH
c: X=CMe$_2$ **d**: X=SiPr$_2$
e: X=O/S   **f**: X=(C=O)
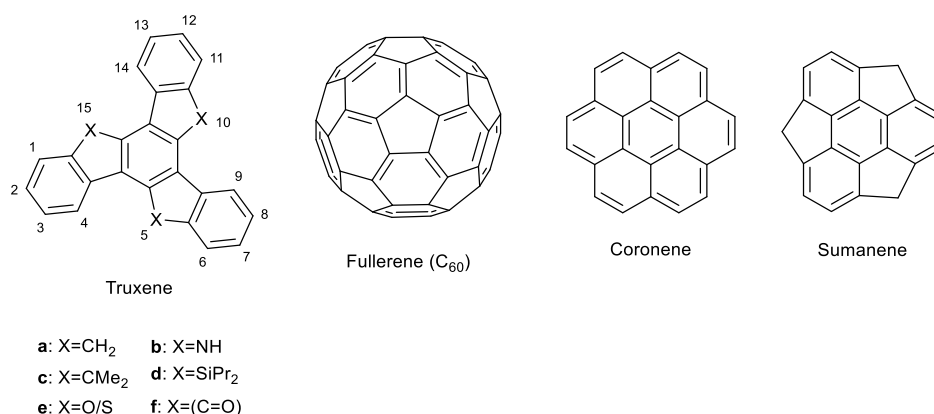
Figure 4.1: Examples of polycyclic aromatic hydrocarbon structures

Truxene is a heptacyclic star shaped π-conjugated polyarene, synthesised by the trimerization of indan-1-one and can be regarded as three annulated fluorene moieties. The truxene unit has a rigid, planar and C$_3$ symmetry structure and can also be considered as a 1,3,5-triphenylbenzene derivative planarized through the three bridging methylenes, creating additional 5 membered rings. These 5 membered rings facilitate the heightened delocalisation of the π-system which culminates in interesting photoactive properties and notable electron donating capabilities.[178]

The synthesis of truxene was first reported in 1894 by Kipping, where 3-phenyl-propanoic acid was cyclised *in situ* to indan-1-one under acidic conditions before the self-condensation to produce a

mixture of truxene and isotruxene.[179] Isotruxene is an asymmetric isomer of truxene with ortho-para connectivity of the rings to the central core compared to the meta-meta connectivity of truxene.[180] Ortho and para conjugated interactions are inherently stronger than meta which impacts the extent of electronic coupling between the three π-conjugated arms.[181,182] The isolated asymmetric isotruxene was initially reported in 1960 by Lang *et al.*, revealing the necessity for harsh conditions (20 atm and 350 °C) and only achieving a low yield which limits the applications.[183] Truxenes selective synthesis was originally developed by Hartke and Schilling-Pindur from (3-methylthio)indene in 1984[184] before Bergman and Egestad achieved success in 1986 by synthesis from indan-1-one.[185] Unfortunately, the yield of these reactions was very low (roughly 22%). The Huang-Minlon reduction procedure was used to increase the yield of truxene to 85%, achieved by reduction of truxenone using the Wolff-Kishner reagent.[186]

Truxene, in its unsubstituted form, exhibits complete insolubility in common organic solvents. Introduction of solubilizing chains was studied as a method of preventing this drawback. Echavarren and coworkers were first to report this, by introducing three alkyl chains at the C2, C7 and C12 positions.[187] Truxene was first hexa-alkylated at the C5, C10 and C15 positions in 2003 to produce highly soluble truxene derivative which considerably widened the range of applications for this structure.[188] The truxene framework has since become a useful and immensely appealing building block for a variety of novel materials due to interesting characteristics including C_{3h}-symmetry, strong blue emission and a planar, rigid structure.[189] This building block has also been utilised in a wide range of applications including DSSCs,[190] OFETs,[191] OLEDs,[192] two-photon absorption (TPA),[193] organic lasers and fluorescent sensors.[194]

4.1.2 Applications of Truxene

4.1.2.1 OLEDs

Blue-emitting materials are important for the development of OLEDs and therefore have obtained increased interest in recent years. Fluorene derivatives are blue emitters however the formation of ketone defects or excimers/aggregates results in long wavelength emission which prevents them from being excellent emitters. Truxene is regarded as three fluorene units annulated by sharing a central benzene ring. Consequently, truxene based, highly stable blue emitters (inherited feature from fluorene) have been developed as a means for preventing this issue.[189]

Dendrimers are highly ordered, branched polymeric molecules which have acquired a great deal of interest due to their fascinating structure and unique photophysical and mechanical properties.[195] Constructing truxene-based dendrimers with large branches is an effective method for minimizing

the formation of excimers or aggregates on account of their large three-dimensional molecular size. Jiang *et al.* developed dendrimers **4.1** and **4.2** (Figure 4.2) with the core and branches composed solely of truxene units. Preliminary OLED devices of these materials achieved a pure blue colour with stable CIE chromaticity coordinates of (0.16, 0.08). These results illustrate that the generation of dendrimers has little effect on the photophysical, electrochemical and EL properties or the device efficiency.[196]
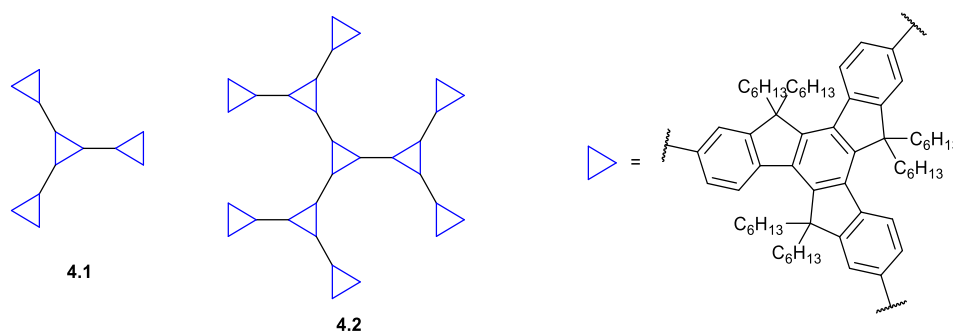
Figure 4.2: Blue-emitting dendrimers based on truxene unit

Jacob and coworkers designed and developed three truxene based molecules bearing *N*-carbazolyl, 1-pyrenyl and *N*-phenyl-*N*-(pyren-1-yl) substituents at the 2,7,12 positions (Figure 4.3).[197] All materials were observed to be blue emitting at 385 nm, 425 nm and 490 nm, respectively. Compound **4.4** achieved the highest PLQY of 0.97. Compounds **4.4** and **4.5** were then used as active materials for the fabrication of solution processed, single layer OLEDs achieving a blue colour with CIE chromaticity coordinates of (0.16, 0.23) and (0.17, 0.36), respectively. Fabrication of multi-layered devices may optimise the performance due to charge balance by the HTL and ETL.
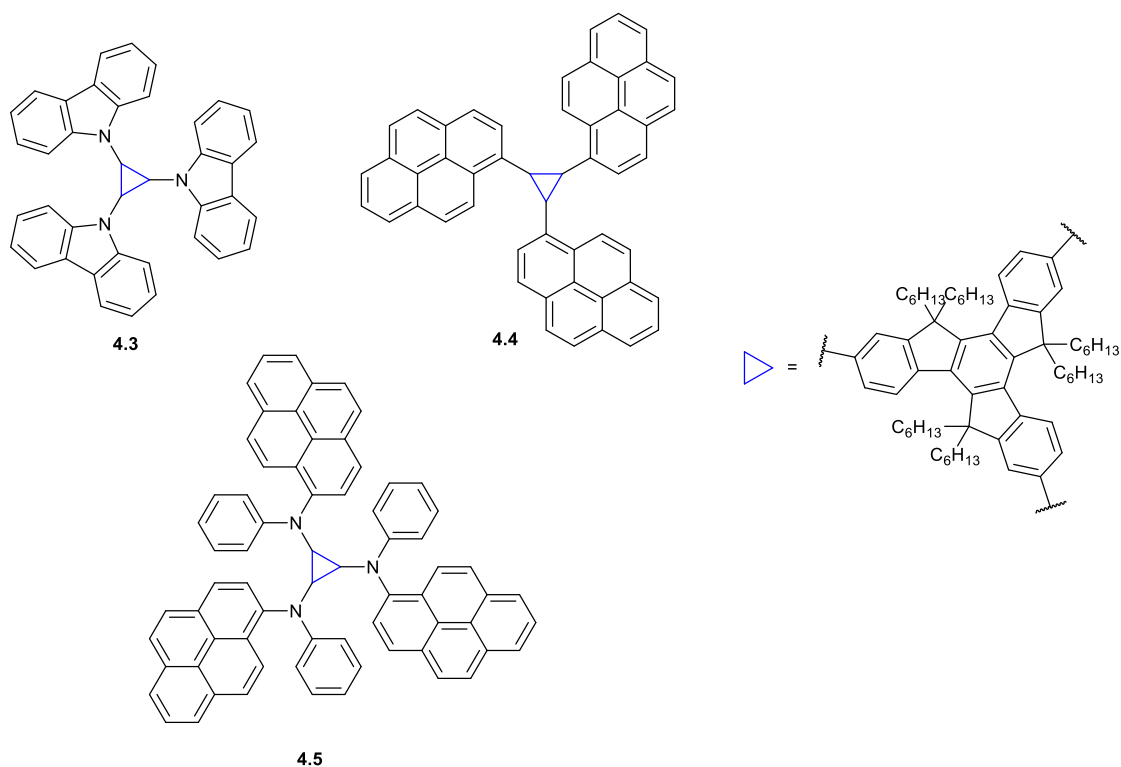
Figure 4.3: Solution-processable truxene-based blue emitters

Star-shaped tetraphenylethene (TPE) and 2,3,3-triphenylacrylonitrile (TPAN)-substituted truxenes (Figure 4.4) were designed and synthesised by Sharma *et al*.[198] The TPE-substituted truxenes **4.6** and **4.7** show aggregation induced emission (AIE) whereas TPAN substituted truxene **4.8** shows aggregation-caused quenching (ACQ) in THF/water due to π-π stacking. Compound **4.6** was utilised as a fluorescent emitter in non-doped OLED devices, producing greenish-white OLEDs with maximum brightness and EQE of 7000 cd/m^2 and 3.8%, respectively.
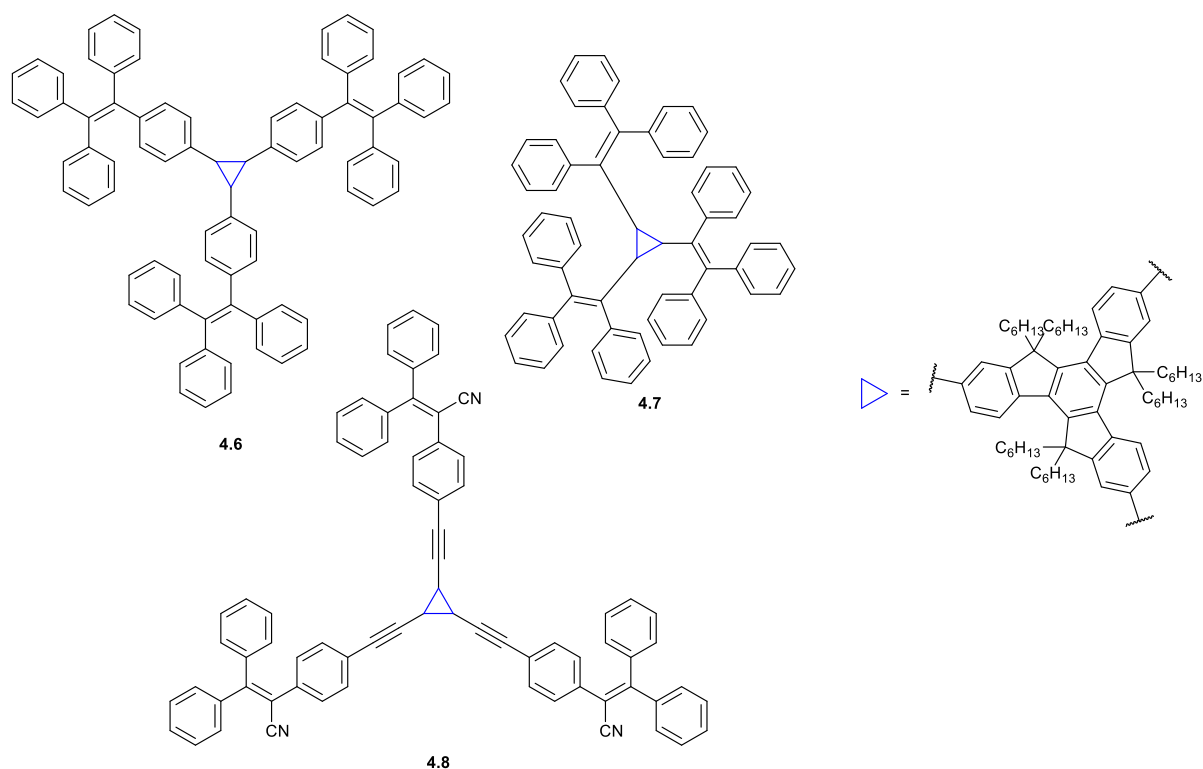
Figure 4.4: Star-shaped tetraphenylethene-substituted truxenes

4.1.2.2 OFETs

The organic semiconductor is the core element of OFETs. Therefore, the development of outstanding organic semiconductors is a key factor for the fabrication of high-performance devices. π-conjugated organic oligomers and polymers are the subject of substantial research for OFET applications. The facile chemical modification of the π-conjugated oligomers structures and ease of purification through vacuum sublimination have influenced their widespread application in OFETs. Polymers are also attractive for OFET applications since polymer-based devices can be fabricated by various solution techniques such as drop-casting, spin-coating and ink-printing. These techniques drastically decrease the environmental requirements, simplify the fabrication processes and reduce device fabrication costs.[191,199]

Mula *et al*. observed the effect of hydrogen bonding as a tool for fabricating robust OFET devices (Figure 4.5).[200] Using the highly soluble dumbbell shaped molecule, **4.9**, which was deprotected by annealing at 200 °C, creating a strong hydrogen bonded network of **4.10** supported by additional π-π stacking. Compound **4.10** showed significantly higher hole mobilities compared to **4.9**, consistent with the hypothesis that a supramolecular organisation based on hydrogen bonding between N-H

groups and adjacent carbonyl groups gives highly ordered and robust molecular arrangements in thin films. This encourages their use in optoelectronic devices.
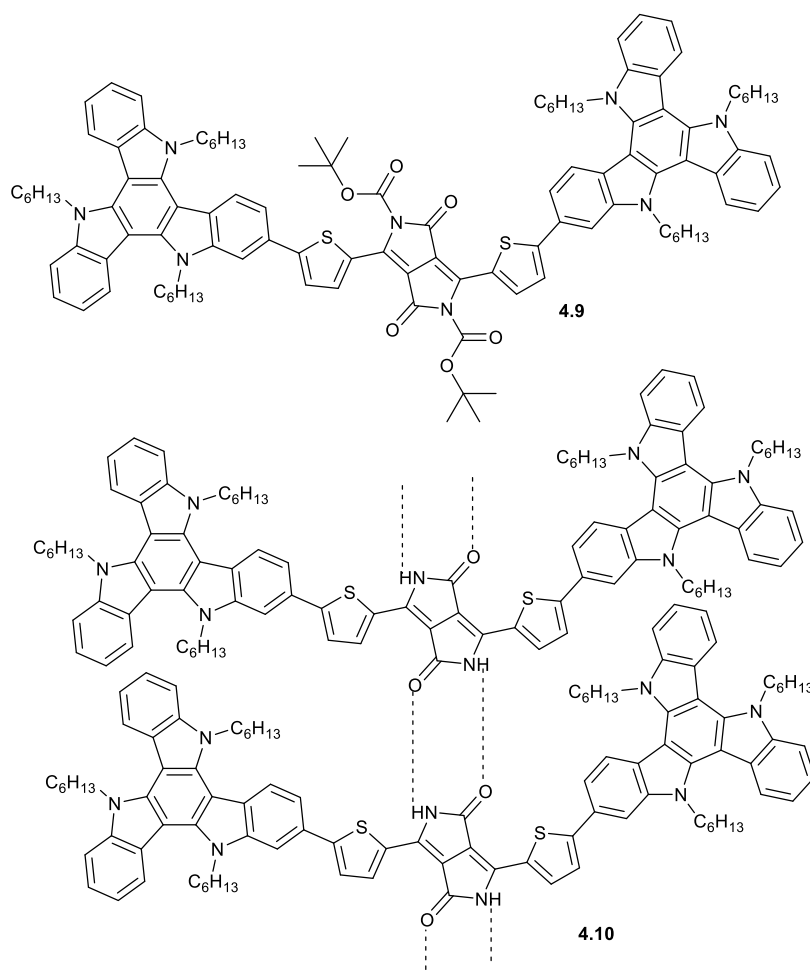
Figure 4.5: Hydrogen bonded triazatruxene derivatives

Sun *et al.* fabricated OFETs using a series of star-shaped oligothiophene functionalised truxene derivatives (Figure 4.6).[191] They observed that with a stepwise increase in thiophene rings on every branch a transition from polycrystalline to amorphous state occurs. The mobility is reliant upon the morphology in the solid state, decreasing with increasing thiophene rings. Compound **2.11** achieved a mobility of 1.03×10^{-3} cm^2 V^{-1} s^{-1} and an on/off ratio of roughly 10^3.
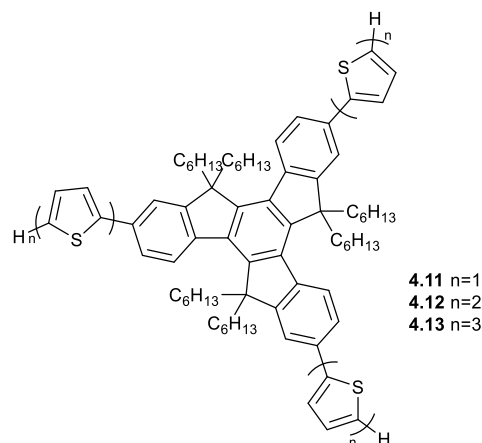
Figure 4.6: Star-shaped oligothiophene functionalised truxene derivatives

4.1.2.3   Photovoltaics

Organic photovoltaic devices (OPVs) have attracted considerable attention due to their facile solution processability, low cost and flexibility. An electron acceptor in a bulk heterojunction (BHJ) is one of the significant factors for the performance of organic solar cells (OSCs). Acceptors must possess an appropriate energy level to fit with donors. Sharma and coworkers developed two novel star shaped electron acceptors (Figure 4.7) based on a truxene core conjugated with three 4,4-difluoro-4-bora-3a,4a-diaza-*s*-indacene (BODIPY).[201] The strong electron donating capability of the dimethylamino group and good π-conjugation effect results in a slightly higher HOMO (−5.40 eV) and deeper LUMO (−3.96 eV) for **4.14** compared to **4.15**. When blended with a donor polymer **P**, the OSCs based on **P:4.14** and **P:4.15** exhibit a superior J_{SC}, high electron mobility and V_{OC}. Optimised OSC devices based on **P:4.14** and **P:4.15** exhibited PCE of 13.41% and 11.75%, respectively. This is one of the highest achieving values for OSCs with a non-fullerene small molecule acceptor.

4.14

4.15

P
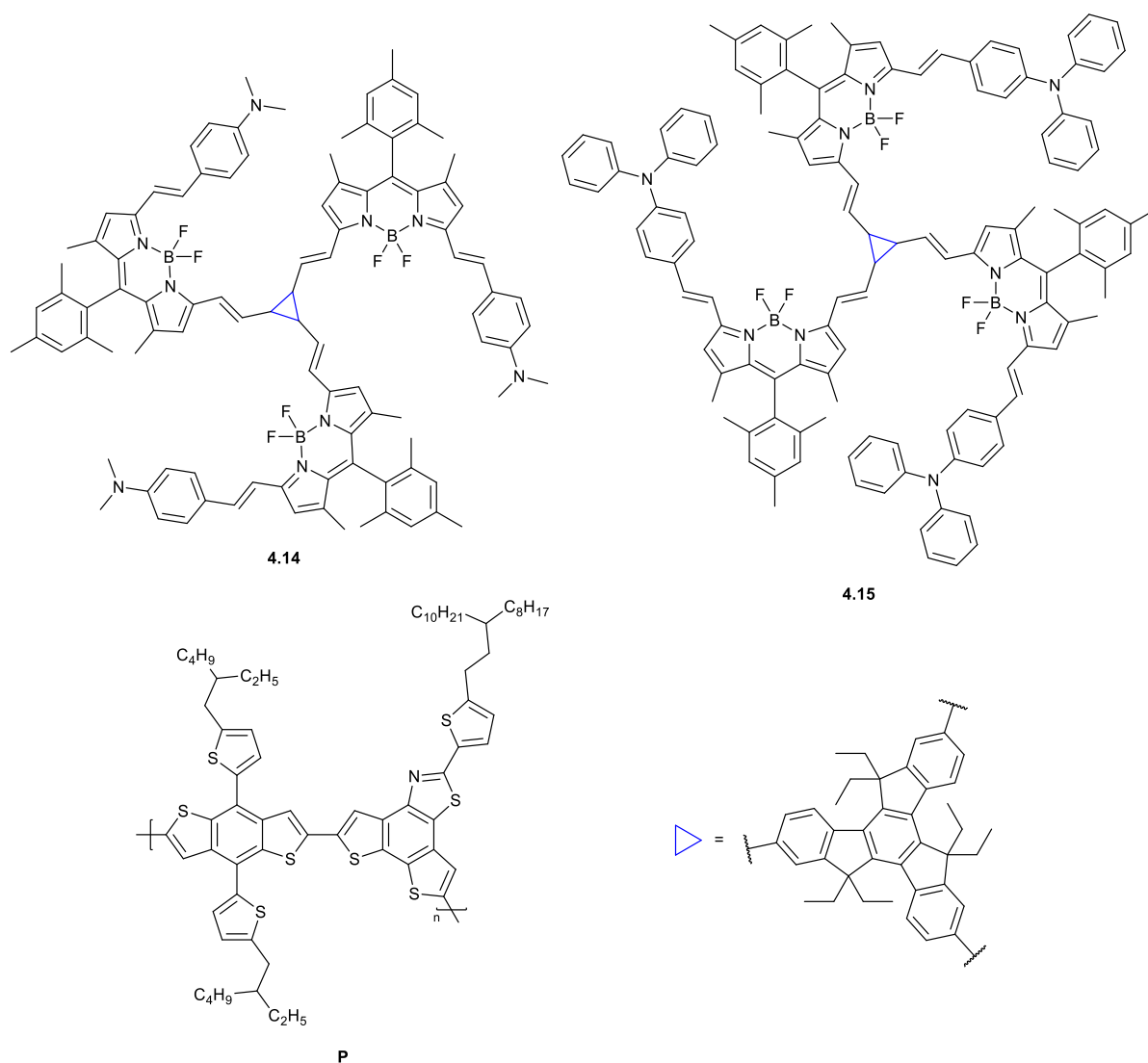
*Figure 4.7: Molecular structures of non-fullerene small molecule acceptors **4.14** and **4.15** and the conjugated D-A polymer **P***

Tang *et al*. designed and synthesised three truxene-bridged perylenediimide (PDI) trimers with varied linkages.[202] BHJ solar cells were fabricated using the truxene-bridged PDI trimers as electron acceptors and PTB7-Th as the electron donor (Figure 4.8). The results demonstrate that the linkage made between the truxene core and PDI units plays a significant role in determining photovoltaic performances of non-fullerene electron acceptors. Compound **4.16** had a fully planar conformation and produced the highest PCE of 4.19% owing to its appropriate morphology, high charge mobility and high V_{OC} of 1.0 V.
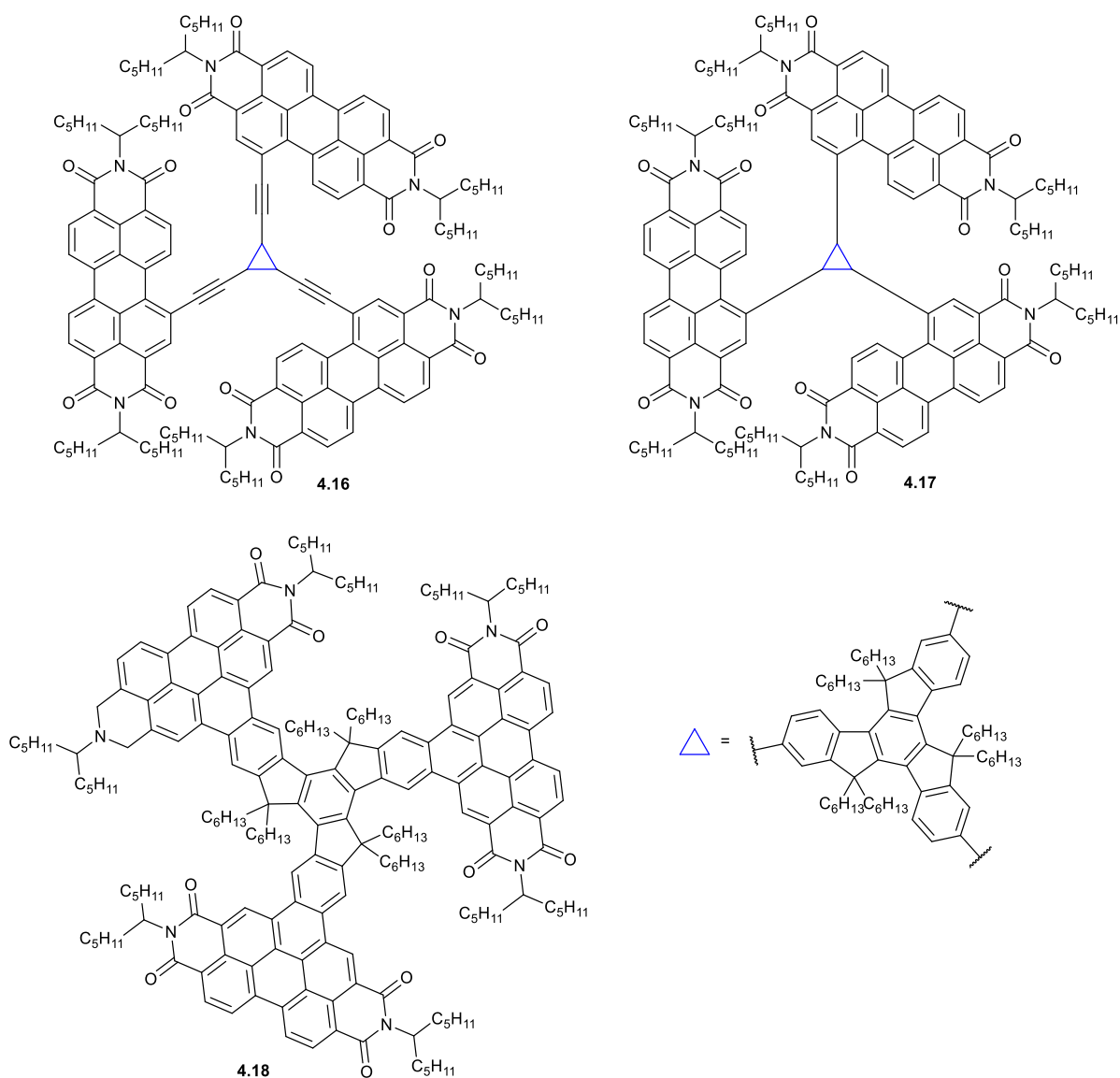
Figure 4.8: Molecular structures of truxene-bridged PDI trimers

In contrast to other applications, truxene has only been applied as a HTM in PSCs a small number of times despite the infinite number of structural possibilities. Truxene based HTMs are promising candidates, particularly as dopant-free HTMs, due to their higher hole mobility and similar T_g compared to spiro-OMeTAD which would lead to PSCs with high PCE and good thermal stability. Wang *et al*. synthesised four truxene based HTMs and applied them in inverted PSCs.[162] It was determined that the introduction of hexyl chains on the truxene core was beneficial for hole transport and extraction. The peripheral arylamines also have an effect on the electrochemical and hole transporting properties of the HTM and therefore the overall performance. PSCs using the dopant free **4.22** achieved PCE of 17.1% compared to 15.5% and 15.7% for **4.20** and **4.21**,

respectively. Truxene HTMs were observed to significantly enhance the durability of the PSC under UV light.
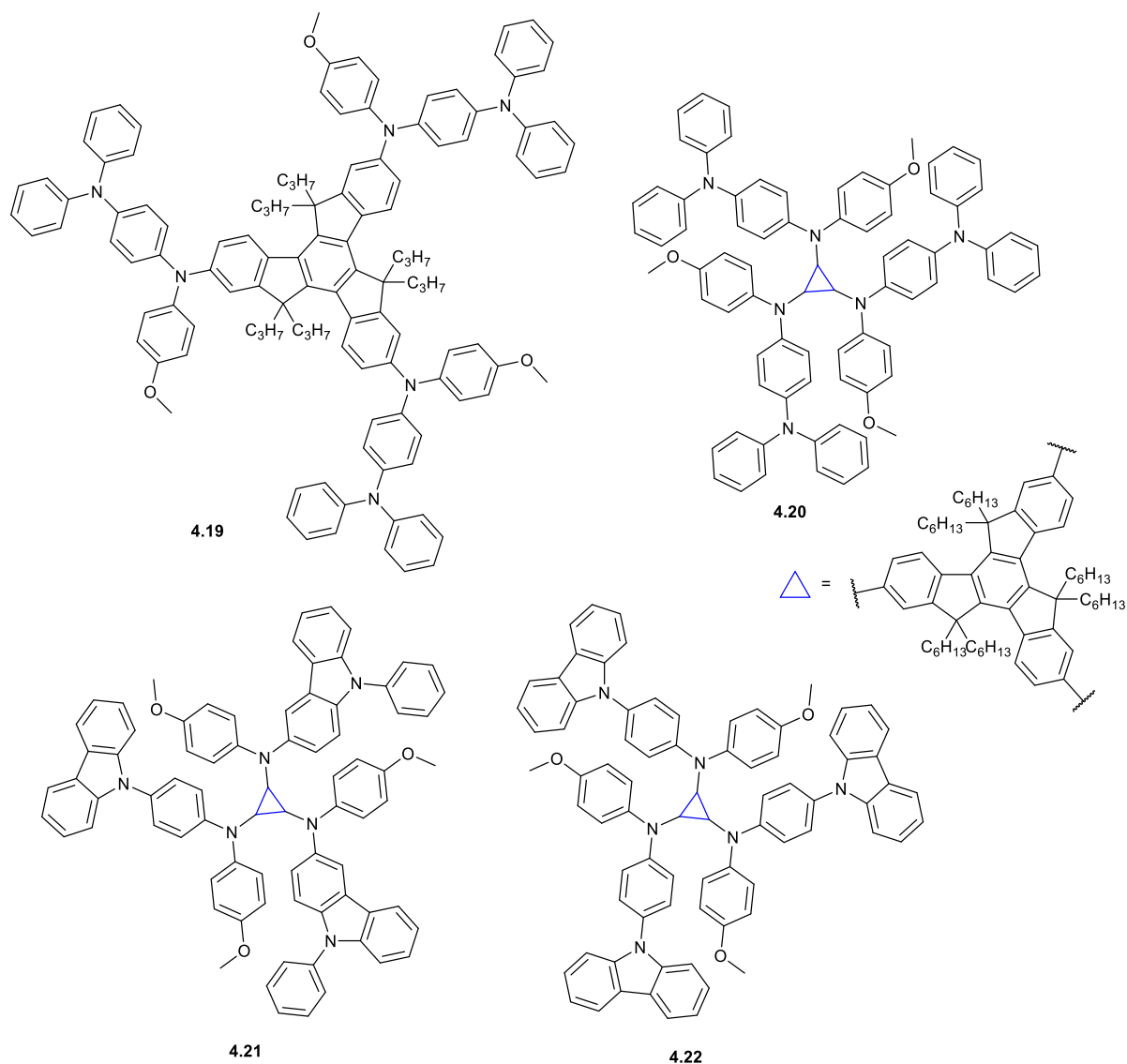
Figure 4.9: Chemical structures of peripheral arylamine derivatives

4.1.2.4   Two-photon absorption

Materials which demonstrate large two-photon absorption cross sections have obtained extensive interest due to their interesting frequency up-conversion mechanism and potential applications in two-photon fluorescence imaging, three-dimensional optical data storage, up-conversion lasing etc. To date, a large amount of research has been devoted to studying strong two-photon absorption compounds to improve understanding of the structure-two-photon absorption-cross section

relationship (which describes the two-photon absorption cross section correlation to donor-acceptor strength), conjugation length and the planarity of the compounds centre. Fluorene has frequently been employed as a building block for chromophores with high two-photon absorption. Since truxene is near-planar and contains three fluorenes sharing a central benzene ring Zhou *et al*. decided to develop a series of star-shaped conjugated oligomers of truxene cored oligo(fluorene-vinylenes) **Tr-OPV *n*** (n = 1, 2, 3, 4) by alternating Heck and Wittig reactions (Figure 4.10).[193] The monodispersed conjugated oligomers possess well-defined and uniform molecular structures as well as superior chemical purity, making them appropriate for systematic investigation of structure-property relationships. The one-photon absorption and single-photon-induced emission became more red-shifted with increasing fluorene-vinyl units due to the extension of conjugation. They observed that without the strong donor and acceptor units these conjugated oligomers showed two-photo absorption properties. These properties suggest a low energy gap can be tuned by the molecular conjugation, which is important for discerning effective coupling channels between the ground and two-photon-allowed states.
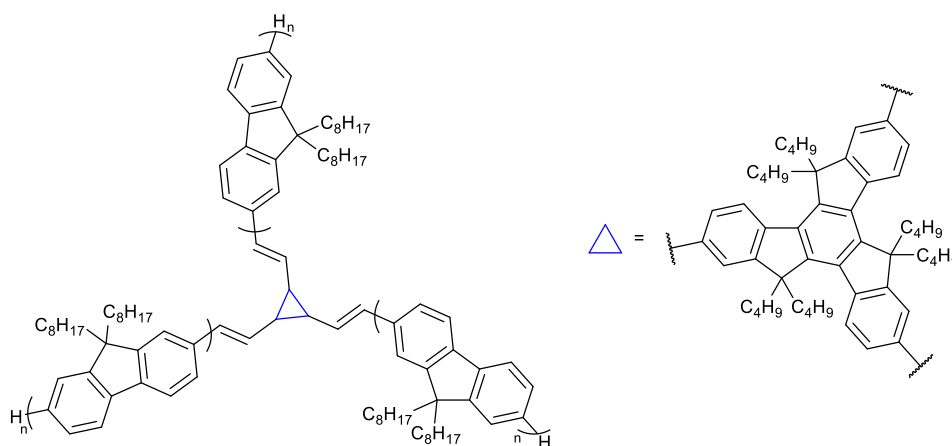
*Figure 4.10: Molecular structure of the star-shaped molecules **Tr-OPV** n*

4.1.2.5 Fluorescent probes

Small molecule fluorescent probes are molecules which change their fluorescence emission in response to a binding event, chemical reaction or change in their immediate environment.[203] These probes are used extensively in a variety of applications (such as drug discovery, cellular imaging, environmental analysis and various medical applications) for a number of reasons including the capacity for fluorescence emission to be measured with great sensitivity; fluorescence microscopy

allows remarkable spectral and temporal resolution in cell imaging and many fluorophores are readily accessible.

Probe structure can be varied to control the excitation and emission wavelengths, target binding affinity, chemical reactivity and subcellular localization.[204] Yuan *et al*. designed and developed two triarylborane-based fluoride fluorescent probes (Figure 4.11) as the fluoride anion (F$^-$) is known for affecting chemical , biological and environmental processes.[205] They determined that the colour loss experienced by the greenish yellow tetrahydrofuran solution of these probes could effectively monitor F$^-$ at a low concentration (10 µM) using the naked eye. The single-photon fluorescence intensity of **4.23** was quenched on addition of F$^-$ to its solution, indicating the formation of a turn-off fluorescent probe. Contrastingly, **4.24** produced a six-fold fluorescence enhancement on addition of F$^-$, denoting the formation of a turn-on fluorescent probe. The high two-photon absorption cross-section (δ) and strong two-photon fluorescence of both compounds make them excellent two-photon fluorescent probes for F$^-$ in organic solutions.
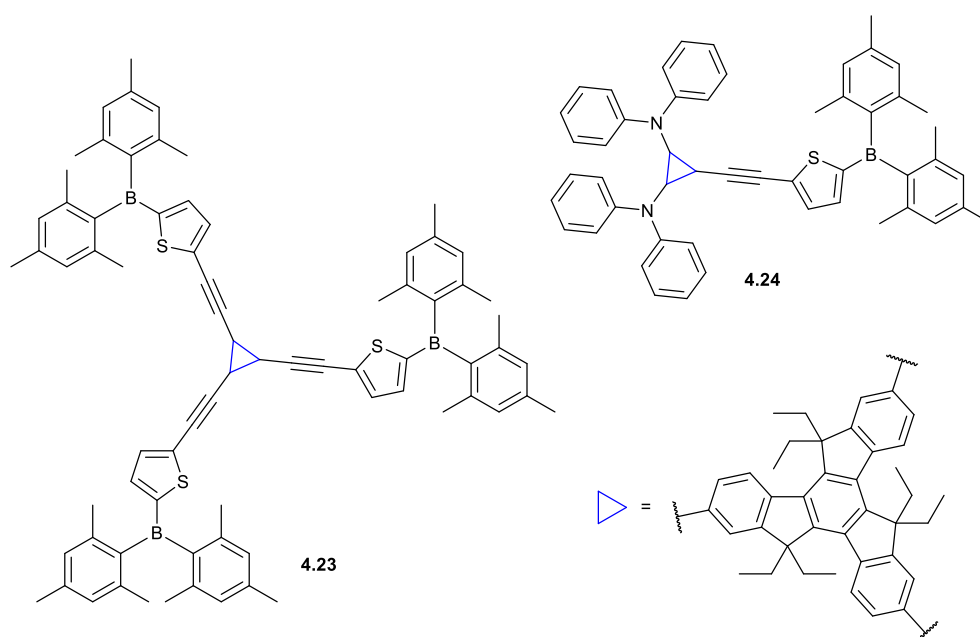
Figure 4.11: Molecular structure of triarylborane-based fluoride fluorescent probes

4.1.2.6   Fluorescent Sensors

Fluorescent sensors are molecular probes which detect and quantify analytes in various setting using the fluorescence phenomenon. They have been utilized over a wide range of applications including analytical chemistry, biochemistry and biology due to their outstanding sensitivity, selectivity and

ease of operation. Compared to some other analytical techniques, fluorescence spectroscopy requires a less-expensive instrument but still provides high selectivity and comparable sensitivity in a short response time. An example fluorescent sensor was reported and synthesised by Rashatasakhon and coworkers containing a truxene core and three ethynyl pyrene peripheries (Figure 4.12) for the detection of nitroaromatics (NACs).[206] NACs are widely used as industrial solvents, insecticides and dyes (such as nitrobenzene, trinitrobenzene and picric acid) or in criminal activities (such as the explosive trinitrotoluene (TNT)). The fluorescent sensor was found to have superior emission properties compared to the parent truxene with quantum yields of 71% and 54% in chloroform and aqueous tetrahydrofuran, respectively. In chloroform, a selective fluorescence quenching occurs towards 2-nitrophenol with a detection limit of 1.54 ppm. Interestingly in aqueous tetrahydrofuran, the fluorescence signal is selectively quenched by picric acid with a detection limit of 0.15 ppm. The Stern-Volmer plot, which were performed at various temperatures, indicated a static or contact quenching of the fluorophore, which was presumed to be a consequence of the π-π interaction between the fluorophore and the electron deficient analytes.
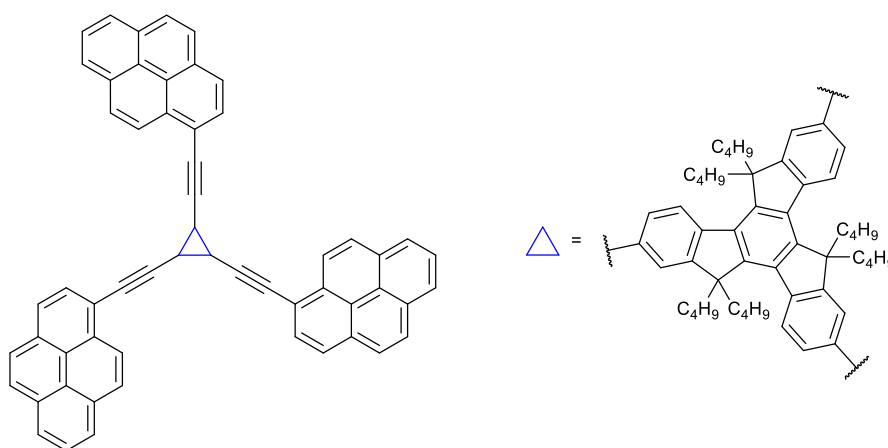
Figure 4.12: Molecular structure of a truxene based fluorophore

4.1.3 Sensors in the Food Industry

Food quality and safety are of increasing importance with consumers, focussing not only on the taste of the food products but also on their quality, safety and traceability over the supply chain.[207] The quality of dietary products can be directly affected by temperature variations, cross contamination during food handling or improper storage. In order to detect and inform on food quality, non-destructive, rapid and reliable methods are needed. Detecting signatures arising from specific

99

volatiles in food product packages is an effective way to determine food quality without needing direct contact with the product.[208]

Chemical sensors have been investigated as inexpensive and reliable devices which can provide fast responses for monitoring of gaseous compounds.[209,210] Generally, these devices have a sensitive material capable of responding to the target analyte to produce a transduction event (a change in an electrical, optical or mass dependent mechanical property) which can convert a molecular binding/reaction into a measurable signal.[211]

There are two main categories to be considered when discussing sensors: those specific to individual compounds attained using highly selective recognition methods and those which identify analytes by pattern recognition using sensors with cross reactivity.[212,213] A variety of strategies have been investigated for detecting the volatile analytes, including those designed for amines which affect food quality.

High protein content food products are among the most perishable, as decarboxylation and deamination reactions arise from amino acid degradation which leads to the formation of both toxic biogenic (examples include are putrescine, cadaverine, spermidine) and volatile amines (examples include ammonia, dimethylamine and trimethylamine).[214] An increase in these species occurs with storage time and are a part of the spoilage process.

The monitoring of volatile and biogenic amine concentrations in food products is a reliable indicator of food freshness, quality and safety. The characteristic amine compound produced during food spoilage and its concentration is dependent on the type of food product.

4.2 Aims

This project set out to design and synthesise a flavin derivative (detailed description of flavins discussed in chapter 5) based on the truxene core, with the expectation that their combined properties (such as the extended π-conjugation of the truxene and unique redox properties of the flavin moiety) would produce an efficient material for applications such as OLEDs, OFETs and sensors (see above). Upon material synthesis, the aim was to investigate the optoelectronic and electrochemical properties of the target material as well as performing theoretical studies to further explore the structure-activity relationship of the material. The final aim of the project was to investigate the OLED, OFET and sensor properties of these derivatives.

4.3 Results and Discussion

4.3.1 Target Compound Design

The proposed synthesis of the truxene derivatives final steps follow a similar procedure to that designed for the extended π-conjugated flavins, discussed in Chapter 5 (Scheme 4.1). First, the synthesis of the truxene core begun with indan-1-one before hexaalkylation to improve the solubility, making it more accessible to a wider variety of applications. This material would then be brominated to allow its amination with butylamine. Compound **4.28** would then be subjected to a condensation with violuric acid to form the flavin derivative, compound **4.36**. To improve the solubility further, alkylation at the N(3) positions of the flavin is a necessary final step for the synthesis.
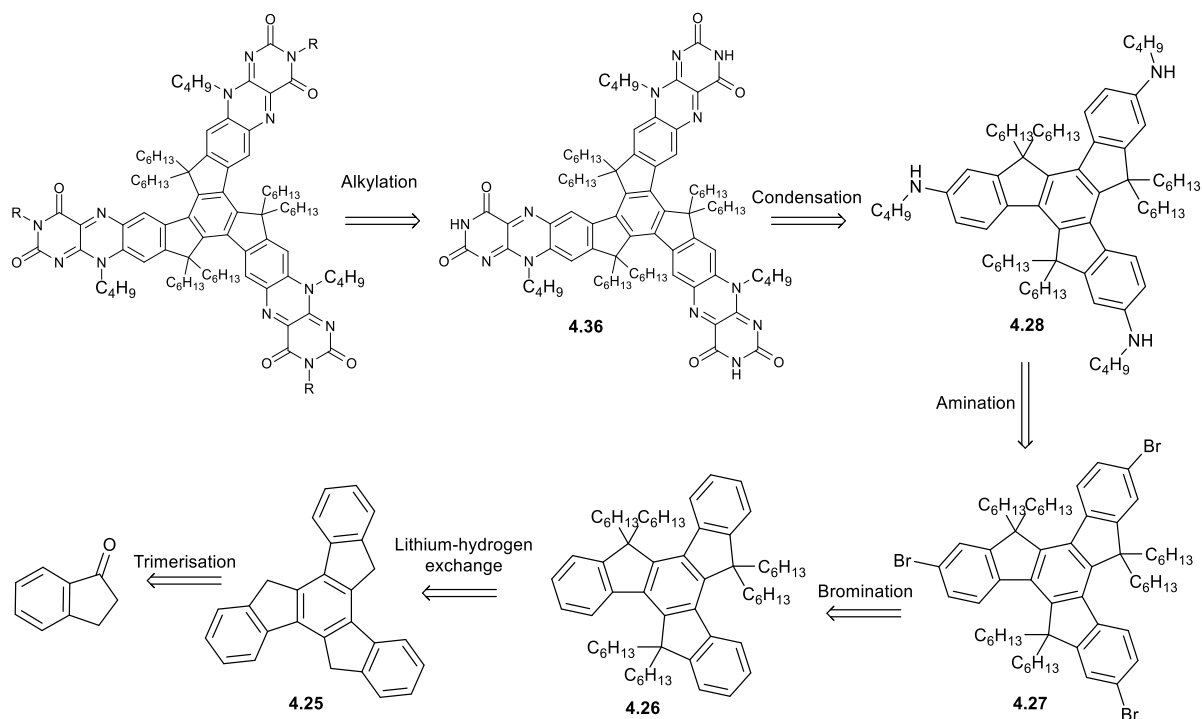
Scheme 4.1: Proposed retrosynthesis analysis of truxene derivatives

4.3.2 Synthesis

The synthesis of the truxene building block was accomplished by following literature conditions designed by Lin *et al*.[215] The trimerization of the commercially available indan-1-one was achieved using acidic conditions to produce compound **4.25** (Scheme 4.2). In order to improve the solubility and allow the material to be utilised in optoelectronics, alkylation was required at the C5, C10 and

C15 positions by lithium-hydrogen exchange following the literature procedure by Kanibolotsky *et al.*[216] to obtain a 19% yield for the hexahexylated truxene compound **4.26**.
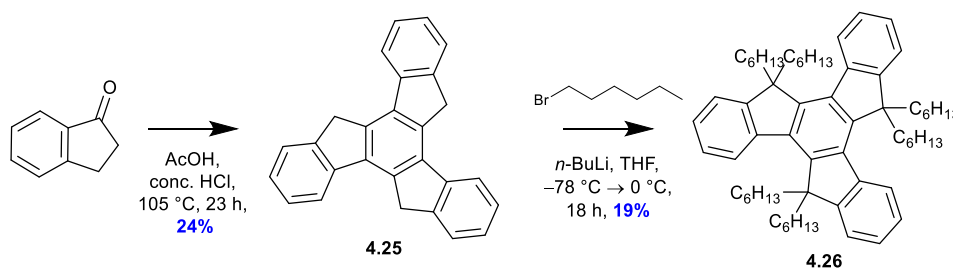
*Scheme 4.2: Synthesis of compound **4.26***

Compound **4.26** was then brominated at the C2, C7 and C12 positions to produce compound **4.27** before being subjected to the Buchwald Hartwig reaction with butylamine (Scheme 4.3). A crude mass spectrum was taken which showed a minimal amount of desired product **4.28** had been formed. However, on purification an insufficient quantity was isolated for further synthesis or analysis and the main product was identified as the starting material **2.27** with minor by-products of the mono- and di- aminated truxene.
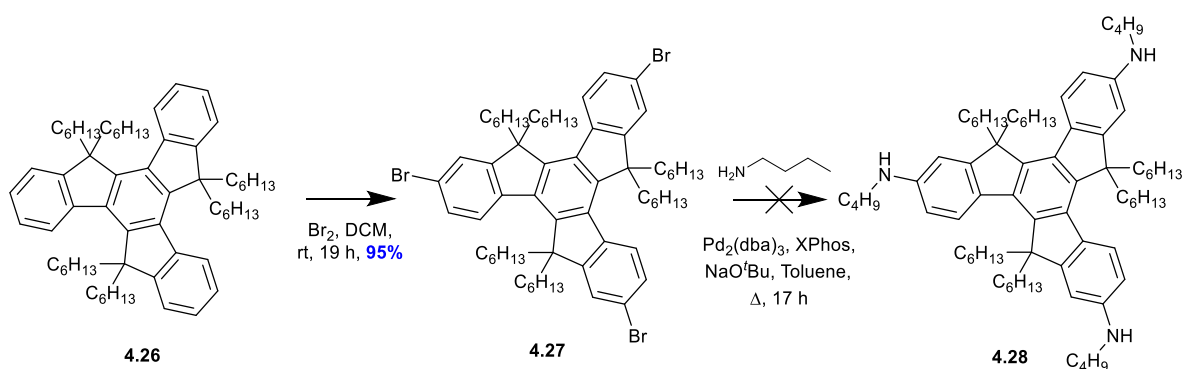
*Scheme 4.3: Attempted synthesis of compound **4.28***

An alternative route was designed, starting from the hexahexylated truxene compound **4.26** and following similar conditions devised by Lin *et al.*[217] with amine intermediates. The first step was the nitration of compound **4.26** using the harsh conditions of fuming nitric acid to form compound **4.29** to a high yield of 86% (Scheme 4.4). This was then reduced with palladium on carbon to the amine,

compound **4.30**. This reduction step was scale sensitive the higher the scale the greater the possibility of the intermediate hydroxylamine (-NHOH) being formed, preventing the complete reduction. Consequently, numerous smaller scale reactions were performed before being combined for the acetylation step to protect the amine groups. This material was then subjected to an additional nitration to form nitro groups at the C3, C8 and C13 positions to produce compound **4.32** to a moderate yield of 40%.
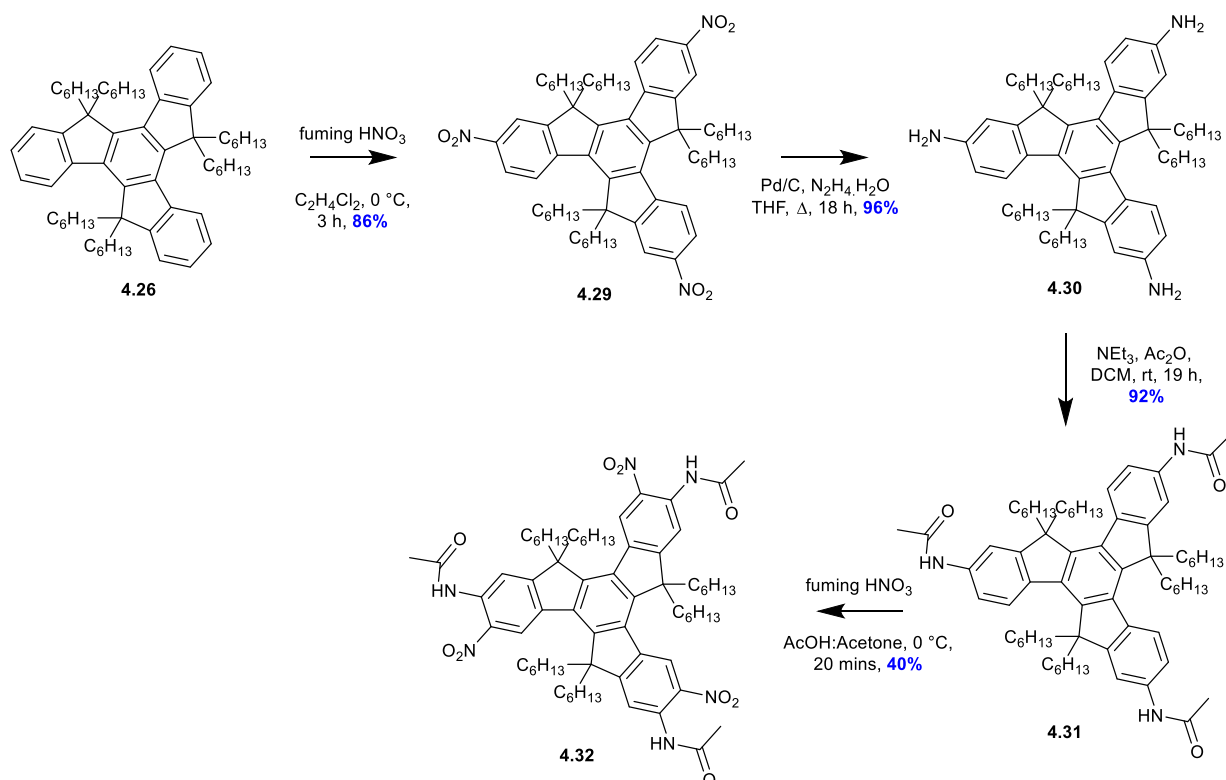
*Scheme 4.4: Synthesis of compound **4.32***

In order to synthesise the flavin derivative, compound **4.32** was first reduced by lithium aluminium hydride which provided sufficiently harsh conditions to reduce both the nitro groups and acylated protecting groups before immediately reacting with alloxan monohydrate via condensation to produce the flavin compound **4.33** to a low yield of 5% (Scheme 4.5). Since three condensations were being performed simultaneously on a material with a number of bulky groups it was expected to be low yielding. Also, from analysis of the crude NMR and TLC it was observed that the mono- and di- flavins were side products of the reaction, which were still produced when the temperature and

103

reaction time were varied. The purification of this material consequently further reduced overall yield of compound **4.33**.
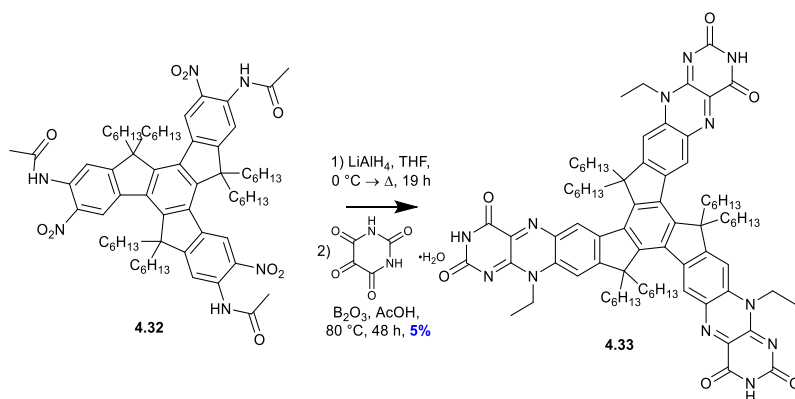
*Scheme 4.5: Synthesis of compound **4.33***

Compound **4.33** was found to be difficult to dissolve in common organic solvents, therefore alkylation of the flavin moieties at the N(3) position was necessary. 1-Iodoheptane and 1-iodododecane were used separately to determine whether the chain length had a noticeable impact on the solubility of the compounds and their photophysical properties. Similar to the flavin condensation step, this was low yielding (11%) as multiple impurities were also formed including the mono- and di- substituted product (Scheme 4.6).
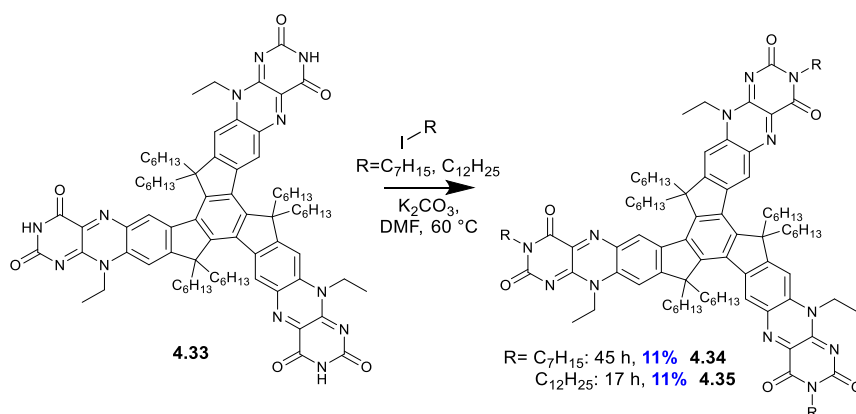
*Scheme 4.6: Synthesis of compounds **4.34** and **4.35***

4.3.3 Optoelectronic Properties

The UV-Vis and fluorescence properties of the truxene compounds **4.34** and **4.35** were studied and recorded in dichloromethane (CH_2Cl_2), with the spectra shown in Figure 4.13 and the data summarised in Table 4.1. Each compound exhibited two main distinct absorption bands, one at 310 nm and the other at a lower energy absorption between 476 and 507 nm. The shorter wavelength absorption correlates to the π-π* transitions characteristic of the truxene chromophore.[177] The longer wavelength absorption is the typical fingerprint pattern of the isoalloxazine (flavin) chromophore, with the two absorbance bands corresponding to π-π* transitions. Since the only difference in these materials is the chain length at the N(3) position, it was expected that the resulting spectra would be very similar. On analysis of the absorption spectra, the main difference observed was a slightly higher ε value for the longer wavelength absorption peak for compound **4.35** compared to compound **4.34**. It is worth mentioning that the ε value for these truxene derivatives are significantly higher than those produced by the extended π-conjugated flavins discussed in chapter 5 due to the truxene core extending the conjugation of the molecule. This results in an optical band gap of 2.32 eV. The normalised absorption and emission spectra exhibit a small Stokes shift of 27 nm (1001 cm^{-1}) and 28 nm (1032 cm^{-1}). The maximum peaks are almost identical however compound **4.34** has a slight vibrational satellite shoulder in the emission spectrum suggesting a π-π* transition.
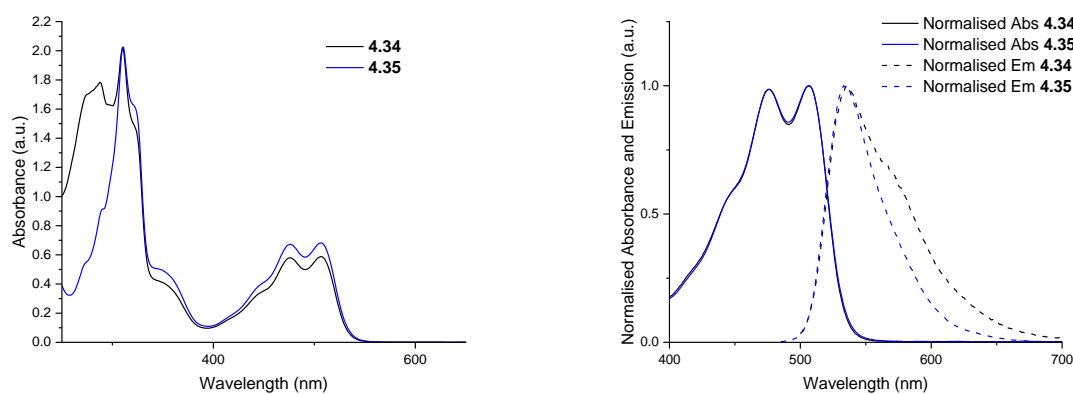
Figure 4.13: Absorption spectra (c = 1 × 10^{-5} M) and combined normalised absorption (solid line)/emission (dashed line) (c = 1 × 10^{-6} M) spectra of **4.34** *and* **4.35** *in CH$_2$Cl$_2$ solutions*

Compound	λ_{max} (nm)	λ_{onset} (nm)	$E_{g, opt}$ (eV)	Emission (nm)	Stokes shift (nm/cm^{-1})	Molar extinction coefficient $\varepsilon \times 10^3$ (L mol^{-1} cm^{-1})
4.34	507	534	2.32	535	28/1032	58.8
4.35	506	534	2.32	533	27/1001	68.2

*Table 4.1: Summary of optoelectronic properties of compounds **4.34** and **4.35**. $E_{g, opt}$ estimated from λ_{onset} of absorption*

4.3.4 Electrochemical Properties

The electrochemical behaviour of compounds **4.34** and **4.35** were explored by CV and SWV in dichloromethane (CH_2Cl_2) (1×10^{-4} M) which are shown in Figure 4.14 and the data summarised in Table 4.2. To calibrate the data, ferrocene was used as an internal standard and the data shifted to 0 V for the redox couple of ferrocene. The first reduction peak was used to determine the EA of each compound, estimated by adding 4.8 eV to the reduction value, assuming the HOMO of ferrocene lies at −4.8 eV against the vacuum level.[144]

On recording the cathodic sweep for the solutions, both compounds exhibit a quasi-reversible reduction between −1.35 V and −1.4 V which corresponds to the flavin moiety. Flavins possess three readily accessible oxidation states: the fully oxidised flavin (Fl_{OX}); the flavinsemiquinone radical, either anionic red (Fl_{rad}^-) or neutral blue ($Fl_{rad}H$); and two-electron reduced flavohydroquinone, either anionic ($Fl_{red}H^-$) or neutral ($Fl_{red}H_2$) form. Flavins are reduced by two-electron reduction directly to flavohydroquinone in aqueous and protic organic solvents. However, this experiment was performed in dichloromethane, an aprotic organic solvent with a low dielectric constant and consequently proceeds via an alternative mechanism, by way of the flavin radical.[218]

In the absence of an alkyl chain at the N(3) position the N(3)-H imide proton acts as a proton donor to the radical anion Fl_{rad}^-, thus in the case of N(3)-alkylated flavins a much simpler reductive mechanism is observed. There is no proton source to protonate Fl_{rad}^- to the neutral species $Fl_{rad}H$ therefore after Fl_{OX} is reduced to Fl_{rad}^- no further chemical steps can immediately take place. On reversing scan direction, the oxidation of Fl_{rad}^- back to Fl_{OX} is observed.[219]
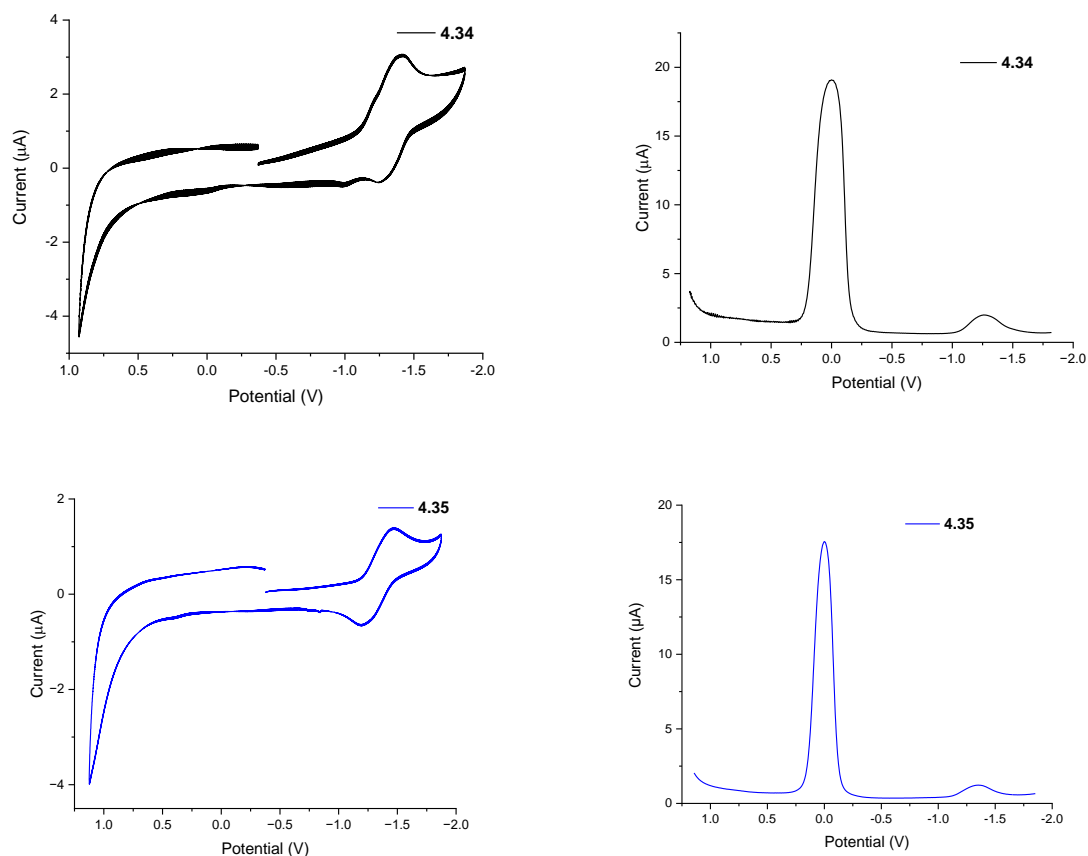
*Figure 4.14: Stacked CV (left) externally referenced to Fc/Fc⁺ and SWV (right) internally referenced to Fc/Fc⁺ for **4.34** (black) and **4.35** (blue) in solution (c = 1 × 10⁻⁴ M in CH₂Cl₂), performed using a Pt disk working electrode, a Pt wire counter electrode and a Ag wire reference electrode. TBAPF₆ (0.1M) was used as supporting electrolyte*

Compound	E_{red} (V)	IP (eV)	EA (eV)
4.34	−1.4	−5.72	−3.40
4.35	−1.35	−5.77	−3.45

Table 4.2: Summary of electrochemical properties of **4.34** and **4.35**. EA and IP calculated using the following equations: SWV EA=-[$E^{0.5}_{red}$-(-4.80)] eV; IP=EA + Eg $_{opt}$

4.3.5 Theoretical Studies

To further understand the structure property relationship of the truxene compounds **4.34** and **4.35** DFT calculations were run using Gaussian09. The geometrically optimised structures and HOMO/LUMO maps were calculated using the basis set 6-311G(d, p) within the B3LYP hybrid functional in the gas phase. The alkyl chains on the truxene core as well as the N(3)and N(10)

positions of the isoalloxazine were truncated to methyl chains to simplify the calculations, therefore the HOMO/LUMO maps are the same for compounds **4.34** and **4.35**.

The frontier molecular orbitals show planarity throughout the molecule, demonstrating its high conjugation, with the alkyl chains being the only out of plane part of the molecule (Figure 4.15). The molecule has doubly degenerate HOMO and LUMO levels caused by the three-fold symmetry which means the first two electronic transitions ($s_0 \rightarrow s_1$ and $s_0 \rightarrow s_2$) are symmetry forbidden. Due to the degenerate nature, the two HOMO and LUMO distributions have very little overlap, when the LUMO is delocalised over one isoalloxazine the HOMO is delocalised over the other two and vice versa.

The electron withdrawing character of the flavin moiety resulted in a decrease in the energy gap compared to the basic flavin as the LUMO value of the truxene core is −1.16 eV compared to −3.13/−3.15 eV of the calculated compound.[189] The results equate with the experimental values and general patterns observed in the electrochemical experiments, with identical energy gap values. However, the calculated HOMO and LUMO values are approximately 0.35 eV lower in the DFT calculation compared to the experimental result.[146] The values obtained experimentally suggest that this material could be useful in a variety of applications such as OLED, OFETs and sensors.

LUMO

−3.15 eV

LUMO

−3.13 eV

HOMO

−6.12 eV

HOMO

−6.13 eV
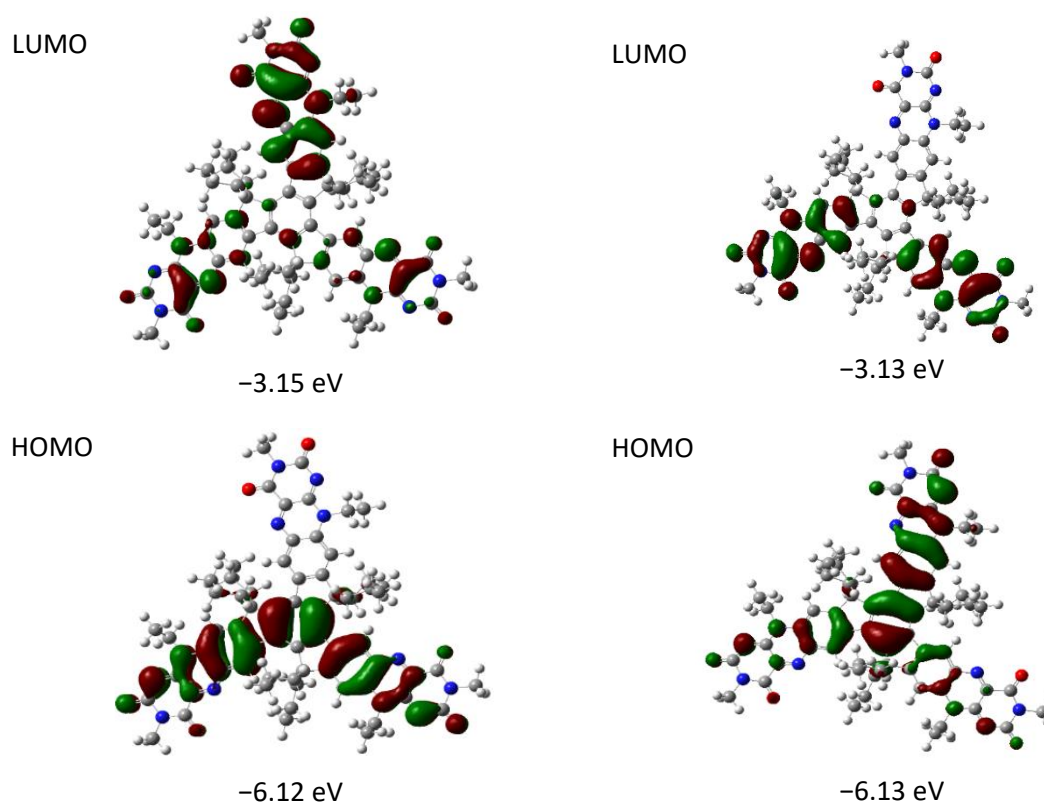
*Figure 4.15: Frontier molecular orbital diagrams with HOMO and LUMO levels for **4.34/4.35***

4.3.6 PLQY

In almost any application, the efficiency of the fundamental processes is one of the key features. In OLEDs, the driving motivation is generally to maximise the EQE of the device. In addition to the careful engineering of device architecture and electronic performance, the efficiency is directly dependent on the inherent efficiency of the luminescent materials used. This efficiency is normally quantified in photoluminescent experiments, leading to PLQY. PLQY is the number of photons emitted as a fraction of the number of photons absorbed. As well as a measure of the competition between radiative and non-radiative pathways in the material after photoexcitation.[220] Generally, truxene derivatives have a high PLQY due to the planarity and rigidity of this material.[221]

The PLQY measurements were performed by Dr. Joseph Cameron of the Prof. Peter Skabara research group in the University of Glasgow. In this collaboration, due to the quantity of material available, only compound **4.34** was analysed. The direct method of measuring PLQY was performed, measuring the fluorescence emission and scatter of the sample and comparing it to that of the blank material on a thin film since OLED devices are solid-state (Figure 4.16). A low PLQY of 0.81% was produced. It was proposed that the low PLQY was a result of aggregation in the films and intermolecular interactions which can produce non-radiative decay channels, thus generating higher optical losses.[222]

TADF is an alternative method for achieving highly emissive materials as they harvest both singlet and triplet states. Generally, this is accomplished by electron donor and acceptor components being present in an individual organic molecule.[223] Another way of obtaining TADF is combining individual electron donor and acceptor materials to form an exciplex, where the HOMO and LUMO are separated naturally. N, N'-bis(3-methylphenyl)-N, N'-diphenylbenzidine (TPD) is a good donor material and was chosen as a corresponding HTM donor material to compound **4.34** which is acting as an ETL acceptor material. Exciplexes possess an innate RISC ability which can upconvert the dark triplet excitons to the singlet excited states thus increasing the fluorescent emission and therefore are known to improve the PLQY.[224] The PLQY measurement was taken of the thin film, a slight red shift of the emission was observed (Figure 4.17). However, this is insufficient for OLED applications.
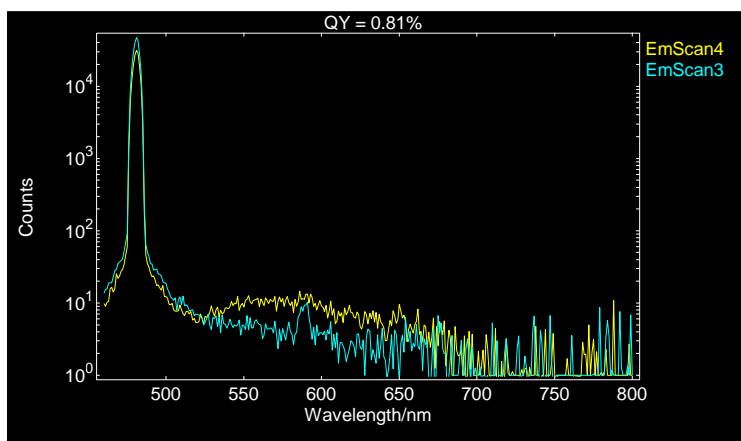
*Figure 4.16: PLQY of thin films of compound **4.34***
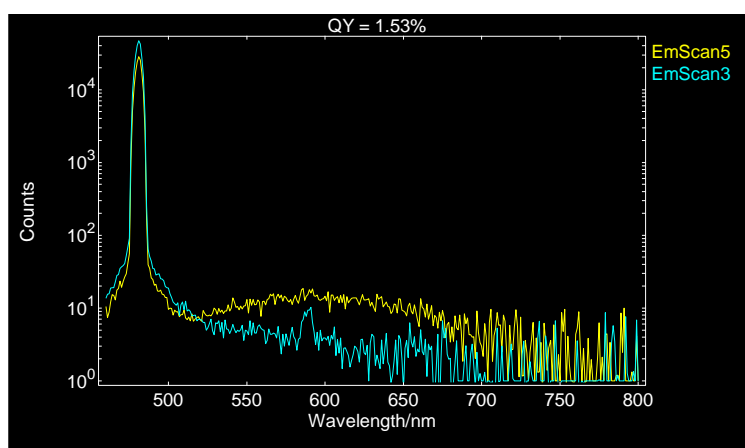
*Figure 4.17: PLQY of thin films of compound **4.34** doped with TPD*

4.3.7   OFET devices

Subsequent to the low PLQY measurements Dr. Joseph Cameron decided to fabricate OFET devices based on compound **4.34** in an attempt to find an appropriate application for this material. The devices were fabricated using the bottom gate, bottom contact architecture where the dielectric is made from a n-doped silicon layer of thermally deposited SiO_2 and the source/drain electrodes are Au with an ITO adhesion layer. Compound **4.34** was prepared in a 10 mg/ mL solution of either toluene or chloroform before being spin coated onto the films. Hexamethyldisilazane (HMDS), a self-assembled monolayer, was deposited by spin coating onto the film in an attempt to promote favourable aggregation (side on packing) along the channel. On applying an increasing voltage to the source-drain and gate electrodes no current response was observed for either n-type or p-type behaviour, suggesting the material behaved as an insulator. It was postulated that this was caused by the alkyl chains on the truxene core preventing favourable aggregation. Unfortunately, this meant that OFETs were not an appropriate application for this material and further research was necessary.

110

4.3.8 Sensing of amines and nitroaromatics

As mentioned previously, detection of amines is an important factor, particularly in the food industry to determine their quality and presence of harmful substances. Organic semiconductors can often operate as fluorescent probes by providing excellent performance including sensitivity, selectivity, high signal-to-noise ratios and simplicity of operations.[225] Fluorescence detection is one type of sensor, the main mode of quenching occurs when a quencher molecule interacts with a fluorophore either through static-based collisions or dynamic collisions between the fluorophore and quencher. In both cases, the fluorescence intensity measured is related to the concentration of the quencher. Therefore, the quenched fluorophore may serve as an indicator for the quenching agent.

4.3.8.1 Sensing of nitroaromatics in the solid state

Solid-state sensing experiments were performed by collaborators in the research group of Prof. Ifor Samuel and Prof. Graham Turnball at the University of St. Andrews by Dr. Ramakant Sharma using the truxene compound **4.34**. The thin films were produced by spin coating a 10 mg/ mL solution of compound **4.34** in chloroform (film thickness range ~90–120 nm). DNT is an analogue of the explosive TNT and is often used in sensing applications due to its easier handling. DNT vapour measurements were performed, where the PL was measured during and after addition of a known quantity of DNT (Figure 4.18). The PL was shown to have no change during the time period measured which may be a result of the low PLQY of compound **4.34** in the solid-state caused by aggregation.
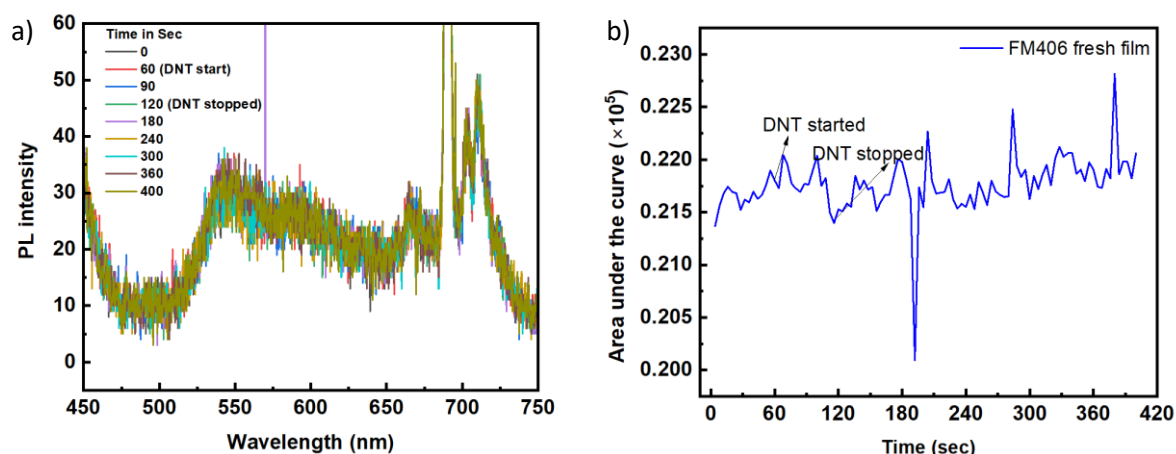
Figure 4.18: a) thin-films fluorescent response to sensing DNT; b) normalised fluorescence intensity as a function of time

4.3.8.2 Sensing of Amines in solution

It has been previously observed that hydrogen-bonding can induce fluorescence quenching.[226] It was proposed that a similar situation could occur between compound **4.34**/**4.35** and the tested amine. From the emission data shown in Section 4.3.3 it was noted that compound **4.34** produced a higher fluorescence in solution, which is common in organic molecules. Therefore, tests were performed in solution to determine if the state of the material had an impact on the results. These tests were performed by a fellow Cooke group member, Dr. Dylan Wilkinson. Aliphatic (butylamine and triethylamine) and aromatic (triphenylamine and 3,4-dimethyl aniline) amines were tested for both absorption and fluorescence detection.

Increasing equivalents of amine were added (0.01, 0.1, 0.5, 1 and 100 equivalents) to a solution of compound **4.34** in tetrahydrofuran (1×10^6 M) and the absorption/emission spectra taken for each addition (Figure 4.19). On analysis of the spectra, it was observed that compound **4.34** did not show efficacy for detecting the tested amines and any slight discrepancies in the intensities are due to experimental error. The only observable trend was the increase in absorption when large amounts of triphenylamine was added. However, this change is likely a result of the triphenylamine absorption. As mentioned in section 4.3.8, it was hypothesised that the interaction between the amine and compound **4.34** would be a result of hydrogen bonding on the flavin moiety. The flavin absorption in the visible region (400–500 nm range) is noticeably unaffected with increasing amine and therefore likely that no interactions were occurring between the flavin moiety and the amine. It is also possible that there is poor alignment between the HOMO and LUMO energy levels of the amine and compound **4.34** which influences the charge transfer due to the band gap being discernibly different between materials.[227,228] Alternative analytes with more appropriate band alignment may produce better results.
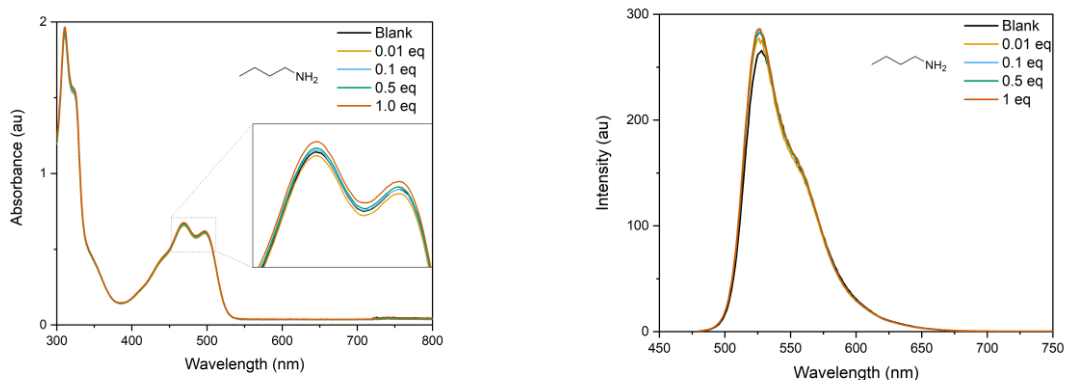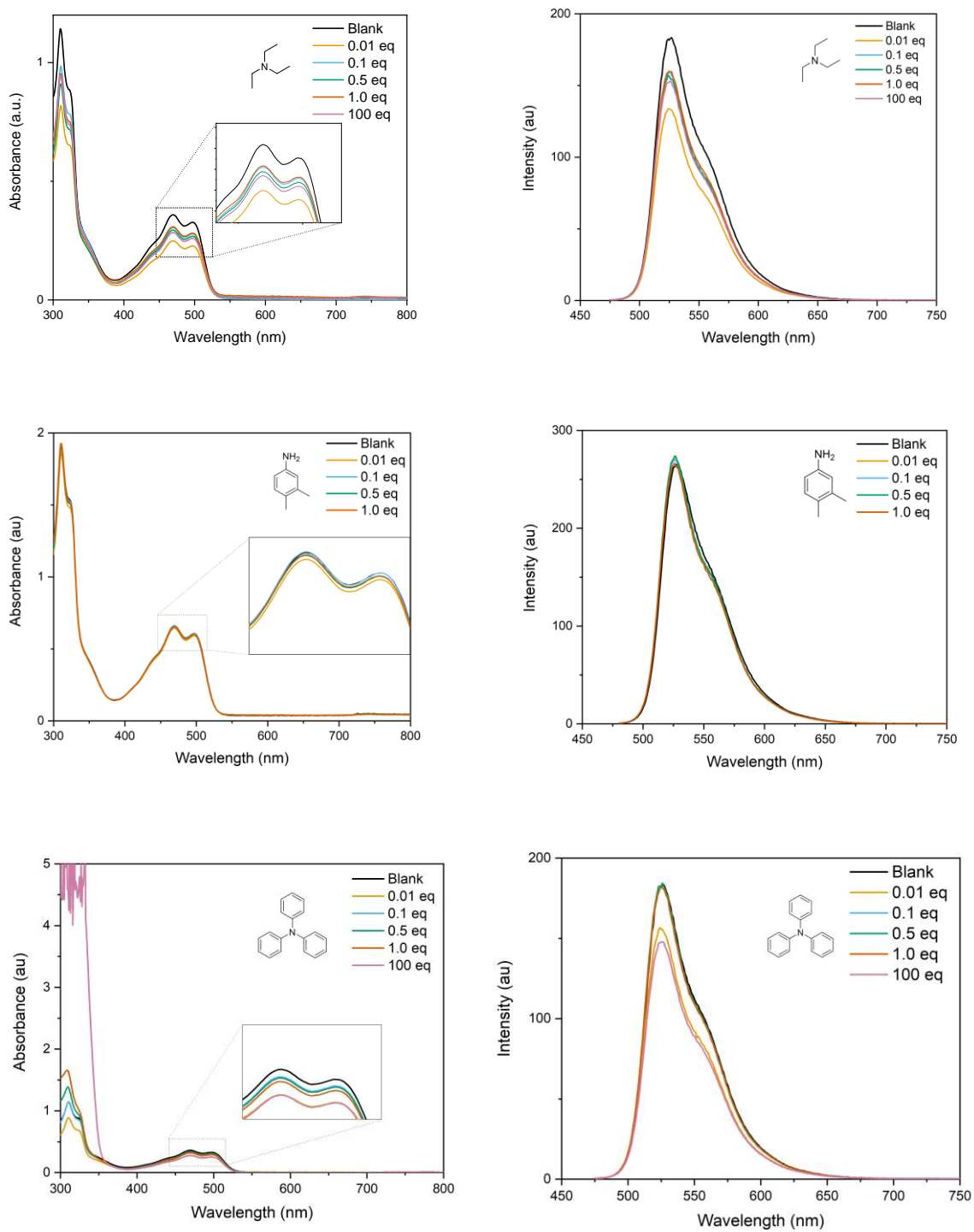
*Figure 4.19: Absorption and emission spectra for amine sensing of compound **4.34***

4.4 Conclusions and Future Work

The synthesis of two flavin-fused truxene materials, compounds **4.34** and **4.35** were explored before the optical and electrochemical properties were studied. Compounds **4.34** and **4.35** produce very similar properties since the only difference was the chain length at the N(3) position of the flavin moiety. Compound **4.35** exhibited a slightly higher molar extinction coefficient. The DFT calculations show planarity throughout the molecule providing high conjugation and show degenerate HOMO and LUMO energy levels.

These compounds have been tested by our collaborators in Prof. Peter Skabara group at the University of Glasgow and Prof. Ifor Samuel and Prof. Graham Turnball at the University of St. Andrews for PLQY in the solid state as well as possible applications including OLEDs, OFETs and sensors. All endeavours for the solid-state were hindered by the aggregation of compound **4.34** which increased the non-radiative decay channels. Dr. Dylan Wilkinson of the Cooke group has also performed tests on compound **4.34** in solution to determine its potential as an amine sensor since the emission is stronger in solution. However, no response was noted from the tested amines.

Future work will include identifying analytes with more appropriate energy level alignment with compound **4.34** in an attempt to find an application for this material.

5 Fluorescent Bio-Mimetic Materials for Optoelectronic Applications

A substantial amount of research has been undertaken over the last decade in developing and utilising biomaterials. Nature has created an extensive variety of organic molecules which display a wide scope for producing materials through easy manufacture, shaping and tuning of material properties compared to inorganic materials.[229] Biomaterials also often show unusual properties which are difficult to reproduce in conventional organic or inorganic materials.[230] Furthermore, natural biomaterials are made from renewable resources and are inherently biodegradable. Given the sustainability, bio compatibility, non-toxicity, versatility, and potential low cost of bio-organic materials, such materials have been considered as candidates for bio-organic semiconductor science and technology.[231]

5.1 Flavins

5.1.1 Introduction

Flavins are generally described as a family of yellow bio-organic dye molecules derived from the 7,8-dimethyl-10-alkylisoalloxazine chromophore.[232] The flavin chromophore is capable of absorbing in a wide spectral range and acts reversibly as either an electron donor or acceptor depending on its environment. Consequently, flavins perform a crucial role in many biological processes acting as coenzymes and photoreceptors.[233] Riboflavin, commonly known as vitamin B2, is the precursor to all significant flavins taking part in DNA repair by photolyase,[234] bacterial luciferase[235] and the photoresponse of fungal sporangiophores. The human body converts riboflavin into enzyme cofactors flavin mononucleotide (FMN) and flavin adenine dinucleotide (FAD) which perform essential biological functions (Figure 5.1).[236–238]

Riboflavin

Flavin mononucleotide (FMN)

Flavin adenine dinucleotide (FAD)
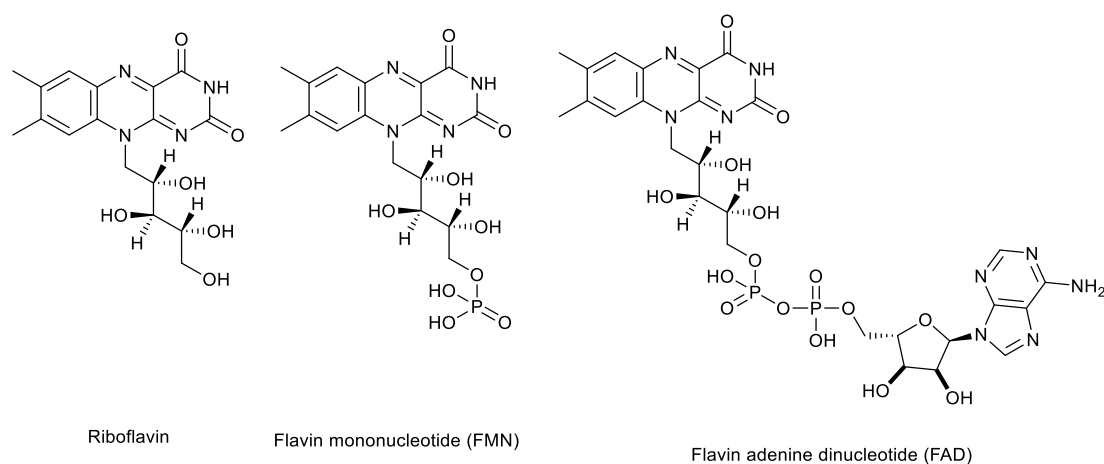
Figure 5.1: Molecular structure of most common natural flavin derivatives

Flavins can be categorised as redox coenzymes, indicating their potential to react as efficient one or two electron redox systems accompanied by photon transfer at the nitrogen of diazabutadiene of the isoalloxazine. Enzymes containing FMN and/or FAD are able to catalyse a number of one- and two-electron oxidation/reduction reactions which are vital for the energy metabolism systems (photosynthesis, aerobic respiration, denitrification and sulfur respiration).[239] The major asset of flavins is their capability to be chemically stable over a wide range of potentials. This is, in part, due to the flavin molecule being able to exist in three redox states: oxidised (quinone), one-electron reduced (semiquinone) and two-electron reduced (hydroquinone) and each of these redox states has three different protonation states (Figure 5.2).[240] Flavins can be tuned by functionalising the N(3) and N(10) positions, likewise changing the functionalisation on the phenyl ring (positions C(6)–C(9)) which can lead to a distinct change in the redox properties as well as their absorption and chemical reactivity. The local environment, hydrogen bonding, π-π stacking or metal coordination to the chromophore and the position of substituents determines the redox potentials and photophysical properties of the flavin derivatives.[241]
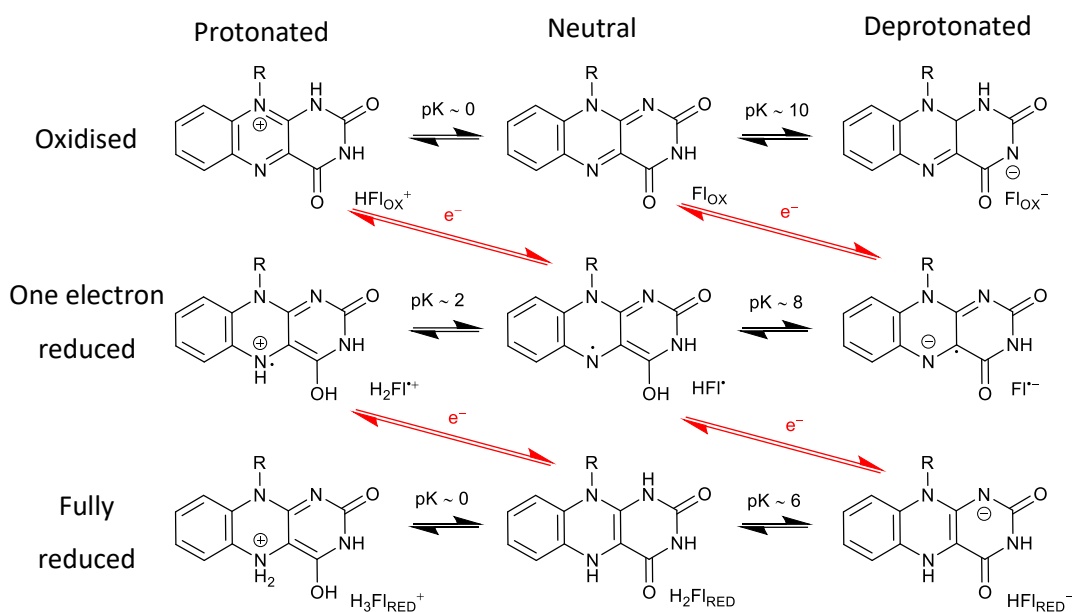
Figure 5.2: Different redox and protonation states of flavin (10-substituted isoalloxazine)

Flavins have a variety of features that explain their extensive application in nature including photostability, reversible electrochemistry and their ability to tune their optical, electronic and redox properties.[233] In addition to their significance in biological applications these properties are a key feature for organic photocatalysis, organic electronics and optoelectronic devices.[233,242]

The photocatalytic cycle starts with the irradiation of the oxidised form of flavin (Fl_{OX}) with blue light, resulting in its excitation into the singlet state ($^1Fl*$) (Figure 5.3). ISC then occurs rapidly to the triplet state ($^3Fl_{OX}*$). In catalysis, $^3Fl_{OX}*$ is the active species and key intermediate which can subsequently be reduced by an appropriate substrate to the radical anion ($Fl^{\cdot-}$). The radical anion is then protonated and further reduced to the flavohydroquinone anion (HFl_{RED}^-). The multiple redox and protonation states of flavin and its derivatives affect the photoabsorption properties, particularly the fluorescent intensity and excited state lifetimes.[242]
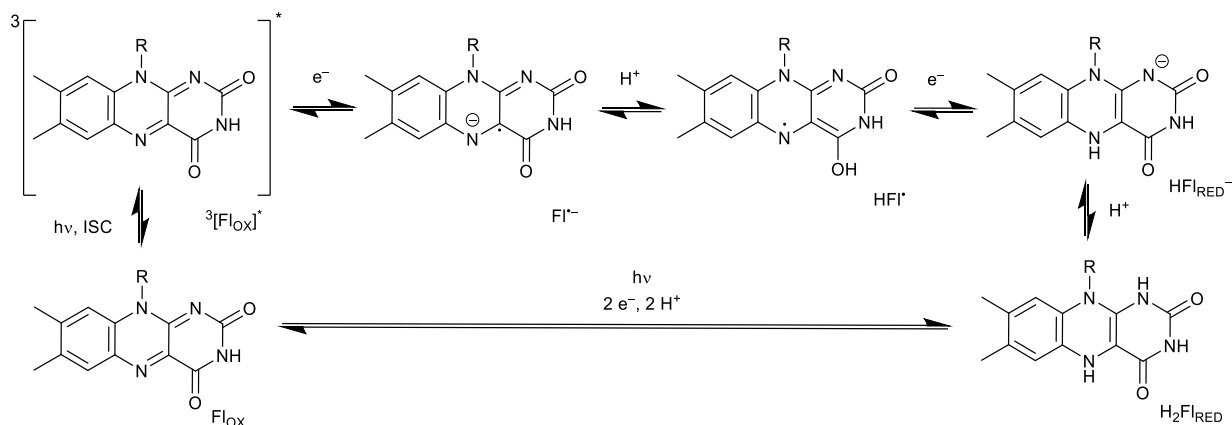
Figure 5.3: The photocatalytic cycle of flavin redox reactions

Oka *et al.* developed the chemoselective synthesis of unsymmetrical disulfides using the oxidative heterocoupling reaction of two different thiols.[243] Under visible light irradiation, the riboflavin-based catalyst was able to promote the formation of the phototropin-like flavin-thiol adduct, the mild reactivity of this adduct was vital in the chemoselective cross-coupling (Figure 5.4). This green oxidative transformation is driven by visible light and molecular oxygen under mild metal-free conditions due to the photo- and redox-organocatalysis of the flavin.
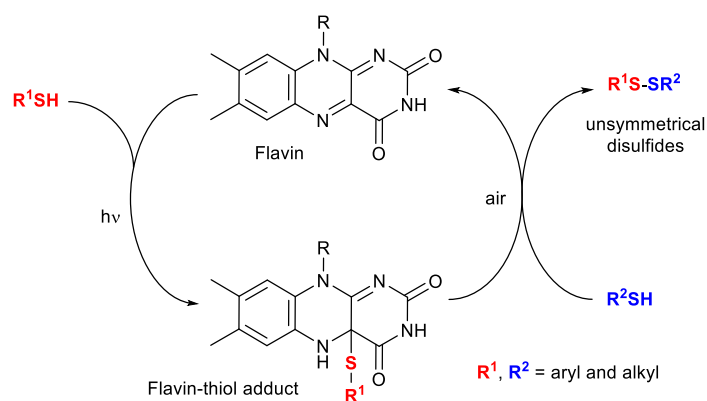
Figure 5.4: Flavin-thiol adduct mediated heterocoupling reaction

Flavins are known to be very versatile in respect to substrate modification and types of reaction. Cooke and coworkers investigated a series of push-pull flavin derivatives with different electron-donor units attached at the C(8) position before determining the impact of these changes on the optical, redox and second harmonic generation properties.[244] They determined that flavins **5.1** and **5.2** (Figure 5.5), which contained the stronger electron donor groups, exhibited higher

118

hyperpolarisabilities and thermal stabilities suggesting their potential for future applications in non-linear optical devices such as optical transistors.
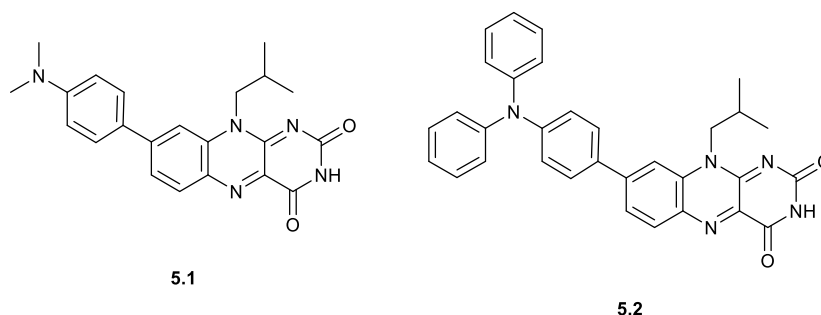
Figure 5.5: Molecular structure of flavin derivatives

Many organic semiconductors have the potential to act as a HTM, however, acting as electron transporting materials is rare. The electron deficient nature of flavins make them a highly appropriate contender for applications in OLEDs. However, there are very few examples of this in the literature. Jurgensen *et al.* reported the characterisation of thin films of riboflavin tetrabutyrate and its use in solution processed OLEDs (Figure 5.6).[245] The fabricated devices showed a maximum luminance of roughly 10 cd m^{-2}, EQE of 0.02% and a broad spectral emission with peak at 640 nm. Despite this material showing vast improvements in thin biomaterial emission layers there is obviously still a requirement to improve the electronic properties either by manipulation of the device architecture or further chemical modification of the compound.
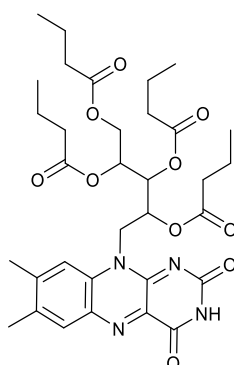
Figure 5.6: Molecular structure of riboflavin tetrabutyrate

Extending the π-conjugation of the flavin molecule is a less explored method for modifying the optical and electronic properties of flavins. Extension of the conjugation length is predicted to shift the absorption maxima and change both the redox properties of the chromophore and the extinction coefficient.[231] König and coworkers have attempted to expand the fused π-systems from the basic *N*-10 butyl substituted flavin core by using either naphthalene (**5.3**), anthracene (**5.4**) or pyrene (**5.5**)-attached derivatives (Figure 5.7). It was determined that a progressive bathochromic shift in both absorption and emission spectra was the outcome of this alteration. All derivatives showed intensive emission while maintaining the parent flavins electrochemical redox behaviour.[241]
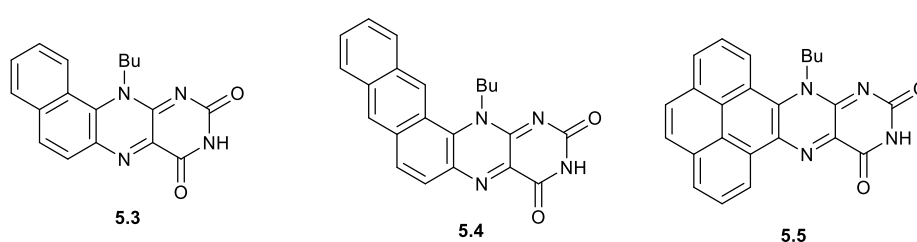
Figure 5.7: Molecular structure of π-extended flavin derivatives

5.1.2 Aims

The aim of this project was to synthesise several novel extended π-conjugated flavin derivatives using relatively straightforward chemistry. With inspiration from the literature, a number of molecules were designed and the changing properties caused by the increased conjugation investigated.

Upon material synthesis, the aim was to fully characterise the molecules before investigating the optoelectronic and electrochemical properties. The final aim was to use computational calculations to further probe structure-activity relationship of the final materials.

5.1.3 Results and Discussion

5.1.3.1 Target Compound Designs

In this work the PAHs investigated were fluorene, fluoranthene and phenanthrene (Figure 5.8). Although fluorene is classified as a PAH the 5-membered ring has no aromaticity. However, the methylene bridge forces the two phenyl rings to be planar which forces their orbital overlap and thus increases the degree of conjugation in the system.[246] Fluoranthene is a structural isomer of

pyrene but is less thermodynamically stable due to the strain on the 5 membered ring. Phenanthrene is a fully conjugated molecule, the fusion of the aromatic rings at an angle results in 5 resonance structures thus producing a stable molecule with good π stability and aromaticity.
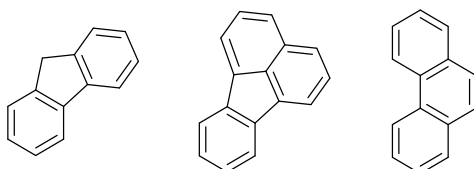
Figure 5.8: PAHs with increasing aromaticity: fluorene, fluoranthene and phenanthrene

The synthetic route designed for the flavin derivatives followed a similar procedure to König and coworkers.[241] The brominated PAH was aminated before being subjected to a condensation with violuric acid (Scheme 5.1 shows the proposed fluorene derivative route). The final step required was the alkylation of the N(3) position of the flavin in order to improve the solubility of the final flavin derivatives.
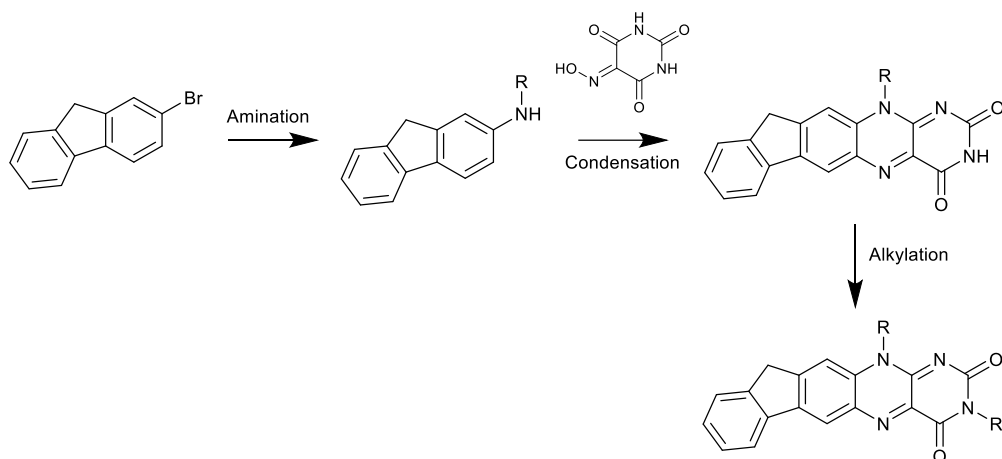
Scheme 5.1: Proposed synthetic route for extended π-conjugated flavin derivatives (fluorene example shown)

5.1.3.2   Synthesis

Compound **5.8** was successfully synthesised starting from commercially available 9-bromophenanthrene. The first step involved the Buchwald-Hartwig amination with butylamine using a modified procedure from König and coworkers to produce compound **5.6** (Scheme 5.2). This then

underwent a condensation reaction with violuric acid in acetic acid to produce compound **5.7** before finally alkylation with 1-iodoheptane to produce an excellent yield of 87% for flavin compound **5.8**.
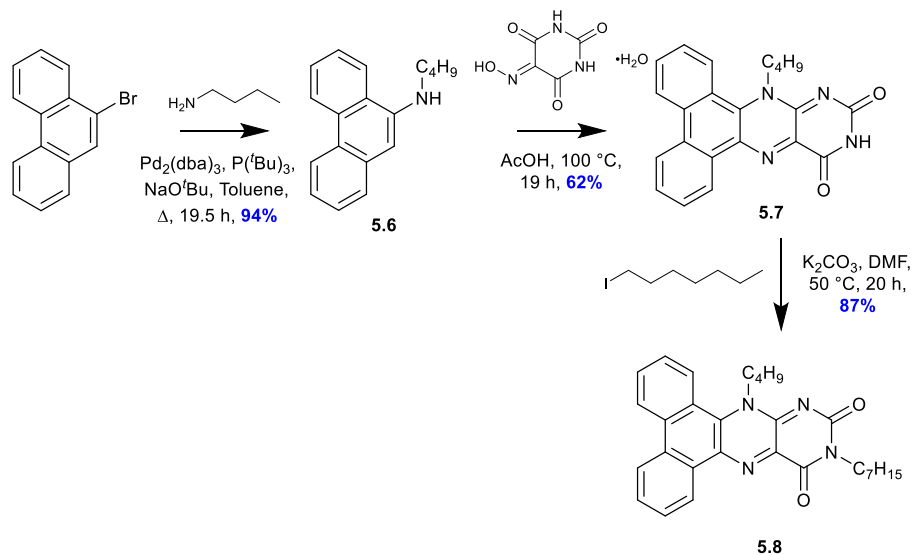
*Scheme 5.2: Synthesis of compound **5.8***

The same synthetic route and reaction conditions were utilised to synthesise compound **5.11** starting from commercially available 3-bromofluoranthene (Scheme 5.3). However, the yield for each step is notably lower (81%, 21% and 42% respectively) than that achieved for compound **5.8** which could be a result of the lower aromaticity and stability of the fluoranthene group.
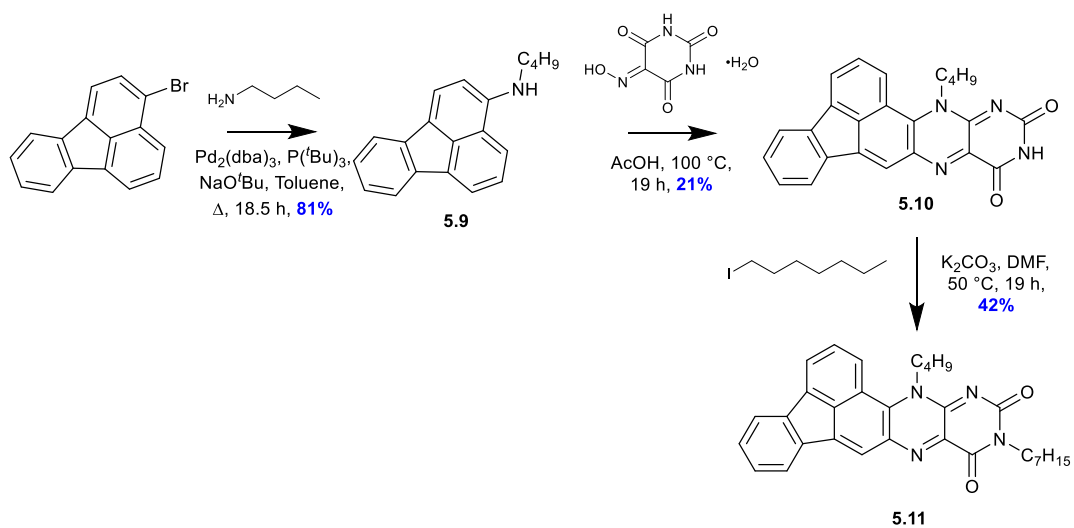
*Scheme 5.3: Synthesis of compound **5.11***

For the fluorene flavin derivative, initially the synthesis of compound **5.13** was attempted. Starting from commercially available 2-bromo-9*H*-fluorene the same Buchwald-Hartwig conditions were used as for the previous flavin derivatives and achieved compound **5.12** to a modest yield of 61%. However, the subsequent condensation reaction with violuric acid was not as successful. On analysis by TLC and NMR it was determined that a minimal amount of the desired product had formed but due to the impurities having similar R$_f$ values it was very difficult to purify resulting in negligible quantities of desired flavin compound **5.13** (Scheme 5.4).
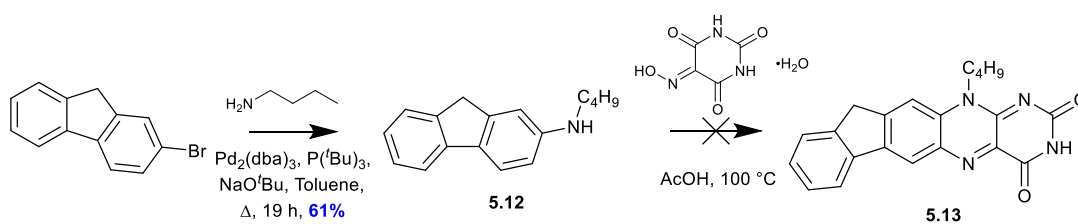
*Scheme 5.4: Attempted synthesis of compound **5.13***

Since the synthesis of the fluorene flavin, compound **5.13**, was unsuccessful an alternative synthetic route was undertaken. The desired amine, compound **5.12** was synthesised over two steps. First, the commercially available 2-aminofluorene underwent a nucleophilic addition/elimination with butyryl chloride before being subjected to reduction conditions to form the amine compound **5.12**. Despite the amine synthesis achieving high yields the condensation reaction again was ineffective (Scheme 5.5). This result is likely due to the bridging methylene protons of the fluorene group which are relatively acidic. Deprotonation of compound **5.12** can generate a reactive species which may lead to a myriad of unwanted side products, hindering the desired reaction. In order to suppress this reaction, double alkylation or acylation can be undergone which has the added advantage of enhancing the compounds solubility in organic solvents.[247,248]
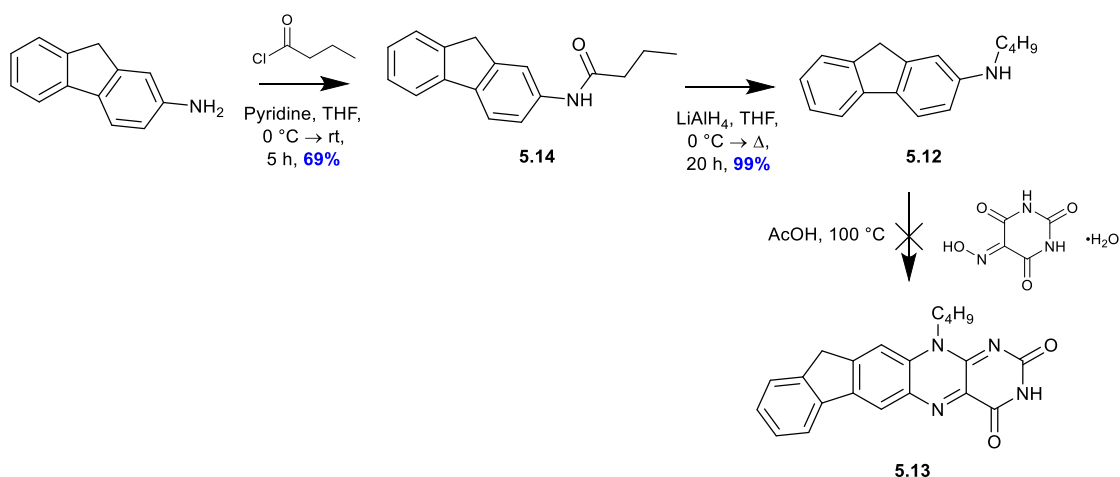
*Scheme 5.5: Second attempted synthesis of compound **5.13***

Alkylation is much easier to accomplish than arylation, therefore, this new route was taken in an attempt to produce the dihexylfluorene flavin compound **5.18**. First, the commercially available 2-bromo-9*H*-fluorene was reacted with 1-bromohexane by nucleophilic substitution to produce an excellent yield of 91% for compound **5.15**. The subsequently Buchwald-Hartwig, condensation and alkylation reactions used the same conditions as the previous flavins. The condensation step only achieved a low yield of 4% which may be caused by the hexyl chains on the fluorene moiety leading to steric hinderance which prevented the violuric acid reaction with compound **5.16** to a higher yield. However, a sufficient scale was undergone that enough material was isolated for the final alkylation to be performed which produced the desired dihexylfluorene flavin compound **5.18** to a modest yield of 47% (Scheme 5.6).
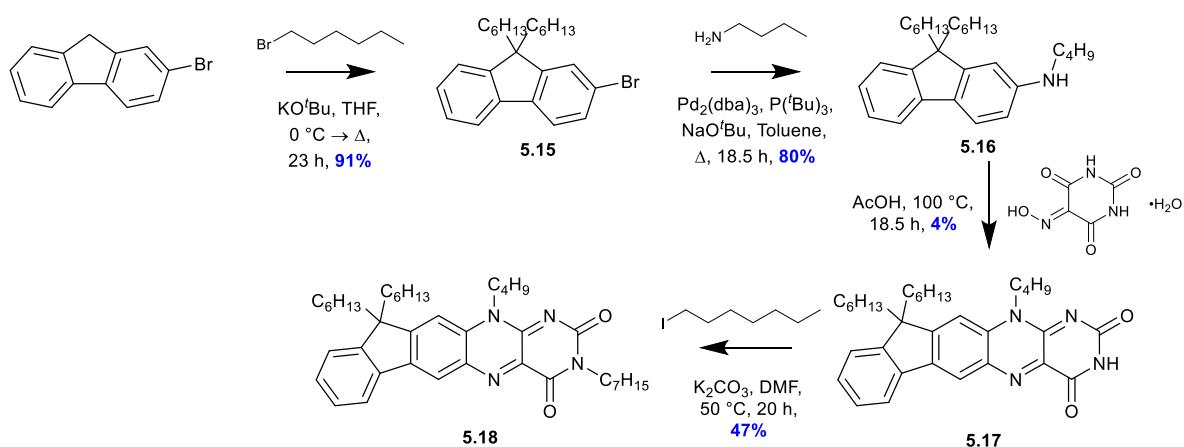
*Scheme 5.6: Synthesis of compound **5.18***

In order to identify the effect of conjugation on the flavins properties the parent flavin, compound **5.21** was synthesised by following Yoneda's route, which is a convenient way of synthesising isoalloxazines.[249] This synthetic route starts with commercially available *N*-methylaniline and consists of a nitrative cyclisation of the 6-(*N*-methylanilino)uracil precursor, compound **5.19** to a 73% yield. This was followed by the consecutive nitration and dehydration to form the stable isoalloxazine *N*-oxide intermediate before deoxygenation using sodium dithionite to achieve the parent flavin, compound **5.20**, to a good yield of 78%. To keep the materials consistent, the N(3) position of the flavin was alkylated to produce flavin compound **5.21** to an excellent yield of 95% (Scheme 5.7).
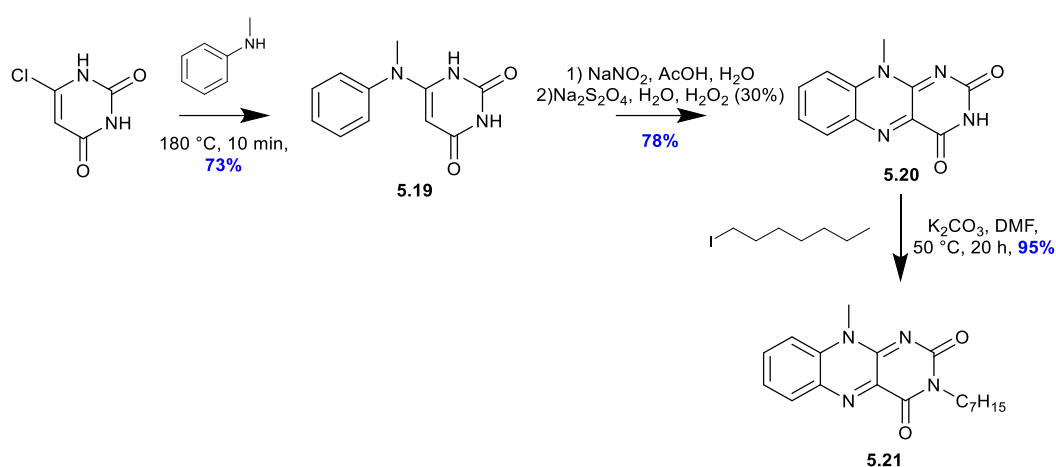
*Scheme 5.7: Synthesis of compound **5.21***

5.1.3.3   Optoelectronic Properties

The UV-Vis and fluorescence properties of the parent flavin compound **5.21** and the three extended π-conjugated flavin compounds **5.8**, **5.11** and **5.18** were studied and recorded in dichloromethane (CH$_2$Cl$_2$) with the spectra shown in Figure 5.9 and the data summarised in Table 5.1. All derivatives show a complex absorption profile characteristic for the presence of multiple chromophores. All flavin derivatives exhibit intense absorption between 285 and 563 nm. The shorter wavelength absorption around 285 – 416 nm correlates to the π-π* transitions characteristic to the isolated fluorene, fluoranthene and phenanthrene chromophores.[250–252] The longer wavelength absorption around 400 – 500 nm is the typical fingerprint pattern of the isoalloxazine chromophore, with two absorbance bands attributed to π-π* transitions. On comparison of the novel flavins to the parent flavin compound **5.21** it was noted that a bathochromic shift occurred in all novel flavins, 12 nm for compound **5.18**, 42 nm for compound **5.8** and 70 nm for compound **5.11** as the conjugation length increased and indicates a decrease in the HOMO-LUMO gap.

Compounds **5.21** and **5.11** are both observed to shows three distinct peaks in the lower energy band ranging from 420 – 509 nm. These peaks are separated by *ca*. 1000 cm^{-1}, suggesting vibrational splitting within single electronic transitions which is common for flavin species in low polarity solvents.[253] On comparison of the peak heights it was observed that the higher energy π-π* transition is more prominent for compound **5.21** whereas for compound **5.11** it is the lower energy π-π* transition. Flavin compound **5.8** appears to only have two peaks for the lower energy π-π* transition at 481 and 506 nm. Flavin compound **5.18** has the most complex absorption band of all the flavin derivatives as four distinct peaks are observed at 424, 451, 473 and 503 nm. These peaks are spaced approximately 1000 cm^{-1} apart, an indication of vibrational levels for the two π-π* transitions. It is possible that for compounds **5.21**, **5.8** and **5.11** the different intensities of absorbance between the two π-π* transitions resulted in the concealment of one or more bands under the broader absorbance peaks. The ε value of compound **5.8** is noticeably higher than that observed for the other derivatives which could be attributed to the higher conjugation of phenanthrene compared to fluorene and fluoranthene. This is further corroborated by the fact that compound **5.8** has the lowest E$_{g, opt}$ of 2.28 eV.

The emission spectrum of compound **5.11** shows a vibrational structure similar to the parent flavin compound **5.21**, with a slight vibrational satellite shoulder about 1000 cm^{-1} red shifted which suggests a π-π* transition. Flavin compound **5.8** has a broad emission and does not exhibit any structure which implies that a state with some charge transfer character causes the emission. Again, compound **5.18** is unconventional as two peaks are observed. The separation between these peaks is greater than 1000 cm^{-1} and therefore cannot be attributed to vibrational π-π* transitions in one state. It is possible that the effective separation and similar absorbance of the two π-π* transitions resulted in both emissions being observed.

The normalised absorption and emission spectra show relatively small Stokes shift for compounds **5.18** and **5.11** (24 nm (1120 cm^{-1}) and 33 nm (1224 cm^{-1}) for compound **5.18** and 34 nm (1230 cm^{-1}) for compound **5.11**) while compound **5.8** has a noticeably higher Stokes shift of 97 nm (3489 cm^{-1}). This higher Stokes shift would make this material more useful as a fluorescent material in optoelectronic devices.
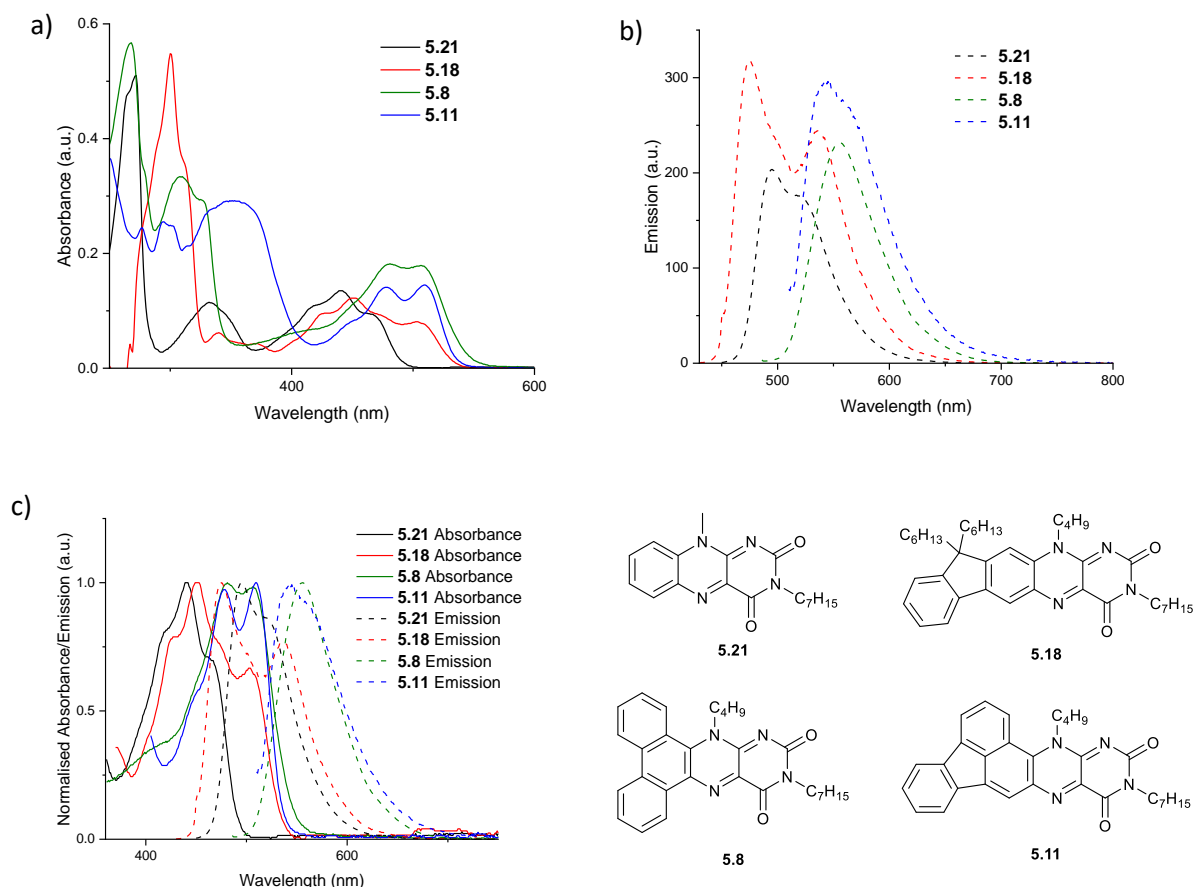
*Figure 5.9: a) Absorption spectra, b) emission spectra and combined normalised absorption (solid line)/emission (dashed line) spectra of **5.21** (black), **5.18** (red), **5.8** (green) and **5.11** (blue) in CH₂Cl₂ solutions (c = 1 × 10⁻⁵ M)*

Compound	λ_{max} (nm)	λ_{onset} (nm)	$E_{g, opt}$ (eV)	Emission (nm)	Stokes shift (nm/cm⁻¹)	Molar extinction coefficient $\varepsilon \times 10^3$ (L mol⁻¹ cm⁻¹)
5.21	439	491	2.53	496	57/2618	13.5
5.18	451	533	2.33	475	24/1120	12.2
5.8	481	543	2.28	578	97/3489	18.2
5.11	509	535	2.32	543	34/1230	14.5

*Table 5.1: Summary of the optoelectronic properties of flavins **5.21, 5.18, 5.8** and **5.11**. $E_{g, opt}$ estimated from λ_{onset} of absorption.*

5.1.3.4 Electrochemical Properties

The electrochemical behaviour of the four flavins were studied by CV and SWV in dichloromethane (CH₂Cl₂), with the spectra shown in Figure 5.10 and the data summarised in Table 5.2. To calibrate the data, ferrocene was used as an internal standard and the data shifted to 0 V for the redox couple

of ferrocene.[144] The first reduction peak was used to determine the EA of each compound. This is estimated by adding 4.8 eV to the reduction value, assuming the HOMO of ferrocene lies at −4.8 eV against the vacuum level.

On recording the cathodic sweep for the solutions, all compounds exhibited a quasi-reversible reduction peak between −1.1 and −1.27 V which corresponds to the reduction of the flavin moiety. The voltametric behaviour and reduction mechanism can be explained using the mechanism of riboflavin which has been intensely studied in previous years.[218,254] As mentioned previously, there are a number of states in which the flavin moiety can appear. Compounds **5.21**, **5.8** and **5.11** show the voltametric reduction being fully chemically reversible which indicates a simple chemically reversible electron transfer reaction. This high reversibility is likely a result of the radical anion ($Fl_{rad}^{\cdot-}$), formed in the initial electron transfer step, undergoing a slow homogeneous reaction with Fl_{ox}. $Fl_{rad}^{\cdot-}$ remains fully formed at the electrode surface and, therefore, is capable of converting back to Fl_{ox} when the scan direction is reversed.[219]

Compound **5.18** is slightly different as a quasi-reversible peak is observed. This may mean that in the second reduction process the radical anion ($Fl_{rad}^{\cdot-}$) was reduced by one electron to form the dianion Fl^{2-}. The appearance of this new wave on the reverse scan indicates a suitable proton donor was available and the dianion Fl^{2-} was protonated to form $Fl_{rad}H^-$ which was then oxidised back to Fl_{ox}. Although no water was deliberately added to the solution it is possible than the water naturally present in CH_2Cl_2 was sufficient, in this case, to act as a proton donor.
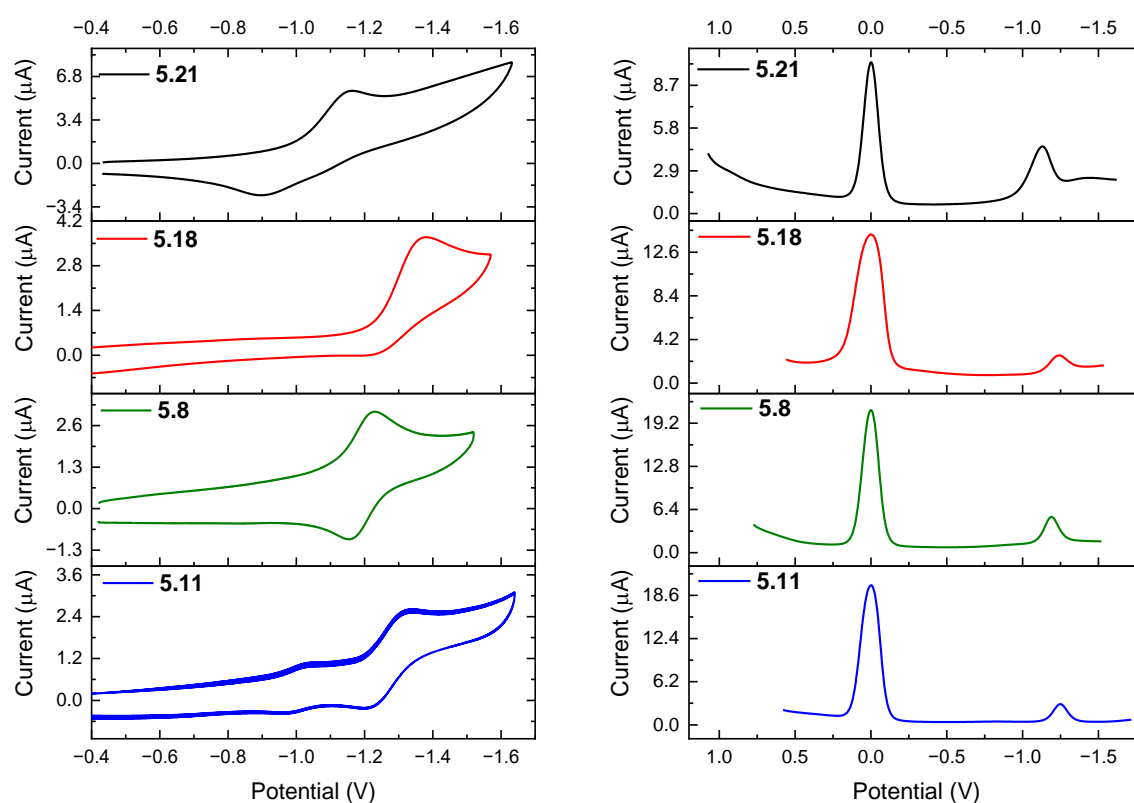
*Figure 5.10: Stacked CV (left) externally referenced to Fc/Fc⁺ and SWV (right) internally referenced to. Fc/Fc⁺ for flavin derivatives **5.21** (black), **5.18** (red), **5.8** (green) and **5.11** (blue) in solution (c = 1 × 10⁻⁴ M in CH₂Cl₂) with a scan rate of 0.1 Vs⁻¹, performed using a Pt disk working electrode, a Pt wire counter electrode and a Ag wire reference electrode. TBAPF₆ (0.1 M) was used as supporting electrolyte and the redox potential of the Fc/Fc⁺ couple as internal standard.*

Compound	E_{red} (V)	EA (eV)	IP (eV)
5.21	−1.1	−6.23	−3.70
5.18	−1.24	−5.89	−3.56
5.8	−1.21	−5.87	−3.59
5.11	−1.27	−5.85	−3.53

*Table 5.2: Summary of the electrochemical properties of flavins **5.21, 5.18, 5.8** and **5.11**. EA and IP calculated using following equations: EA = −[$E^{0.5}_{red}$ −(−4.80)] eV; IP = EA − $E_{g,opt}$*

5.1.3.5   Theoretical Studies

Computational calculations were executed to aid in further understanding the structure-property relationship at the molecular level. DFT calculations were carried out in Gaussian09 using the basis set 6-311G(d, p) within the B3LYP hybrid functional in order to calculate the molecular orbital levels in the gas phase. This level of calculation was utilised to provide sufficiently reliable qualitative insights into the experimental results. The electronic distribution of the frontier molecular orbitals

for all compounds are displayed with the associated band gaps in Figure 5.11. The alkyl chains on the fluorene moiety as well as the N(3) and N(10) positions of the isoalloxazine were truncated to methyl chains to simplify the calculations. The function of the alkyl chains is to increase the solubility of the molecule and therefore the length has little to no effect on the electronic properties of the overall molecule. Since all derivatives have the same chain length at N(3) and N(10) the results are still capable of producing reliable comparisons.

On comparison of the LUMO electronic distribution of the π-extended flavin derivatives to compound **5.21** it appears that the π-extension has little effect on the electronic distribution as it is mainly observed over the isoalloxazine moiety. The LUMO energies for flavin compounds **5.8** and **5.11** are identical at −3.08 eV while compound **5.18** has a higher level at -3.03 eV and compound **5.21** has a lower energy of −3.14 eV. In comparison, the HOMO energies of the new derivatives are delocalised over large parts of the molecule with compounds **5.18** and **5.8** having energies at −6.19 eV while compound **5.11** has a deeper energy of −6.22 eV. This results in compound **5.18** having a larger fundamental band gap than the other derivatives. Compound **5.21** has a much lower HOMO energy of −6.66 eV which results in a significantly larger fundamental band gap compared to the extended π-conjugated derivatives.

The results equate with the experimental values and general patterns observed in the electrochemical experiments. However, the LUMO levels are calculated to be approximately 0.5 eV higher in the DFT compared to the experimental EA for each flavin derivative. In general, the calculated HOMO levels are slightly lower than the experimental IP values which means the calculated fundamental band gap is greater than that determined experimentally.
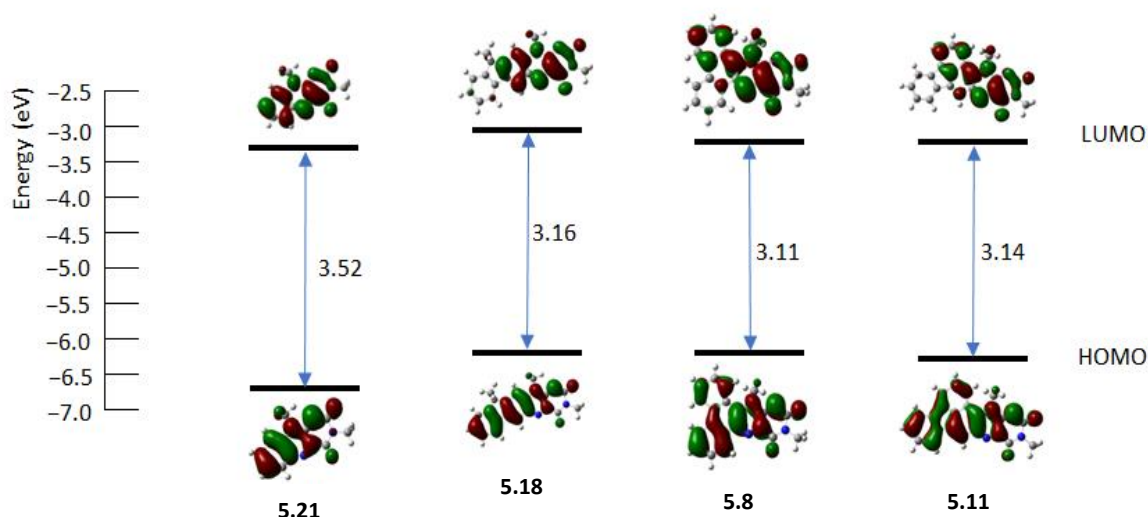
*Figure 5.11: Frontier molecular orbital diagrams with HOMO and LUMO levels for **5.21, 5.18, 5.8** and **5.11***

Time dependent calculations (TD-DFT) were also carried out and revealed the transitions between the frontier molecular orbitals which determine the lowest excited singlet state S_1, transition energies of 2.77 eV (**5.18**), 2.73 eV (**5.8**) and 2.73 eV (**5.11**) were obtained. This coincided with the experimental data as compounds **5.8** and **5.11** have similar emission spectra while compound **5.18** is blue shifted. This trend is also observed in the absorption spectra.

The absorption spectra were simulated using the TD-DFT (Figure 5.12) and compared to the experimental results. As a result of the calculations being carried out in the gas phase, which disregards intermolecular interactions in the bulk solution, there are discrepancies observed. The position of the peaks for compounds **5.21**, **5.18**, **5.8** and **5.11** are more blue shifted than observed experimentally, however, they seem to follow similar trends. Compound **5.8** has a narrow peak at 256 nm with a smaller vibrational shoulder and a broader, less intense peak at 450 nm. Compound **5.11** has a similar peak at 261 nm with a broader peak at 335 nm which covers the area of the lower energy peak. Compound **5.18**, similar to the experimental, has different characteristic peaks. The lower energy peak seen for compound **5.8** is also observed at 448 nm. However, unlike the other π-extended derivatives, at higher energy there are two distinct peaks observed at 221 nm and 292 nm which have similar characteristics to compound **5.21** which has two distinct peaks at 208 nm and 250 nm. Contrary to compound **5.21** with almost identical peak intensity, compound **5.18** has larger variation in intensity for these two peaks which could explain the variation in the spectra observed experimentally.
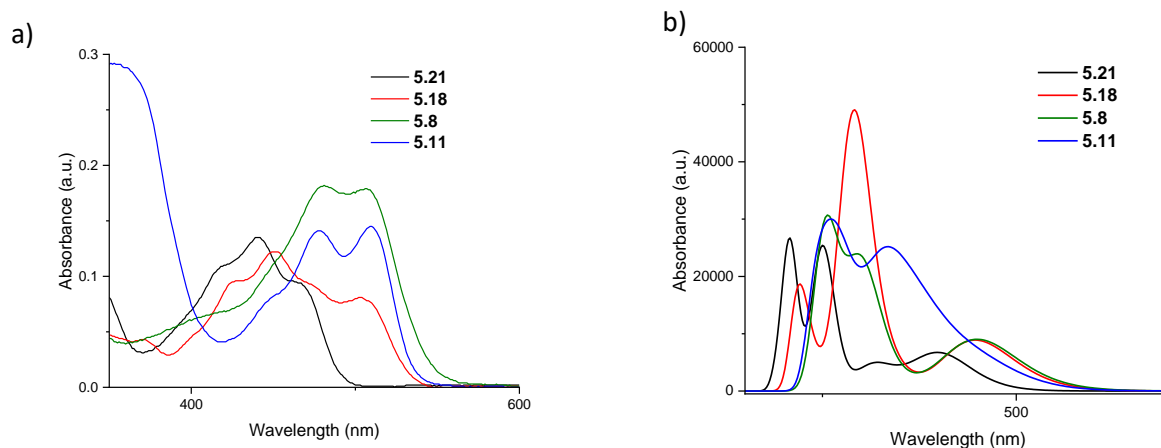
*Figure 5.12: a) Experimental and b) Simulated UV-Vis spectra for **5.21**, **5.18**, **5.8** and **5.11***

5.1.4   Conclusions and Future Work

Novel extended π-conjugated flavins were successfully synthesised and their photophysical, electrochemical and theoretical properties studied. It was observed that by extending the π-system the electronic and redox properties of the chromophore were altered. The absorption has a bathochromic shift for all novel derivatives and intense emission compared to the parent flavin compound **5.21**. The reduction mechanism of the extended π-conjugated flavins were observed by CV and SWV which can be interpreted in a similar fashion to the previously investigated flavins with a slight difference in voltametric behaviour being a result of the varying equilibrium constants produced from the homogeneous reactions following electron transfer.

It has been previously shown that the absorption peaks can change shape and position depending on the solvent polarity, therefore, measuring the absorption in various solvents could aid in the better understanding of the unusual features observed for compound **5.18**.

Gregor Macleod, a fellow Cooke group member, has tested compounds **5.8** and **5.11** to determine if they have gel like properties using a variety of solvents. Only a small number of flavin-based low molecular weight gelators have previously been reported.[255,256] The only solvent to show any potential was toluene for compound **5.8** which may be due to the flavins lack of amphiphilicity. The procedure applied was 5 mg of compound **5.8** was added to 0.25 mL toluene in a 3 mL vial. The sample was sonicated prior to heating in an oil bath until compound **5.8** was fully dissolved. After 24 hours at room temperature, the 20 mg/mL sample of compound **5.8** was found to be stable under inversion, which may indicate the existence of a gel network (Figure 5.13). Compound **5.8** has been

given to our collaborator Prof. Dave Adams in the University of Glasgow for further testing of their gel properties and to determine a suitable application of this material.

*Figure 5.13: Compound **5.8** showing gel like properties*

5.2 Green Fluorescent Proteins

5.2.1 Introduction

Fluorescent proteins (FPs) are complex 3D polypeptide structures that contain an organic chromophore responsible for the luminescent features. Green fluorescent proteins (GFPs) were first discovered by Shimomura and Johnson in 1961 when they isolated two closely associated proteins: a calcium binding photoprotein *aequorin* and a chromophore containing GFP. These were isolated from the bioluminescence system of the jellyfish *Aequorea Victoria* (Figure 5.14).[257]
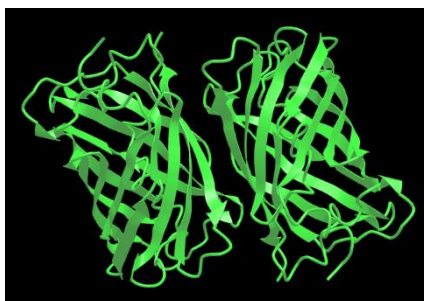
Figure 5.14: 3D structure of Aequorea Victoria *green fluorescent protein*

It took until 1994 before the value of the GFP was identified as a genetically encoded fluorescent marker, requiring O_2 for its self-assembly, vital for fluorophore synthesis from a tripeptide.[258] The imidazolinone substructure has since been identified in a number of naturally occurring FPs acting as chromophores including GFP, cyan fluorescent protein (CFP), blue fluorescent protein (BFP) and red kaede fluorescent protein (RFP) (Figure 5.15).[259] In naturally occurring GFP, the chromophore exhibits a 4-(*p*-hydroxybenzylidene)-5-imidazolinone basic structure which can occur in either an anionic or neutral form. The relative concentration of these forms is controlled by the environmental conditions, such as ionic strength, pH and temperature.[260]

GFP

CFP

BFP

RFP
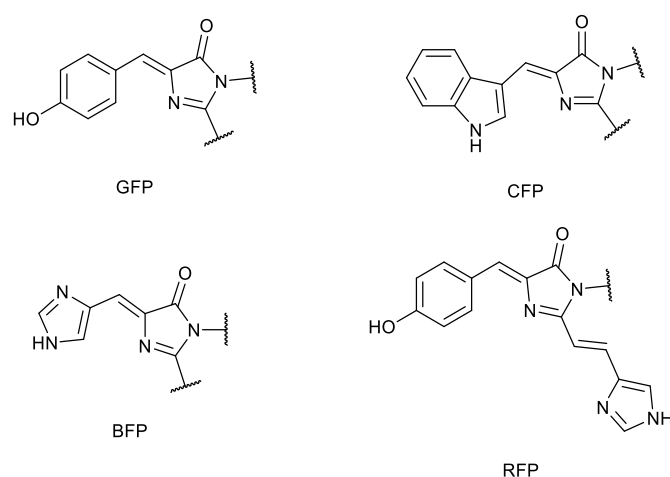
Figure 5.15: Examples of Imidazolinone containing FP chromophores in nature

The chromophore is positioned inside a β-barrel fold (Figure 5.14). GFP is formed by cyclization of the protein backbone at positions 65-67 (Ser-Tyr-Gly in GFP), followed by dehydrogenation of Cα-Cβ of Tyr66 with molecular oxygen.[261] Reactions result in a two-ring structure representing a conjugated π-system that is large, polarized and planar enough to absorb and emit light within the visible range. The basic chromophore structure can be covalently modified, leading to changes in the π-conjugated system which culminates in variations to the spectral characteristics. The protein structure also provides the framework to fine tune the spectroscopic features of the FPs through different mechanisms, including formation of the chromophore, positioning of amino acids close to the chromophore or modifying the electrostatic field created by the protein matrix at the chromophore.

GFPs have become one of the most widely studied and utilised proteins being broadly utilised for imaging and tracing in cell biology and medicine due to their ability to generate a highly visible, efficiently emitting internal chromophore.[262,263] More recently, there has been an increased scrutiny

of these materials for use in photonic applications. This is a result of their good photoluminescence features, photostability, sustainable production by bacteria and eco-friendly recycling.[260]

The discovery and development of genetically encoded FPs has led to a radical alteration into scientists' ability to analyse biological phenomena directly within living matter.[264] The potential to visualise cell movements and dynamic changes in sub-cellular structures in living mammals significantly enhances our understanding of biology.[265] Recent advances in multiphoton imaging technologies have allowed researchers to study cell-cell interactions and the microenvironment of living tissues. Sahai et al. were able to study two cell types in the same organ *in vivo* with differing fluorescent proteins in order to detect tumours.[265] The fluorescent pairs need to be selected such that they excite equally at a common wavelength. GFP and CFP were chosen as their expression is well tolerated by most cell types and can be easily excited by the standard Ti-sapphire lasers (tuneable lasers which emit red and near-IR light in the 650 – 1100 nm range). These fluorophores were also chosen to aid in the study of sub-cellular compartments and protein localisation in living tissues. This enabled the direct comparison of the behaviour of control and experimental manipulated cells in the same environment. This is pivotal for determining the effects of genetic manipulations on cell behaviour *in vivo*.

In relation to bio-based optoelectronic devices FPs can act as the light responsive element. FPs have been applied as colour down converting materials for lighting applications, such as hybrid white light emitting diodes (HWLEDs) and lasers, to produce devices with superior performances in luminous efficiencies and stabilities as well as laser threshold energies to develop some of the leading HWLEDs and lasers.[260] Costa and coworkers reported a novel approach for constructing HWLEDs by integrating LEDs with a coating system of FP-based rubber materials (mTagBFP, eGFP and mCherry) (Figure 5.16).[266] This structure design resulted in the first bio-HWLED with 50 lm W^{-1} with a loss of less than 10% after more than 100 hours under operation conditions. This demonstrates that the synergy of the interesting features of FPs with the easy processibility of the rubber material can be used for constructing a cascade coating suitable for lighting applications.
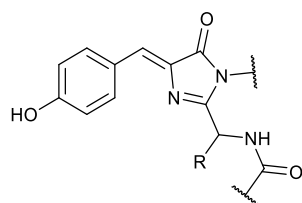
Figure 5.16: Chromophore for mTagBFP, eGFP and mCherry

GFPs have been considered a potential material for use in OLEDs due to their ability to form nanometre-scale films, high brightness, wide colour gamut and simple fabrication ability.[267] The first application of GFPs in OLEDs was achieved by You *et al*. by using a biomimetic approach to generate light based on the excitation of the GFP found in jellyfish.[268] The scaffold for GFP is known to add an insulating layer around the chromophore, therefore impeding the energy or electron transfer between the fluorophore and the surrounding matrix. Consequently, You *et al*. prepared synthetic derivatives of GFPs imidazolidinone and oxazolone to remove the scaffold (Figure 5.17). A strong electron-donor group was amalgamated into the molecule in order to increase the electron donating strength.[269] They determined that a wider colour tuneable range was achievable compared to those in the biological system and similar photophysical properties of GFP were achieved. However, the oxazolone derivatives produced notably lower luminance efficiency than those in natural systems in solution but this was improved for solid state OLEDs. Compounds **5.24** and **5.25** were tested in OLEDs and were able to achieve EQEs of 0.3% and 0.2%, respectively. The opportunity to further manipulate naturally occurring materials may result in the development of efficient electronic and optoelectronic applications.

Compound	
5.22	R=R'=H; X=NC$_4$H$_9$
5.23	R=R'=H; X=O
5.24	R=N(CH$_3$)$_2$; R'=H; X=O
5.25	R= N(CH$_3$)$_2$; R'=CN; X=O
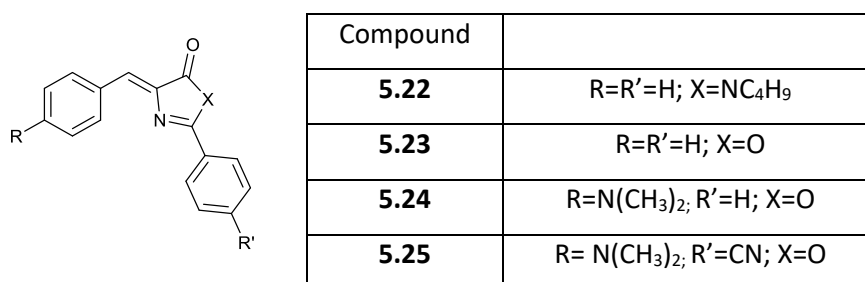
Figure 5.17: Fluorophore structure for imidazolidinone and oxazolone compounds

Synthetic replications of the GFP are known to only produce weak to no fluorescence in both solutions and polymer films.[270] This suggests that the key to achieving the highly emissive state is dependent on the specificity of the surrounding protein matrix.[271] It is customarily recognised that the protein β-barrel backbone increases the quantum yield of the fluorophore by impeding its rotational freedom. Research has been undergone to find an alternative method for restricting the chromophores rotation, without the necessity for the β-barrel skeleton. Some metal-organic frameworks (MOFs) have been found to mimic the protein system and allow for near 100% energy transfer which could lead to a wider range of applications for FPs including organic photovoltaics.[272] Dolgopolova *et al*. prepared a library of *p*-hydroxybenzilidinimidazolinone (HBI)-based chromophores with various electron donating or electron withdrawing groups and identified the

changes in emission profiles gained from the chromophore being inside a rigid MOF matrix (Zn$_3$(BTC)$_2$) or co-ordinately immobilised inside the MOF scaffold Zr$_6$O$_4$(OH)$_4$(BDC-BI)$_6$.[272] The MOF can either preserve or alter the photophysical properties of the chromophore and therefore serve as an efficient platform for achieving high efficiency energy transfer.
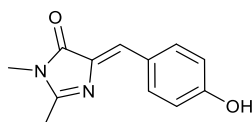
Figure 5.18: HBI chromophore structure

5.2.2 Aims

The aim of this project was to design and synthesise effective fluorescent chromophores using a simple synthetic route for easy reproducibility and upscale for a variety of derivatives. On completion of the syntheses, the aim was to fully characterise the molecules and investigate their optoelectronic and electrochemical properties to determine their suitability for optoelectronic applications. GFPs have previously shown good photoluminescent features and photostability, therefore, their utilisation in OLED devices has been investigated.

Since the flavin derivatives by König and coworkers and the synthesised flavin compound **5.18** showed improved fluorescent properties with extended π-conjugation it was hypothesised that integrating materials, such as fluorene, and anthracene could also benefit the fluorescent properties of the GFP (Figure 5.19).
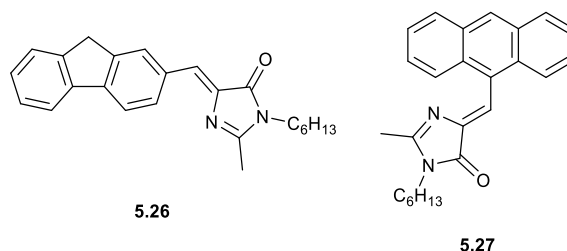
Figure 5.19: Fluorene and anthracene based GFPs

5.2.3 Results and Discussion

5.2.3.1 Target Compound Design

One of the many synthetic routes already identified for synthesising FPs involves the Erlenmeyer azlactone synthesis.[273] The fluorene based azlactone has previously been synthesised by Jiang *et al.* to a moderate yield so these conditions were utilised.[274] The final step would be condensation with a chosen alkylamine to produce the desired imidazolinone chromophore (Scheme 5.8).
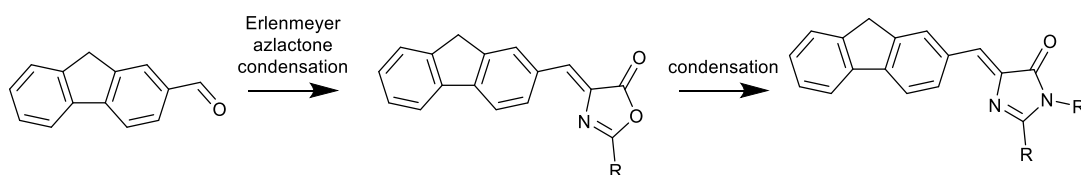
Scheme 5.8: Proposed synthetic route for GFP derivatives (fluorene example shown)

5.2.3.2 Synthesis

The first step in the synthetic route was to produce *N*-acetylglycine (**5.28**) which was achieved by following the literature procedure. Acetylation of glycine occurred when reacted with acetic anhydride in methanol to a modest yield of 62% (Scheme 5.9).[275]
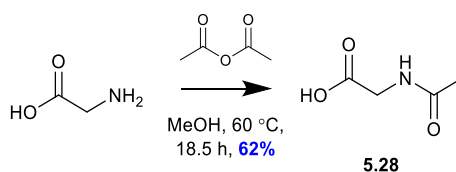
*Scheme 5.9: Synthesis of compound **5.28***

The next step was to synthesise the azlactone, by subjecting fluorene-2-carboxaldehyde to Erlenmeyer azlactone reaction conditions the desired product, compound **5.29**, was attained to a yield of 36% with very minimal purification required. The final step involved the direct condensation with butylamine to form the imidazolinone, compound **5.26** (Figure 5.10). This was found to be an exceedingly challenging synthetic step as multiple impurities were also formed which made isolation of compound **5.29** difficult to achieve. As a result, a variety of conditions were utilised in an endeavour to produce a higher yielding and cleaner product (Table 5.3). Initially, the mild conditions using ethanol were employed, the low solubility of compound **5.29** may have hindered this reaction

138

completion. Consequently, harsher conditions were implemented utilising acetic acid as the solvent which improved solubility. These conditions were more successful as product was identified by NMR. Unfortunately, due to a variety of impurities, isolation of compound **5.26** was not obtained. Finally, reaction of compound **5.29** with imidazole as the solvent was attempted. In order to achieve this, imidazole and compound **5.29** were heated to 130 °C to allow all the imidazole to melt before hexylamine was added. Unlike the previous attempts, isolation of the product material was attained, although to a low yield of 5%. One possible explanation for the difficulty in this synthesis is the formation of 2-acetanido-3-(*9H*-fluoren-2-yl)-*N*-methylacrylamide. It has been noted in the literature that the uncyclized product was produced during alternative GFP derivative synthesis.[276] Lee *et al*. observed that an excess of amine and simple structures were the only samples which could achieve the imidazolinone product by the method attempted above.
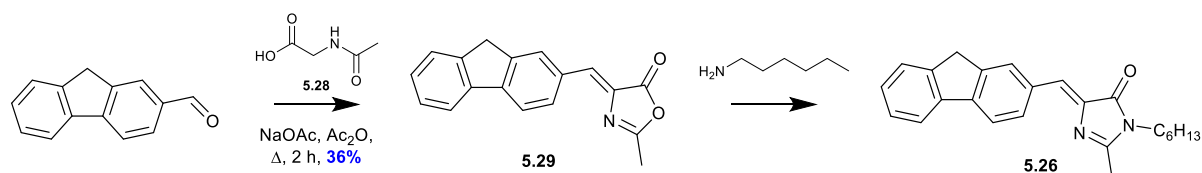
*Scheme 5.10: Synthesis of compound **5.26***

Attempt	Conditions	Yield
1	Potassium carbonate, Ethanol, 75 °C	–
2	Potassium acetate, Acetic acid, 100 °C	–
3	Imidazole, 140 °C	5%

*Table 5.3: Attempted reaction conditions for synthesis of **5.26** and yield achieved*

The azlactone reaction conditions were also utilised in attempting to synthesise the anthracene-based derivative, compound **5.30** (Scheme 5.11). Unlike compound **5.29**, on analysis by TLC a number of impurities were also formed with a similar R$_f$ and, therefore, purification was unsuccessful. As a result of time constraints and the success of compound **5.26** this synthetic route was put on hold to focus on different synthetic targets.
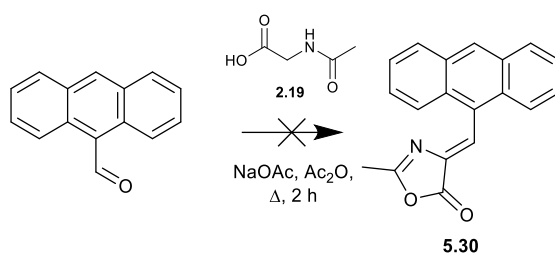
*Scheme 5.11: Attempted synthesis of compound **5.30***

5.2.3.3   Optoelectronic Properties

The UV-Vis and fluorescence properties of compounds **5.29** and **5.26** were studied and recorded in dichloromethane (CH_2Cl_2) with the spectra shown in Figure 5.20 and the data summarised in Table 5.4. Red shift of FPs spectra corresponds to an increase in conjugation and double bonds in the chromophore as well as its planarity.[277] Protonation of the chromophore results in a blue shift in absorbance. Compounds **5.29** and **5.26** have a simple absorption and emission spectra with only one peak observed for each. For the donor-acceptor system of compound **5.29**, the fluorene moiety is the donor and the azlactone ring the acceptor while in compound **5.26** the imidazolinone ring is the acceptor. Increasing conjugation via a coplanar moiety of fluorene facilitates the charge transfer while also causing a bathochromic shift compared to the basic GFP chromophore. For compound **5.29**, the absorption peak appears at 375 nm which correlates to a π-π * transition and the emission peak is observed at 441 nm. A slight bathochromic shift in peak position is detected for compound **5.26** for the absorbance peak, however, a blue shift is observed for the emission peak due to a slight vibrational satellite shoulder appearing in this spectrum correlating to a π-π* transition. Comparing absorbance and emission of compounds **5.29** and **5.26** it is noted that the absorbance has a greater intensity for compound **5.29**, while the emission is more intense for compound **5.26** thus implying that compound **5.26** would be more effective as a fluorescent material in devices.
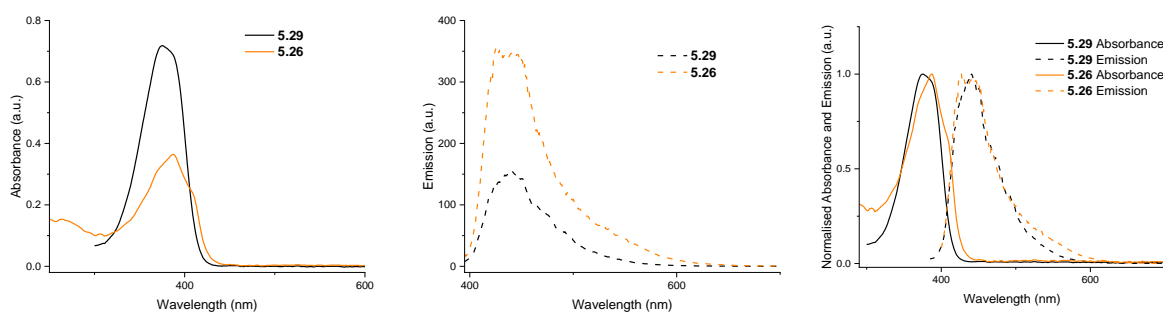
*Figure 5.20: Left to right: Absorption spectra, fluorescence spectra and combined normalised absorption (solid line)/fluorescence (dashed line) of **5.29** (black) and **5.26** (orange) in solution (c = 1 × 10⁻⁵ M in CH₂Cl₂)*

Compound	λ_{max} (nm)	λ_{onset} (nm)	$E_{g, opt}$ (eV)	Emission (nm)	Stokes Shift (nm/cm^{-1})
5.29	375	414	3.00	441	66/3991
5.26	387	425	2.92	427	40/2421

*Table 5.4: Summary of the optoelectronic properties of GFP chromophores **5.29** and **5.26**. $E_{g, opt}$ estimated from λ_{onset} of absorption.*

FPs related to GFP are thought to undergo Z/E isomerisation between the fluorescent and dark states. Generally, the Z form is the resting fluorescent form while the E form is nonfluorescent. This means that without the rigidity of the β-barrel the chromophore can switch forms resulting in "blinking".[278] The fluorescence emission of GFP is known to be considerably influenced by hydrogen bonding between the core fluorophore and the surrounding side chains or water molecules.[270]

To observe the effect of hydrogen bonding on compound **5.29**, 1,3-dipropylurea was added in increments (0.5, 1 and 2 equivalents) and the absorbance spectra taken for each (Figure 5.21). The initial addition of the urea derivative caused a decrease in ϵ value from 71800 L mol^{-1} cm^{-1} to 71200 L mol^{-1} cm^{-1}. On addition of a further 0.5 equivalents of 1,3-dipropylurea the ϵ value increases from 72800 to 74000 L mol^{-1} cm^{-1}. On addition of a further 1 equivalent of the urea derivative, the ϵ value increased slightly to 74900 L mol^{-1} cm^{-1}. This shows that the introduction of hydrogen bonding between the two molecules prevented some of the non-radiative relaxation pathways by increasing the rigidity of the molecule. Due to time constraints and minimal sample this test was not repeated for compound **5.26** however, alternative hydrogen bonding materials should be studied to improve the rigidity of the chromophore.
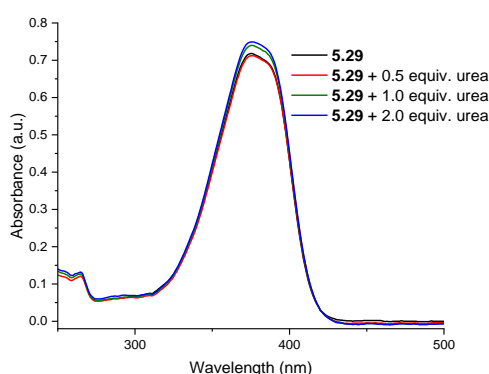
*Figure 5.21: Effect of hydrogen bonding on the absorbance spectra of compound **5.29** by addition of 1,3-dipropylurea*

5.2.3.4 Electrochemical Properties

The electrochemical behaviour of compound **5.29** was studied by CV and SWV in acetonitrile (MeCN), with the spectra shown in Figure 5.22 and the data summarised in Table 5.5. An Ag/AgCl reference electrode was used to provide an internal standard with $E^0 = 0.205$ V. To estimate the IP and EA from the measured redox potentials it was necessary to correlate the electrochemical potentials to the vacuum. It is convenient to use the standard hydrogen electrode (SHE) as the reference for the potential values and the potentials corrected using the vacuum level reference which was initially reported by Trasatti.[279] Trasatti determined the energy corresponding to the SHE was 4.6 ± 0.1 eV on the zero vacuum level scale. For the Ag/AgCl electrode the energy is 4.4 ± 0.1 eV.

On recording the cathodic sweep for compound **5.29** solution (1×10^{-4} M), no redox properties were observed. Consequently, a 1×10^{-3} M solution was made which produced a minor quasi-reversible reduction peak at −1.53 V. Similar to the optoelectronic experiments, the CV and SWV had 0.5 and 1 equivalents of 1,3-dipropylurea added, no effect was visible for the 0.5 equivalent addition (Figure 5.23). On addition of 1 equivalent of 1,3-dipropylurea the graph changed slightly but this is likely due to the 1,3-dipropylurea rather than interaction with compound **5.29**. As a result, the application of compound **5.29** would likely be ineffective in optoelectronic devices and therefore further research into compound **5.26** were performed.
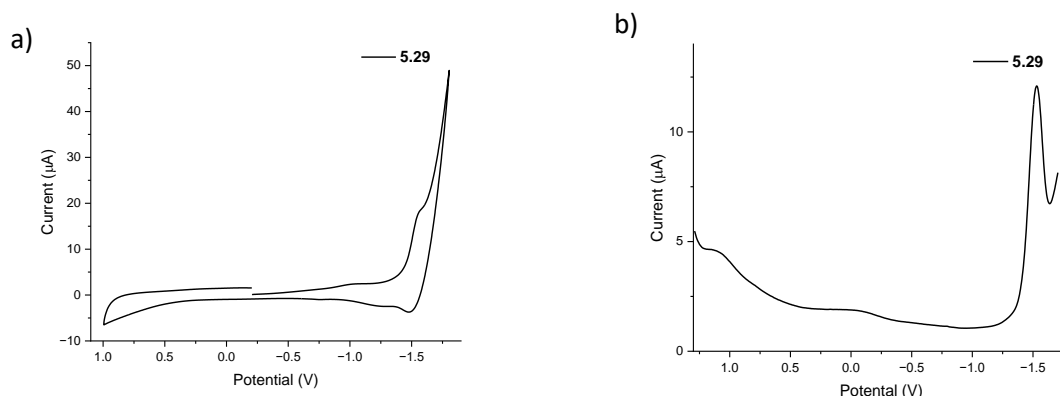
*Figure 5.22: a) CV and b) SWV internally referenced to Ag/AgCl for azlactone derivative **5.29** in solution (c = 1 × 10⁻³ M, in MeCN) with a scan rate of 0.1 Vs⁻¹, performed using a Pt disk working electrode, a Pt wire counter electrode and a Ag/AgCl reference electrode. TBAPF₆ (0.1 M) was used as supporting electrolyte and the redox potential of the Ag/AgCl couple as internal standard.*

Compound	E_{red} (V)	IP (eV)	EA (eV)
5.29	−1.53	−5.87	−2.87

*Table 5.5: Summary of the electrochemical properties of **5.29**. EA and IP calculated using following equations: EA = −[$E^{0.5}_{red}$ −(−5.24)] eV; IP = EA − $E_{g,opt}$*
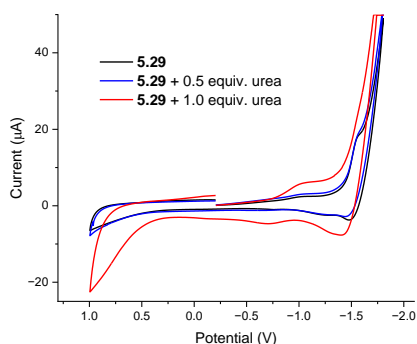
*Figure 5.23: CV with urea internally referenced to Ag/AgCl for azlactone derivative **5.29** in solution (c = 1 × 10⁻³ M, in MeCN) with a scan rate of 0.1 Vs⁻¹, performed using a Pt disk working electrode, a Pt wire counter electrode and a Ag/AgCl reference electrode. TBAPF₆ (0.1 M) was used as supporting electrolyte and the redox potential of the Ag/AgCl couple as internal standard.*

5.2.3.5 Theoretical Studies

The HOMO and LUMO energies of compound **5.26** were calculated using the B3LYP/6-311G(d, p) basis set. The frontier molecular orbitals show planarity throughout the molecule, demonstrating its high conjugation (Figure 5.24). The fundamental energy gap was of a similar value, only 0.42 eV greater, to the $E_{g,\,opt}$ calculated experimentally. The electronic distribution of the LUMO is shifted towards the oxazolinone part while the HOMO is delocalised over the whole molecule.

HOMO: −5.59 eV   LUMO: −2.25 eV

*Figure 5.24: Frontier molecular orbital diagrams with HOMO and LUMO levels for **5.26***

5.2.3.6 New Target Compound Design

A new derivative was designed, attaching a diphenylamine donor group, to the opposite side of the fluorene to the imidazolinone in order to increase the donor-acceptor properties of the molecule which should, in turn, produce a further bathochromic shifted spectrum and hopefully furnish the material with better redox properties. The synthesis was designed around the commercially available 2,7-dibromo-9,9-dimethylfluorene (Scheme 5.12). It was hoped that by performing an one-fold bromine-lithium exchange with *N*, *N*-dimethylformamide followed by Buchwald-Hartwig

amination compound **5.32** would be formed. Compound **5.32** could then undergo the Erlenmeyer azlactone synthesis before the final condensation to produce the desired imidazolinone compound **5.34**.
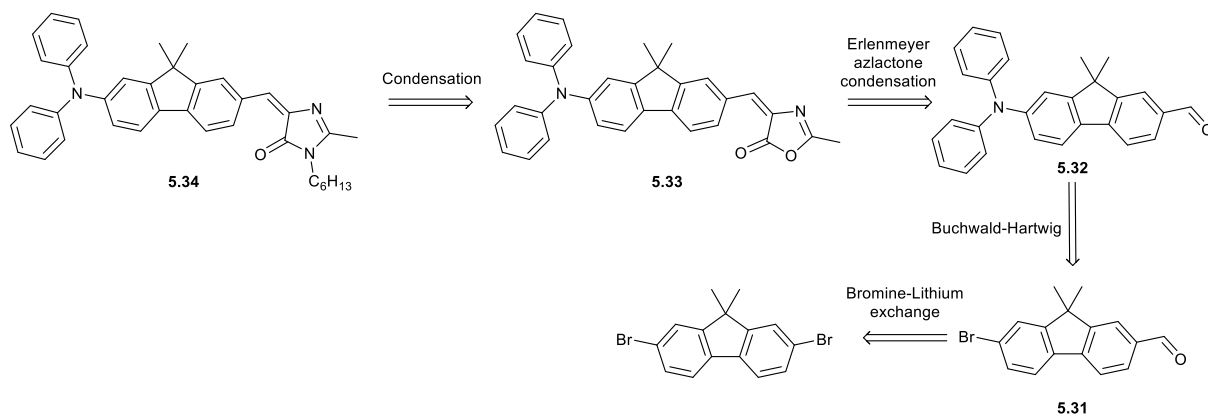
Scheme 5.12: Proposed retrosynthetic analysis of GFP chromophore

5.2.3.7 Synthesis

The initial steps for the synthesis of chromophore compound **5.34** followed the literature procedure by Singh *et al.*[280] First the asymmetric bromine-lithium exchange was performed with *N, N*-dimethylformamide acting as a reagent to form compound **5.31** to a modest yield of 67% (Scheme 5.13).[281] Modified Buchwald-Hartwig conditions were then utilised to produce compound **5.32** to a good yield of 81%.
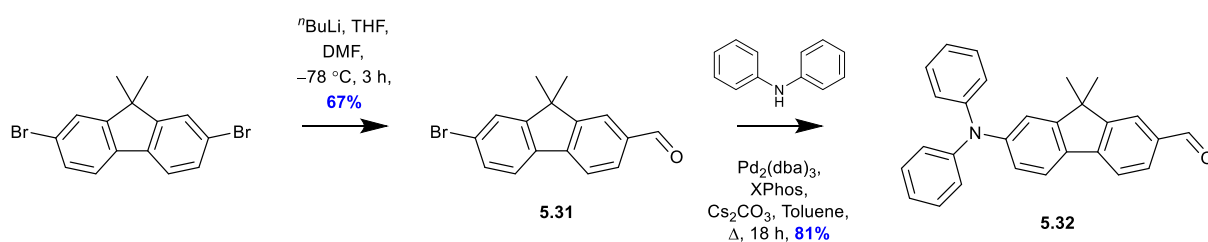
*Scheme 5.13: Synthesis of compound **5.32***

The next stage in the synthesis was to produce compound **5.33** following the same conditions used for synthesising compound **5.29**. Unfortunately, this route was determined to be unsuccessful as starting material was identified as the major compound present on inspection by TLC. Due to time

144

constraints and lack of success it was decided that research into different projects (discussed elsewhere in this thesis) should be the priority.
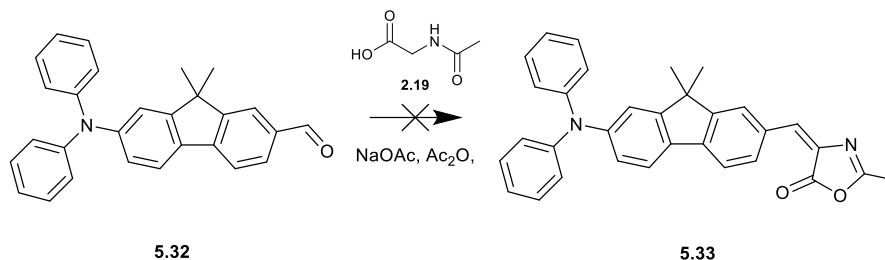
*Scheme 5.14: Attempted synthesis of compound **5.33***

5.2.3.8 Theoretical Studies

Similar to compound **5.26**, the HOMO and LUMO levels were determined by DFT calculations using the basis set the B3LYP/6-311G(d, p). The frontier molecular orbitals are shown in Figure 5.25. The fundamental energy gap is smaller for this material than compound **5.26** at 2.88 eV. Again, the electronic distribution of the LUMO is shifted towards the oxazolinone part, with the diphenylamine having very little effect on the LUMO. However, unlike compound **5.26**, the HOMO is shifted towards the other end of the molecule, namely the diphenylamine donor group. This information confirms the predicted effect of the addition of a donor group as the HOMO level was more effected by the addition than the LUMO.

HOMO: −5.08 eV   LUMO: −2.20 eV

*Figure 5.25: Frontier molecular orbital diagrams with HOMO and LUMO levels for **5.34***

5.2.4 Conclusions and Future Work

Novel GFP chromophores were designed and their synthesis developed. The fluorene azlactone precursor **5.29** had the photophysical and electrochemical properties studied. It was determined that the azlactone derivative did not provide appropriate characteristics, in this freely rotating state, to be effective in optoelectronic devices. Consequently, the oxazolinone derivative compound **5.26**

was successfully synthesised and the photophysical and theoretical properties studied. The oxazolinone had a bathochromic shift in absorption and emission spectra compared to compound **5.29** and produced a more intense emission.

Future work would include taking the optoelectronic experiments in the solid state to determine the effect on the materials properties. Production of the crystal structure would also be useful as it would indicate the preferred isomeric form of the chromophore and thus its preferred fluorescent properties. Finally, hydrogen bonding the chromophore to a protein β-barrel or MOF to retain the desired isomer before characterisation of its optoelectronic and electrochemical properties.

Efforts were made to synthesis a diphenylamine derivative of compound **5.26**. Unfortunately, the attempted route was unsuccessful and due to time constraints was abandoned. Alternative methods have been proposed for the synthesis of compound **5.34**. The uncyclized *N*-alkyl-2-acylamine-3-arylacrylimide could be synthesised from the azlactone before dehydrative cyclisation to form the desired oxazolinone product (Scheme 5.15). Another method would be to start with compound **5.32** and only cyclise the material at the final step.[282]
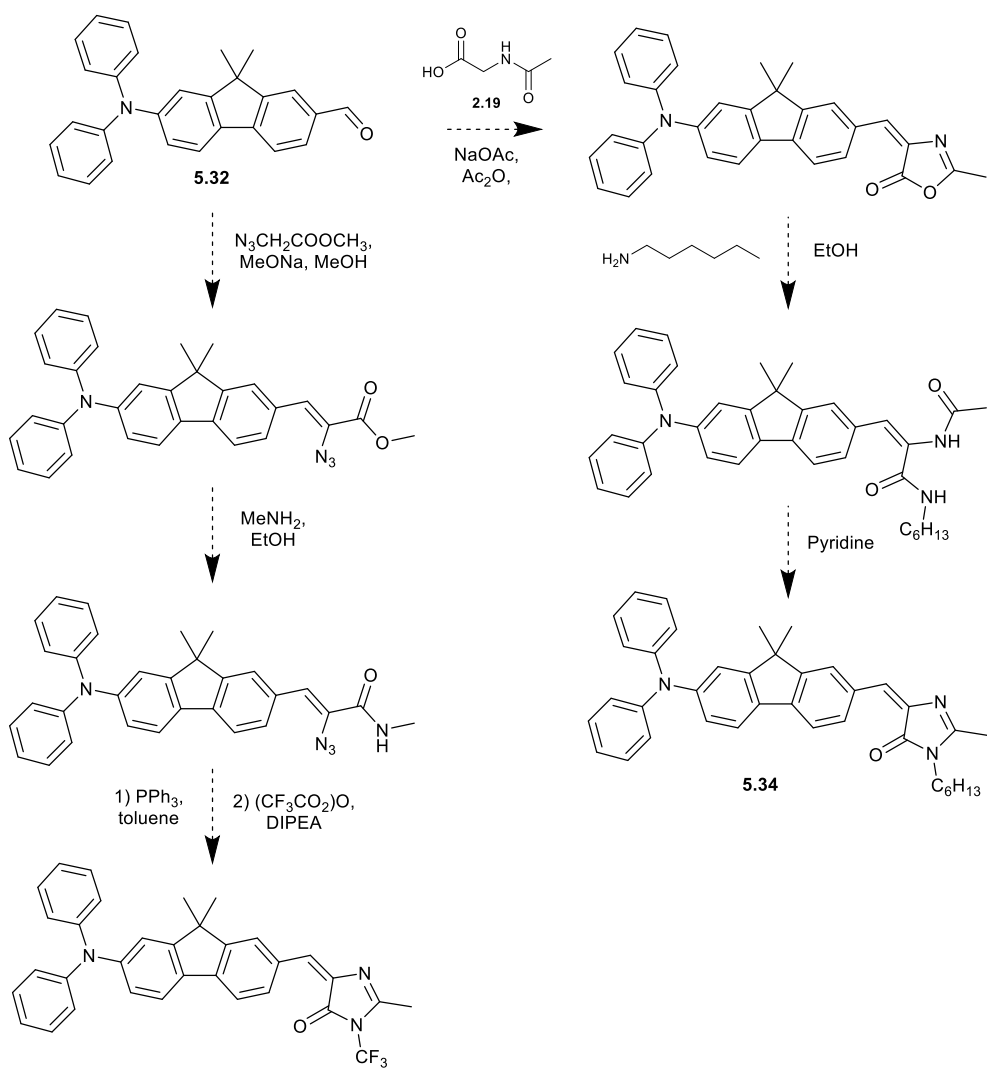
Scheme 5.15: Proposed future synthetic routes for GFP targets

6 Experimental

6.1 General Experimental

All reagents and starting materials were obtained from commercial sources and used as received. *n*-Butyllithium solutions were purchased from Sigma Aldrich and titrated either against (+)−menthol (with 1,10-Phenanthroline as an indicator) acid before use. Flash column chromatography was carried out using silica gel (Sigma-Aldrich® or Fluorochem®) 40–63 nm 60 Å. The solvent system is specified in each experiment. Merck silica gel 60 covered aluminium plates F254 were used for thin layer chromatography and visualised by staining with $KMnO_4$ or vanillin. Dry solvents were obtained either Innovative Technology inc. Pure Solv 400-5-MD^{TM} solvent purification system (activated alumina columns) or Sigma Aldrich®. Reaction temperatures: room temperature refers to 20–25 °C. Other temperatures were obtained using a temperature controlled hot plate, an ice-water bath for 0 °C, and an acetone-dry ice bath for −78 °C.

Mass spectrometry and elemental analysis were obtained from the mass spectrometry service at the University of Glasgow. Melting points (mp) were recorded on a SMP-10 Stuart Scientific melting point machine. Melting points are uncorrected. NMRs were recorded on either Bruker Avance III 400 or Bruker Avance III 500 spectrometers. ^{1}H and ^{13}C NMR spectra were obtained with a Bruker AVIII 400 MHz spectrometer with chemical shift values in ppm relative to TMS (δ_H 0.00 and δ_C 0.0). Proton and carbon assignments are based on two-dimensional COSY and DEPT experiments, respectively. NMR spectra were analysed using MNova® (licensed edition). Signals in ^{1}H-NMR spectra are described as singlet (s), doublet (d), triplet (t), quartet (q), quintet (quint), multiplet (m), broad (b) or a combination of these, which refers to the spin-spin coupling pattern observed. DEPT NMR spectroscopy was used where appropriate to assist the assignment of signals of ^{13}C NMR spectra. Infrared spectroscopy were performed on a Shimadzu IRAffinity-1S Fourier Transform Infrared Spectrophotometer. Electrochemistry was performed using a CH Instrument Electrochemical Workstation (CHI 440a), Austin, TX, USA. Samples were analysed at 1.0 mM concentrations with a scan rate of 0.1 V/s, unless specified, using tetrabutylammonium hexafluorophosphate (0.1 M in corresponding solvent) as the supporting electrolyte and were purged with nitrogen gas for 3 minutes prior to recording the electrochemical data. A platinum disk working electrode, a platinum wire counter electrode and a silver wire pseudo reference electrode were used for all measurements. The reduction potentials are referred to ferrocene (internal or external reference) with the Fc/Fc+ redox couple adjusted to 0.00 V. Absorbance spectrometry was performed using a Shimadzu UV-3600 UV-Vis-NIR spectrophotometer and a Perkin Elmer Lambda 25 UV/Vis

Spectrometer. Optical band gaps (Eg_{opt}) were estimated using the onset of the longest wavelength absorption (λ_{onset}) using Eg_{opt} (eV) = (1240/ λ_{onset}). The electron affinity (EA) was calculated using the calculated ionisation potential (IP) and Eg_{opt} using EA = IP − Eg_{opt}. Qualitative fluorescence spectroscopy was performed using a Shimadzu RF-5301PC168 spectrofluorophotometer. All the spectroscopic and electrochemical data were processed using Origin Pro 8.5 software suite.

Calculations were performed using Gaussian '09 software suites.[283] Molecular geometries were initially optimized semi-empirically (PM6)[284,285] and then re-optimized by DFT (B3LYP/6- 311G d,p).[286–288] Energy minima were confirmed by the absence of imaginary frequencies from vibrational frequency calculations. To facilitate the convergence of the geometry optimizations, in molecules where long alkyl chains were present the alkyl chains were replaced by methyl units.

Gel Permeation Chromatography (GPC) was performed using a Shimadzu HPLC system that includes: a Shimadzu DGU-20A5R degassing unit, a Shimadzu LC-20AT prominence liquid chromatograph, a Shimadzu CTO-20A prominence column oven and a Shimadzu RID-20A refractive index detector. The columns used were two Agilent PLgel 5 µm Mixed-D 300×7.5 mm and Agilent PLgel Guard 50×7.5 mm. The calibration was performed with a set of PMMA samples with narrow distributed molecular weights.

6.2 Experimental Procedures

2,2',7,7'-Tetrabromo-9,9'-spirobifluorene (2.9)[289]

To a mixture of 9,9'-spirobifluorene (1.00 g, 3.16 mmol) and sodium bromide (5.21 g, 50.6 mmol) in 1,2-dichloroethane (5 mL) was added a solution of 10% sulfuric acid (20 mL), To this, a solution of 35% hydrogen peroxide (1.78 mL) was added slowly. The resulting mixture was stirred at room temperature for 40 h, then poured in ice-water (50 mL) and allowed to warm to room temperature while stirring. The organic fraction was extracted with dichloromethane (3 × 100 mL) and the combined organic layers were washed with water (3 × 150 mL), dried over MgSO$_4$, filtered and concentrated *in vacuo*. The crude product was purified by flash column chromatography on silica gel, eluting with 10% dichloromethane in petroleum ether to produce 2,2',7,7'-tetrabromo-9,9'-spirobifluorene (**2.9**) (1.97 g, 98%) as a white solid. R$_f$ 0.27 (10% dichloromethane in petroleum ether); δ$_H$ (400 MHz, CDCl$_3$) 7.68 (4H, d, J 8.2 Hz, 4 × ArH), 7.54 (4H, dd, J 8.2, 1.8 Hz, 4 × ArH), 6.83 (4H, d, J 1.8 Hz, 4 × ArH); δ$_C$ (101 MHz, CDCl$_3$) 149.0 (4 × C), 139.7 (4 × C), 131.9 (4 × CH), 127.5 (4 × CH), 122.3 (4 × C), 121.8 (4 × CH), 65.3 (C); *m/z* (EI) 636 (18), 634 (68), 632 (M$^+$, 100), 630 (66), 628 (17).

(4-Bromophenoxy)(*tert*-butyl)dimethylsilane (2.10)[290]
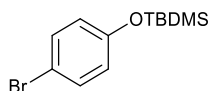
4-Bromophenol (10.0 g, 57.8 mmol) was dissolved in *N*, *N*-dimethylformamide (80 mL) and cooled to 0 °C before imidazole (6.69 g, 98.3 mmol) and *tert*-butyldimethylsilyl chloride (13.1 g, 86.7 mmol). The mixture was then warmed to room temperature and stirred for 4 h. The resulting mixture was then cooled to 0 °C, quenched with a saturated ammonium chloride solution (50 mL), extracted with diethyl ether (3 × 100 mL) and washed with water (150 mL). The combined organic layers were then dried over MgSO$_4$, filtered and concentrated *in vacuo*. The crude product was purified by flash column chromatography on silica gel, eluting with 100% petroleum ether to produce (4-bromophenoxy)(*tert*-butyl)dimethylsilane (**2.10**) (16.4 g, 99%) as a colourless oil. R$_f$ 0.32 (100% petroleum ether); δ$_H$ (400 MHz, CDCl$_3$) 7.32 (2H, d, J 8.8 Hz, 2 × ArH), 6.71 (2H, d, J 8.8 Hz, 2 × ArH), 0.97 (9H, s, 3 × CH$_3$), 0.18 (6H, s, 2 × CH$_3$); δ$_C$ (101 MHz, CDCl$_3$) 155.0 (C), 132.4 (2 × CH), 122.1 (2 × CH), 113.8 (C), 25.8 (3 × CH$_3$), 18.4 (C), −4.3 (2 × CH$_3$); *m/z* (EI) 288 (M$^+$, 40%), 231 (100), 229 (97), 150 (22), 135 (19).

4-((tert-Butyldimethylsilyl)oxy)-*N*-(4-methoxyphenyl)aniline (2.11)[291]
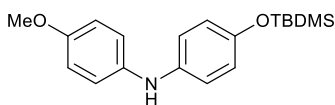
(4-Bromophenoxy)(*tert*-butyl)dimethylsilane (**2.10**) (5.00 g, 17.4 mmol), *p*-anisidine (2.36 g, 19.2 mmol), sodium *tert*-butoxide (2.34 g, 24.4 mmol), tris(dibenzylideneacetone)dipalladium (0) (638 mg, 0.698 mmol) and 2-dicyclohexylphosphino-2',4',6'-triisopropylbiphenyl (664 mg, 1.39 mmol) were suspended in dry toluene (125 mL). The mixture was degassed under argon before being heated to 90 °C for 16 h. The reaction was then cooled to room temperature, diluted with ethyl acetate (50 mL) and washed with water (3 × 100 mL). The organic extract was then dried over MgSO$_4$, filtered and concentrated *in vacuo*. The crude product was purified by flash column

chromatography on silica gel, eluting with 10% diethyl ether in petroleum ether to produce 4-((*tert*-butyldimethylsilyl)oxy)-*N*-(4-methoxyphenyl)aniline (**2.11**) (4.72 g, 82%) as a pink/grey solid. R_f 0.23 (10% diethyl ether in petroleum ether); δ_H (400 MHz, MeOD) 6.95 (2H, d, *J* 9.0 Hz, 2 × ArH), 6.87 (2H, d, *J* 9.0 Hz, 2 × ArH), 6.80 (2H, d, *J* 9.0 Hz, 2 × ArH), 6.70 (2H, d, *J* 9.0 Hz, 2 × ArH), 3.74 (3H, s, OMe), 0.99 (9H, 3 × CH$_3$), 0.17 (6H, s, 2 × CH$_3$); δ_C (101 MHz, MeOD) 155.4 (C), 150.3 (C), 140.8 (C), 139.7 (C), 121.5 (2 × CH), 120.5 (2 × CH), 119.5 (2 × CH), 115.6 (2 × CH), 56.0 (CH$_3$), 26.2 (3 × CH$_3$), 19.0 (C), -4.3 (2 × CH$_3$); *m/z* (ESI) 330.1871 ([M + H]$^+$ C$_{19}$H$_{28}$NO$_2$Si requires 330.5167).

N7-4-((*tert*-Butyldimethylsilyl)oxy)phenyl-*N2,N2,N2',N2',N7,N7',N7'*-heptakis(4-methoxyphenyl)-9,9'-spirobi(fluorene)-2,2',7,7'-tetramine (2.12)[130]
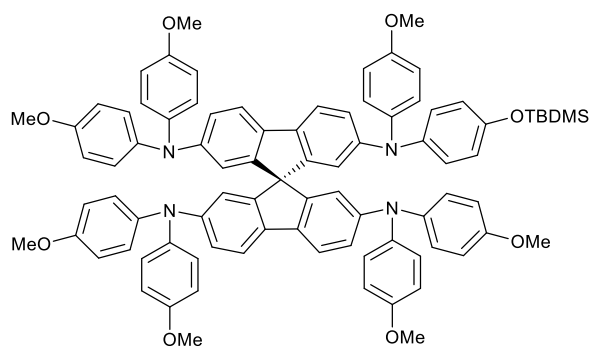
2,2′,7,7′-Tetrabromo-9,9′-spirobifluorene (**2.9**) (750 mg, 1.19 mmol), 4,4′-dimethoxydiphenylamine (818 mg, 3.57 mmol), 4-((*tert*-butyldimethylsilyl)oxy)-*N*-(4-methoxyphenyl)aniline (**2.11**) (588 mg, 1.79 mmol), sodium *tert*-butoxide (480 mg, 5.00 mmol), tris(dibenzylideneacetone)dipalladium (0) (44.0 mg, 0.048 mmol), 2-dicyclohexylphosphino-2′,4′,6′-triisopropylbiphenyl (45 mg, 0.095 mmol) were dissolved in dry toluene (4 mL). The mixture was degassed under argon before being left to stir at 110 °C for 19 h. The reaction was cooled to room temperature before being extracted with ethyl acetate (3 × 25 mL) and washed with water/brine (3 × 50 mL). The combined organic layers were then dried over MgSO$_4$, filtered and concentrated *in vacuo*. The crude product was purified by flash column chromatography on silica gel, eluting with 30% ethyl acetate in petroleum ether to produce *N*7-4-((*tert*-butyldimethylsilyl)oxy)phenyl-*N2,N2,N2',N2',N7,N7',N7'*-heptakis(4-methoxyphenyl)-9,9'-spirobi(fluorene)-2,2',7,7'-tetramine (**2.12**) (475 mg, 30%) as an off-white solid. R_f 0.32 (10% ethyl acetate in petroleum ether); δ_H (400 MHz, C$_6$D$_6$) 7.14–7.10 (2H, m, 2 × ArH), 7.10–6.94 (26H, m, 26 × ArH), 6.85–6.77 (2H, m, 2 × ArH), 6.77–6.68 (14H, m, 14 × ArH), 3.26 (21H, s, 7 × CH$_3$), 1.00 (9H, s, 3 ×

CH$_3$), 0.13 (6H, s, 2 × CH$_3$); δ$_C$ (101 MHz, C$_6$D$_6$) 156.0 (7 × C), 151.4 (C), 150.9 (4 × C), 148.2 (4 × C), 142.8 (C), 142.0 (7 × C), 135.9 (4 × C), 128.7 (2 × CH), 125.9 (14 × CH), 125.4 (4 × CH), 122.9 (2 × CH), 120.9 (4 × CH), 118.3 (4 × CH), 115.0 (16 × CH), 66.5 (C), 55.0 (7 × CH$_3$), 26.0 (3 × CH$_3$), 18.5 (C), -4.3 (2 × CH$_3$); *m/z* (FAB$^+$) 1324.5760 (M$^+$ C$_{86}$H$_{80}$N$_4$O$_8$Si requires 1324.5745).

4-((4-Methoxyphenyl)((2,2',7'-tris(bis(4-methoxyphenyl)amino)-9,9'-spirobi(fluoren)-7-yl))amino)phenol (2.13)[130]
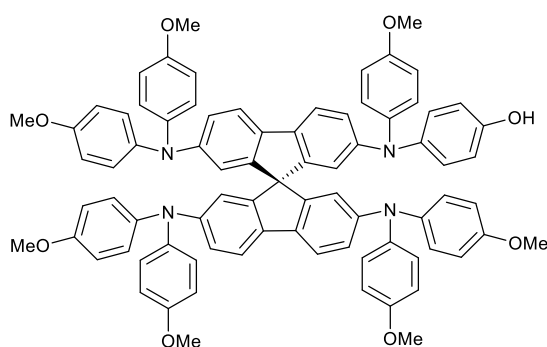

*N*7-4-((*tert*-Butyldimethylsilyl)oxy)phenyl-*N*2,*N*2,*N*2',*N*2',*N*7,*N*7',*N*7'-heptakis(4-methoxyphenyl)-9,9'-spirobi(fluorene)-2,2',7,7'-tetramine (**2.12**) (200 mg, 0.150 mmol) was dissolved in dry tetrahydrofuran (2 mL) and left to stir before a solution of 1.0 M tetra-*N*-butylammonium fluoride in tetrahydrofuran (0.30 mL, 0.30 mmol) was added. The reaction mixture was left to stir at 70 °C for 30 minutes before being concentrated *in vacuo*. The crude product was purified by flash column chromatography on silica gel, eluting with 50% ethyl acetate in petroleum ether to produce 4-((4-methoxyphenyl)((2,2',7'-tris(bis(4-methoxyphenyl)amino)-9,9'-spirobi(fluoren)-7- yl))amino)phenol (**2.13**) (171 mg, 94%) as an off-white solid. R$_f$ 0.16 (40% ethyl acetate in petroleum ether); δ$_H$ (400 MHz, C$_6$D$_6$) 7.17–7.06 (8H, m, 8 × ArH), 7.07–6.94 (20H, m, 20 × ArH), 6.81–6.57 (16H, m, 16 × ArH), 3.25 (21H, s, 7 × CH$_3$); δ$_C$ (101 MHz, C$_6$D$_6$) 155.9 (8 × C), 150.9 (4 × C), 148.2 (4 × C), 142.0 (8 × C), 135.9 (4 × C), 128.7 (2 × CH), 125.8 (14 × CH), 123.0 (4 × CH), 120.7 (4 × CH), 118.4 (4 × CH), 114.9 (16 × CH), 66.5 (C), 54.9 (7× CH$_3$); *m/z* (FAB$^+$) 121.04915 (M$^+$ C$_{80}$H$_{66}$N$_4$O$_8$ requires 1210.4881).

2-[2-(2-Iodoethoxy)ethoxy]ethanol (2.14)[292]
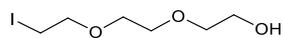
To a solution of 2-[2-(2-chloroethoxy)ethoxy]ethanol (1.00 g, 5.93 mmol) in acetone (10 mL) was added sodium iodide (1.78 g, 11.9 mmol). The reaction mixture was left to stir at reflux for 19 h before being cooled to room temperature, filtered and the filtrate concentrated *in vacuo*. The crude product was then extracted with diethyl ether (3 × 50 mL) and washed with water (100 mL). The combined organic layers were then dried over MgSO$_4$, filtered and concentrated *in vacuo* to produce 2-[2-(2-iodoethoxy)ethoxy]ethanol (**2.14**) (1.49 g, 97%) as a pale yellow oil. R$_f$ 0.2 (30% ethyl acetate in petroleum ether); δ_H (400 MHz, CDCl$_3$) 3.79–3.69 (4H, m, 2 × CH$_2$), 3.70–3.64 (4H, m, 2 × CH$_2$), 3.64–3.57 (2H, m, CH$_2$), 3.26 (2H, t, *J* 6.8 Hz, CH$_2$); δ_C (101 MHz, CDCl$_3$) 72.6 (CH$_2$), 72.0 (CH$_2$), 70.5 (CH$_2$), 70.3 (CH$_2$), 61.9 (CH$_2$), 2.8 (CH$_2$), *m/z* (ESI) 282.9801 ([M + Na]$^+$ C$_6$H$_{13}$IO$_3$Na requires 282.9809).

2-[2-(2-Iodoethoxy)ethoxy]ethyl methacrylate (2.15)[293]
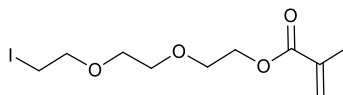
2-[2-(2-Iodoethoxy)ethoxy]ethanol (**2.14**) (1.00 g, 3.84 mmol), methacrylic anhydride (572 μL, 3.84 mmol), 4-dimethylaminopyridine (5 mg, 0.038 mmol) and triethylamine (588 μL, 4.22 mmol) were combined and left to stir at room temperature for 17 h before methanol (1 mL) was added and the reaction mixture stirred for 1 h. The reaction mixture was then quenched with saturated ammonium chloride solution (1 mL), extracted with dichloromethane (3 × 15 mL) and washed with water (50 mL). The combined organic layers were then dried over MgSO$_4$, filtered and concentrated *in vacuo*. The crude product was then purified by flash column chromatography on silica gel, gradient elution 20% ethyl acetate in petroleum ether to 30% ethyl acetate in petroleum ether to produce 2-[2-(2-iodoethoxy)ethoxy]ethyl methacrylate (**2.15**) (558 mg, 44%) as a yellow oil. R$_f$ 0.48 (60% ethyl acetate in petroleum ether); δ_H (400 MHz, CDCl$_3$) 6.13 (1H, dq, J 2.0, 1.0 Hz, alkene H), 5.58 (1H, p, J 2.0 Hz, alkene H), 4.34–4.27 (2H, m, CH$_2$), 3.81–3.71 (4H, m, 2 × CH$_2$), 3.69–3.66 (4H, m, 2 × CH$_2$),

3.29–3.21 (2H, m, CH$_2$), 1.99–1.93 (3H, m, CH$_3$); δ$_C$ (101 MHz, CDCl$_3$) 167.5 (C), 136.3 (C), 125.9 (CH$_2$), 72.2 (CH$_2$), 70.8 (CH$_2$), 70.4 (CH$_2$), 69.4 (CH$_2$), 64.0 (CH$_2$), 18.5 (CH$_3$), 2.9 (CH$_2$); *m/z* (ESI) 351.0077 ([M + Na]$^+$ C$_{10}$H$_{17}$IO$_4$Na requires 351.0072).

2-(2-(2-(4-((4-Methoxyphenyl)(2,2',7'-tris(bis(4-methoxyphenyl)amino)-9,9'-spirobi[fluoren]-7-yl)amino)phenoxy)ethoxy)ethoxy)ethanol (2.17)
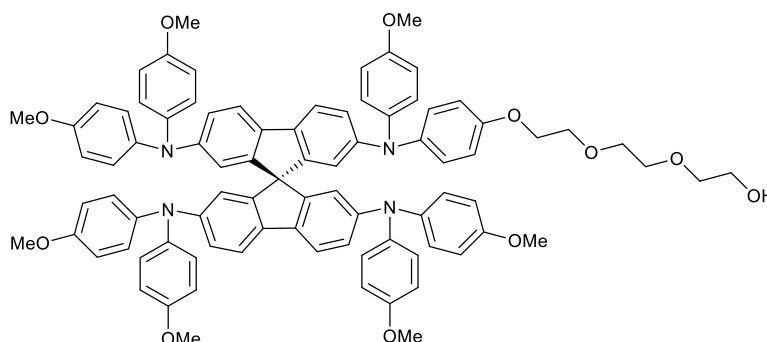
4-((4-Methoxyphenyl)((2,2',7'-tris(bis(4-methoxyphenyl)amino)-9,9'-spirobi(fluoren)-7-yl))amino)phenol (**2.13**) (500 mg, 0.410 mmol) and sodium hydride (82.0 mg, 2.05 mmol, 60% dispersion in mineral oil) were dissolved in *N*, *N*-dimethyl formamide (24 mL). The reaction mixture was left to stir at 60 °C for 1 h before 2-[2-(2-iodoethoxy)ethoxy]ethanol (**2.14**) (161 mg, 0.620 mmol) in *N*, *N*-dimethyl formamide (1 mL) was added. The reaction mixture was then left to stir at 60 °C for 19 h before being cooled to room temperature, extracted with ethyl acetate (3 × 50 mL) and washed with water (100 mL). The combined organic layers were then dried over MgSO$_4$, filtered and concentrated *in vacuo* to produce 2-(2-(2-(4-((4-methoxyphenyl)(2,2',7'-tris(bis(4-methoxyphenyl)amino)-9,9'-spirobi[fluoren-7-yl)amino)phenoxy)ethoxy)ethoxy)ethanol (**2.17**) (301 mg, 55%) as an off-white solid. R$_f$ 0.32 (100% ethyl acetate); ν$_{max}$/cm^{-1} (neat) 2952 (CH), 2360, 1591 (C=C), 1500, 1237(CO), 1165, 1028 (CO), 825; δ$_H$ (400 MHz, C$_6$D$_6$) 7.14 (4H, d, J 6.6 Hz, 4 × ArH), 7.07 (4H, d, J 2.1 Hz, 4 × ArH), 7.06–6.95 (22H, m, 22 × ArH), 6.78 (2H, d, J 9.0 Hz, 2 × ArH), 6.79–6.69 (12H, m, 12 × ArH), 3.76–3.66 (2H, m, CH$_2$), 3.55–3.48 (2H, m, CH$_2$), 3.46 (2H, dd, J 5.7, 4.0 Hz, CH$_2$), 3.41–3.31 (4H, m, 2 × CH$_2$), 3.32–3.22 (23H, m, CH$_2$ and 7 × CH$_3$); δ$_C$ (101 MHz, C$_6$D$_6$) 157.5 (7 × C), 156.0 (C), 150.9 (4 × C), 148.2 (4 × C), 142.0 (8 × C), 135.2 (4 × C), 128.7 (4 × CH), 125.8 (14 × CH), 123.0 (4 × CH), 120.7 (4 × CH), 118.4 (4 × CH), 115.0 (14 × CH), 72.8 (CH$_2$), 71.1 (2 × CH$_2$), 70.6 (CH$_2$),

67.8 (CH$_2$), 65.4 (C), 60.9 (CH$_2$), 55.0 (7 × CH$_3$); *m/z* (ESI) 1365.5583 ([M + Na]$^+$ C$_{86}$H$_{78}$N$_4$O$_{11}$Na requires 1365.5567).

2-(2-(2-(4-((4-Methoxyphenyl)(2,2',7'-tris(bis(4-methoxyphenyl)amino)-9,9'-spirobi[fluoren]-7-yl)amino)phenoxy)ethoxy)ethoxy)ethyl methacrylate (2.18)

2-(2-(2-(4-((4-Methoxyphenyl)(2,2',7'-tris(bis(4-methoxyphenyl)amino)-9,9'-spirobi[fluoren]-7-yl)amino)phenoxy)ethoxy)ethoxy)ethanol (**2.17**) (1.50 g, 1.12 mmol), methacrylic anhydride (167 µL, 1.12 mmol), 4-dimethylaminopyridine (1.4 mg, 0.011 mmol) and triethylamine (171 µL, 1.23 mmol) were combined and left to stir at room temperature for 17 h before methanol (6 mL) was added and the reaction mixture stirred for 1 h. The reaction mixture was then quenched with saturated ammonium chloride solution (5 mL), extracted with dichloromethane (3 × 30 mL) and washed with water (100 mL). The combined organic layers were then dried over MgSO$_4$, filtered and concentrated *in vacuo*. The crude product was then purified by flash column chromatography on silica gel, gradient elution 20% ethyl ace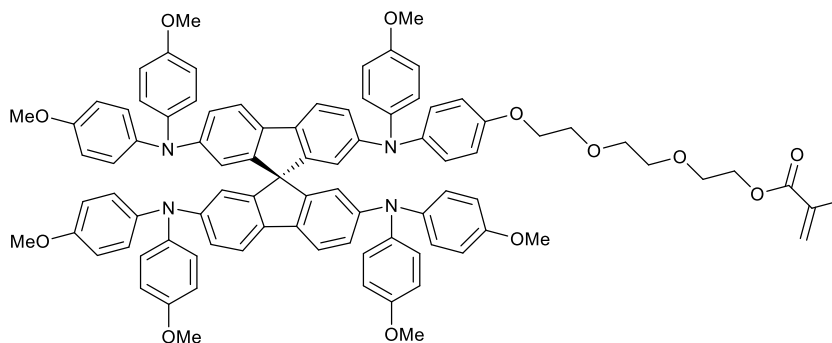tate in petroleum ether to 30% ethyl acetate in petroleum ether to produce 2-(2-(2-(4-((4-Methoxyphenyl)(2,2',7'-tris(bis(4-methoxyphenyl)amino)-9,9'-spirobi[fluoren]-7-yl)amino)phenoxy)ethoxy)ethoxy)ethyl methacrylate (**2.18**) (1.10 g, 55%) as an off-white solid. R$_f$ 0.49 (60% ethyl acetate in petroleum ether); δ$_H$ (400 MHz, C$_6$D$_6$) 7.14 (2H, d, *J* 2.3 Hz, 2 × ArH), 7.07 (4H, d, *J* 2.3 Hz, 4 × ArH), 7.06–6.96 (22H, m, 22 × ArH), 6.80–6.71 (16H, m, 16 × ArH), 6.16 (1H, dqf, J 2.0, 1.0, alkene H), 5.19 (1H, p, J 2.0 Hz, alkene H), 4.21–4.12 (2H, m, CH$_2$), 3.78–3.69 (2H, m, CH$_2$), 3.54–3.46 (2H, m, CH$_2$), 3.45–3.38 (2H, m, CH$_2$), 3.38–3.32 (4H, m, 2 × CH$_2$), 3.30–3.24 (21H, m, 7 × CH$_3$), 1.85–1.80 (3H, m, CH$_3$); δ$_C$ (101 MHz, C$_6$D$_6$) 156.0 (7 × C), 155.1 (C), 150.9 (4 × C), 148.2 (4 × C), 142.0 (8 × C), 135.9 (4 × C), 128.7 (14 × CH), 125.8 (CH$_2$, alkene), 125.3 (2 × CH), 123.0 (4 × CH), 120.7 (4 × CH), 118.4 (4 × CH), 115.6 (4 × CH), 115.0 (14 × CH), 71.0 (CH$_2$), 70.9

(CH$_2$), 70.0 (CH$_2$), 69.4 (CH$_2$), 67.8 (CH$_2$), 66.5 (C), 64.0 (CH$_2$), 55.0 (7 × CH$_3$), 18.4 (CH$_3$); *m/z* (ESI) 1433.5823 ([M + Na]$^+$ C$_{90}$H$_{82}$N$_4$NaO$_{12}$ requires 1433.5829).

Poly[2-(2-(2-(4-((4-Methoxyphenyl)(2,2',7'-tris(bis(4-methoxyphenyl)amino)-9,9'-spirobi[fluoren]-7-yl)amino)phenoxy)ethoxy)ethoxy)ethyl methacrylate] (2.19)

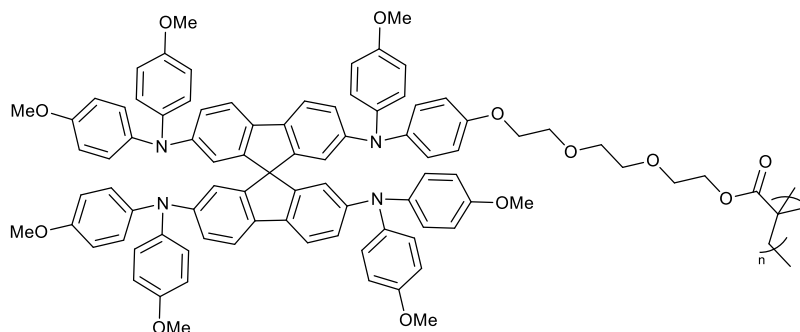A 2 mL microwave vial and stirrer bar were oven dried and then charged with 2-(2-(2-(4-((4-methoxyphenyl)(2,2',7'-tris(bis(4-methoxyphenyl)amino)-9,9'-spirobi[fluoren]-7-yl)amino)phenoxy)ethoxy)ethoxy)ethyl methacrylate (**2.18**) (500 mg, 0.350 mmol). The flask was then subjected to three vacuum/nitrogen filling steps. A stock solution of 2,2'-azobis(2-methylpropronitrile) (10 mg, 0.06 mmol) in dry *N*, *N*-dimethylformamide (1 mL) was made. To the reaction flask was added stock solution (0.2 mL). The reaction was degassed for 5 minutes before being left to stir at 70 °C for 22 h. The reaction mixture was then cooled to room temperature before *N*, *N*-dimethylformamide (30 mL) added and concentrated *in vacuo*. The reaction mixture was dissolved in ethyl acetate (10 mL) and the polymer was precipitated by dropwise addition into petroleum ether (300 mL). The precipitate was collected by vacuum filtration to produce the 100 mol% polymer (**2.19**) (318 mg, 64%) as pale-yellow solid. δ$_H$ (400 MHz, C$_6$D$_6$) 7.09–6.87 (28H, m, 28 × ArH), 6.80–6.66 (16H, m, 16 × ArH), 4.15 (2H, br, CH$_2$), 3.90 (2H, br, CH$_2$), 3.59 (8H, br, 4 × CH$_2$), 3.45–3.19 (21H, m, 7 × CH$_3$), 1.46–1.26 (3H, m, CH$_3$); M$_n$=94581; M$_w$/M$_n$=1.60

Poly[2-(2-(2-(4-((4-Methoxyphenyl)(2,2',7'-tris(bis(4-methoxyphenyl)amino)-9,9'-spirobi[fluoren]-7-yl)amino)phenoxy)ethoxy)ethoxy)ethyl methacrylate]-*co*-poly(methyl methacrylate)
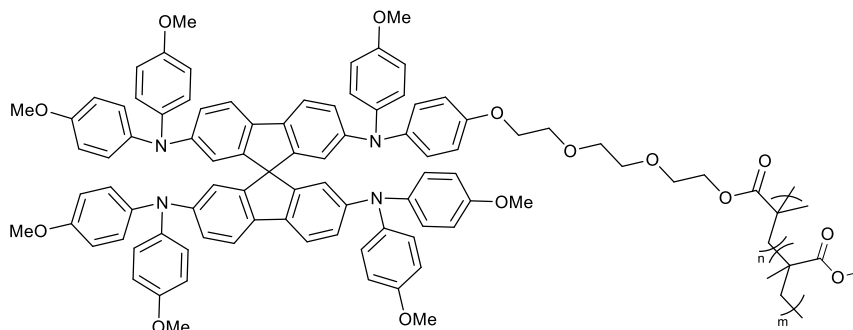
1 mol% spiro polymer (**2.22**): A 2 mL microwave vial and stirrer bar were oven dried and then charged with 2-(2-(2-(4-((4-methoxyphenyl)(2,2',7'-tris(bis(4-methoxyphenyl)amino)-9,9'-spirobi[fluoren]-7-yl)amino)phenoxy)ethoxy)ethoxy)ethyl methacrylate (**2.18**) (100 mg, 0.071 mmol). The flask was then subjected to three vacuum/nitrogen filling steps. A stock solution of 2,2'-azobis(2-methylpropronitrile) (10 mg, 0.06 mmol) in dry N, N-dimethylformamide (1 mL) was made. To the reaction flask was added stock solution (0.7 mL) and methyl methacrylate (747 μL, 6.93 mmol). The reaction was degassed for 5 minutes before being left to stir at 70 °C for 22 h. The reaction mixture was then cooled to room temperature before N, N-dimethylformamide (30 mL) added and concentrated *in vacuo*. The reaction mixture was dissolved in ethyl acetate (10 mL) and the polymer was precipitated by dropwise addition into petroleum ether (300 mL). The precipitate was collected by vacuum filtration to produce the 1 mol% polymer (**2.22**) (814 mg, 20%) as an off-white solid. δ_H (400 MHz, C_6D_6) 7.09–6.92 (28H, m, 28 × ArH), 6.88–6.68 (16H, m, 16 × ArH), 4.10 (2H, br, CH_2), 3.87 (2H, br, CH_2), 3.63 (2H, br, CH_2), 3.51 (6H, br, 3 × CH_2), 3.53–3.31 (21H, m, 7 × CH_3), 2.30–2.14 (2H, m, CH_2), 2.20–1.95 (136H, m, CH_2), 1.62–1.40 (2H, m, CH_3), 1.53–1.06 (372H, m, CH_3); M_n= 54489; M_w/M_n=1.88

20 mol% spiro polymer (**2.21**): A 2 mL microwave vial and stirrer bar were oven dried and then charged with 2-(2-(2-(4-((4-methoxyphenyl)(2,2',7'-tris(bis(4-methoxyphenyl)amino)-9,9'-spirobi[fluoren]-7-yl)amino)phenoxy)ethoxy)ethoxy)ethyl methacrylate (**2.18**) (300 mg, 0.213 mmol). The flask was then subjected to three vacuum/nitrogen filling steps. A stock solution of 2,2'-azobis(2-methylpropronitrile) (10 mg, 0.06 mmol) in dry N, N-dimethylformamide (1 mL) was made. To the reaction flask was added stock solution (0.1 mL) and methyl methacrylate (113 μL, 1.05 mmol). The

reaction was degassed for 5 minutes before being left to stir at 70 °C for 22 h. The reaction mixture was then cooled to room temperature before N, N-dimethylformamide (30 mL) added and concentrated *in vacuo*. The reaction mixture was dissolved in ethyl acetate (10 mL) and the polymer was precipitated by dropwise addition into petroleum ether (300 mL). The precipitate was collected by vacuum filtration to produce the 20 mol% polymer (**2.21**) (221 mg, 84%) as a pale-yellow solid. δ_H (400 MHz, C_6D_6) 7.06 – 6.91 (28H, m, 28 × ArH), 6.82 (2H, d, J 8.5 Hz, 2× ArH), 6.75 (14H, dd, J 8.7 Hz, 5.1 Hz, 14 × ArH), 4.10 (2H, br, CH_2), 3.88 (2H, br, CH_2), 3.65 (2H, br, CH_2), 3.58 (2H, br, CH_2), 3.49 (4H, br, 2 × CH_2), 3.38 – 3.23 (21H, m, 7 × CH_3), 2.09 (10H, br, 5 × CH_2), 1.49 – 1.19 (21H, m, 7 × CH_3); M_n=94875; M_w/M_n=1.95

25 mol% spiro polymer (**2.20**): A 2 mL microwave vial and stirrer bar were oven dried and then charged with 2-(2-(2-(4-((4-methoxyphenyl)(2,2',7'-tris(bis(4-methoxyphenyl)amino)-9,9'-spirobi[fluoren]-7-yl)amino)phenoxy)ethoxy)ethoxy)ethyl methacrylate (**2.18**) (353 mg, 0.200 mmol). The flask was then subjected to three vacuum/nitrogen filling steps. A stock solution of 2,2'-azobis(2-methylpropronitrile) (10 mg, 0.06 mmol) in dry N, N-dimethylformamide (1 mL) was made. To the reaction flask was added stock solution (0.1 mL) and methyl methacrylate (85.0 µL, 0.800 mmol). The reaction was degassed for 5 minutes before being left to stir at 70 °C for 22 h. The reaction mixture was then cooled to room temperature before N, N-dimethylformamide (30 mL) added and concentrated *in vacuo*. The reaction mixture was dissolved in ethyl acetate (10 mL) and the polymer was precipitated by dropwise addition into petroleum ether (300 mL). The precipitate was collected by vacuum filtration to produce the 25 mol% polymer (**2.20**) (247 mg, 65%) as a pale-yellow solid. v_{max}/cm^{-1} (neat) 2958 (CH), 2360, 1592 (C=C), 1503, 1239(CO), 1166, 1029 (CO), 827 (C=C); δ_H (400 MHz, C_6D_6) 7.09 (2H, br, 2× ArH), 7.06–6.94 (26H, m, 26 × ArH), 6.81 (2H, d, J 8.6 Hz, 2 × ArH), 6.77–6.70 (14H, m, 14 × ArH), 4.09 (2H, br, CH_2), 3.86 (2H, br, CH_2), 3.64 (2H, br, CH_2), 3.57 (2H, br, CH_2), 3.41 (4H, br, 2 × CH_2), 3.31 (21H, s, 7 × CH_3), 2.07 (8H, br, 4 × CH_2), 1.47–1.15 (12H, m, 4 × CH_3); M_n=106582; M_w/M_n=2.33

2,2',7,7'-Tetranitro-9,9'-spirobi[9H-fluorene] (3.24)[294]
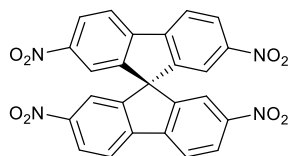
9,9'-Spirobifluorene (1.00 g, 3.16 mmol) was added to fuming nitric acid (6 mL) portionwise over 15 minutes at 0 °C before being left to stir at 0 °C for 3 h. A solution of acetic anhydride (2 mL) in glacial acetic acid (3 mL) was then added dropwise over 10 minutes before being left to stir at room temperature for 1 h. The resulting precipitate was then filtered, washed with water and glacial acetic acid and dried *in vacuo* for 12 h to produce 2,2',7,7'-tetranitro-9,9'-spirobi[9H-fluorene] (**3.24**) (1.34 g, 85%) as a pale-yellow solid. mp = >300 ° C; δ_H (400 MHz, DMSO) 8.59 (4H, d, *J* 8.5 Hz, 4 × ArH), 8.47 (4H, dd, *J* 8.5, 2.0 Hz, 4 × ArH), 7.65 (4H, d, *J* 2.0 Hz, 4 × ArH); δ_C (101 MHz, DMSO) 148.5 (4 × C), 147.7 (4 × C), 145.8 (4 × C), 125.3 (4 × CH), 124.0 (4 × CH), 119.2 (4 × CH), 65.1 (C); *m/z* (ESI) 496.0668 ([M]$^-$ $C_{25}H_{12}N_4O_8$ requires 496.0655).

2,2',7,7'-Tetraamino-9,9'-spirobifluorene (3.25)[294]
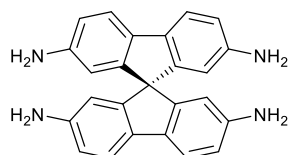
2,2',7,7'-Tetranitro-9,9'-spirobifluorene (**3.24**) (1.00 g, 2.01 mmol) was suspended in ethanol (20 mL) before palladium on carbon (100 mg, 0.940 mmol) was added. The reaction mixture was then heated to reflux before hydrazine hydrate (1.56 mL, 32.2 mmol) was added. The resulting mixture was stirred at reflux for 19 h before being filtered hot on Celite to remove the palladium on carbon and washed with ethanol (20 ml). The solution was then concentrated *in vacuo* to produce 2,2',7,7'-tetraamino-9,9'-spirobifluorene (**3.25**) (690 mg, 91%) as an off-white solid. R$_f$ 0 (40% ethyl acetate in petroleum ether); δ_H (400 MHz, DMSO) 7.30 (4H, d, *J* 8.0 Hz, 4 × ArH), 6.45 (4H, dd, *J* 8.0, 2.1 Hz, 4 ×

ArH), 5.84 (4H, d, J 2.1 Hz, 4 × ArH), 4.80 (8H, s, 4 × NH$_2$); δ$_C$ (101 MHz, DMSO) 150.4 (4 × C), 146.9 (4 × C), 130.7 (4 × C), 118.6 (4 × CH), 112.9 (4 × CH), 109.5 (4 × CH), 56.0 (C).

2,7-Fluorenediamine (3.26)[295]
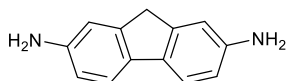
2,7-Dinitrofluorene (1.00 g, 3.90 mmol) was suspended in dry ethanol (70 mL). 10% palladium on carbon (100 mg, 0.940 mmol) and hydrazine hydrate (1.51 mL, 31.2 mmol) were then added and the resulting mixture left to stir at 75 °C for 20 h. After cooling to room temperature, the reaction mixture was filtered on Celite to remove the palladium on carbon and washed with ethanol (100 mL). The solution was then concentrated *in vacuo* to produce 2,7-fluorenediamine (**3.26**) (644 mg, 84%) as an off-white solid. δ$_H$ (400 MHz, CDCl$_3$) 7.41 (2H, d, J 8.0 Hz, 2 × ArH), 6.83 (2H, s, 2 × ArH), 6.67 (2H, dd, J 8.0, 2.2 Hz, 2 × ArH), 3.72 (2H, s, CH$_2$), 3.64 (4H, s, 2 × NH$_2$).

***N,N*-Bis(4-methoxyphenyl)aniline (3.27)**[296]
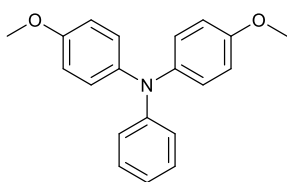
Bis(4-methoxyphenyl)amine (5.00 g, 21.81 mmol), bromobenzene (2. 53 mL, 23.99 mmol), tris(dibenzylideneacetone)dipalladium(0) (502 mg, 0.872 mmol), tri-*tert*-butylphosphonium tetrafluoroborate (253 mg, 0.872 mmol) and sodium *tert*-butoxide (31.44 g, 327 mmol) were suspended in dry toluene (150 mL). The mixture was degassed under argon before being heated to 85 °C for 17 h. The reaction was then cooled to room temperature before water (100 mL) added and extracted with dichloromethane (3 × 100 mL). The combined organic layers were then dried over MgSO$_4$, filtered and concentrated *in vacuo*. The crude product was purified by flash column

chromatography on silica gel, gradient elution 100% petroleum ether to 50% dichloromethane in petroleum ether to produce *N,N*-bis(4-methoxyphenyl)aniline (**3.27**) (5.42 g, 80%) as a yellow solid. R_f 0.39 (100% petroleum ether); mp = 110 – 112 °C (lit.,[297] mp = 104 – 106 °C); δ_H (400 MHz, DMSO) 7.22–7.12 (2H, m, 2 × ArH), 7.05–6.94 (4H, m, 4 × ArH), 6.93–6.86 (4H, m, 4 × ArH), 6.83 (1H, tt, J 7.3, 1.1 Hz, ArH), 6.80–6.74 (2H, m, 2 × ArH), 3.73 (6H, s, 2 × CH₃); δ_C (101 MHz, DMSO) 155.6 (2 × C), 148.4 (C), 140.3 (2 × C), 129.1 (2 × CH), 126.4 (4 × CH), 120.2 (CH), 119.8 (2 × CH), 114.9 (4 × CH), 55.2 (2 × CH₃); *m/z* (ESI) 306.1498 ([M + H]⁺ $C_{20}H_{20}NO_2$ requires 306.1496).

4-(Bis(4-methoxyphenyl)amino)benzaldehyde (3.28)[298]
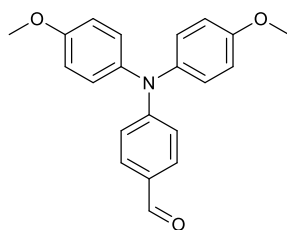
Phosphoryl chloride (1.45 mL, 15.6 mmol) and dry *N, N*-dimethylformamide (1.20 mL, 15.6 mmol) were slowly added to dry dichloromethane (40 mL) at 0 °C before being left to stir at 0 ° for 1 h. *N,N*-Bis(4-methoxyphenyl)aniline (**3.27**) (2.50 g, 8.19 mmol) was then added and left to stir at reflux for 17 h. The reaction mixture was then poured into water (50 mL) before being extracted with dichloromethane (3 × 50 mL). The combined organic layers were then dried over MgSO₄, filtered and concentrated *in vacuo*. The crude product was purified by flash column chromatography on silica gel, eluting with 100% dichloromethane to produce 4-(bis(4-methoxyphenyl)amino)benzaldehyde (**3.28**) (2.12g, 78%) as a yellow solid. R_f 0.24 (100% dichloromethane); δ_H (400 MHz, CDCl₃) 9.76 (1H, s, aldehyde H), 7.63 (2H, d, J 8.9 Hz, 2 × ArH), 7.13 (4H, d, J 8.9 Hz, 4 × ArH), 6.89 (4H, d, J 8.9 Hz, 4 × ArH), 6.85 (2H, d, J 8.9 Hz, 2 × ArH), 3.82 (6H, s, 2 × CH₃); δ_C (101 MHz, CDCl₃) 190.4 (CH), 157.5 (2 × C), 154.2 (C), 139.0 (2 × C), 131.6 (2 × CH), 128.0 (C), 128.2 (4 × CH), 116.9 (2 × CH), 115.2 (4 × CH), 55.6 (2 × CH₃); *m/z* (ESI) 334.1443 ([M + H]⁺ $C_{21}H_{20}NO_3$ requires 334.1445).

3,3'-Dimethoxy-1,1'-biphenyl (3.29)[299]

3-Methoxyphenylboronic acid (486 mg, 3.20 mmol), 3-bromoanisole (500 mg, 2.67mmol), tetrakis(triphenylphosphine)palladium(0) (77.0 mg, 0.067 mmol) and sodium carbonate solution (2M) were dissolved in dry toluene (4 mL) in a 25 mL microwave vial. The mixture was degassed under argon before being sealed and left to stir at 90 °C for 24 h. The reaction mixture was then cooled to room temperature before being extracted with chloroform (3 × 30 mL) and washed with water/brine (100 mL). The combined organic layers were then dried over $MgSO_4$, filtered and concentrated *i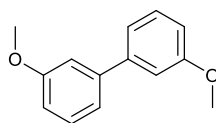n vacuo*. The crude product was then purified by flash column chromatography on silica gel, eluting with 5% ethyl acetate in petroleum ether to produce 3,3'-dimethoxy-1,1'-biphenyl (**3.29**) (501 mg, 88%) as a colourless oil. R_f 0 43 (10% ethyl acetate in petroleum ether); δ_H (400 MHz, $CDCl_3$) 7.35 (2H, dd, J 8.2, 7.6 Hz, 2 × ArH), 7.18 (2H, ddd, J 7.6, 2.1, 0.8 Hz, 2 × ArH), 7.12 (2H, t, J 2.1 Hz, 2 × ArH), 6.90 (2H, ddt, J 8.2, 2.1, 0.8 Hz, 2 × ArH), 3.87 (6H, s, 2 × CH_3); δ_C (101 MHz, $CDCl_3$) 160.0 (2 × C), 142.8 (2 × C), 129.9 (2 × CH), 119.9 (2× CH), 113.1 (2 × CH), 113.0 (2 × CH), 55.5 (2 × CH_3).

2,2'-Dibromo-5,5'-dimethoxy-1,1'-biphenyl (3.30)[300]
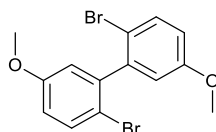
3,3'-Dimethoxy-1,1'-biphenyl (**3.29**) (500 mg, 2.33 mmol) in dry *N*,*N*-dimethylformamide (1.3 mL) was added slowly to *N*-bromosuccinimide (829 mg, 4.66 mmol) in dry *N*,*N*-dimethylformamide (3.7 mL) at 0 °C. The reaction as left to stir at room temperature in the dark for 20 h before being quenched with ice water (50 mL). The resulting precipitate was filtered and washed with warm water (30 mL) and warm hexane (30 mL). This was then placed in the drying oven for 1 hour to produce 2,2'-dibromo-5,5'-dimethoxy-1,1'-biphenyl (**3.30**) (520 mg, 60%) as a white solid. δ_H (400

MHz, CDCl$_3$) 7.56 (2H, d, J 8.7 Hz, 2 × ArH), 6.85 (2H, dd, J 8.7, 3.0 Hz, 2 × ArH), 6.82 (2H, d, J 3.0 Hz, 2 × ArH), 3.83 (6H, s, 2 × CH$_3$).

3,6-Dibromo-9*H*-carbazole (3.33)[301]
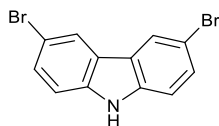
To a 0°C solution of carbazole (3.00 g, 18.0 mmol) in ethyl acetate (150 mL) was added *N*-bromosuccinimide (6.37 g, 36.0 mmol). The reaction was left to stir at room temperature in the dark for 5 h before being quenched with water (200 mL) and extracted with ethyl acetate (3 × 100 mL). The combined organic layers were then dried over MgSO$_4$, filtered and concentrated *in vacuo*. The crude product was purified by flash column chromatography on silica gel, eluting with 30% ethyl acetate in petroleum ether to produce 3,6-dibromo-9*H*-carbazole (**3.33**) (4.78 g, 82%) as an off-white solid. R$_f$ 0.29 (30% ethyl acetate in petroleum ether); mp = 211 – 213 °C (lit.,[301] mp = 215 – 216 °C); δ$_H$ (400 MHz, DMSO) 8.43 (2H, d, J 2.0 Hz, 2 × ArH), 7.53 (2H, dd, J 8.6, 2.0 Hz, 2 × ArH), 7.47 (2H, d, J 8.6 Hz, 2 × ArH); *m/z* (ESI) 324.8917 ([M]$^+$ C$_{12}$H$_7$Br$_2$N requires 324.8925).

3,6-Dimethoxy-*9H*-carbazole (3.34)[302]
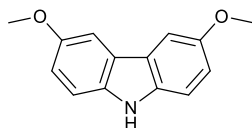
Sodium (2.83 g, 123 mmol) was added slowly to dry methanol (33 mL). Once all the sodium was completely dissolved, dry *N,N*-dimethylformamide (66 mL), copper iodide (4.93 g, 25.9 mmol) and 3,6-dibromo-9*H*-carbazole (**3.33**) (2.00 g, 6.16 mmol) were added before being left to stir at 110 °C for 3 h. Ethyl acetate (200 mL) was then added and the solution filtered on Celite to remove copper powder. The filtrate was concentrated *in vacuo* before being extracted with ethyl acetate (3 × 50 mL)

and washed with water/brine (100 mL). The combined organic layers were then dried over MgSO$_4$, filtered and concentrated *in vacuo*. The crude product was purified by flash column chromatography on silica gel, gradient elution 70% dichloromethane in petroleum ether to 100% dichloromethane to produce 3,6-dimethoxy-*9H*-carbazole (**3.34**) (1.04 g, 74%) as a white solid. R$_f$ 0.21 (50% dichloromethane in petroleum ether); δ$_H$ (400 MHz, DMSO) 10.79 (1H, s, NH), 7.66 (2H, d, *J* 2.6 Hz, 2 × ArH), 7.33 (2H, dd, *J* 8.8, 0.5 Hz, 2 × ArH), 6.98 (2H, dd, *J* 8.8, 2.6 Hz, 2 × ArH), 3.84 (6H, s, 2 × CH$_3$); δ$_C$ (101 MHz, DMSO) 152.6 (2 × C), 135.3 (2 × C), 122.7 (2 × C), 114.9 (2 × CH), 111.7 (2 × CH), 102.8 (2 × CH), 55.6 (2 × CH$_3$); *m/z* (ESI) 228.1019 ([M + H]$^+$ C$_{14}$H$_{13}$NO$_2$ requires 228.1026).

3,6-Dimethoxy-9-phenyl-9*H*-carbazole (3.31)[303]
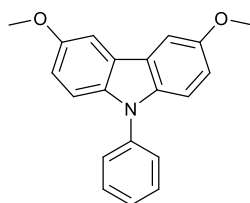
3,6-Dimethoxy-*9H*-carbazole (**3.34**) (500 mg, 2.20 mmol), bromobenzene (921 μL, 8.80 mmol), potassium carbonate (882 mg, 6.38 mmol) and copper iodide (209 mg, 1.10 mmol) were suspended in dimethylacetamide (14 mL) before being left to stir at 180 °C for 16 h. The reaction mixture was then cooled to room temperature before being extracted with diethyl ether (3 × 50 mL) and washed with water (150 mL). The combined organic layers were then dried over MgSO$_4$, filtered and concentrated *in vacuo*. The crude product was then purified by flash column chromatography on silica gel, eluting with 30% ethyl acetate in petroleum ether to produce 3,6-dimethoxy-9-phenyl-9*H*-carbazole (**3.31**) (648 mg, 97%) as a pale yellow solid. R$_f$ 0.56 (100% dichloromethane); δ$_H$ (400 MHz, CDCl$_3$) 7.64–7.48 (6H, m, 6 × ArH), 7.47–7.37 (1H, m, ArH), 7.33 (2H, d, J 8.9 Hz, 2 × ArH), 7.04 (2H, dd, J 8.9, 2.5 Hz, 2 × ArH), 3.95 (6H, s, 2 × CH$_3$); δ$_C$ (101 MHz, CDCl$_3$) 144.8 (2 × C), 129.9 (2 × CH), 127.1 (CH), 126.9 (2 × CH), 123.8 (4 × C), 115.3 (2 × CH), 110.9 (2 × CH), 103.1 (2 × CH), 56.3 (2 × CH$_3$); *m/z* (ESI) 304.1324 ([M + H]$^+$ C$_{20}$H$_{18}$NO$_2$ requires 304.1339).

4-(3,6-Dimethoxy-*9H*-carbazol-9-yl)benzaldehyde (3.32)[304]
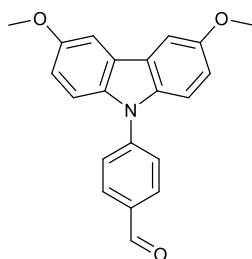
3,6-Dimethoxy-*9H*-carbazole (**3.34**) (500 mg, 2.20 mmol), 4-bromo benzaldehyde (407 mg, 2.20 mmol), copper powder (280 mg, 4.4 mmol), potassium carbonate (1.22 g, 8.80 mmol) and dibenzo-18-crown-6 (79 mg, 0.22 mmol) were suspended in dry *N*,*N*-dimethylformamide (8.5 mL). The reaction mixture was left to stir at 150 °C for 45 h before being cooled to room temperature and water added (15 mL). This was left to stir at room temperature for 1 h before being filtered and the precipitate purified by flash column chromatography on silica gel, gradient elution 90% dichloromethane in petroleum ether to 100% dichloromethane to produce 4-(3,6-dimethoxy-*9H*-carbazol-9-yl)benzaldehyde (**3.32**) (413 mg, 57%) as a pale yellow solid. R$_f$ 0.26 (30% ethyl acetate in petroleum ether); δ$_H$ (400 MHz, CDCl$_3$) 10.09 (1H, s, aldehyde H), 8.10 (2H, d, *J* 8.4 Hz, 2 × ArH), 7.76 (2H, d, *J* 8.4 Hz, 2 × ArH), 7.55 (2H, d, *J* 2.5 Hz, 2 × ArH), 7.44 (2H, d, *J* 8.9 Hz, 2 × ArH), 7.06 (2H, dd, *J* 8.9 Hz, 2.5 Hz, 2 × ArH), 3.96 (6H, s, 2 × CH$_3$); δ$_C$ (101 MHz, CDCl$_3$) 191.1 (CH), 154.8 (C), 144.1 (C), 135.4 (C), 134.2 (C), 131.5 (2 × CH), 126.2 (2 × CH), 124.6 (C), 115.5 (2 × CH), 111.0 (2 × CH), 103.3 (2 × CH), 56.2 (2 × CH$_3$); *m/z* (ESI) 332.1265 ([M + H]$^+$ C$_{121}$H$_{18}$NO$_3$ requires 332.1288).

(N2E,N7E)-N2,N7-Bis(4-(bis(4-methoxyphenyl)amino)benzylidene)-9*H*-fluorene-2,7-diamine (3.35)
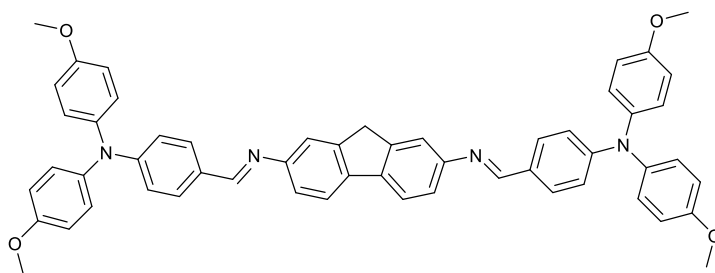
2,7-Fluorenediamine (**3.26**) (238 mg, 1.21 mmol), 4-(bis(4-methoxyphenyl)amino)benzaldehyde (**3.28**) (807 mg, 2.42 mmol) and *p*-toluenesulfonic acid (1.00 mg, 0.005 mmol) were dried *in vacuo* for 30 minutes before dry ethanol (71.5 mL) was added. The reaction mixture was left to stir at reflux for 18 h before being added to water (200 mL). The resulting precipitate was then filtered before being purified by flash column chromatography on silica gel, gradient elution 1% triethylamine, 19% ethyl acetate in petroleum ether to 1% triethylamine in ethyl acetate to produce (N2E,N7E)-N2,N7-bis(4-(bis(4-methoxyphenyl)amino)benzylidene)-9*H*-fluorene-2,7-diamine (**3.35**) (320 mg, 32%) as a yellow solid. R_f 0.26 (1% triethylamine, 59% dichloromethane in petroleum ether); mp = 115–117 °C; v_{max}/cm^{-1} (neat) 2964 (CH), 60, 1591 (C=C), 1498, 1235 (CO), 1167, 1028 (CN), 823, 572; δ_H (400 MHz, CDCl$_3$) 8.42 (2H, s, 2 × N=CH), 7.73 (2H, d, J 8.1 Hz, 2 × ArH), 7.70 (4H, d, J 8.8 Hz, 4 × ArH), 7.38 (2H, s, 2 × ArH), 7.23 (2H, dd, J 8.1, 2.0 Hz, 2 × ArH), 7.16–7.07 (8H, m, 8 × ArH), 6.93 (4H, d, J 8.8 Hz, 4 × ArH), 6.90–6.84 (8H, m, 8 × ArH), 3.93 (2H, s, CH$_2$), 3.82 (12H, s, 4 × CH$_3$); δ_C (101 MHz, CDCl$_3$) 159.1 (2 × N=CH), 156.8 (4 × C), 151.4 (2 × C), 144.6 (2 × C), 143.3 (2 × C), 140.8 (4 × C), 140.0 (2 × C), 132.5 (2 × C), 130.0 (4 × CH), 127.6 (8 × CH), 120.4 (2 × CH), 120.2 (2 × CH), 118.8 (4 × CH), 117.7 (2 × CH), 115.0 (8 × CH), 55.7 (4 × CH$_3$), 37.0 (CH$_2$); *m/z* (ESI) 827.3595 ([M + H]$^+$ C$_{55}$H$_{47}$N$_4$O$_4$ requires 827.3599).

(N2E,N7E)-N2,N7-Bis(4-(3,6-dimethoxy-9H-carbazol-9-yl)benzylidene)-9H-fluorene-2,7-diamine (3.36)
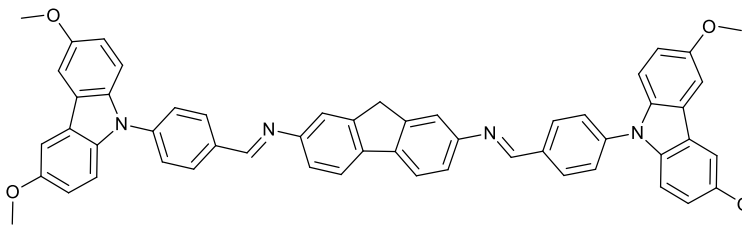
2,7-Fluorenediamine (**3.26**) (100 mg, 0.510 mmol), 4-(3,6-dimethoxy-*9H*-carbazol-9-yl)benzaldehyde (**3.32**) (338 mg, 1.02 mmol) and *p*-toluenesulfonic acid (1.00 mg, 0.005 mmol) were dried *in vacuo* for 30 minutes before dry ethanol (30 mL) was added. The reaction mixture was left to stir at reflux for 18 h before being added to water (100 mL). The resulting precipitate was then filtered before being purified by flash column chromatography on silica gel, gradient elution 1% triethylamine, 39% ethyl acetate in petroleum ether to 1% triethylamine in ethyl acetate to produce (N2E,N7E)-N2,N7-bis(4-(3,6-dimethoxy-9H-carbazol-9-yl)benzylidene)-9H-fluorene-2,7-diamine (**3.36**) (125 mg, 30%) as a yellow solid. R_f 0.64 (1% triethylamine in ethyl acetate); mp = 152-154 °C; v_{max}/cm^{-1} (neat) 2966 (CH), 2363, 1597 (C=C), 1455, 1198(CN), 1155, 1031 (CO), 806; δ_H (400 MHz, CDCl$_3$) 8.67 (2H, s, 2 × N=CH), 8.19–8.12 (4H, m, 4 × ArH), 7.83 (2H, d, J 8.0 Hz, 2 × ArH), 7.74–7.67 (4H, m, 4 × ArH), 7.57 (4H, d, J 2.5 Hz, 4 × ArH), 7.51 (2H, d, J 1.9 Hz, 2 × ArH), 7.43 (4H, s, 4 × ArH), 7.35 (2H, dd, J 8.0, 1.9 Hz, 2 × ArH), 7.07 (4H, dd, J 8.9, 2.5 Hz, 4 × ArH), 4.03 (2H, s, CH$_2$), 3.97 (12H, s, 4 × CH$_3$); δ_C (101 MHz, CDCl$_3$) 158.4 (2 × N=CH), 154.5 (4 × C), 150.8 (2 × C), 144.8 (2 × C), 141.1 (2 × C), 140.0 (2 × C), 136.0 (4 × C), 134.8 (2 × C), 130.4 (4 × CH), 126.6 (4 × CH), 124.3 (4 × C), 120.5 (4 × CH), 117.9 (2 × CH), 115.4 (4 × CH), 111.0 (4 × CH), 103.2 (4 × CH), 56.3 (4 × CH$_3$), 37.2 (CH$_2$); *m/z* (ESI) 823.3304 ([M + H]$^+$ C$_{55}$H$_{43}$N$_4$O$_4$ requires 823.3286).

(N2E,N7E)-N2,N7-Bis(ferrocenylidene)-9*H*-fluorene-2,7-diamine (3.37)
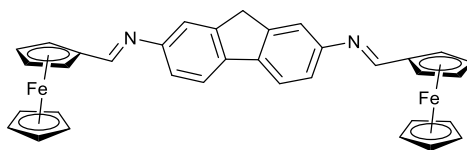
2,7-Fluorenediamine (**3.26**) (50 mg, 0.25 mmol) and ferrocene carboxaldehyde (107 mg, 0.500 mmol) were suspended in dry methanol (5 mL) and left to stir at reflux for 18 h. The resulting precipitate was filtered and washed with cold methanol (30 mL) before being left in the drying oven for 2 h to produce (N2E,N7E)-N2,N7-bis(ferrocenylidene)-9*H*-fluorene-2,7-diamine (**3.37**) (121 mg, 82%) as a pale pink/brown solid. R_f 0.38 (1% triethylamine, 29% ethyl acetate in petroleum ether); mp = >300 °C; v_{max}/cm^{-1} (neat) 2961 (CH), 2358, 1592 (C=C), 1496, 1238, 1032 (CN), 825, 570; δ_H (400 MHz, CDCl$_3$) 8.43 (2H, s, 2 × N=CH), 7.74 (2H, d, J 8.0 Hz, 2 × ArH), 7.34 (2H, s, 2 × ArH), 7.19 (2H, d, J 8.0 Hz, 2 × ArH), 4.83 (4H, s, 4 × Cp ring CH), 4.50 (4H, s, 4 × Cp ring CH), 4.27 (8H, s, 8 × Cp ring CH), 3.96 (2H, s, 2 × Cp ring CH), 3.49 (2H, d, J 5.5 Hz, CH$_2$); *m/z* (ESI) 589.1030 ([M + H]$^+$ C$_{35}$H$_{29}$Fe$_2$N$_2$ requires 589.1031).

(*N*12*E*,*N*2*E*,*N*7*E*)-*N*2,*N*7,*N*12-Tris(4-(bis(4-methoxyphenyl)amino)benzylidene)-5,5,10,10,15,15-hexahexyl-10,15-dihydro-5H-diindeno[1,2-a:1',2'-c]fluorene-2,7,12-triamine (3.42)
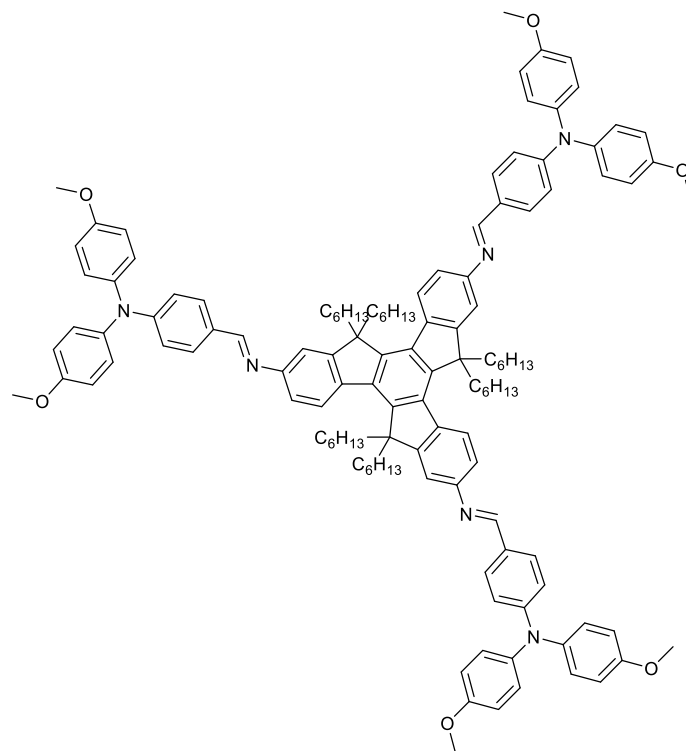
5,5,10,10,15,15-Hexahexyl-10,15-dihydro-5*H*-diindeno[1,2-*a*:1',2'-*c*]fluorene-2,7,12-triamine (**4.30**) (1.00 g, 1.12 mmol) and 4-(bis(4-methoxyphenyl)amino)benzaldehyde (**3.28**) (560 mg, 1.68 mmol) were dissolved in dry toluene (30 mL). Trifluoroacetic acid (6.00 μL, 0.078 mmol) was then added before being left to stir at room temperature for 18 h. The reaction mixture was then extracted with ethyl acetate (3 × 50 mL) and washed with water (100 mL). The combined organic layers were then dried over MgSO₄, filtered and concentrated *in vacuo*. The crude product was then purified by flash column chromatography on silica gel, gradient elution 1% triethylamine, 9% dichloromethane in petroleum ether to 1% triethylamine, 49% dichloromethane in petroleum ether. The product was then dissolved in diethyl ether and precipitated in petroleum ether to produce (*N*12*E*,*N*2*E*,*N*7*E*)-*N*2,*N*7,*N*12-tris(4-(bis(4-methoxyphenyl)amino)benzylidene)-5,5,10,10,15,15-hexahexyl-10,15-dihydro-5H-diindeno[1,2-a:1',2'-c]fluorene-2,7,12-triamine (**3.42**) (591 mg, 29%) as a yellow solid. R*f* 0.25 (1% triethylamine, 29% dichloromethane in petroleum ether); mp = 130–132 °C; ν$_{max}$/cm⁻¹ (neat) 2925 (CH), 2360, 1587 (C=C), 1501, 1236 (CN), 1160, 1030 (CO), 826; δ$_H$ (400 MHz, C₆D₆) 8.60 (3H, d, *J* 8.6 Hz, 3 × ArH), 8.47 (3H, s, 3 × ArH), 7.94–7.86 (6H, m, 6 × ArH), 7.71 (3H, d, *J* 2.1 Hz, 3 × ArH), 7.31 (3H, dd, *J* 8.6, 2.0 Hz, 3 × ArH), 7.08 (6H, d, *J* 8.6 Hz, 6 × ArH), 7.06–7.02 (12H, m, 12 ×

170

ArH), 6.77–6.66 (12H, m, 12 × ArH), 3.29 (18H, s, 6 × CH$_3$), 3.28–3.15 (6H, m, 6 × CH), 2.34–2.23 (6H, m, 6 × CH), 1.17–0.90 (48H, m, 24 × CH$_2$), 0.73 (18H, t, J 6.8 Hz, 6 × CH$_3$); δ$_C$ (101 MHz, C$_6$D$_6$) 158.9 (3 × CH), 157.2 (6 × C), 155.6 (3 × C), 152.2 (3 × C), 151.9 (3 × C), 144.8 (3 × C), 140.5 (6 × C), 139.0 (3 × C), 138.5 (3 × C), 130.6 (6 × CH), 128.7 (3 × C), 127.9 (12 × CH), 125.7 (3 × CH), 119.3 (3 × CH), 119.0 (6 × CH), 116.4 (3 × CH), 115.3 (12 × CH), 56.3 (3 × C), 55.0 (6 × CH$_3$), 37.8 (6 × CH$_2$), 32.2 (6 × CH$_2$), 30.2 (6 × CH$_2$), 24.8 (6 × CH$_2$), 22.9 (6 × CH$_2$), 14.3 (6 × CH$_3$); m/z (ESI) 1838.1142 ([M]$^+$ C$_{126}$H$_{144}$N$_6$O$_6$ requires 1838.1181).

Truxene: (10,15-dihydro-5*H*-diindeno[1,2-*a*;1',2'-*c*]fluorene) (4.25)[305]
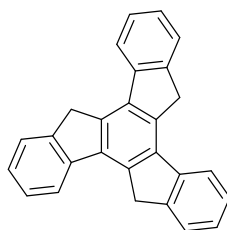
1-Indanone (10.0 g, 75.7 mmol) was added to a 2:1 mixture of glacial acetic acid (60 mL) and concentrated hydrochloric acid (30 mL). The solution was left to stir at 105 °C for 23 h before being added dropwise into a stirred solution of ice/water (400 mL) and left to stir for 1 h to form precipitate. The solid precipitate was washed with water (200 mL), acetone (200 mL) and dichloromethane (200 mL) to produce truxene (**4.25**) (6.25 g, 24%) as an off-white solid. mp = >300 °C (lit.,[186] mp = 368 – 369 °C (dec)); δ$_H$ (400 MHz, CDCl$_3$) 7.97 (3H, d, J 7.4 Hz, 3 × ArH), 7.71 (3H, d, J 7.4 Hz, 3 × ArH), 7.51 (3H, t, J 7.4 Hz, 3 × ArH), 7.40 (3H, td, J 7.4 Hz, 1.1 Hz, 3 × ArH), 4.29 (6H, s, 3 × CH$_2$); δ$_C$ (101 MHz, CDCl$_3$) 144.0 (3 × C), 141.9 (3 × C), 137.3 (3 × C), 135.4 (3 × C), 127.1 (3 × CH), 126.5 (3 × CH), 125.3 (3 × CH), 122.1 (3 × CH), 36.7 (3 × CH$_2$); m/z (EI$^+$) 342.1426 ([M]$^+$ C$_{27}$H$_{18}$ requires 342.1409).

5,5,10,10,15,15-Hexahexyl-10,15-dihydro-5*H*-diindeno[1,2-a:1',2'-c]fluorene (4.26)[216]
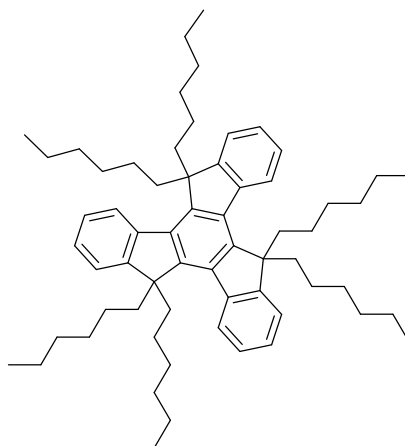
To a stirred solution of truxene (**4.25**) (300 mg, 0.880 mmol) in tetrahydrofuran (10 mL) under nitrogen, *n*-butyllithium (2.5 M solution *n*-hexane, 1.41 mL, 3.52 mmol) was added over a 10-minute period at −78 °C. The solution was stirred for 30 minutes at −78 °C before 1-bromohexane (494 μL, 3.52 mmol) was added dropwise over 10 minutes. The reaction was then left to stir at room temperature for 4 h before being cooled to −78 °C and the second portion of *n*-butyllithium (2.5 M solution in hexane, 1.41 mL, 3.52 mmol) was added. After 30 minutes the second portion of 1-bromohexane (494 μL, 3.52 mmol) was added and the flask left to stir at room temperature for 18 h. The reaction was quenched with saturated ammonium chloride solution (35 mL), extracted with ethyl acetate (3 × 50 mL) and washed with water (50 mL). The combined organic layers were dried over MgSO$_4$, filtered and concentrated *in vacuo*. The crude product was purified by flash column chromatography on silica gel, eluting with 100% petroleum ether to produce 5,5,10,10,15,15-hexahexyl-10,15-dihydro-5*H*-diindeno[1,2-a:1',2'-c]fluorene (**4.26**) (143 mg, 19%) as a yellow oil. R$_f$ 0.42 (100% petroleum ether); δ$_H$ (400 MHz, CDCl$_3$) 8.37 (3H, d, *J* 7.3 Hz, 3 × ArH), 7.46 (3H, dd, *J* 7.3 Hz, 1.6 Hz, 3 × ArH), 7.42–7.33 (6H, m, 6 × ArH), 3.04–2.88 (6H, m, 6 × CH), 2.12–2.01 (6H, m, 6 × CH), 1.00–0.77 (36H, m, 18 × CH$_2$), 0.60 (18H, t, *J* 7.1 Hz, 6 × CH$_3$), 0.54–0.42 (12H, m, 6 × CH$_2$); δ$_C$ (101 MHz, CDCl$_3$) 153.8 (3 × C), 145.0 (3 × C), 140.5 (3 × C), 138.5 (3 × C), 126.5 (3 × CH), 126.1 (3 × CH), 124.8 (3 × CH), 122.3 (3 × CH), 55.7 (3 × C), 37.1 (6 × CH$_2$), 31.6 (6 × CH$_2$), 29.6 (6 × CH$_2$), 24.0 (6 × CH$_2$), 22.4 (6 × CH$_2$), 14.0 (6 × CH$_3$); *m/z* (ESI) 869.6939 ([M + Na]$^+$ C$_{63}$H$_{90}$Na requires 869.6943).

2,7,12-Tribromo-5,5',10,10',15,15'-hexahexyl-10,15-dihydro-5*H*-diindeno[1,2-a:1',2'-c]fluorene (4.27)[216]
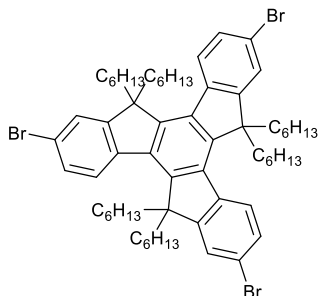
Bromine (30.0 µL, 0.578 mmol) was added to a stirred solution of 5,5,10,10,15,15-hexahexyltruxene (**4.26**) (140 mg, 0.165 mmol) in dichloromethane (5 mL) over a 5-minute period at room temperature under the protection from light. After 19 h the reaction was washed with sodium dithionite (20 mL) and extracted with dichloromethane (3 × 30 mL). The combined organic layers were then dried over MgSO$_4$, filtered and concentrated *in vacuo* to produce 2,7,12-tribromo-5,5',10,10',15,15'-hexahexyl-10,15-dihydro-5*H*-diindeno[1,2-a:1',2'-c]fluorene (**4.27**) (170 mg, 95%) as an off-white solid. R$_f$ 0.53 (100% petroleum ether); δ$_H$ (400 MHz, CDCl$_3$) 8.17 (3H, d, *J* 8.5 Hz, 3 × ArH), 7.56 (3H, d, *J* 2.0 Hz, 3 × ArH), 7.51 (3H, dd, *J* 8.5 Hz, 2.0 Hz, 3 × ArH), 2.90–2.77 (6H, m, 6 × CH), 2.07–1.94 (6H, m, 6 × CH), 1.01–0.77 (36H, m, 18 × CH$_2$), 0.62 (18H, t, *J* 7.1 Hz, 6 × CH$_3$), 0.52–0.39 (12H, m, 6 × CH$_2$).

5,5,10,10,15,15-Hexahexyl-2,7,12-trinitro-10,15-dihydro-5*H*-diindeno[1,2-a:1',2'-c]fluorene (4.29)[217]
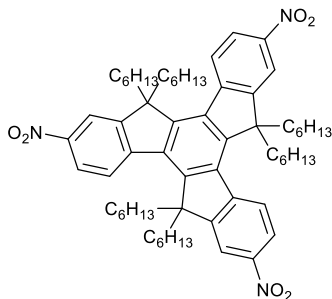
To a stirred solution of 5,5,10,10,15,15-hexahexyl-10,15-dihydro-5*H*-diindeno[1,2-a:1',2'-c]fluorene (**4.26**) (500 mg, 0.590 mmol) and 1,2-dichloroethane (65 mL) was added fuming nitric acid (496 µL, 11.8 mmol) at 0 °C. The resulting mixture was stirred for 3 h at 0 °C before being poured onto ice and the pH adjusted to neutral by addition of sodium hydroxide solution (10 mL). The solution was then extracted with ethyl acetate (3 × 75 mL) before the combined organic layers were dried over $MgSO_4$, filtered and concentrated *in vacuo* to produce 5,5,10,10,15,15-hexahexyl-2,7,12-trinitro-10,15-dihydro-5*H*-diindeno[1,2-a:1',2'-c]fluorene (**4.29**) (500 mg, 86%) as a pale yellow solid. R_f 0.56 (20% ethyl acetate in petroleum ether); δ_H (400 MHz, $CDCl_3$) 8.52 (3H, d, *J* 8.7 Hz, 3 × ArH), 8.40–8.34 (6H, m, 6 × ArH), 3.00–2.86 (6H, m, 3 × CH_2), 2.29–2.15 (6H, m, 3 × CH_2), 1.00–0.73 (36H, m, 18 × CH_2), 0.60 (18H, t, *J* 7.1 Hz, 6 × CH_3), 0.51–0.37 (12H, m, 6 × CH_2); δ_C (101 MHz, $CDCl_3$) 155.0 (3 × C), 149.7 (3 × C), 147.2 (3 × C), 145.4 (3 × C), 137.6 (3 × C), 125.0 (3 × CH), 122.8 (3 × CH), 117.7 (3 × CH), 56.8 (3 × C), 36.9 (6 × CH_2), 31.5 (6 × CH_2), 29.4 (6 × CH_2), 24.2 (6 × CH_2), 22.3 (6 × CH_2), 13.9 (6 × CH_3); *m/z* (ESI) 1004.6471 ([M+ Na]⁺ $C_{63}H_{87}N_3NaO_6$ requires 1004.6495).

5,5,10,10,15,15-Hexahexyl-10,15-dihydro-5*H*-diindeno[1,2-*a*:1',2'-*c*]fluorene-2,7,12-triamine (4.30)[217]
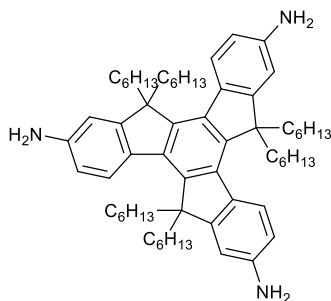
5,5,10,10,15,15-Hexahexyl-2,7,12-trinitro-10,15-dihydro-5*H*-diindeno[1,2-a:1',2'-c]fluorene (**4.29**) (400 mg, 0.410 mmol) was dissolved in tetrahydrofuran (20 mL) and degassed under argon for 20 minutes before 10% palladium on carbon (40 mg, 0.38 mmol) and hydrazine hydrate (418 µL, 8.61 mmol) were added. The resulting mixture was stirred for 18 h under reflux. After cooling to room temperature, the reaction mixture was filtered on Celite to remove the palladium on carbon and washed with ethyl acetate (50 mL). The solution was then concentrated *in vacuo* to produce 5,5,10,10,15,15-hexahexyl-10,15-dihydro-5*H*-diindeno[1,2-*a*:1',2'-*c*]fluorene-2,7,12-triamine (**4.30**) (352 mg, 96%) as a yellow solid. R_f 0.27 (20% ethyl acetate in petroleum ether); δ_H (400 MHz, CDCl$_3$) 8.05 (3H, d, *J* 8.3 Hz, 3 × ArH), 6.74 (3H, d, *J* 2.3 Hz, 3 × ArH), 6.68 (3H, dd, *J* 8.3 Hz, 2.3 Hz, 3 × ArH), 3.80 (6H, brs, 3 × NH$_2$), 2.93–2.73 (6H, m, 3 × CH$_2$), 1.95–1.80 (6H, m, 3 × CH$_2$), 1.03–0.75 (36H, m, 18 × CH$_2$), 0.60 (18H, t, *J* 7.1 Hz, 6 × CH$_3$), 0.55–0.41 (12H, m, 6 × CH$_2$); δ_C (101 MHz, CDCl$_3$) 155.9 (3 × C), 144.8 (3 × C), 141.2 (3 × C), 138.2 (3 × C), 132.5 (3 × C), 125.5 (3 × CH), 113.4 (3 × CH), 109.1 (3 × CH), 55.3 (3 × C), 37.4 (6 × CH$_2$), 31.8 (6 × CH$_2$), 29.8 (6 × CH$_2$), 24.1 (6 × CH$_2$), 22.5 (6 × CH$_2$), 14.1 (6 × CH$_3$); *m/z* (ESI) 892.7455 ([M+H]$^+$. C$_{63}$H$_{94}$N$_3$ requires 892.7450).

N,N',N''-(5,5,10,10,15,15-Hexahexyl-10,15-dihydro-5H-diindeno[1,2-a:1',2'-c]fluorene-2,7,12-triyl)triacetamide (4.31)[217]
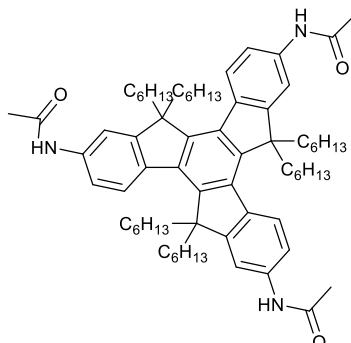
5,5,10,10,15,15-Hexahexyl-10,15-dihydro-5H-diindeno[1,2-a:1',2'-c]fluorene-2,7,12-triamine (**4.30**) (350 mg, 0.390 mmol) and triethylamine (196 µL, 1.41 mmol) were dissolved in dichloromethane (25 mL) before acetic anhydride (133 µL, 1.41 mmol) was added dropwise. The reaction mixture was left to stir at room temperature for 19 h before being quenched with saturated ammonium chloride solution (50 mL) and extracted with ethyl acetate (3 × 30 mL). The combined organic layers were then dried over $MgSO_4$, filtered and concentrated *in vacuo* to produce *N,N',N''*-(5,5,10,10,15,15-hexahexyl-10,15-dihydro-5H-diindeno[1,2-a:1',2'-c]fluorene-2,7,12-triyl)triacetamide (**4.31**) (366 mg, 92%) as a yellow solid. R_f 0.13 (40% ethyl acetate in petroleum ether); δ_H (400 MHz, DMSO) 10.10 (3H, s, 3 × NH), 8.19 (3H, d, *J* 8.7 Hz, 3 × ArH), 7.74 (3H, s, 3 × ArH), 7.61 (3H, d, *J* 8.7 Hz, 3 × ArH), 3.00–2.80 (6H, m, 3 × CH₂), 2.09 (9H, s, 3 × CH₃), 1.98–1.88 (6H, m, 3 × CH₂), 0.92–0.70 (36H, m, 18 × CH₂), 0.53 (18H, t, *J* 7.1 Hz, 6 × CH₃), 0.46–0.34 (12H, m, 6 × CH₂); *m/z* (ESI) 1040.7524 ([M + Na]⁺ $C_{69}H_{99}N_3NaO_3$ requires 1040.7586).

N,N',N''-(5,5,10,10,15,15-Hexahaxyl-3,8,13-trinitro-10,15-dihydro-5H-diindeno[1,2-a:1',2'-c]fluorene-2,7,12-triyl)triacetamide (4.32)[217]
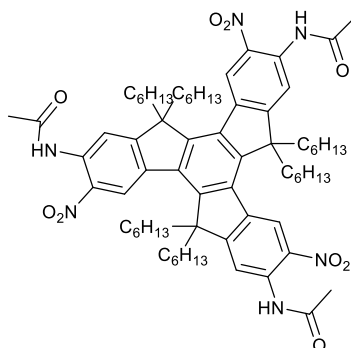
N,N',N''-(5,5,10,10,15,15-Hexahexyl-10,15-dihydro-5*H*-diindeno[1,2-*a*:1',2'-*c*]fluorene-2,7,12-triyl)triacetamide (**4.31**) (366 mg, 0.360 mmol) was dissolved in a 3:1 mixture of glacial acetic acid (18 mL) and acetone (6 mL). The reaction mixture was cooled to 0 °C before fuming nitric acid (435 μL, 10.4 mmol) was added dropwise. The reaction mixture was stirred at 0 °C for 20 minutes before being poured onto ice and the pH adjusted to neutral by addition of sodium hydroxide solution (15 mL). The solution was then extracted with ethyl acetate (3 × 50 mL) and the combined organic layers dried over MgSO$_4$, filtered and concentrated *in vacuo*. The crude product was purified by flash column chromatography on silica gel, eluting with 20% ethyl acetate in petroleum ether to produce *N,N',N''*-(5,5,10,10,15,15-hexahaxyl-3,8,13-trinitro-10,15-dihydro-5*H*-diindeno[1,2-*a*:1',2'-*c*]fluorene-2,7,12-triyl)triacetamide (**4.32**) (160 mg, 40%) as a yellow/orange solid. R$_f$ 0.55 (40% ethyl acetate in petroleum ether); δ$_H$ (40MHz, CDCl$_3$) 10.68 (3H, s, 3 × NH), 9.20 (3H, s, 3 × ArH), 9.00 (3H, s, 3 × ArH), 2.99–2.74 (6H, m, 3 × CH$_2$), 2.38 (9H, s, 3 × CH$_3$), 2.31–2.20 (6H, m, 3 × CH$_2$), 1.00–0.79 (36H, m, 18 × CH$_2$), 0.60 (18H, t, *J* 7.1 Hz, 6 × CH$_3$), 0.56–0.43 (12H, m, 6 × CH$_2$); δ$_C$ (101 MHz, CDCl$_3$) 169.4 (3 × C carbonyl), 162.8 (3 × C), 145.9 (3 × C), 136.7 (3 × C), 135.2 (3 × C), 134.8 (3 × C), 134.7 (3 × C), 121.3 (3 × CH), 115.6 (3 × CH), 57.2 (3 × C), 36.9 (6 × CH$_2$), 31.5 (6 × CH$_2$), 29.4 (6 × CH$_2$), 26.0 (3 × CH$_3$), 24.4 (6 × CH$_2$), 22.4 (6 × CH$_2$), 14.0 (6 × CH$_3$); *m/z* (ESI) 1151.7180 ([M-H]$^-$ C$_{69}$H$_{95}$N$_6$O$_9$ requires 1151.7159).

N,N',N''-(5,5,10,10,15,15-Hexahaxyl 12-ethyl-5,5,10,10,19,19-hexahexyl-15,19-dihydro-5H-diindeno[2',1':5,6;2'',1'':7,8]fluoreno[3,2-g]pteridine-14,16(10H,12H)-dione (4.33)
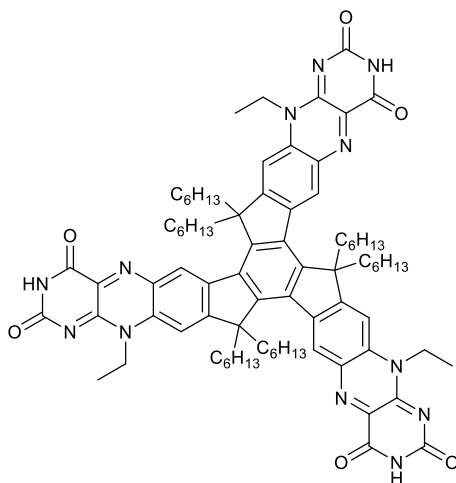
N,N',N''-(5,5,10,10,15,15-Hexahaxyl-3,8,13-trinitro-10,15-dihydro-5*H*-diindeno[1,2-*a*:1',2'-*c*]fluorene-2,7,12-triyl)triacetamide (**4.32**) (1.00 g, 0.870 mmol) was dissolved in dry tetrahydrofuran before being cooled to 0 °C. Lithium aluminium hydride (792 mg, 20.9 mmol) was then added portionwise to the reaction mixture over 10 minutes. The reaction was then left to stir at reflux for 19 h before being cooled to 0 °C and quenched with dropwise addition of water (1 mL), 10% sodium hydroxide (1 mL) and water (3 mL), sequentially. The suspension was stirred for 25 minutes before being filtered and the precipitate washed with diethyl ether (50 mL). The filtrate was concentrated *in vacuo*, extracted with dichloromethane (3 × 50 mL) and washed with water (100 mL). The combined organic layers were then dried over MgSO₄, filtered and concentrated *in vacuo* to produce intermediate N2, N7-diethyl-5,5,10,10,15,15-hexahexyl-N12-isopropyl-10,15-dihydro-5H-diindeno[1,2-a:1',2'-c]fluorene-2,3,7,8,12,13-hexaamine (880 mg, 99%) as a brown oil.

N2,N7-Diethyl-5,5,10,10,15,15-hexahexyl-N12-isopropyl-10,15-dihydro-5H-diindeno[1,2-a:1',2'-c]fluorene-2,3,7,8,12,13-hexaamine (880 mg, 0.860 mmol), alloxan monohydrate (826 mg, 5.16 mmol) and boric anhydride (718 mg, 10.3 mmol) were suspended in glacial acetic acid (48.5 mL). The reaction mixture was then left to stir at 80 °C for 48 h before being extracted in dichloromethane (5 × 100 mL) and washed with water (100 mL). The combined organic layers were then dried over MgSO₄, filtered and concentrated *in vacuo*. The crude product was purified by flash column chromatography on silica gel, gradient elution 30% acetone in dichloromethane to 50% acetone in dichloromethane to produce *N,N',N''*-(5,5,10,10,15,15-hexahaxyl 12-ethyl-5,5,10,10,19,19-

hexahexyl-15,19-dihydro-5H-diindeno[2',1':5,6;2'',1'':7,8]fluoreno[3,2-g]pteridine-14,16(10H,12H)-dione (**4.33**) (54 mg, 5%) as an orange solid. R$_f$ 0.43 (40% acetone in dichloromethane); mp = >300 °C; δ$_H$ (400 MHz, DMSO) 11.47 (3H, s, 3 × NH), 9.16–8.72 (3H, m, 3 × ArH), 8.33 (3H, s, 3 × ArH), 5.09–4.72 (6H, m, 3 × CH$_2$), 3.21–2.99 (6H, m, 3 × CH$_2$), 2.73–2.52 (6H, m, 3 × CH$_2$), 1.42 (9H, t, J 6.9 Hz, 3 × CH$_3$), 1.00–0.68 (48H, m, 24 × CH$_2$), 0.64–0.30 (18H, m, 6 × CH$_3$).

Compound 4.34

N,N',N''-(5,5,10,10,15,15-Hexahaxyl 12-ethyl-5,5,10,10,19,19-hexahexyl-15,19-dihydro-5H-diindeno[2',1':5,6;2'',1'':7,8]fluoreno[3,2-g]pteridine-14,16(10H,12H)-dione (**4.33**) (600 mg, 0.440 mmol) and potassium carbonate (547 mg, 3.96 mmol) were suspended in dry *N,N*-dimethylformamide (48 mL) before 1-iodoheptane (649 μL, 3.96 mmol) was added dropwise. The reaction was then left to stir at 60 °C for 45 h before water (50 mL) was added and the reaction extracted with dichloromethane (3 × 50 mL). the combined organic layers were then dried over MgSO$_4$, filtered and concentrated *in vacuo*. The crude product was purified by flash column chromatography on silica gel, gradient elution 2% acetone in dichloromethane to 5% acetone in dichloromethane before being recrystallised from 2-propanol to produce compound **4.34** (78 mg, 11%) as an orange solid. R$_f$ 0.25 (1% acetone in dichloromethane);mp = >300 °C; ν$_{max}$/cm^{-1} (neat) 2917 (NH), 2342, 1707 (C=O), 1662 (C=N), 1545 (CC), 1455, 1217, 1172; δ$_H$ (400 MHz, CDCl$_3$) 9.17 (3H, s, 3 × ArH), 7.72 (3H, s, 3 × ArH), 5.03–4.96 (6H, m, 3 × CH$_2$), 4.17 (6H, t, *J* 7.5, 3 × CH$_2$), 3.30–3.18 (6H, m, 3 × CH$_2$), 2.31–2.19 (6H, m, 3 × CH$_2$), 1.84–1.72 (6H, m, 3 × CH$_2$), 1.68–1.60 (9H, m, 3 ×

CH₃), 1.49–1.19 (26H, m, 13 × CH$_2$), 1.01–0.70 (43H, m, 17 × CH$_2$, 3 × CH$_3$), 0.54 (18H, t, *J* 7.1, 6 × CH$_3$), 0.52–0.42 (12H, m, 6 × CH$_2$); δ$_C$ (101 MHz, CDCl$_3$) 163.3 (3 × C), 160.1 (3 × C), 155.7 (3 × C), 148.6 (3 × C), 147.5 (3 × C), 138.3 (3 × C), 136.9 (3 × C), 136.8 (3 × C), 136.1 (3 × C), 132.4 (3 × C), 128.6 (3 × CH), 108.4 (3 × CH), 57.7 (3 × C), 42.4 (3 × CH$_2$), 40.5 (3 × CH$_2$), 37.6 (3 × CH$_2$), 31.9 (3 × CH$_2$), 31.6 (3 × CH$_2$), 29.4 (3 × CH$_2$), 29.2 (3 × CH$_2$), 27.9 (3 × CH$_2$), 27.1 (3 × CH$_2$), 24.6 (3 × CH$_2$), 22.8 (3 × CH$_2$), 22.3 (3 × CH$_2$), 14.2 (3 × CH$_3$), 13.9 (6 × CH$_3$), 12.7 (3 × CH$_3$); *m/z* (ESI) 1634.1404 ([M]$^+$ C$_{102}$H$_{144}$N$_{12}$O$_6$ requires 1634.1365).

Compound 4.35
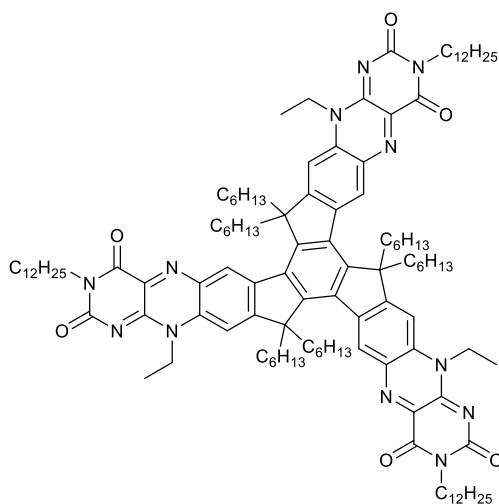
N,N',N''-(5,5,10,10,15,15-Hexahaxyl 12-ethyl-5,5,10,10,19,19-hexahexyl-15,19-dihydro-5H-diindeno[2',1':5,6;2'',1'':7,8]fluo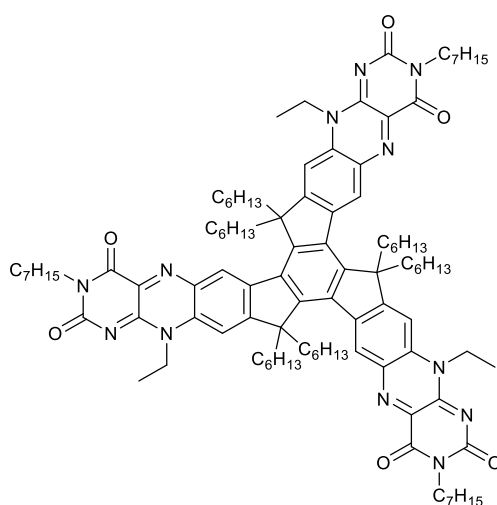reno[3,2-g]pteridine-14,16(10H,12H)-dione (**4.33**) (300 mg, 0.220 mmol) and potassium carbonate (274 mg, 1.98 mmol) were suspended in dry *N,N*-dimethylformamide (24 mL) before 1-iodododecane (488 μL, 1.98 mmol) was added dropwise. The reaction was then left to stir at 60 °C for 17 h before water (20 mL) was added and the reaction extracted with dichloromethane (3 × 50 mL). the combined organic layers were then dried over MgSO$_4$, filtered and concentrated *in vacuo*. The crude product was purified by flash column chromatography on silica gel, gradient elution 2% acetone in dichloromethane to 4% acetone in dichloromethane before being recrystallised from 2-propanol to produce compound **4.35** (78 mg, 11%) as an orange solid. mp = >300 °C; R$_f$ 0.24 (1% acetone in dichloromethane); δ$_H$ (400 MHz, CDCl$_3$) 9.17 (3H, s, 3 × ArH), 7.72 (3H, s, 3 × ArH), 5.03–4.96 (6H, m, 3 × CH$_2$), 4.21–4.13 (6H, m, 3 ×

CH$_2$), 3.27–3.23 (6H, m, 3 × CH$_2$), 2.31–2.19 (6H, m, 3 × CH$_2$), 1.84–1.72 (6H, m, 3 × CH$_2$), 1.64 (9H, t, J 7.2 Hz, 3 × CH$_3$), 1.49–1.19 (54H, m, 27 × CH$_2$), 1.01–0.71 (45H, m, 18 × CH$_2$, 3 × CH$_3$), 0.55 (18H, t, J 7.0 Hz, 6 × CH$_3$), 0.51–0.41 (12H, m, 6 × CH$_2$); δ_C (101 MHz, CDCl$_3$) 163.3 (3 × C), 160.1 (3 × C), 155.7 (3 × C), 148.6 (3 × C), 147.5 (3 × C), 138.3 (3 × C), 136.9 (3 × C), 136.8 (3 × C), 136.1 (3 × C), 132.4 (3 × C), 128.7 (3 × CH), 108.4 (3 × CH), 57.7 (3 × C), 42.5 (3 × CH$_2$), 40.6 (3 × CH$_2$), 37.6 (3 × CH$_2$), 32.1 (6 × CH$_2$), 31.6 (6 × CH$_2$), 29.9 (3 × CH$_2$), 29.8 (6 × CH$_2$), 29.7 (3 × CH$_2$), 29.6 (3 × CH$_2$), 29.5 (6 × CH$_2$), 29.4 (3 × CH$_2$), 28.0 (3 × CH$_2$), 27.2 (3 × CH$_2$), 24.6 (3 × CH$_2$), 22.8 (6 × CH$_2$), 22.3 (6 × CH$_2$), 14.3 (3 × CH$_3$), 13.9 (6 × CH$_3$), 12.7 (3 × CH$_3$); m/z (ESI) 1844.3755 ([M]$^+$ C$_{117}$H$_{174}$N$_{12}$O$_6$ requires 1844.3713).

N-Butyl-9-phenanthrenamine (5.6)[306]
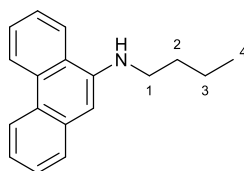
9-Bromophenanthrene (200 mg, 0.778 mmol), butylamine (93.0 µL, 0.934 mmol), tris(dibenzylideneacetone)dipalladium (29.0 mg, 0.031 mmol), tri-*tert*-butylphosphine (16.0 µL, 0.062 mmol) and sodium *tert*-butoxide (105 mg, 1.09 mmol) were dissolved in dry toluene (2 mL) in a 25 mL microwave vial. The mixture was degassed under argon before being sealed and left to stir under reflux for 19.5 h. After cooling to room temperature, the solution was extracted with dichloromethane (3 × 20 mL) and washed with water (40 mL). The combined organic layers were dried over MgSO$_4$, filtered and concentrated *in vacuo*. The crude product was purified by flash column chromatography on silica gel, gradient elution 5% ethyl acetate in petroleum ether to 10% ethyl acetate in petroleum ether to produce *N*-butyl-9-phenanthrenamine (**5.6**) (183 mg, 94%) as a yellow solid. R$_f$ 0.42 (10% ethyl acetate in petroleum ether); δ_H (400 MHz, CDCl$_3$) 8.69 (1H, d, J 7.8 Hz, ArH), 8.53 (1H, d, J 8.8 Hz, ArH), 7.98 (1H, d, J 7.4 Hz, ArH), 7.71 (1H, d, J 7.8 Hz, ArH), 7.69–7.60 (2H, m, 2 × ArH), 7.49 (1H, t, J 7.4 Hz, ArH), 7.42 (1H, t, J 7.8 Hz, ArH), 6.98 (1H, s, ArH), 3.39 (2H, t, J 7.4 Hz, 1-H$_2$), 1.91–1.78 (2H, m, 2-H$_2$), 1.60–1.48 (2H, m, 3-H$_2$), 1.01 (3H, t, J 7.4 Hz, 4-H$_3$); δ_C (101 MHz, CDCl$_3$) 133.5 (C), 132.2 (C), 131.3 (C), 128.7 (CH), 127.1 (CH), 126.8 (CH), 126.7 (CH), 126.6 (CH), 125.4 (C), 123.6 (CH), 122.8 (C), 122.5 (CH), 120.7 (CH), 100.1 (CH), 45.4 (CH$_2$), 31.2 (CH$_2$), 20.7 (CH$_2$), 14.1 (CH$_3$); m/z (ESI) 250.1601 ([M + H]$^+$. C$_{18}$H$_{20}$N requires 250.1597).

9-Butylphenanthro[9,10-*g*]pteridine-11,13(9*H*,12*H*)-dione (5.7)
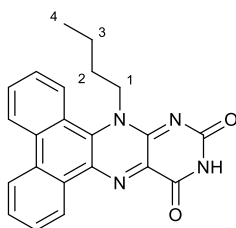
N-Butyl-9-phenanthrenamine (**5.6**) (150 mg, 0.602 mmol) and violuric acid monohydrate (158 mg, 0.903 mmol) were dissolved in glacial acetic acid (5 mL). The reaction was degassed under argon for 20 minutes before being left to stir at 100 °C for 19 h. After cooling to room temperature, the reaction was concentrated *in vacuo*. The crude product was purified by flash column chromatography on silica gel, eluting with 2% methanol in dichloromethane to produce 9-butylphenanthro[9,10-*g*]pteridine-11,13(9*H*,12*H*)-dione (**5.7**) (139 mg, 62%) as an orange solid. R_f 0.21 (2% methanol in dichloromethane); δ_H (400 MHz, DMSO) 11.44 (1H, s, NH), 8.94 (2H, dd, *J* 19.5 Hz, 7.7 Hz, 2 × ArH), 8.82 (1H, d, *J* 7.7 Hz, ArH), 8.51 (1H, d, *J* 8.4 Hz, ArH), 7.98 (1H, t, *J* 7.7 Hz, ArH), 7.89–7.77 (3H, m, 3 × ArH), 4.75 (2H, t, *J* 7.4 Hz, 1-H_2), 2.28–2.01 (2H, m, 2-H_2), 1.47–1.17 (2H, m, 3-H_2), 0.90 (3H, t, *J* 7.4 Hz, 4-H_3); δ_C (101 MHz, DMSO-d6) 160.2 (C), 155.5 (C), 152.8 (C), 135.9 (C), 134.5 (C), 133.9 (C), 132.1 (C), 131.3 (CH), 128.9 (C), 128.7 (CH), 128.5 (CH), 128.0 (CH), 127.0 (CH), 124.8 (C), 124.2 (CH), 123.6 (CH), 123.1 (CH), 122.0 (C), 53.6 (CH_2), 29.1 (CH_2), 19.2 (CH_2), 13.4 (CH_3); *m/z* (ESI) 393.1312 ([M + Na]$^+$ $C_{22}H_{18}N_4NaO_2$ requires 393.1330).

9-Butyl-12-heptylphenanthro[9,10-g]pteridine-11,13(9H,12H)-dione (5.8)
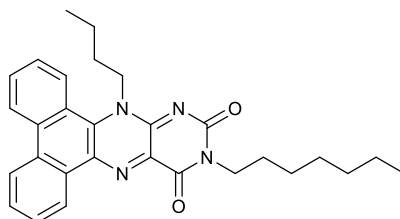
9-Butylphenanthro[9,10-*g*]pteridine-11,13(9*H*,12*H*)-dione (**5.7**) (700 mg, 1.89 mmol) and potassium carbonate (784 mg, 5.67 mmol) were suspended in dry *N*, *N*-dimethylformamide (50 mL) before 1-iodoheptane (930 μL, 5.67 mmol) was added dropwise. The reaction was then left to stir at 50 °C for 20 h before water (50 mL) was added and the reaction extracted with dichloromethane (3 × 50 mL). The combined organic layers were then dried over MgSO$_4$, filtered and concentrated *in vacuo*. The crude product was purified by flash column chromatography on silica gel, gradient elution 1% acetone in dichloromethane to 3% acetone in dichloromethane to produce 9-butyl-12-heptylphenanthro[9,10-g]pteridine-11,13(9*H*,12*H*)-dione (**5.8**) (773 mg, 87%) as an orange solid. R$_f$ 0.82 (40% acetone in dichloromethane); mp = 198–200 °C; ν$_{max}$/cm^{-1} (neat) 2918 (NH), 2358, 1640 (C=N), 1543 (C=C), 1512 (CC), 1209, 754; δ$_H$ (400 MHz, CDCl$_3$) 9.23–9.13 (1H, m, ArH), 8.74 (1H, dd, *J* 8.5, 1.3 Hz, ArH), 8.59–8.51 (1H, m, ArH), 8.40 (1H, dd, *J* 8.5, 1.3 Hz, ArH), 7.90 (1H, ddd, *J* 8.5, 7.0, 1.1 Hz, ArH), 7.81–7.74 (2H, m, 2 × ArH), 7.71 (1H, ddd, *J* 8.5, 7.0, 1.2 Hz, ArH), 4.94 (2H, s), 4.15 (2H, t, *J* 7.4 Hz, CH$_2$), 2.24 (2H, s, CH$_2$), 1.84–1.72 (2H, m, CH$_2$), 1.50–1.23 (10H, m, 5 × CH$_2$), 0.96 (3H, t, *J* 7.4 Hz, CH$_3$), 0.88 (32H, t, *J* 7.0 Hz, CH$_3$); δ$_C$ (101 MHz, CDCl$_3$) 160.3 (C), 155.8 (C), 151.0 (C), 135.3 (C), 134.7 (C), 134.6 (C), 134.0 (C), 133.3 (C), 131.6 (CH), 129.3 (CH), 129.0 (CH), 127.9 (CH), 125.2 (CH), 125.1 (C), 124.9 (CH), 123.9 (C) 122.4 (CH), 122.2 (CH), 54.1 (CH$_2$), 42.3 (CH$_2$), 31.9 (CH$_2$), 30.2 (CH$_2$), 29.2 (CH$_2$), 27.9 (CH$_2$), 27.2 (CH$_2$), 22.8 (CH$_2$), 19.9 (CH$_2$), 14.3 (CH$_3$), 13.7 (CH$_3$); *m/z* (ESI) 491.2413 ([M + Na]$^+$. C$_{29}$H$_{32}$N$_4$NaO$_2$ requires 491.2425).

N-Butylfluoranthren-3-amine (5.9)
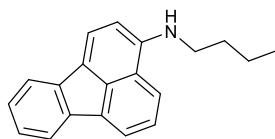
3-Bromofluoranthene (500 mg, 1.78 mmol), butylamine (210 μL, 2.14 mmol), tris(dibenzylideneacetone)dipalladium (65.0 mg, 0.071 mmol), tri-*tert*-butylphosphine (35.0 μL, 0.142 mmol) and sodium *tert*-butoxide (239 mg, 2.49 mmol) were dissolved in dry toluene (5 mL) in a 25 mL microwave vial. The mixture was degassed under argon before being sealed and left to stir under reflux for 18.5 h. After cooling to room temperature, the solution was extracted with dichloromethane (3×50 mL) and washed with water (100 mL). The combined organic layers were dried over $MgSO_4$, filtered and concentrated *in vacuo*. The crude product was purified by flash column chromatography on silica gel, eluting with 10% diethyl ether in petroleum ether to produce *N*-butylfluoranthren-3-amine (**5.9**) (393 mg, 81%) as a pale yellow oil. R_f 0.34 (10% diethyl ether in petroleum ether); δ_H (400 MHz, CDCl$_3$) 7.98 (1H, d, *J* 6.9 Hz, ArH), 7.90 (1H, d, *J* 7.5 Hz, ArH), 7.85 (1H, d, *J* 8.2 Hz, ArH), 7.80 (2H, dd, *J* 7.5 Hz, 1.8 Hz, 2 × ArH), 7.60 (1H, dd, *J* 8.2 Hz, 6.9 Hz, ArH), 7.35 (1H, td, *J* 7.5 Hz, 1.1 Hz, ArH), 7.31–7.25 (2H, m, 2 × ArH), 3.39 (2H, t, *J* 6.9 Hz, CH$_2$), 1.90–1.71 (2H, m, CH$_2$), 1.66–1.45 (2H, m, CH$_2$), 1.04 (3H, t, *J* 7.4 Hz, CH$_3$); *m/z* (ESI) 274.1564 ([M + H]$^+$ C$_{20}$H$_{20}$N requires 274.1597).

**14-Butylfluorantheno[2,3-g]pteridine-10,12(11H,14H)-dione (5.10)**
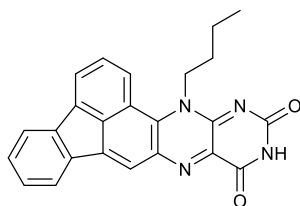
N-Butylfluoranthren-3-amine (**5.9**) (250 mg, 0.91 mmol) and violuric acid monohydrate (240 mg, 1.37 mmol) were dissolved in glacial acetic acid (7 mL). The reaction flask was degassed under argon for 10 minutes before being left to stir at 100 °C for 19 h. After cooling to room temperature, the reaction was concentrated *in vacuo*. The crude product was purified by flash column chromatography on silica gel, gradient elution 15% acetone in dichloromethane to 20% acetone in dichloromethane to produce 14-butylfluorantheno[2,3-g]pteridine-10,12(11H,14H)-dione (**5.10**) (75.6 mg, 21%) as an orange solid. R_f 0.12 (15% acetone in dichloromethane); δ_H (400 MHz, DMSO) 11.49 (1H, s, NH), 8.73 (1H, s, ArH), 8.55 (1H, d, *J* 8.9 Hz, ArH), 8.48 (1H, d, *J* 7.2 Hz, ArH), 8.24 (1H, d, *J* 4.0 Hz, ArH), 8.20–8.12 (2H, m, 2 × ArH), 8.11–7.98 (1H, m, ArH), 7.58–7.43 (2H, m, 2 × ArH), 2.18–2.06 (2H, m, CH$_2$), 1.71–1.61 (2H, m, CH$_2$), 1.32–1.20 (2H, m, CH$_2$), 1.09 (3H, t, *J* 7.2 Hz, CH$_3$); *m/z* (ESI) 417.1339 ([M + Na]$^+$ C$_{24}$H$_{18}$N$_4$NaO$_2$ requires 417.1330).

14-Butyl-11-heptylfluorantheno[2,3-g]pteridine-10,12(11H,14H)-dione (5.11)
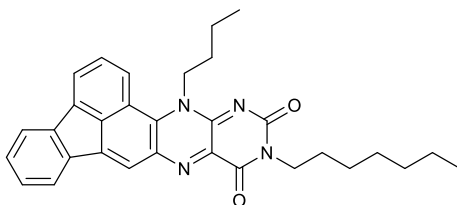
14-Butylfluorantheno[2,3-g]pteridine-10,12(11H,14H)-dione (**5.10**) (600 mg, 1.53 mmol) and potassium carbonate (634 mg, 4.59 mmol) were suspended in dry *N,N*-dimethylformamide (45 mL) before 1-iodoheptane (753 µL, 4.59 mmol) was added dropwise. The reaction was then left to stir at 50 °C for 19 h before water (50 mL) was added and the reaction extracted with dichloromethane (3 ×

50 mL). the combined organic layers were then dried over MgSO$_4$, filtered and concentrated *in vacuo*. The crude product was purified by flash column chromatography on silica gel, gradient elution 100% dichloromethane to 5% acetone in dichloromethane to produce 14-butyl-11-heptylfluorantheno[2,3-g]pteridine-10,12(11H,14H)-dione (**5.11**) (315 mg, 42%) as an orange solid. R$_f$ 0.52 (10% acetone in dichloromethane); mp= 208–210; ν$_{max}$/cm^{-1} (neat) 2925 (NH), 2306, 1705 (C=O), 1650 (C=N), 1548, 1213 (CC), 772; δ$_H$ (400 MHz, CDCl$_3$) 8.40 (1H, s, ArH), 8.35 (1H, d, *J* 8.8, ArH), 8.14 (1H, d, *J* 7.0, ArH), 7.94–7.82 (2H, m, 2 × ArH), 7.86–7.78 (1H, m, ArH), 7.45 (2H, dd, *J* 5.6, 3.0, 2 × ArH), 5.07 (2H, brs, CH$_2$), 4.18–4.09 (2H, m, CH$_2$), 2.20 (2H, brs, CH$_2$), 1.75 (4H, ddt, *J* 18.2, 15.1, 7.5, 2 × CH$_2$), 1.56–1.21 (8H, m, 4 × CH$_2$), 1.14 (3H, t, *J* 7.0, CH$_3$), 0.89 (3H, t, *J* 7.0, CH$_3$); δ$_C$ (101 MHz, CDCl$_3$) 159.9 (C), 155.7 (C), 150.0 (C), 139.1 (C), 138.7 (C), 137.6 (C), 136.5 (C), 136.1 (C), 135.2 (C), 133.6 (C), 129.6 (CH), 129.3 (CH), 129.0 (CH), 125.6 (CH), 123.6 (2 × CH), 122.5 (CH), 121.7 (CH), 120.1 (C), 50.5 (C), 42.3 (CH$_2$), 31.9 (CH$_2$), 29.2 (CH$_2$), 28.9 (CH$_2$), 27.9 (CH$_2$), 27.2 (CH$_2$), 22.8 (CH$_2$), 20.0 (CH$_2$), 14.2 (CH$_3$), 14.0 (CH$_3$); *m/z* (ESI) 493.2614 ([M+H]$^+$. C$_{31}$H$_{33}$N$_4$O$_2$ requires 493.2605).


N-Butyl-9H-fluoren-2-amine (5.12)[307]
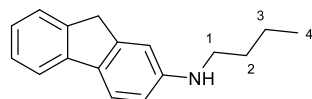
2-Bromo-9*H*-fluorene (150 mg, 0.61 mmol), butylamine (72.0 μL, 0.73 mmol), tris(dibenzylideneacetone)dipalladium (22.0 mg, 0.024 mmol), tri-*tert*-butylphosphine (12.0 μL, 0.049 mmol) and sodium *tert*-butoxide (82.0 mg, 0.850 mmol) were dissolved in dry toluene (2 mL) in a 25 mL microwave vial. The mixture was degassed under argon before being sealed and left to stir under reflux for 19 h. After cooling to room temperature, the solution was extracted with dichloromethane (3 × 20 mL) and washed with water (40 mL). The combined organic layers were then dried over MgSO$_4$, filtered and concentrated *in vacuo*. The crude product was purified by flash column chromatography on silica gel, eluting with 10% diethyl ether in petroleum ether to produce *N*-butyl-9*H*-fluoren-2-amine (**5.12**) (89.0 mg, 61%) as a red solid. R$_f$ 0.25 (10% diethyl ether in petroleum ether); δ$_H$ (400 MHz, CDCl$_3$) 7.61 (1H, d, *J* 7.5 Hz, ArH), 7.57 (1H, d, *J* 8.2 Hz, ArH), 7.45 (1H, d, *J* 7.5 Hz, ArH), 7.30 (1H, t, *J* 7.1 Hz, ArH), 7.16 (1H, td, *J* 7.5 Hz, 1.1 Hz, ArH), 6.80 (1H, d, *J* 1.6 Hz, ArH), 6.63 (1H, dd, *J* 8.2 Hz, 2.2 Hz, ArH), 3.81 (2H, s, CH$_2$), 3.69 (1H, br s, NH), 3.18 (2H, t, *J* 7.1 Hz, 1-H$_2$), 1.73–1.59 (2H, m, 2-H$_2$), 1.52–1.39 (2H, m, 3-H$_2$), 0.98 (3H, t, *J* 7.1 Hz, 4-H$_3$); δ$_C$ (101 MHz,

CDCl$_3$) 148.3 (C), 145.4 (C), 142.6 (C), 142.3 (C), 131.8 (C), 126.7 (CH), 124.8 (CH), 120.8 (CH), 118.5 (CH), 112.0 (CH), 109.2 (CH), 44.2 (CH$_2$), 37.1 (CH$_2$), 31.9 (CH$_2$), 20.5 (CH$_2$), 14.1 (CH$_3$); *m/z* (ESI) 238.1644 ([M + H]$^+$. C$_{17}$H$_{19}$N requires 238.1597).

N-Fluoren-2-yl-butyramide (5.14)
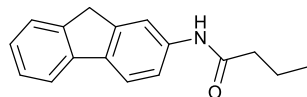
2-Aminofluorene (200 mg, 1.10 mmol) and pyridine (98.0 µL, 1.21 mmol) were dissolved in dry tetrahydrofuran (6 mL) before being cooled to 0 °C. Butyryl chloride (126 µL, 1.21 mmol) was then added dropwise to the reaction mixture before being left to stir at room temperature for 5 h. Water (20 mL) was then added dropwise to the mixture forming a white precipitate which was collected by filtration and recrystallised from ethanol (80 mL) to produce *N*-fluoren-2-yl-butyramide (**5.14**) (190 mg, 69%) as a white solid. δ$_H$ (400 MHz, CDCl$_3$) 7.92 (1H, s, ArH), 7.71 (2H, t, *J* 8.3 Hz, 2 × ArH), 7.52 (1H, d, *J* 7.4 Hz, ArH), 7.36 (2H, t, *J* 7.4 Hz, 2 × ArH), 7.27 (1H, t, *J* 7.4 Hz, ArH), 3.88 (2H, s, CH$_2$), 2.37 (2H, t, *J* 7.4 Hz, CH$_2$), 1.90–1.65 (2H, m, CH$_2$), 1.04 (3H, t, *J* 7.4 Hz, CH$_3$); δ$_C$ (101 MHz, CDCl$_3$) 171.2 (C), 144.4 (C), 143.2 (C), 141.3 (C), 138.0 (C), 136.8 (C), 126.8 (CH), 126.3 (CH), 125.0 (CH), 120.1 (CH), 119.5 (CH), 118.5 (CH), 116.8 (CH), 39.8 (CH$_2$), 37.0 (CH$_2$), 19.1 (CH$_2$), 13.8 (CH$_3$); *m/z* (ESI) 274.1196 ([M + Na]$^+$ C$_{17}$H$_{17}$NNaO requires 274.1210).

N-Butyl-9*H*-fluoren-2-amine (5.12)[307]
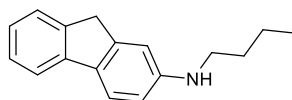
N-Fluoren-2-yl-butyamide (**5.14**) (190 mg, 0.756 mmol) was dissolved in dry tetrahydrofuran (20 mL) before being cooled to 0 °C. Lithium aluminium hydride (115 mg, 3.04 mmol) was then added portionwise to the reaction mixture over 10 minutes. The reaction was then left to stir under reflux

for 20 h before being cooled to 0 °C and quenched with dropwise addition of water (1 mL), 10% sodium hydroxide (1 mL) and water (4 mL), sequentially. The suspension was stirred for 15 minutes before being filtered and the precipitate washed with diethyl ether (20 mL). The filtrate was concentrated *in vacuo*, extracted with diethyl ether (3 × 30 mL) and washed with water (50 mL). The combined organic layers were then dried over $MgSO_4$, filtered and concentrated *in vacuo* to produce *N*-butyl-9*H*-fluoren-2-amine (**5.12**) (148 mg, 99%) as a red solid. R_f 0.25 (10% diethyl ether in petroleum ether); δ_H (400 MHz, $CDCl_3$) 7.61 (1H, d, *J* 7.5 Hz, ArH), 7.57 (1H, d, *J* 8.2 Hz, ArH), 7.45 (1H, d, *J* 7.5 Hz, ArH), 7.30 (1H, t, *J* 7.5 Hz, ArH), 7.16 (1H, td, *J* 7.5 Hz, 1.1 Hz, ArH), 6.80 (1H, d, *J* 2.0 Hz, ArH), 6.63 (1H, dd, *J* 8.2 Hz, 2.0 Hz, ArH), 3.81 (2H, s, CH_2), 3.18 (1H, t, *J* 7.2 Hz, CH_2), 1.71–1.57 (2H, m, CH_2), 1.55–1.38 (2H, m, CH_2), 0.98 (3H, t, *J* 7.2 Hz, CH_3).

2-Bromo-9,9-dihexyl-9*H*-fluorene (5.15)[308]
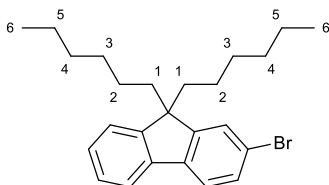
2-Bromo-9*H*-fluorene (500 mg, 2.04 mmol) and potassium *tert*-butoxide (687 mg, 6.12 mmol) were dissolved in dry tetrahydrofuran (4.5 mL) before being cooled to 0 °C. 1-Bromohexane (716 µL, 5.10 mmol) was then added dropwise to the reaction mixture before being left to stir under reflux for 23 h. After cooling to room temperature, the reaction was extracted with diethyl ether (3 × 30 mL) and washed with water (50 mL). The combined organic layers were then dried over $MgSO_4$, filtered and concentrated *in vacuo*. The crude product was purified by flash column chromatography on silica gel, eluting with 10% ethyl acetate in petroleum ether to produce 2-bromo-9,9-dihexyl-9*H*-fluorene (**5.15**) (767 mg, 91%) as a pale-yellow oil. R_f 0.63 (10% ethyl acetate in petroleum ether); δ_H (400 MHz, $CDCl_3$) 7.68–7.63 (1H, m, ArH), 7.57–7.52 (1H, m, ArH), 7.46–7.42 (2H, m, 2 × ArH), 7.34–7.29 (3H, m, 3 × ArH), 2.00–1.88 (4H, m, 1-H_2), 1.19–0.96 (12H, m, 2-H_2, 3-H_2 and 4-H_2), 0.77 (6H, t, *J* 7.1 Hz, 6-H_3), 0.67–0.53 (4H, m, 5-H_2); δ_C (101 MHz, $CDCl_3$) 153.1 (C), 150.5 (C), 140.3 (C), 140.2 (C), 130.0 (CH), 127.6 (CH), 127.1 (CH), 126.3 (CH), 123.0 (CH), 121.2 (CH), 121.1 (C), 119.9 (CH), 55.5 (C), 40.4 (CH_2), 31.6 (CH_2), 29.8 (CH_2), 23.8 (CH_2), 22.7 (CH_2), 14.1 (CH_3); *m/z* (EI$^+$) 412.1752 ([M]$^+$ $C_{25}H_{33}Br$ requires 412.1766).

_N_-Butyl-9,9-dihexylfluoren-2-amine (5.16)
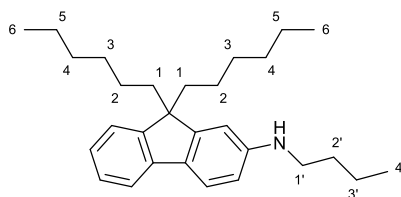
2-Bromo-9,9-dihexyl-9*H*-fluorene (**5.15**) (850 mg, 2.06 mmol), butylamine (245 μL, 2.47 mmol), tris(dibenzylideneacetone)dipalladium (75.0 mg, 0.082 mmol), tri-*tert*-butylphosphine (40.0 μL, 0.165 mmol) and sodium *tert*-butoxide (277 mg, 2.88 mmol) were dissolved in dry toluene (10 mL) in a 25 mL microwave vial. The mixture was degassed under argon before being sealed and left to stir under reflux for 18.5 h. After cooling to room temperature, the solution was extracted with dichloromethane (3 × 50 mL) and washed with water (100 mL). The combined organic layers were dried over MGSO$_4$, filtered and concentrated *in vacuo*. The crude product was purified by flash column chromatography on silica gel, eluting with 5% ethyl acetate in petroleum ether to produce *N*-butyl-9,9-dihexylfluoren-2-amine (**5.16**) (668 mg, 80%) as a yellow oil. R$_f$ 0.38 (5% ethyl acetate in petroleum ether); δ$_H$ (400 MHz, CDCl$_3$) 7.62–7.46 (2H, m, 2 × ArH), 7.32–7.27 (1H, m, ArH), 7.26–7.21 (2H, m, 2 × ArH), 7.16 (1H, t, *J* 7.3 Hz, ArH), 6.60 (1H, s, ArH), 3.19 (1H, t, J 7.3 Hz, NH).1.97–1.80 (4H, m, 2 × CH$_2$), 1.70–1.61 (2H, m, CH$_2$), 1.52–1.40 (2H, m, CH$_2$), 1.34–1.24 (2H, m, CH$_2$), 1.18–1.01 (12H, m, 6 × CH$_2$), 0.89–0.85 (3H, m, CH$_3$), 0.81–0.73 (6H, m, 2 × CH$_3$), 0.71–0.60 (4H, m, 2 × CH$_2$).

13-Butyl-11,11-dihexyl-11,13-dihydro-2H-fluoreno[3,2-g]pteridine-2,4(3H)-dione (5.17)
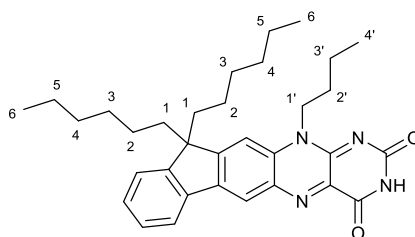
N-Butyl-9,9-dihexylfluoren-2-amine (**5.16**) (650 mg, 1.60 mmol) and violuric acid monohydrate (420 mg, 2.40 mmol) were dissolved in glacial acetic acid (12 mL). The reaction flask was degassed under argon for 10 minutes before being left to stir at 100 °C for 18.5 h. After cooling to room temperature, the reaction was concentrated *in vacuo*. The crude product was purified by flash column chromatography on silica gel, eluting with 15% acetone in dichloromethane to produce 13-butyl-11,11-dihexyl-11,13-dihydro-2H-fluoreno[3,2-g]pteridine-2,4(3H)-dione (**5.17**) (34.3 mg, 4%) as a red solid. R_f 0.37 (15% acetone in dichloromethane); δ_H (400 MHz, CDCl$_3$) 8.55 (1H, s, NH), 7.86–7.80 (1H, m, ArH), 7.62 (1H, d, *J* 7.3 Hz, ArH), 7.46–7.42 (2H, m, 2 × ArH), 7.42–7.38 (1H, m, ArH), 7.28 (2H, dd, *J* 6.0 Hz, 4.3 Hz, 2 × ArH), 2.12–2.02 (4H, m, 2 × CH$_2$), 1.98–1.86 (3H, m, CH$_3$), 1.77–1.68 (2H, m, CH$_2$), 1.64–1.54 (2H, m, CH$_2$), 1.49–1.40 (2H, m, CH$_2$), 1.14–0.99 (12H, m, 6 × CH$_2$), 0.74 (6H, t, *J* 7.0 Hz, 2 × CH$_3$), 0.64–0.52 (4H, m, 2 × CH$_2$); δ_C (101 MHz, CDCl$_3$) 161.8 (C), 159.9 (C), 155.6 (C), 150.1 (C), 143.3 (C), 141.5 (C), 138.0 (C), 136.5 (C), 136.3 (C), 132.5 (C), 129.6 (CH), 128.0 (CH), 123.3 (CH), 122.8 (CH), 121.3 (CH), 119.5 (CH), 56.6 (C), 41.1 (2 × CH$_2$), 31.5 (2 × CH$_2$), 29.6 (2 × CH$_2$), 29.4 (CH$_3$), 24.0 (2 × CH$_2$), 23.9 (2 × CH$_2$), 22.6 (CH$_2$), 20.3 (CH$_2$), 20.1 (CH$_2$), 14.0 (2 × CH$_3$); *m/z* (ESI) 549.3229 ([M + Na]$^+$ C$_{33}$H$_{42}$N$_4$NaO$_4$ requires 549.3208).

13-Butyl-3-heptyl-11,11-dihexyl-11,13-dihydro-2H-fluoreno[3,2-g]pteridine-2,4(3H)-dione (5.18)
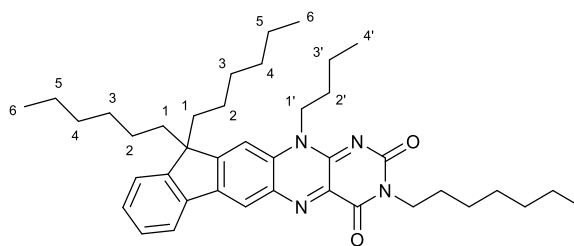
13-Butyl-11,11-dihexyl-11,13-dihydro-2H-fluoreno[3,2-g]pteridine-2,4(3H)-dione (**5.17**) (90 mg, 0.17 mmol) and potassium carbonate (70 mg, 0.51 mmol) were suspended in dry *N*, *N*-dimethylformamide (7 mL) before 1-iodoheptane (84 μL, 0.51 mmol) was added dropwise. The reaction was then left to stir at 50 °C for 20 h before water (25 mL) was added and the reaction extracted with dichloromethane (3 × 25 mL). The combined organic layers were then dried over MgSO$_4$, filtered and concentrated *in vacuo*. The crude product was purified by flash column chromatography on silica gel, gradient elution 1% acetone in dichloromethane to 3% acetone in dichloromethane to produce 13-butyl-3-heptyl-11,11-dihexyl-11,13-dihydro-2H-fluoreno[3,2-g]pteridine-2,4(3H)-dione (**5.18**) (50 mg, 47%) as an orange solid. R$_f$ 0.4 (100% dichloromethane); δ$_H$ (400 MHz, CDCl$_3$) 7.87–7.76 (1H, m, ArH), 7.52 (1H, s, ArH), 7.46–7.35 (4H, m, 4 × ArH), 4.81 (2H, s, CH$_2$), 4.16–4.08 (2H, m, CH$_2$), 2.19–1.95 (4H, m, 2 × CH$_2$), 1.88 (2H, q, J 8.0 Hz, CH$_2$), 1.80–1.68 (2H, m, CH$_2$), 1.59 (2H, dt, J 8.0, 7.2 Hz, CH$_2$), 1.44–1.20 (8H, m, 4 × CH$_2$), 1.16–0.93 (9H, m, 3 × CH$_2$, CH$_3$), 0.91–0.82 (3H, m, CH$_3$), 0.74 (6H, t, J 7.2 Hz, 2 × CH$_3$), 0.71–0.48 (4H, m, 2 × CH$_2$); δ$_C$ (101 MHz, CDCl$_3$) 161.0 (C), 159.9 (C), 155.9 (C), 150.1 (C), 148.6 (C), 140.8 (C), 138.3 (C), 136.4 (C), 136.1 (C), 132.4 (C), 129.4 (CH), 128.0 (CH), 123.2 (CH), 122.8 (CH), 121.2 (CH), 109.1 (CH), 56.5 (C), 42.2 (CH$_2$), 41.1 (CH$_2$), 31.9 (2 × CH$_2$), 31.5 (CH$_2$), 29.6 (CH$_2$), 29.5 (CH$_2$), 29.2 (CH$_2$), 27.9 (CH$_2$), 27.1 (CH$_2$), 24.0 (2 × CH$_2$), 22.7 (CH$_2$), 22.6 (CH$_2$), 20.3 (CH$_2$), 14.2 (CH$_3$), 14.0 (3 × CH$_3$).

6-[Methyl(phenyl)amino]-1,2,3,4-tetrahydropyrimidine-2,4-dione (5.19)[256]
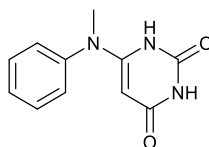
N-Methylaniline (1.50 mL, 13.8 mmol) and 6-chlorouracil (1.03 g, 6.90 mmol) were stirred at 180 °C for 10 mins. The mixture was then cooled to room temperature and the resulting precipitate, formed from adding a mixture of methanol and diethyl ether (1:5), was filtered and collected to give 6-[methyl(phenyl)amino]-1,2,3,4-tetrahydropyrimidine-2,4-dione (**5.19**) (1.10 g, 73%) as a white solid. mp = 298–300 °C (lit.,[309] mp = 302 °C) δ_H (400 MHz, DMSO) 10.43 (1H, s, NH), 10.27 (1H, s, NH), 7.50–7.40 (2H, m, 2 × ArH), 7.38–7.29 (1H, m, ArH), 7.30–7.24 (2H, m, 2 × ArH), 4.26 (1H, d, J 1.3 Hz, CH), 3.25 (3H, s, CH$_3$).

10-Methyl-2H,3H,4H,10H-benzo[g]pteridine-2,4-dione (5.20)[256]
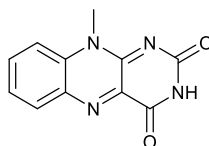
Sodium nitrite (1.75 g, 25.2 mmol) was added to a solution of 6-[methyl(phenyl)amino]-1,2,3,4-tetrahydropyrimidine-2,4-dione (**5.19**) (1.10 g, 5.06 mmol) in glacial acetic acid (44 mL). The resulting mixture was stirred at room temperature for 3 h before being poured into water (88 mL) and stirred for a further 2 h. The resulting precipitate was filtered, washed with water (20 mL) and dried under vacuum. The yellow solid was then added to a solution of sodium dithionite (2.14 g, 12.3 mmol) in water (41 mL). The mixture was stirred at room temperature for 3 h before an aqueous solution of 30% hydrogen peroxide (8.2 mL) was slowly added and left to stir at room temperature for 18 h. The resulting yellow solid was filtered and washed with water (25 mL) and methanol (5 mL) to produce 10-methyl-2H,3H,4H,10H-benzo[g]pteridine-2,4-dione (**5.20**) (936 mg, 78%) as a yellow solid. mp= >300 °C (lit.,[309] 352 °C) ν_{max}/cm^{-1} (neat) 3196 (CH), 3063, 2816 (CH), 1670 (C=N), 1547 (C=N), 1268,

1179, 829 766, 638; δ_H (400 MHz, DMSO) 11.39 (1H, s, NH), 8.13 (1H, d, J 7.8 Hz, ArH), 8.00–7.90 (2H, m, 2 × ArH), 7.68–7.60 (1H, m, ArH), 3.98 (3H, s, CH₃); δ_C (101 MHz, DMSO) 159.7 (C), 155.5 (C), 150.9 (C), 138.6 (C), 134.9 (C), 134.6 (C), 133.3 (CH), 131.6 (CH), 126.0 (CH), 116.5 (CH), 31.9 (CH₃); *m/z* (ESI) 251.0540 (MNa⁺. C₁₁H₈N₄O₂Na requires 251.0547).

3-Heptyl-10-methylbenzo[g]pteridine-2,4(3H,10H)-dione (5.21)
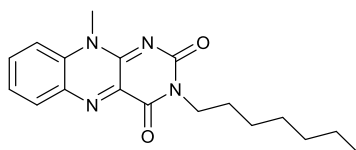
10-Methyl-2H,3H,4H,10H-benzo[g]pteridine-2,4-dione (**5.20**) (700 mg, 3.07 mmol) and potassium carbonate (1.27 g, 9.21 mmol) were suspended in dry *N*, *N*-dimethylformamide (50 mL) before 1-iodoheptane (1.51 mL, 9.21 mmol) was added dropwise. The reaction was then left to stir at 50 °C for 20 h before water (50 mL) was added and the reaction extracted with dichloromethane (3 × 50 mL). The combined organic layers were then dried over MgSO₄, filtered and concentrated *in vacuo*. The crude product was purified by flash column chromatography on silica gel, eluting with 10% acetone in dichloromethane to produce 3-heptyl-10-methylbenzo[g]pteridine-2,4(3H,10H)-dione (**5.21**) (950 mg, 95%). as a yellow solid. mp = 208–210 °C; v_{max}/cm⁻¹ (neat) 2920 (CH), 1714, 1650, (C=N), 1554 (C=N), 1465, 1198, 766; δ_H (400 MHz, CDCl₃) 8.37–8.29 (1H, m, ArH), 7.94–7.86 (1H, m, ArH), 7.67–7.60 (2H, m, 2 × ArH), 4.13 (3H, s, CH₃), 4.10 (2H, d, J 7.6 Hz, CH₂), 1.72 (2H, dt, J 15.2, 7.6 Hz, CH₂), 1.44–1.22 (8H, m, 4 × CH₂), 0.87 (3H, t, J 6.9 Hz, CH₃); δ_C (101 MHz, CDCl₃) 159.6 (C), 155.6 (C), 142.1 (C), 136.1 (C), 135.8 (CH), 134.4 (C), 133.5 (CH), 127.1 (C), 126.6 (CH), 115.2 (CH), 42.4 (CH₃), 32.1 (CH₂), 31.9 (CH₂), 29.2 (CH₂), 27.9 (CH₂), 27.1 (CH₂), 22.8 (CH₂), 14.2 (CH₃); *m/z* (ESI) 349.1633 ([M + Na]⁺ C₁₈H₂₂N₄O₂Na requires 349.1643).

N-Acetylglycine (5.28)[310]
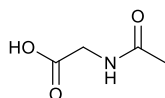
Glycine (600 mg, 8.00 mmol) was suspended in methanol (20 mL) and left to stir at room temperature for 15 minutes before acetic anhydride (2.04 mL, 21.6 mmol) was added. The reaction mixture was then left to stir at 60 °C for 18.5 h before being cooled to room temperature and concentrated *in vacuo*. The crude product was then collected and recrystallised from methanol to give N-acetylglycine (**5.28**) (582 mg, 62%) as a white solid. δ_H (400 MHz, DMSO) 12.49 (1H, s, OH), 8.16 (1H, t, *J* 5.5 Hz, NH), 3.72 (2H, d, *J* 5.5 Hz, CH_2), 1.85 (3H, s, CH_3); δ_C (101 MHz, DMSO) 171.4 (C), 169.6 (C), 40.6 (CH_2), 22.3 (CH_3).

(Z)-4-((9H-Fluoren-2-yl)methylene)-2-methyloxazol-5(4H)-one (5.29)[274]
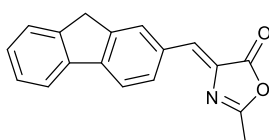
Fluorene-2-carboxaldehyde (301 mg, 1.55 mmol), N-acetylglycine (**5.28**) (200 mg, 1.71 mmol) and sodium acetate (127 mg, 1.55 mmol) were dissolved in acetic anhydride (2 mL) before being left to stir under reflux for 2 h. After cooling to room temperature, ethanol (10 mL) was added dropwise to the reaction mixture forming a precipitate which was collected by filtration to produce (Z)-4-(9H-fluoren-2-yl)methylene)-2-methyloxazol-5(4H)-one (**5.29**) (153 mg, 36%) as a yellow solid. R_f 0.5 (30% ethyl acetate in petroleum ether); v_{max}/cm^{-1} (neat) 2927 (CH), 2029, 1763 (C=O), 1655 (C=N), 1383, 1252, 1160, 894, 729; δ_H (400 MHz, $CDCl_3$) 8.46 (1H, d, *J* 14.1 Hz, ArH), 8.18 (1H, d, *J* 7.9 Hz, ArH), 8.03 (1H, d, *J* 7.9 Hz, ArH), 7.98 (1H, d, *J* 7.0 Hz, ArH), 7.64 (1H, d, *J* 7.0 Hz, ArH), 7.47–7.36 (2H, m, ArH), 7.30 (1H, s, CH), 4.02 (2H, s, CH_2), 2.43 (3H, s, CH_3); δ_C (101 MHz, $CDCl_3$) 173.0 (C), 166.2 (C), 148.2 (C), 144.2 (C), 143.5 (C), 140.2 (C), 133.7 (CH), 131.7 (2 × CH), 130.5 (CH), 127.9 (C), 127.0 (C),

125.3 (CH), 123.5 (CH), 120.9 (CH), 120.4 (CH), 36.3 (CH_2), 15.4 (CH_3); *m/z* (ESI) 298.0834 ([M + Na]$^+$ $C_{18}H_{13}NNaO_2$ requires 298.0846).

(Z)-((9*H*-Fluoren-2-yl)methylene)-1-hexyl-2-methyl-1*H*-imidazol-5(4*H*)-one (5.26)
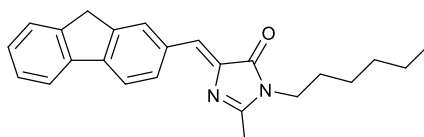
(*Z*)-4-(9*H*-Fluoren-2-yl)methylene)-2-methyloxazol-5(4*H*)-one (**5.29**) (800 mg, 2.91 mmol) and imidazole (20.0 g, 294 mmol) were heated to 140 °C. Hexylamine (671 μL, 5.08 mmol) was added to the reaction mixture once all the imidazole had melted and left to stir at 140 °C for 18 h before being cooled to room temperature. 20% potassium hydroxide solution (50 mL) was then added before being extracted with dichloromethane (3 × 100 mL). The combined organic layers were then dried over MgSO$_4$, filtered and concentrated *in vacuo*. The crude product was then purified by flash column chromatography on silica gel, gradient elution 100% dichloromethane to 40% acetone in dichloromethane to produce (Z)-((9*H*-fluoren-2-yl)methylene)-1-hexyl-2-methyl-1*H*-imidazol-5(4*H*)-one (24 mg, 5%) (**5.26**) as a yellow solid. R$_f$ 0.34 (30% ethyl acetate in petroleum ether); v$_{max}$/cm^{-1} (neat) 3302, 2917 (CH), 2359, 1694 (CO), 1644 (C=C), 1402, 1129 (CN), 768, 728; δ$_H$ (400 MHz, CDCl$_3$) 8.44 (1H, s, C=CH), 8.07 (1H, d, J 8.0 Hz, ArH), 7.81 (2H, d, J 8.0 Hz, 2 × ArH), 7.57 (1H, d, J 7.4 Hz, ArH), 7.44–7.27 (2H, m, 2 × ArH), 7.18 (1H, s, ArH), 3.97 (2H, s, CH$_2$), 3.65–3.57 (2H, m, N-CH$_2$), 2.43 (3H, s, CH$_3$), 1.69–1.59 (2H, m, CH$_2$), 1.35–1.28 (8H, m, 4 × CH$_2$), 0.93–0.85 (3H, m, CH$_3$); *m/z* (ESI) 381.4789 ([M + Na]$^+$ $C_{24}H_{26}N_2NaO$ requires 381.4750).

7-Bromo-9,9-dimethylfluorene-2-carbaldehyde (5.31)[280]
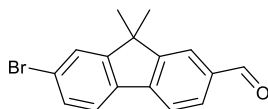
2,7-Dibromo-9,9-dimethylfluorene (1.00 g, 2.84 mmol) was dissolved in dry tetrahydrofuran (7.5 mL) before being cooled to −78 °C. *n*-Butyllithium (1.8 M solution in hexane, 1.58 mL, 2.84 mmol) was then added dropwise and left to stir at −78 °C. After 1 h, dry *N*, *N*-dimethylformamide (0.29 mL) was added dropwise and left to stir for a further 2 h at −78 °C before being warmed to room temperature. Hydrochloric acid (20 mL, 2.0 M) was then poured portionwise into the reaction mixture and stirred before being extracted with ethyl acetate (3 × 50 mL). The combined organic layers were then dried over MgSO$_4$, filtered and concentrated *in vacuo*. The crude product was purified by flash column chromatography on silica gel, gradient elution 10% ethyl acetate in petroleum ether to 30% ethyl acetate in petroleum ether to produce 7-bromo-9,9-dimethylfluorene-2-carbaldehyde (**5.31**) (571 mg, 67%) as an off-white solid. R$_f$ 0.47 (20% ethyl acetate in petroleum ether); δ$_H$ (400 MHz, CDCl$_3$) 10.06 (1H, s, aldehyde H), 7.96 (1H, d, J 0.7 Hz, ArH), 7.87 (1H, dd, J 8.0, 1.4 Hz, ArH), 7.84 (1H, d, J 0.7 Hz, ArH), 7.66 (1H, d, J 8.0 Hz, ArH), 7.61 (1H, d, J 1.4 Hz, ArH), 7.52 (1H, dd, J 8.0, 1.4 Hz, ArH), 1.52 (6H, s, 2 × CH$_3$); δ$_C$ (101 MHz, CDCl$_3$) 192.1 (CH), 157.0 (C), 154.1 (2 × C), 144.6 (C), 136.8 (C), 136.0 (C), 130.8 (CH), 130.7 (CH), 126.7 (CH), 123.3 (CH), 122.7 (CH), 120.5 (CH), 47.4 (C), 26.9 (2 × CH$_3$).

7-(Diphenylamino)-9,9-dimethyl-fluorene-2-carbaldehyde (5.32)[280]
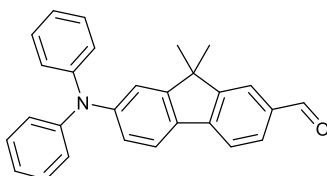
7-Bromo-9,9-dimethyl-fluorene-2-carbaldehyde (**5.31**) (200 mg, 66.0 mmol), diphenylamine (168 mg, 0.990 mmol) and caesium carbonate (323 mg, 0.99 mmol) were suspended in dry toluene (5 mL) and degassed under argon. Tris(dibenzylideneacetone)dipalladium(0) (24 mg, 0.026 mmol) and 2-dicyclohexylphosphino-2',4',6'-triisopropylbiphenyl (25 mg, 0.053 mmol) were added. The reaction was left to stir at reflux for 18 h before being cooled to room temperature. The reaction mixture was then filtered on Celite and washed with ethyl acetate (20 mL) before being concentrated *in vacuo*. The crude product was then purified by flash column chromatography, gradient elution 100% petroleum ether to 20% ethyl acetate in petroleum ether to produce 7-(diphenylamino)-9,9-dimethyl-fluorene-2-carbaldehyde (**5.32**) (208 mg, 81%) as a pale yellow solid. R_f 0.44 (100% petroleum ether); δ_H (400 MHz, CDCl$_3$) 9.99 (1H, s, aldehyde H), 7.91 – 7.86 (1H, m, ArH), 7.80 (1H, dd, J 7.8, 1.4 Hz, ArH), 7.70 (1H, d, J 7.8 Hz, ArH), 7.59 (1H, d, J 8.3 Hz, ArH), 7.32 – 7.19 (4H, m, 4 × ArH), 7.17 – 7.10 (5H, m, 5 × ArH), 7.07 – 6.97 (3H, m, 3 × ArH), 1.41 (6H, s, 2 × CH$_3$).

7 References

1   R. A. Rohde and Z. Hausfather, *Earth Syst. Sci. Data.*, 2020, **12**, 3469–3479.

2   *Nat. Clim. Chang.*, 2022, **12**, 693.

3   J. Song, G. Tong, J. Chao, J. Chung, M. Zhang, W. Lin, T. Zhang, P. M. Bentler and W. Zhu, *Sci. Rep.*, 2023, **13**, 536.

4   A. G. Olabi and M. A. Abdelkareem, in *Renewable Energy Resources and Climate Change Mitigation*, 2011, vol. 158, pp. 161–208.

5   B. Gavurova, M. Rigelsky and V. Ivankova, *Front. Public Health*, 2021, **9**, 1–13.

6   P. C. Jain, *Renew Energy*, 1993, **3**, 403–420.

7   P. A. Owusu and S. Asumadu-Sarkodie, *Cogent Eng*, 2016, **3**, 1167990.

8   R. A. Soref and S. Member, *IEEE*, 1993, **81**, 1687–1706.

9   B. Kumar, B. K. Kaushik and Y. S. Negi, *Polym. Rev.*, 2014, **54**, 33–111.

10   J. C. Slater, *J. Phys. Chem. Solids*, 1959, **8**, 21–25.

11   A. Rockett, *The Materials Science of Semiconductors*, Springer New York, NY, Illinois, Urbana, USA, 1st edn., 2008.

12   A. J. Heeger, *Rev. Mod. Phys.*, 2001, **73**, 681–700.

13   P. Atkins and J. de Paula, in *Atkins' Physical Chemistry*, Oxford University Press, London, England, 10th edn., 2014, pp. 531–559.

14   J. R. Lakowicz, *Principles of Fluorescence Spectroscopy*, Springer New York, NY, 3rd edn., 2013.

15   F. B. Dias, K. N. Bourdakos, V. Jankus, K. C. Moss, K. T. Kamtekar, V. Bhalla, J. Santos, M. R. Bryce and A. P. Monkman, *Adv. Mater.*, 2013, **25**, 3707–3714.

16   P.-A. Will and S. Reineke, in *Handbook of Organic Materials for Electronic and Photonic Devices*, Elsevier, 2019, pp. 695–726.

17   J. Eng and T. J. Penfold, *Chem. Rec.*, 2020, **20**, 831–856.

18   P. Atkins and J. de Paula, in *Atkins' Physical Chemistry*, Oxford University Press, London, England, 10th edn., 2014, pp. 736–785.

19   C. W. Tang and S. A. Vanslyke, *Appl. Phys. Lett*, 1987, **51**, 913–915.

20   Q. Wei, N. Fei, A. Islam, T. Lei, L. Hong, R. Peng, X. Fan, L. Chen, P. Gao and Z. Ge, *Adv. Optical Mater.*, 2018, **6**, 1800512.

21   N. T. Kalyani, H. Swart and S. J. Dhoble, in *Principles and Applications of Organic Light Emitting Diodes (OLEDs)*, ed. S. J. D. N. Thejo Kalyani, Hendrik Swart, Woodhead Publishing, 2017, pp. 141–170.

22   S. J. Zou, Y. Shen, F. M. Xie, J. De Chen, Y. Q. Li and J. X. Tang, *Mater Chem Front*, 2020, **4**, 788–820.

23   Mitsuhiro Koden, *OLED Displays and Lighting*, Wiley-IEEE Press, Japan, 1st edn., 2016.

24   C. Xiang, W. Koo, F. So, H. Sasabe and J. Kido, *Light Sci Appl*, 2013, **2**, e74.

25   F. Zhao and D. Ma, *Mater Chem Front*, 2017, **1**, 1933–1950.

26   B. Geffroy, P. le Roy and C. Prat, *Polym Int*, 2006, **55**, 572–582.

27   J. Bauri, R. B. Choudhary and G. Mandal, *J. Mater. Sci.*, 2021, **56**, 18837–18866.

28   M. Pope, H. P. Kallmann and P. Magnante, *J Chem Phys*, 1963, **38**, 2042–2043.

29   Z. Wang, P. Lu, S. Chen, Z. Gao, F. Shen, W. Zhang, Y. Xu, H. S. Kwok and Y. Ma, *J. Mater. Chem.*, 2011, **21**, 5451–5456.

30   H. Bi, K. Ye, Y. Zhao, Y. Yang, Y. Liu and Y. Wang, *Org Electron*, 2010, **11**, 1180–1184.

31   Y. Huang, *J Phys Conf Ser*, 2023, **2608**, 012012.

32   J. Zhang, D. Ding, Y. Wei, F. Han, H. Xu and W. Huang, *Adv. Mater.*, 2016, **28**, 479–485.

33   Q. Zhang, D. Tsang, H. Kuwabara, Y. Hatae, B. Li, T. Takahashi, S. Y. Lee, T. Yasuda and C. Adachi, *Adv. Mater.*, 2015, **27**, 2096–2100.

34   H. Uoyama, K. Goushi, K. Shizu, H. Nomura and C. Adachi, *Nature*, 2012, **492**, 234–238.

35   J. H. Burroughes, C. A. Jones and R. H. Friend, *Nature*, 1988, **335**, 137–141.

36   G. Horowitz, D. Fichou, X. Peng, Z. Xu and F. Garnier, *Solid State Commun*, 1989, **72**, 381–384.

37   S. Yuvaraja, A. Nawaz, Q. Liu, D. Dubal, S. G. Surya, K. N. Salama and P. Sonar, *Chem Soc Rev*, 2020, **49**, 3423–3460.

38   M. Kus, T. Y. Alic, C. Kirbiyik, C. Baslak, K. Kara and D. A. Kara, in *Handbook of Nanomaterials for Industrial Applications*, Elsevier Inc., 2018, pp. 392–429.

39   Z. A. Lamport, H. F. Haneef, S. Anand, M. Waldrip and O. D. Jurchescu, *J Appl Phys*, 2018, **124**, 071101.

40   Y. Niu, Z. Qin, Y. Zhang, C. Chen, S. Liu and H. Chen, *Mater. Futures*, 2023, **2**, 044401.

41   D. Choi, P. H. Chu, M. McBride and E. Reichmanis, *Chem. Mater*, 2015, **27**, 4167–4168.

42   C. Wang, H. Dong, W. Hu, Y. Liu and D. Zhu, *Chem. Rev.*, 2012, **112**, 2208–2267.

43   J. Sworakowski, *Synth Met*, 2018, **235**, 125–130.

44   H. Liu, D. Liu, J. Yang, H. Gao and Y. Wu, *Small*, 2023, **19**, 2206938.

45   T. Sekitani, U. Zschieschang, H. Klauk and T. Someya, *Nat Mater*, 2010, **9**, 1015–1022.

46   V. Raghuwanshi, D. Bharti and S. P. Tiwari, *Org Electron*, 2016, **31**, 177–182.

47   D. Shukla, S. F. Nelson, D. C. Freeman, M. Rajeswaran, W. G. Ahearn, D. M. Meyer and J. T. Carey, *Chem. Mater*, 2008, **20**, 7486–7491.

48   V. Jindal, S. Mittal and R. Gupta, *Int. J. Eng. Res. Technol.*, 2013, **1**, 40–43.

49   M. Javaid, A. Haleem, S. Rab, R. Pratap Singh and R. Suman, *Sensors International*, 2021, **2**, 100121.

50   M. F. S. Ferreira, E. Castro-Camus, D. J. Ottaway, J. M. López-Higuera, X. Feng, W. Jin, Y. Jeong, N. Picqué, L. Tong, B. M. Reinhard, P. M. Pellegrino, A. Méndez, M. Diem, F. Vollmer and Q. Quan, *J. Opt.*, 2017, **19**, 083001.

51   J. R. Stetter and W. R. Penrose, *Sensors Update*, 2002, **10**, 189–229.

52   K. S. Johnson, J. A. Needoba, S. C. Riser and W. J. Showers, *Chem. Rev.*, 2007, **107**, 623–640.

53   H. Bi and X. Han, *Chemical sensors for environmental pollutant determination*, Elsevier Inc., 2019.

54   H. Nazemi, A. Joseph, J. Park and A. Emadi, *Sensors (Switzerland)*, 2019, **19**, 1285.

55   N. Yamazoe, *Sens Actuators B Chem*, 2005, **108**, 2–14.

56   G. Korotcenkov, *Handbook of Gas Sensor Materials: Properties, Advantages and Shortcomings for Applications*, 2013, vol. 1.

57   D. Long, *IEEE Trans Electron Devices*, 1969, **16**, 836–839.

58   J. Hopkins, K. Fidanovski, A. Lauto and D. Mawad, *Front Bioeng Biotechnol*, 2019, **7**, 1–8.

59   B. B. Patowary, *International Journal of Advanced Research in Electrical, Electronics and Instrumentation Engineering*, 2014, **3**, 9351–9360.

60   D. A. Bernards, R. M. Owens and G. G. Malliaras, *Organic Semiconductors in Sensor Applications*, Springer Berlin Heidelberg, 1st edn., 2008.

61   C. D. Dimitrakopoulos and D. J. Mascaro, *IBM J. Res & Dev.*, 2001, **45**, 11–27.

62   C. Zhang, P. Chen and W. Hu, *Chem. Soc. Rev.*, 2015, **44**, 2087–2107.

63   A. Nasri, M. Pétrissans, V. Fierro and A. Celzard, *Mater Sci Semicond Process*, 2021, **128**, 105744.

64   A. Kumar, P. Jha, A. Singh, A. K. Chauhan, S. K. Gupta, D. K. Aswal, K. P. Muthe and S. C. Gadkari, *Chem Phys Lett*, 2018, **698**, 7–10.

65   X. Zhou, Z. Wang, R. Song, Y. Zhang, L. Zhu, D. Xue, L. Huang and L. Chi, *J. Mater. Chem. C*, 2021, **9**, 1584–1592.

66   G. Tang, S. S. Y. Chen, P. E. Shaw, K. Hegedus, X. Wang, P. L. Burn and P. Meredith, *Polym. Chem.*, 2011, **2**, 2360–2368.

67   D. Zhao and T. M. Swager, *Macromolecules*, 2005, **38**, 9377–9384.

68   I. A. Campbell and G. A. Turnbull, *Phys. Chem. Chem. Phys.*, 2021, **23**, 10791–10798.

69   E. B. Ogugu, R. N. Gillanders, S. Mohammed and G. A. Turnbull, *Phys. Chem. Chem. Phys.*, 2023, **25**, 29548–29555.

70   S.C. Bhatia, in *Adv. Renewable Energy Syst.*, ed. S.C. Bhatia, Woodhead Publishing India, 2014, pp. 1–31.

71   J. Lee, H and Romero, *IPCC, 2023: Summary for Policymakers. In: Climate Change 2023: Synthesis Report. Contribution of Working Groups I, II and III to the Sixth Assessment Report of the Intergovernmental Panel on Climate Change*, 2020.

72   F.-C. Chen, in *Encyclopedia of Modern Optics*, Elsevier, 2nd edn., 2018, vol. 1–5, pp. 220–231.

73   Z. Li, Y. Zhao, X. Wang, Y. Sun, Z. Zhao, Y. Li, H. Zhou and Q. Chen, *Joule*, 2018, **2**, 1559–1572.

74   Best Research-Cell Efficiencies, https://www.nrel.gov/pv/cell-efficiency.html, (accessed 5 September 2023).

75   F. Rehman, I. H. Syed, S. Khanam, S. Ijaz, H. Mehmood, M. Zubair, Y. Massoud and M. Q. Mehmood, *Energy Adv.*, 2023, **2**, 1239–1262.

76   A. Kojima, K. Teshima, Y. Shirai and T. Miyasaka, *J. Am. Chem. Soc.*, 2009, **131**, 6050–6051.

77   H. J. S. Michael M. Lee, Joel Teuscher, Tsutomu Miyasaka, Takurou N. Murakami, *Science*, 2012, **338**, 643–647.

78   O. Ostroverkhova, *Chem. Rev.*, 2016, **116**, 13279–13412.

79   X. Zhao and M. Wang, *Mater Today Energy*, 2018, **7**, 208–220.

80   X. Tong, F. Lin, J. Wu and Z. M. Wang, *Adv. Sci.*, 2015, **3**, 1–18.

81   H. Pan, X. Zhao, X. Gong, H. Li, N. H. Ladi, X. L. Zhang, W. Huang, S. Ahmad, L. Ding, Y. Shen, M. Wang and Y. Fu, *Mater. Horiz.*, 2020, **7**, 2276–2291.

82   A. Marchioro, J. Teuscher, D. Friedrich, M. Kunst, R. Van De Krol, T. Moehl, M. Grätzel and J.-E. Moser, *Nat Photonics*, 2014, **8**, 250–255.

83   D. Ompong and J. Singh, *Org. Electron.*, 2018, **63**, 104–108.

84   M. Stolterfoht, C. M. Wolff, Y. Amir, A. Paulke, L. Perdigón-Toro, P. Caprioglio and D. Neher, *Energy Environ. Sci.*, 2017, **10**, 1530–1539.

85   S. Li, Y. L. Cao, W. H. Li and Z. S. Bo, *Rare Metals*, 2021, **40**, 2712–2729.

86   J. A. Christians, R. C. M. Fung and P. V. Kamat, *J Am Chem Soc*, 2014, **136**, 758–764.

87   P. Qin, S. Tanaka, S. Ito, N. Tetreault, K. Manabe, H. Nishino, M. K. Nazeeruddin and M. Grätzel, *Nat Commun*, 2014, **5**, 3834.

88   S. Ye, W. Sun, Y. Li, W. Yan, H. Peng, Z. Bian, Z. Liu and C. Huang, *Nano Lett*, 2015, **15**, 3723–3728.

89   A. Velusamy, S. Yau, C.-L. Liu, Y. Ezhumalai, P. Kumaresan and M.-C. Chen, *J. Chin. Chem. Soc.*, 2023, **70**, 2046–2063.

90   J. H. Heo, S. H. Im, J. H. Noh, T. N. Mandal, C.-S. Lim, J. A. Chang, Y. H. Lee, H. Kim, A. Sarkar, Md. K. Nazeeruddin, M. Grätzel and S. Il Seok, *Nat Photonics*, 2013, **7**, 486–491.

91 W. S. Yang, J. H. Noh, N. J. Jeon, Y. C. Kim, S. Ryu, J. Seo and S. Il Seok, *Science* , 2015, **348**, 1234–1237.

92 D. Xu, Z. Gong, Y. Jiang, Y. Feng, Z. Wang, X. Gao, X. Lu, G. Zhou, J. M. Liu and J. Gao, *Nat Commun*, 2022, **13**, 7020.

93 X. Li, X. Tang, Y. Yang, T. Ye, D. Wu, H. Wang, J. Li and X. Wang, *Prog. Photovolt. Res. Appl.*, 2018, **26**, 994–1002.

94 S. A. Krishna, A. C. Grimsdale, A. Krishna and A. Andrew, *J. Mater. Chem. A*, 2017, **5**, 16446–16466.

95 Z. Hawash, L. K. Ono and Y. Qi, *Adv. Mater. Interfaces*, 2018, **5**, 1700623.

96 J. Wang, X. Wu, Y. Liu, T. Qin, K. Zhang, N. Li, J. Zhao, R. Ye, Z. Fan, Z. Chi and Z. Zhu, *Adv. Energy Mater.*, 2021, **11**, 2100967.

97 X. Liu, X. Ding, Y. Ren, Y. Yang, Y. Ding, X. Liu, A. Alsaedi, T. Hayat, J. Yao and S. Dai, *J. Mater. Chem. C*, 2018, **6**, 12912–12918.

98 M. Cheng, C. Chen, X. Yang, J. Huang, F. Zhang, B. Xu and L. Sun, *Chem. Mater*, 2015, **27**, 1808–1814.

99 Y. Shen, K. Deng and L. Li, *Small Methods*, 2022, **6**, 2200757.

100 W. Sun, M. Zhang, S. Wang, F. Cao, J. Zou, Y. Du, Z. Lan and J. Wu, *J. Mater. Chem. C*, 2021, **9**, 7726–7733.

101 H. S. Kim, C. R. Lee, J. H. Im, K. B. Lee, T. Moehl, A. Marchioro, S. J. Moon, R. Humphry-Baker, J. H. Yum, J. E. Moser, M. Grätzel and N. G. Park, *Sci Rep*, 2012, **2**, 1–7.

102 G. W. Kim, G. Kang, J. Kim, G. Y. Lee, H. Il Kim, L. Pyeon, J. Lee and T. Park, *Energy Environ Sci*, 2016, **9**, 2326–2333.

103 C. H. Teh, R. Daik, E. L. Lim, C. C. Yap, M. A. Ibrahim, N. A. Ludin, K. Sopian and M. A. Mat Teridi, *J. Mater. Chem. A*, 2016, **4**, 15788–15822.

104 M. Ulfa, T. Zhu, F. Goubard and T. Pauporté, *J. Mater. Chem. A*, 2018, **6**, 13350–13358.

105 F. Di Giacomo, S. Razza, F. Matteocci, A. D'Epifanio, S. Licoccia, T. M. Brown and A. Di Carlo, *J Power Sources*, 2014, **251**, 152–156.

106 J. Luo, J. Xia, H. Yang, H. A. Malik, F. Han, H. Shu, X. Yao, Z. Wan and C. Jia, *Nano Energy*, 2020, **70**, 104509.

107   W. Zhang, L. Wang, Y. Guo, B. Zhang, V. Leandri, B. Xu, Z. Li, J. M. Gardner, L. Sun and L. Kloo, *Chem. Commun*, 2020, **56**, 1589–1592.

108   Y. Li, H. Li, C. Zhong, G. Sini and J.-L. Brédas, *npj Flexible Electronics*, 2017, **1**, 2.

109   G. Ren, W. Han, Y. Deng, W. Wu, Z. Li, J. Guo, H. Bao, C. Liu and W. Guo, *J. Mater. Chem. A*, 2021, **9**, 4589–4625.

110   X. Yang, H. Wang, B. Cai, Z. Yu and L. Sun, *J. Energy Chem.*, 2018, **27**, 650–672.

111   J. Urieta-Mora, I. Garcí a-Benito, A. Molina-Ontoria and N. Martí, *Chem. Soc. Rev.*, 2018, **47**, 8541–8571.

112   M. Urbani, G. De La Torre, M. K. Nazeeruddin and T. Torres, *Chem. Soc. Rev.*, 2019, **48**, 2738–2766.

113   A. Abate, T. Leijtens, S. Pathak, J. Teuscher, R. Avolio, M. E. Errico, J. Kirkpatrik, J. M. Ball, P. Docampo, I. McPherson and H. J. Snaith, *Phys. Chem. Chem. Phys.*, 2013, **15**, 2572–2579.

114   F. Lamberti, T. Gatti, E. Cescon, R. Sorrentino, A. Rizzo, E. Menna, G. Meneghesso, M. Meneghetti, A. Petrozza and L. Franco, *Chem*, 2019, **5**, 1806–1817.

115   W. Zhang, F. Zhang, B. Xu, Y. Li, L. Wang, B. Zhang, Y. Guo, J. M. Gardner, L. Sun and L. Kloo, *ACS Appl. Mater. Interfaces*, 2020, **12**, 33751–33758.

116   S. Wang, W. Yuan and Y. S. Meng, *ACS Appl. Mater. Interfaces*, 2015, **7**, 24791–24798.

117   T. H. Schloemer, J. A. Christians, J. M. Luther and A. Sellinger, *Chem. Sci.*, 2019, **10**, 1904–1935.

118   E. J. Juarez-Perez, M. R. Leyden, S. Wang, L. K. Ono, Z. Hawash and Y. Qi, *Chem. Mater*, 2016, **28**, 5702–5709.

119   U. Bach, D. Lupo, P. Comte, J. E. Moser, F. Weissörtel, J. Salbeck, H. Spreitzer and M. Grätzel, *Nature*, 1998, **395**, 583–585.

120   H. J. Snaith and M. Grätzel, *Appl. Phys. Lett*, 2006, **89**, 262114.

121   J. Krüger, R. Plass, L. Cevey, M. Piccirelli, M. Grätzel and U. Bach, *Appl. Phys. Lett*, 2001, **79**, 2085.

122   J. Hong Noh, N. Joong Jeon, Y. Chan Choi, M. K. Nazeeruddin and M. Grätzel, *J Mater Chem A Mater*, 2013, **1**, 11842–11847.

123 G. Zhu, L. Yang, C. Zhang, G. Du, N. Fan, Z. Luo, X. Zhang and J. Zhang, *ACS Appl Energy Mater*, 2022, **5**, 3595–3604.

124 Y. Liu, Y. Hu, X. Zhang, P. Zeng, F. Li, B. Wang, Q. Yang and M. Liu, *Nano Energy*, 2020, **70**, 104483.

125 L. Vaghi and F. Rizzo, *Sol. RRL*, 2023, **7**, 2201108.

126 N. J. Jeon, H. G. Lee, Y. C. Kim, J. Seo, J. H. Noh, J. Lee and S. Il Seok, *J Am Chem Soc*, 2014, **136**, 7837–7840.

127 D. Tomkute-Luksiene, M. Daskeviciene, T. Malinauskas, V. Jankauskas, R. Degutyte, R. Send, N. G. Pschirer, H. Wonneberger, I. Bruder, V. Getautis and A. Substituent, *RSC Adv*, 2016, **6**, 60587–60594.

128 Z. Deng, M. He, Y. Zhang, F. Ullah, K. Ding, J. Liang, Z. Zhang, H. Xu, Y. Qiu, Z. Xie, T. Shan, Z. Chen, H. Zhong and C. C. Chen, *Chem. Mater*, 2021, **33**, 285–297.

129 N. Onozawa-Komatsuzaki, D. Tsuchiya, S. Inoue, A. Kogo, T. Funaki, M. Chikamatsu, T. Ueno and T. N. Murakami, *ACS Appl Energy Mater*, 2022, **5**, 6633–6641.

130 M. Cariello, N. Pant, A. H. Harkiss, F. M. Tracey, J. Cameron, P. J. Skabara, P. J. Holliman, P. Docampo and G. Cooke, *Mol. Syst. Des. Eng*, 2022, **7**, 899–905.

131 Z. Hawash, L. K. Ono, S. R. Raga, M. V. Lee and Y. Qi, *Chem. Mater*, 2015, **27**, 562–569.

132 C. D. Bailie, E. L. Unger, S. M. Zakeeruddin, M. Grätzel and M. D. McGehee, *Phys. Chem. Chem. Phys.*, 2014, **16**, 4864–4870.

133 A. Mahapatra, D. Prochowicz, M. M. Tavakoli, S. Trivedi, P. Kumar and P. Yadav, *J. Mater. Chem. A*, 2020, **8**, 27–54.

134 A. Cabrera-Espinoza, S. Collavini and J. L. Delgado, *Sustainable Energy Fuels*, 2020, **4**, 3264–3281.

135 J. Wang, Z. Yu, D. D. Astridge, Z. Ni, L. Zhao, B. Chen, M. Wang, Y. Zhou, G. Yang, X. Dai, A. Sellinger and J. Huang, *ACS Energy Lett*, 2022, **7**, 3353–3361.

136 J. Ali, J. Song, Y. Li, K. Qian, Q. Zhang, G. Zhou, M. Zhang, L. Zhu, C. Qiu, J. Xu, J. Wang, R. Haider, W. Feng, H. Hu, H. Zhu, Y. Zhang and F. Liu, *J. Mater. Chem. C*, 2019, **7**, 11932–11942.

137 M. Chen, M. Z. Mokhtar, E. Whittaker, Q. Lian, B. Hamilton, P. O'Brien, M. Zhu, Z. Cui, S. A. Haque and B. R. Saunders, *Nanoscale*, 2017, **9**, 10126–10137.

138   Y. Ko, Y. Kim, C. Lee, Y. Kim and Y. Jun, *Synth Met*, 2019, **249**, 47–51.

139   J. Peng, J. I. Khan, W. Liu, E. Ugur, T. Duong, Y. Wu, H. Shen, K. Wang, H. Dang, E. Aydin, X. Yang, Y. Wan, K. J. Weber, K. R. Catchpole, F. Laquai, S. De Wolf and T. P. White, *Adv. Mater. Chem.*, 2018, **8**, 1801208.

140   M. Taguchi, A. Suzuki, N. Ueoka and T. Oku, *AIP Conf. Proc.*, 2019, **2067**, 020018.

141   S. Mete, K. G. Goswami and P. De, *J. Polym. Sci.*, 2020, **58**, 766–778.

142   W. K. Czerwinski, *Macromol.*, 1995, **28**, 5405–5410.

143   N. Elgrishi, K. J. Rountree, B. D. McCarthy, E. S. Rountree, T. T. Eisenhart and J. L. Dempsey, *J Chem Educ*, 2018, **95**, 197–206.

144   R. R. Gagne, C. A. Koval and G. C. Lisensky, *Inorg. Chem.*, 1980, **19**, 285–2857.

145   Z. Yu and L. Sun, *Adv Energy Mater*, 2015, **5**, 1–17.

146   J.-L. Bredas, *Mater. Horiz.*, 2014, **1**, 17–19.

147   E. A. A. Alkhudhayr, D. Sirbu, M. Fsadni, B. Vella, B. T. Muhammad, P. G. Waddell, M. R. Probert, T. J. Penfold, T. Hallam, E. A. Gibson and P. Docampo, *ACS Appl Energy Mater*, 2023, **6**, 11573–11582.

148   M. L. Petrus, K. Schutt, M. T. Sirtl, E. M. Hutter, A. C. Closs, J. M. Ball, J. C. Bijleveld, A. Petrozza, T. Bein, T. J. Dingemans, T. J. Savenije, H. Snaith and P. Docampo, *Adv. Energy Mater.*, 2018, **8**, 1801605.

149   S. Daskeviciute-Geguziene, Z. Yi, K. Rakstys, G. Kreiza, S. B. Khan, H. Kanda, S. Paek, M. Daskeviciene, A. M. A. Egidijus Kamarauskas, Vygintas Jankauskas, V. Getautis and M. K. Nazeeruddin, *Angew. Chem., Int. Ed.*, 2022, **61**, e202113207.

150   L. K. Ono, S. R. Raga, M. Remeika, A. J. Winchester, A. Gabe and Y. Qi, *J. Mater. Chem. A*, 2015, **3**, 15451–15456.

151   A. Binek, M. L. Petrus, N. Huber, H. Bristow, Y. Hu, T. Bein and P. Docampo, *ACS Appl. Mater. Interfaces*, 2016, **8**, 12881–12886.

152   M. Saliba, S. Orlandi, T. Matsui, S. Aghazada, M. Cavazzini, J. P. Correa-Baena, P. Gao, R. Scopelliti, E. Mosconi, K. H. Dahmen, F. De Angelis, A. Abate, A. Hagfeldt, G. Pozzi, M. Graetzel and M. K. Nazeeruddin, *Nat Energy*, 2016, **1**, 15017.

153   K. H. Hendriks, W. Li, G. H. L. Heintges, G. W. P. Van Pruissen, M. M. Wienk and R. A. J. Janssen, *J. Am. Chem. Soc.*, 2014, **136**, 11128–11133.

154   F. Zhang, S. Wang, H. Zhu, X. Liu, H. Liu, X. Li, Y. Xiao, S. M. Zakeeruddin and M. Grätzel, *ACS Energy Lett*, 2018, **3**, 1145–1152.

155   F. Zhang, Z. Wang, H. Zhu, N. Pellet, J. Luo, C. Yi, X. Liu, H. Liu, S. Wang, X. Li, Y. Xiao, S. M. Zakeeruddin, D. Bi and M. Grätzel, *Nano Energy*, 2017, **41**, 469–475.

156   I. M. Abdellah, T. H. Chowdhury, J. J. Lee, A. Islam, M. K. Nazeeruddin, M. Gräetzel and A. El-Shafei, *Sustainable Energy Fuels*, 2021, **5**, 199–211.

157   M. Zhai, M. Li, Z. Deng, R. Yao, L. Wang, C. Chen, H. Wang, X. Ding, L. Liu, X. Li and M. Cheng, *ACS Energy Lett.*, 2023, **8**, 4966–4975.

158   M. Koole, R. Frisenda, M. L. Petrus, M. L. Perrin, H. S. J. Van Der Zant and T. J. Dingemans, *Org Electron*, 2016, **34**, 38–41.

159   M. L. Petrus, A. Music, A. C. Closs, J. C. Bijleveld, M. T. Sirtl, Y. Hu, T. J. Dingemans, T. Bein and P. Docampo, *J. Mater. Chem. A*, 2017, **5**, 25200–25210.

160   P.-H. Lin, K.-M. Lee, C.-C. Ting and C.-Y. Liu, *J. Mater. Chem. A*, 2019, **7**, 5934–5937.

161   A. Jegorove, C. Momblona, M. Daškeviciene, A. Magomedov, R. Degutyte, A. M. Asiri, Vygintas Jankauskas, A. A. Sutanto, H. Kanda, K. Brooks, N. Klipfel, M. K. Nazeeruddin and V. Getautis, *Sol. RRL*, 2022, **6**, 21000990.

162   B. Wang, Q. Zeng, Z. Sun, S. Xue and M. Liang, *Dyes and Pigments*, 2019, **165**, 81–89.

163   K. Nozaki, K. Takahashi, K. Nakano, T. Hiyama, H.-Z. Tang, M. Fujiki, S. Yamaguchi and K. Tamao, *Angew. Chem. Int. Ed.*, 2003, **42**, 2051–2053.

164   J. Jia, L. Duan, Y. Chen, X. Zong, Z. Sun, Q. Wu and S. Xue, *RSC Adv.*, 2019, **9**, 216–223.

165   Q. Chen, X. Li, T. Jiu, S. Ma, J. Li, X. Xiao and W. Zhang, *Dyes and Pigments*, 2017, **147**, 113–119.

166   L. H. Slooff, A. R. Burgers and M. G. Debije, *High and Low Concentration for Solar Electric Applications III*, 2008, **7043**, 704306.

167   J. Burschka, F. Kessler, M. K. Nazeeruddin and M. Grätzel, *Chem. Mater*, 2013, **25**, 2986–2990.

168   J. C. Hindson, B. Ulgut, R. H. Friend, N. C. Greenham, B. Norder, A. Kotlewski and T. J. Dingemans, *J. Mater. Chem.*, 2010, **20**, 937–944.

169 D. Sek, A. Iwan, B. Jarzabek, B. Kaczmarczyk, J. Kasperczyk, Z. Mazurak, M. Domanski, K. Karon and M. Lapkowski, *Macromol.*, 2008, **41**, 6653–6663.

170 M. Del Poeta, W. A. Schell, C. C. Dykstra, S. Jones, R. R. Tidwell, A. Czarny, M. Bajic, M. Bajic, A. Kumar, D. Boykin and J. R. Perfect, *Antimicrob. Agents Chemother.*, 1998, **42**, 2495–2502.

171 S. Che, Z. Yang, I. Popovs, H. Luo, Y. Luo, W. Guo, H. Chen, T. Wang, K. Jie, C. Wang and S. Dai, *Chem. Commun.*, 2019, **55**, 13450–13453.

172 S. A. Wagay, I. A. Rather and R. Ali, *Chemistry Select*, 2019, 4, 12272–12288.

173 S. Gámez-Valenzuela, M. Echeverri, B. Gómez-Lor, J. I. Martínez and M. C. Ruiz Delgado, *J. Mater. Chem. C*, 2020, **8**, 15416–15425.

174 N. Méndez-Gil, S. Gámez-Valenzuela, M. Echeverri, G. H. Suyo, M. Iglesias, M. C. R. Delgado and B. Gómez-Lor, *Adv. Mater. Chem.*, 2024, 2316754.

175 E. Johnston, A. M. Haughey, M. Scullion, A. L. Kanibolotsky, P. J. Skabara and N. Laurand, *2019 IEEE 2nd British and Irish Conference on Optics and Photonics (BICOP)*, 2019, 1–4.

176 A. M. Haughey, B. Guilhabert, A. L Kanibolotsky, P. J Skabara, M. D Dawson, G. A Burley and N. Laurand, *Biosens. Bioelectron.*, 2014, **54**, 679–686.

177 S. Alvi and R. Ali, *Beilstein J. Org. Chem.*, 2021, **17**, 1374–1384.

178 M. Echeverri, S. Gámez-Valenzuela, R. C. González-Cano, J. Guadalupe, S. Cortijo-Campos, J. T. López Navarrete, M. Iglesias, M. C. Ruiz Delgado and B. Gómez-Lor, *Chem. Mater*, 2019, **31**, 6971–6978.

179 F. S. Stanley, *J. Chem. Soc., Trans.,* 1893, **65**, 269–290.

180 T. Anuj and P. Chetti, *J. Phys. Org. Chem.*, 2019, **32**, e3944.

181 J.-S. Yang, H.-H. Huang and S.-H. Lin, *J. Org. Chem.*, 2009, **74**, 3974–3977.

182   and M.-C. L. Jye-Shane Yang, Yar-Ru Lee, Jyu-Lun Yan, *Org. Lett.*, 2006, **8**, 5813–5816.

183 K. F. Lang, M. Zander and E. A. Theiling, *Chem. Ber.*, 1960, **93**, 321–325.

184 K. Hartke and A. Schilling-Pindur, *Liebigs Ann. Chem.*, 1984, **3**, 552–563.

185 J. Bergman and B. Egestad, *Chem. Scr.*, 1986, **26**, 287.

186 Y. N. Oded and I. Agranat, *Tetrahedron Lett*, 2014, **55**, 636–638.

187 O. de Frutos, B. Gomez-Lor, T. Granier, M. A. Monge, E. Gutierrez-Puebla and A. M. Echavarren, *Angew. Chem., Int. Ed.*, 1999, **338**, 204–207.

188 J. Pei, J. L. Wang, X. Y. Cao, X. H. Zhou and W. Bin Zhang, *J. Am. Chem. Soc.*, 2003, **125**, 9944–9945.

189 K. Shi, J. Y. Wang and J. Pei, *Chem. Rec*, 2015, **15**, 52–78.

190 P. Dai, H. Dong, M. Liang, H. Cheng, Z. Sun and S. Xue, *ACS Sustainable Chem. Eng.*, 2017, **5**, 97–104.

191 Y. Sun, K. Xiao, Y. Liu, J. Wang, J. Pei, G. Yu and D. Zhu, *Adv. Funct. Mater.*, 2005, **15**, 818–822.

192 Z. Yang, B. Xu, J. He, L. Xue, Q. Guo, H. Xia and W. Tian, *Org. Electron.*, 2009, **10**, 954–959.

193 H. Zhou, X. Zhao, T. Huang, R. Lu, H. Zhang, X. Qi, P. Xue, X. Liu and X. Zhang, *Org. Biomol. Chem.*, 2011, **9**, 1600–1607.

194 M. Sen Yuan, Z. Q. Liu and Q. Fang, *J. Org. Chem.*, 2007, **72**, 7915–7922.

195 J. M. J. Fréchet, *J. Polym. Sci. Part a: Polym. Chem.:*, 2003, **41**, 3713–3725.

196 Y. Jiang, L. Wang, Y. Zhou, Y.-X. Cui, J. Wang, Y. Cao and J. Pei, *Chem. Asian J.*, 2009, **4**, 548–553.

197 B. Kaur, D. Moghe, A. Dey, D. Kabra and J. Jacob, *J. Lumin.*, 2018, **196**, 511–519.

198 R. Sharma, D. Volyniuk, C. Popli, O. Bezvikonnyi, J. V. Grazulevicius and R. Misra, *J. Phys. Chem. C*, 2018, **122**, 15614–15624.

199 C. Di, G. Yu, Y. Liu and D. Zhu, *J. Phys. Chem. B*, 2007, **111**, 14083–14096.

200 S. Mula, T. Han, T. Heiser, P. Lévêque, N. Leclerc, A. P. Srivastava, A. Ruiz-Carretero and G. Ulrich, *Chem. Eur. J*, 2019, **25**, 8304–8312.

201 P. Li, F. Wu, Y. Fang, H. Dahiya, M. L. Keshtov, H. Xu, A. Agrawal and G. D. Sharma, *ACS Appl. Energy Mater.*, 2002, **5**, 2279–2289.

202 F. Tang, K. Wu, Z. Zhou, G. Wang, Y. Pei, B. Zhao and S. Tan, *Dyes and Pigments*, 2018, **156**, 276–284.

203 Y. Fu and N. S. Finney, *RSC Adv.*, 2018, **8**, 29051–29061.

204 B. Valeur and N. Berberan-santos, *J. Chem. Educ.*, 2011, 731–738.

205   M. Sen Yuan, Q. Wang, W. Wang, D. E. Wang, J. Wang and J. Wang, *Analyst*, 2014, **139**, 1541–1549.

206   P. Sam-Ang, D. Raksasorn, M. Sukwattanasinitt and P. Rashatasakhon, *RSC Adv.*, 2014, **4**, 58077–58082.

207   C. Ruiz-Capillas and A. M. Herrero, *Foods*, 2019, **8**, 62.

208   L. Franceschelli, A. Berardinelli, S. Dabbou, L. Ragni and M. Tartagni, *Sensors*, 2021, **21**, 1373.

209   M. J. Bezdek, S. X. L. Luo, K. H. Ku and T. M. Swager, *Proc. Natl. Acad. Sci. U. S. A.*, 2021, **118**, e2022515118.

210   M. Khatib and H. Haick, *ACS Nano*, 2022, **16**, 7080–7115.

211   J. L. Klockow, K. S. Hettie and T. E. Glass, in *Comprehensive Supramolecular Chemistry II*, Elsevier, Second Edi., 2017, vol. 8, pp. 447–467.

212   Z. Li and K. S. Suslick, *ACS Sens*, 2016, **1**, 1330–1335.

213   W. Wojnowski, K. Kalinowska, T. Majchrzak, J. Płotka-Wasylka and J. Namieśnik, *Sensors*, 2019, **19**, 1580.

214   C. Chen, J. Zhang and T. Delaurentis, *Int. J. Production Economics*, 2014, **152**, 188–199.

215   K. Lin, B. Xie, Z. Wang, R. Xie, Y. Huang, C. Duan, F. Huang and Y. Cao, *Org Electron*, 2018, **52**, 42–50.

216   A. L. Kanibolotsky, R. Berridge, P. J. Skabara, I. F. Perepichka, D. D. C. Bradley and M. Koeberg, *J. Am. Chem. Soc.*, 2004, **126**, 13695–13702.

217   T. C. Lin, B. K. Tsai, T. Y. Huang, W. Chien, Y. Y. Liu, M. H. Li and M. Y. Tsai, *Dyes and Pigments*, 2015, **120**, 99–111.

218   A. Niemz, J. Imbriglio and V. M. Rotello, *J. Am. Chem. Soc.*, 1997, **119**, 887–892.

219   S. L. J. Tan, M. L. Novianti and R. D. Webster, *J. Phys. Chem. B*, 2015, **119**, 14053–14064.

220   F. Fries and S. Reineke, *Sci Rep*, 2019, **9**, 15638.

221   C. Yao, Y. Yu, X. Yang, H. Zhang, Z. Huang, X. Xu, G. Zhou, L. Yue and Z. Wu, *J. Mater. Chem. C*, 2015, **3**, 5783–5794.

222   L. O. Pålsson, C. Wang, D. L. Russell, A. P. Monkman, M. R. Bryce, G. Rumbles and I. D. W. Samuel, *Chem Phys*, 2002, **279**, 229–237.

223   X. Xu, Y. Zhao, X. Zhou, Y. Wu and G. He, *Phys. Status Solidi A*, 2021, **218**, 2100064.

224   M. Sarma, L. M. Chen, Y. S. Chen and K. T. Wong, *Materials Science & Engineering R*, 2022, **150**, 100689.

225   R. S. Andre, L. A. Mercante, M. H. M. Facure, R. C. Sanfelice, L. Fugikawa-Santos, T. M. Swager and D. S. Correa, *ACS Sens.*, 2022, **7**, 2104–2131.

226   T. Hossen and K. Sahu, *J. Phys. Chem. A*, 2018, **122**, 2394–2400.

227   B. C. Wang, H. R. Liao, J. C. Chang, L. Chen and J. T. Yeh, *J Lumin*, 2007, **124**, 333–342.

228   H. Liu, Y. Wang, W. Mo, H. Tang, Z. Cheng, Y. Chen, S. Zhang, H. Ma, B. Li and X. Li, *Adv. Funct*, 2020, **30**, 1910275.

229   G. P. Neupane, W. Ma, T. Yildirim, Y. Tang, L. Zhang and Y. Lu, *Nano Materials Science*, 2019, **1**, 246–259.

230   T. B. Singh, N. S. Sariciftci and J. G. Grote, in *Organic Electronics*, eds. Tibor Grasser, Gregor Meller and Ling Li, Springer, Berlin, Heidelberg, 2009, pp. 73–112.

231   J. Richtar, P. Heinrichova, D. H. Apaydin, V. Schmiedova, C. Yumusak, A. Kovalenko, M. Weiter, N. S. Sariciftci and J. Krajcovic, *Molecules*, 2018, **23**, 2271.

232   A. Sheldrick, D. Müller, A. Günther, P. Nieto and O. Dopfer, *Phys. Chem. Chem. Phys*, 2018, **20**, 7407–7414.

233   S. Weber and E. Schleicher, *Flavins and Flavoproteins. Methods in Molecular Biology (Methods and Protocols)*, Springer New York, 1st edn., 2014.

234   A. Sancar, *Chem. Rev.*, 2003, **103**, 2203–2237.

235   T. O. Baldwin, J. A. Christopher, F. M. Raushel, J. F. Sinclair, M. M. Ziegler, A. J. Fisher and I. Rayment, *Curr Opin Struct Biol*, 1995, **5**, 798–809.

236   C. T. Walsh and T. A. Wencewicz, *Nat. Prod. Rep.*, 2013, **30**, 175–200.

237   P. F. Heelis, *Chem Soc Rev*, 1982, **11**, 15–39.

238   X. Yu, S. Eymur, V. Singh, B. Yang, M. Tonga, A. Bheemaraju, G. Cooke, C. Subramani, D. Venkataraman, R. J. Stanley and V. M. Rotello, *Phys. Chem. Chem. Phys.*, 2012, **14**, 6749–6754.

239   S. O. Mansoorabadi, C. J. Thibodeaux and H. W. Liu, *J. Org. Chem.*, 2007, **72**, 6329–6342.

240   B. H. Robert H Van Den Heuvel, M. W. Fraaije, W. J. H Van Berkel, S. A. Susin, H. K. Lorenzo, N. Zamzami, I. Marzo, B. E. Snow, G. M. Brothers, J. Mangion, E. Jacotot, P. Costantini, M. Loeffler, N. Larochette, D. R. Goodlett, R. Aebersold, D. P. Siderovski, J. M. Penninger and G. Kroemer, in *Methods in Enzymology*, ed. L. P. Chandan K. Sen, Elsevier, 2002, vol. 353, pp. 177–186.

241   L. N. Mataranga-Popa, I. Torje, T. Ghosh, M. J. Leitl, A. Späth, M. L. Novianti, R. D. Webster and B. König, *Org. Biomol. Chem.*, 2015, **13**, 10198–10204.

242   V. Srivastava, P. K. Singh, A. Srivastava and P. P. Singh, *RSC Adv.*, 2021, **11**, 14251–14259.

243   M. Oka, D. Katsube, T. Tsuji and H. Iida, *Org. Lett.*, 2020, **22**, 9244–9248.

244   N. Mohammed, A. A. Wiles, M. Belsley, S. S. M. Fernandes, M. Cariello, V. M. Rotello, M. M. M. Raposo and G. Cooke, *RSC Adv.*, 2017, **7**, 24462–24469.

245   N. Jürgensen, M. Ackermann, T. Marszalek, J. Zimmermann, A. J. Morfa, W. Pisula, U. H. F. Bunz, F. Hinkel and G. Hernandez-Sosa, *ACS Sustainable Chem. Eng.*, 2017, **5**, 5368–5372.

246   R. Abbel, A. P. H. J. Schenning and E. W. Meijer, *J. Polym. Sci., Part A: Polym. Chem.*, 2009, **47**, 4215–4233.

247   D. Neher, *Macromol. Rapid Commun.*, 2001, **22**, 1365–1385.

248   A. C. Grimsdale and K. Mullen, in *Polyfluorenes. Advances in Polymer Science*, ed. D. Scherf, U., Neher, Springer, Berlin, Heidelberg, 2008, vol. 212, pp. 1–48.

249   F. Yoneda, Y. Sakuma, M. Ichiba and K. Shinomura, *J. Am. Chem. Soc.*, 1976, **98**, 830–835.

250   D. Kumar, K. R. J. Thomas, Y. L. Chen, Y. C. Jou and J. H. Jou, *Tetrahedron*, 2013, **69**, 2594–2602.

251   J. N. Ikumi Kawajiri, Masaya Nagahara, Hiroyuki Ishikawa, Yuma Yamamoto and and T. K. Chitoshi Kitamura, *Can. J. Chem.*, 2017, **95**, 371–380.

252   C. Zhang, L. Zhang, C. Sun, W. Sun and X. Liu, *Org. Lett.*, 2019, **21**, 3476–3480.

253   J. Koziol, *Photochem. Photobiol.*, 1969, **9**, 45–53.

254   S. L. J. Tan and R. D. Webster, *J. Am. Chem. Soc*, 2012, **134**, 5954–5964.

255   P. Bairi, B. Roy and A. K. Nandi, *Chem. Commun*, 2012, **48**, 10850–10852.

256 M. Cariello, B. Dietrich, L. Thomson, V. Gauci, A. Boyer, S. Sproules, G. Cooke, A. Seddon and D. J. Adams, *Chem. Eur. J*, 2022, **28**, e202201725.

257 O. Shimomura, K. H. Johnson and Y. O. Saiga, *J Cell Comp Physiol*, 1962, **59**, 223–239.

258 M. Chalfie, Y. Tu, G. Euskirchen, W. W. Ward and D. C. Prasher, *Science (1979)*, 1994, **263**, 802–805.

259 T. P. Singh and R. Shunmugam, *New J. Chem.*, 2016, **40**, 3024–3027.

260 V. Fernández-Luna, R. D. Costa and P. B. Coto, *Angew. Chem. Int. Ed.*, 2018, **130**, 8962–8973.

261 K. Suhling, J. Siegel, D. Phillips, P. M. W. French, S. Lévêque-Fort, S. E. D. Webb and D. M. Davis, *Biophysical J.*, 2002, **83**, 3589–3595.

262 M. W. D. David W. Piston, George H. Patterson, Jennifer Lippincott-Schwartz, Nathan S. Claxton, Introduction to Fluorescent Proteins, https://www.microscopyu.com/techniques/fluorescence/introduction-to-fluorescent-proteins, (accessed 25 September 2023).

263 R. Y. Tsien, *Annu. Rev. Biochem*, 1998, **67**, 509–544.

264 F. Cardarelli, *Int. J. Mol. Sci.*, 2020, **21**, 4164.

265 E. Sahai, J. Wyckoff, U. Philippar, J. E. Segall, F. Gertler and J. Condeelis, *BMC Biotechnol*, 2005, **5**, 14.

266 M. D. Weber, L. Niklaus, M. Pröschel, P. B. Coto, U. Sonnewald and R. D. Costa, *Adv. Mater.*, 2015, **27**, 5493–5498.

267 S. Sönmezoğlu, Y. Ulusu, F. Gedikli, Ö. A. Snmezolu and I. Gökçe, *Philos Mag Lett*, 2012, **92**, 211–216.

268 B. Yujian You, Y. He, P. E. Burrows, S. R. Forrest, N. A. Petasis and M. E. Thompson, *Adv. Mater.*, 2000, **12**, 1678–1681.

269 A. Salih, in *Optical Biomimetics*, ed. M. Large, Woodhead Publishing, Sydney, Australia, 1st edn., 2012, pp. 199–233.

270 L. Yang, S. Nian, G. Zhang, E. Sharman, H. Miao, X. Zhang, X. Chen, Y. Luo and J. Jiang, *Sci Rep*, 2019, **9**, 11640.

271 T. D. Craggs, *Chem. Soc. Rev.*, 2009, **38**, 2865–2875.

272 E. A. Dolgopolova, A. M. Rice, M. D. Smith and N. B. Shustova, *Inorg. Chem.*, 2016, **55**, 7257–7264.

273 S. Kojima, H. Ohkawa, T. Hirano, S. Maki, H. Niwa, M. Ohashi, S. Inouye and F. I. Tsuji, *Tetrahedron Lett.*, 1998, **39**, 5239–5242.

274 M. Jiang, Z. He, Y. Zhang, H. H. Y. Sung, J. W. Y. Lam, Q. Peng, Y. Yan, K. S. Wong, I. D. Williams, Y. Zhao and B. Z. Tang, *J. Mater. Chem. C*, 2017, **5**, 7191–7199.

275 E. L. Glaisyer, M. S. Watt and K. I. Booker-Milburn, *Org. Lett.*, 2018, **20**, 5877–5880.

276 C. Y. Lee, Y. C. Chen, H. C. Lin, Y. Jhong, C. W. Chang, C. H. Tsai, C. L. Kao and T. C. Chien, *Tetrahedron*, 2012, **68**, 5898–5907.

277 F. V. Subach and V. V. Verkhusha, *Chem. Rev.*, 2012, **112**, 4308–4327.

278 J. Dong, F. Abulwerdi, A. Baldridge, J. Kowalik, K. M. Solntsev and L. M. Tolbert, *J. Am. Chem. Soc.*, 2008, **130**, 14096–14098.

279 S. Trasa'tti, *Pure Appl. Chem.*, 1986, **58**, 955–966.

280 V. Singh, S. Wang and E. T. Kool, *J. Am. Chem. Soc.*, 2013, **135**, 6184–6191.

281 J. Praz, J. Graff, L. Egger, L. Guénée, S. Wagschal, E. P. Kündig and A. Alexakis, *Chem. Commun.*, 2015, **51**, 16912–16915.

282 W. Song, R. L. Strack, N. Svensen and S. R. Jaffrey, *J. Am. Chem. Soc.*, 2014, **136**, 1198–1201.

283 M. J. Frisch, G. W. Trucks, H. B. Schlegel, G. E. Scuseria, M. A. Robb, J. R. Cheeseman, G. Scalmani, V. Barone, G. A. Petersson, H. Nakatsuji, M. C. X. Li, A. Marenich, J. Bloino, B. G. Janesko, R. Gomperts, B. Mennucci, H. P. Hratchian, J. V. Ortiz, A. F. Izmaylov, J. L. Sonnenberg, D. Williams-Young, F. Ding, F. Lipparini, F. Egidi, J. Goings, B. Peng, A. Petrone, T. Henderson, D. Ranasinghe, V. G. Zakrzewski, J. Gao, N. Rega, G. Zheng, W. Liang, M. Hada, M. Ehara, K. Toyota, R. Fukuda, J. Hasegawa, M. Ishida, T. Nakajima, Y. Honda, O. Kitao, H. Nakai, T. Vreven, K. Throssell, Jr. J. A. Montgomery, J. E. Peralta, F. Ogliaro, M. Bearpark, J. J. Heyd, E. Brothers, K. N. Kudin, V. N. Staroverov, T. Keith, R. Kobayashi, J. Normand, K. Raghavachari, A. Rendell, J. C. Burant, S. S. Iyengar, J. Tomasi, M. Cossi, J. M. Millam, M. Klene, C. Adamo, R. Cammi, J. W. Ochterski, R. L. Martin, K. Morokuma, O. Farkas, J. B. Foresman and D. J. Fox, 2016.

284 J. J. P. Stewart, *J. Mol. Model.*, 2008, **14**, 499–535.

285   J. J. P. Stewart, *J. Mol. Model.*, 2007, **13**, 1173–1213.

286   A. D. Becke, *J. Chem. Phys.*, 1993, **98**, 5648–5652.

287   C. Lee, W. Yang and R. G. Parr, *Phys. Rev. B*, 1988, **37**, 785.

288   R. Krishnan, J. S. Binkley, R. Seeger and J. A. Pople, *J. Chem. Phys.*, 1980, **72**, 650–654.

289   W. F. Jiang, H. L. Wang, A. G. Wang and Z. Q. Li, *Synth Commun*, 2008, **38**, 1888–1895.

290   H. J. Martin, I. Kampatsikas, R. Oost, M. Pretzler, E. Al-Sayed, A. Roller, G. Giester, A. Rompel and N. Maulide, *Chem. Eur. J*, 2018, **24**, 15756–15760.

291   Y. Z. Fan, C. H. Chen and G. S. Liou, *Macromol Rapid Commun*, 2019, **40**, 1900118.

292   S. Chakravarty, S. J. Sarma, L. N. Goswami, Q. Y. Cai, E. M. Shapiro, M. F. Hawthorne and L. Ma, *Chem. Commun.*, 2019, **55**, 12348–12351.

293   C. Chanthad, K. A. Masser, K. Xu, J. Runt and Q. Wang, *J Mater Chem*, 2012, **22**, 341–344.

294   Z. Wu, B. Han, C. Zhang, D. Zhu and Z. Yang, *Polymer (Guildf)*, 2019, **179**, 121605.

295   Y. Sugiyama, N. Endo, K. Ishihara, Y. Kobayashi, H. Hamamoto, T. Shioiri and M. Matsugi, *Tetrahedron*, 2015, **71**, 4958–4966.

296   Y. Xue, P. Guo, H. L. Yip, Y. Li and Y. Cao, *J. Mater. Chem. A*, 2017, **5**, 3780–3785.

297   S. G. Modha, M. V. Popescu and M. F. Greaney, *J. Org. Chem.*, 2017, **82**, 11933–11938.

298   S. H. Lau, P. Yu, L. Chen, C. B. Madsen-Duggan, M. J. Williams and B. P. Carrow, *J. Am. Chem. Soc.*, 2020, **142**, 20030–20039.

299   S. S. Meng, F. Li, X. Tang and A. S. C. Chan, *Org. Lett.*, 2023, **25**, 3718–3722.

300   H. Kaku, A. Mitarai, N. Okamoto, K. Tanaka, S. Ichikawa, T. Yamamoto, M. Inai, T. Nishii, M. Horikawa and T. Tsunoda, *Eur. J. Org. Chem.*, 2018, **2018**, 6991–6999.

301   B. Derince, K. Gorgun, Y. Caglar and M. Caglar, *J. Mol. Struct.*, 2022, **1250**, 131689.

302   M. Denißen, R. Hannen, D. Itskalov, L. Biesen, N. Nirmalananthan-Budau, K. Hoffmann, G. J. Reiss, U. Resch-Genger and T. J. J. Müller, *Chem. Commun.*, 2020, **56**, 7407–7410.

303   M. Feofanov, V. Akhmetov, R. Takayama and K. Amsharov, *Org. Biomol. Chem.*, 2021, **19**, 7172–7175.

304   X. R. Jia, H. J. Yu, J. Chen, W. J. Gao, J. K. Fang, Y. S. Qin, X. K. Hu and G. Shao, *Chem. Eur. J*, 2018, **24**, 19053–19059.

305   E. V. Dehmlow and T. Kelle, *Synth. Commun.*, 1997, **27**, 2021–2031.

306   J. L. Jeffrey, E. S. Bartlett and R. Sarpong, *Angew. Chem., Int. Ed.*, 2013, **52**, 2194–2197.

307   R. Adam, J. R. Cabrero-Antonino, K. Junge, R. Jackstell and M. Beller, *Angew. Chem., Int. Ed.*, 2016, **55**, 11049–11053.

308   J. W. Liu, Y. N. Xu, C. Y. Qin, Z. N. Wang, C. J. Wu, Y. H. Li, S. Wang, K. Y. Zhang and W. Huang, *Dalton Trans.,* 2019, **48**, 13305–13314.

309   M. Á. Farrán, R. M. Claramunt, C. López, E. Pinilla, M. R. Torres and J. Elguero, *Arkivoc*, 2007, **2007**, 20–38.

310   F. Ke, Y. Xu, S. Zhu, X. Lin, C. Lin, S. Zhou and H. Su, *Green Chem.,* 2019, **21**, 4329–4333.